



# Low-complexity direct-detection optical OFDM systems for high data rate communications

Fatima Barrami

► **To cite this version:**

Fatima Barrami. Low-complexity direct-detection optical OFDM systems for high data rate communications. Signal and Image processing. Université Grenoble Alpes, 2015. English. <NNT : 2015GREAT057>. <tel-01223935>

**HAL Id: tel-01223935**

**<https://tel.archives-ouvertes.fr/tel-01223935>**

Submitted on 3 Nov 2015

**HAL** is a multi-disciplinary open access archive for the deposit and dissemination of scientific research documents, whether they are published or not. The documents may come from teaching and research institutions in France or abroad, or from public or private research centers.

L'archive ouverte pluridisciplinaire **HAL**, est destinée au dépôt et à la diffusion de documents scientifiques de niveau recherche, publiés ou non, émanant des établissements d'enseignement et de recherche français ou étrangers, des laboratoires publics ou privés.

## THÈSE

Pour obtenir le grade de

## DOCTEUR DE L'UNIVERSITÉ DE GRENOBLE

Spécialité : **Signal, image, parole, télécoms (SIPT)**

Arrêté ministériel : 7 août 2006

Présentée par

**Fatima BARRAMI**

Thèse dirigée par **Emil NOVAKOV** et  
codirigée par **Yannis LE GUENNEC**

préparée au sein du **Laboratoire IMEP-LAHC**  
dans l'**École Doctorale EEATS**

# Low-complexity direct-detection optical OFDM systems for high data rate communications

(Systèmes OFDM optiques à détection directe à complexité  
réduite pour les communications à haut débit)

Thèse soutenue publiquement le **09 Avril 2015**,  
devant le jury composé de :

**Mme. AUPETIT-BERTHELEMOT Christelle**

Professeur, Université de Limoges (Rapporteur)

**M. Mohammad-Ali KALIGHI**

Maître de conférences, Ecole centrale de Marseille (Rapporteur)

**M. Bruno FRACASSO**

Professeur, Telecom Bretagne (Président)

**M. Emil, NOVAKOV**

Professeur, Université de Joseph-Fourier (Directeur de thèse)

**M. Yannis LE GUENNEC**

Maître de conférences, IMEP-LAHC/INPG (Co-directeur de thèse)

**M. Pierre BUSSON**

Ingénieur, STMicroelectronics (Co-encadrant de thèse)

**M. Jean-Marc Brossier**

Professeur, Université de Joseph-Fourier (Invité)

**M. Jean-Marc Duchamp**

Maître de conférences, IMEP-LAHC/INPG (Invité)



*To my mother...*

# Acknowledgments

Ce travail de thèse est le fruit de plusieurs rencontres instructives avec de nombreuses personnes à qui je tiens à exprimer mes plus vifs remerciements.

Ma reconnaissance s'adresse au premier à Yannis Le Guennec, qui a encadré ce travail de thèse. Je le remercie vivement pour toutes les heures qu'il a consacrées à ma thèse. Grâce à ses grandes compétences professionnelles, ses qualités humaines, sa patience, sa disponibilité, ses suggestions et son encadrement sans faille, j'ai pu mener à bien ce projet. Sa compréhension, son soutien, ses encouragements et ses précieux conseils m'ont beaucoup aidé à surmonter les difficultés et pallier les obstacles.

Je tiens à remercier vivement Emil Novakov, pour avoir accepté de diriger cette thèse. Je le remercie pour sa détermination et toute l'aide qu'il m'a apportée. Je le remercie pour avoir toujours trouvé les bonnes solutions et pris les bonnes décisions pour remédier aux différentes difficultés rencontrées tout au long de cette thèse, notamment vis-à-vis du changement de sujet.

Je remercie très sincèrement Jean-Marc Duchamp, pour avoir accepté d'encadrer ma thèse. Je le remercie pour son accompagnement, son soutien, sa disponibilité et ses explications. Grâce à sa compréhension, sa patience et ses grandes compétences professionnelles, j'ai pu acquérir un solide bagage dans un domaine qui m'était inexploré.

Je tiens à remercier Pascal Urard et Pierre Busson pour la confiance qu'ils m'ont accordée en m'offrant l'opportunité de réaliser cette thèse dans une société prestigieuse et connue mondialement telle que STMicroelectronics. Cette thèse était une expérience extrêmement enrichissante tant sur le plan professionnel qu'humain.

J'adresse toute ma gratitude à Christelle Aupetit-Berthelemot et Ali Kalighi pour avoir accepté de rapporter ma thèse et pour leurs remarques précieuses. J'exprime mes

remerciements respectueux à Bruno Fracasso et Jean-Marc Brossier pour avoir accepté d'évaluer ma thèse en tant qu'examineurs. Je remercie vivement tous les membres du jury pour m'avoir fait l'honneur d'assister à ma soutenance. Malgré les imprévus et les circonstances défavorables, grâce à leurs compétences professionnelles et qualités humaines et l'intérêt qu'ils ont apporté à mon travail de thèse, la soutenance a été un moment d'échange très agréable et enrichissant.

Je remercie tout particulièrement Nicolas CORRAO pour toutes les heures qu'il a consacrées à mes manip. Grâce à sa disponibilité, sa patience, sa compréhension, ses explications et sa pédagogie, j'ai pu mener à bien la partie expérimentale de la thèse.

Je remercie vivement tout le personnel du laboratoire IMEP/LAHC, notamment Brigitte, Annaïck, Joelle, Valerie, Dalila, Isabelle..., pour leur gentillesse, leur sympathie, leur disponibilité, leur compréhension et leur bonne humeur. Je tiens à remercier tout particulièrement Chahla pour son accueil chaleureux, pour sa sympathie et pour tous ses compliments.

Je tiens à exprimer toute ma reconnaissance à Amine Didioui pour tous ses conseils et son soutien tout au long de la thèse. Je reconnais entièrement que sans tes conseils précieux tout au long de ces années, je ne serais pas où j'en suis aujourd'hui. Je te remercie vivement pour l'aide précieuse que tu m'as apportée pour l'organisation du pot de thèse.

Un grand merci à tous mes amis au labo et en dehors du labo : Julien, Mirna, Kanza, Pierre, Vitor, Ramin, Alexandra, Paco, Alfredo, Inès, Hamza, Dahbia, Leila, Aline, Eva, Sotiris, Cecilia, Tapas.. , pour la bonne ambiance, pour leur soutien et les sorties de ski. Un merci particulier à Thomas BENOIST pour ses conseils très précieux qui m'ont apporté une grande aide au moment le plus difficile de cette thèse.

Finalement, le plus grand merci va à la personne exceptionnelle qui a fait de moi ce que je suis aujourd'hui, ma chère maman. Je ne te remercierais jamais assez pour tous les sacrifices que tu as faits pour moi. Je te remercie pour ta compréhension, ta bonne écoute et tes conseils. Je te remercie pour avoir subi, avec une grande patience, mes mauvaises humeurs. Tu as toujours su trouver les mots pour me reconforter, m'aider à me surpasser et vaincre toutes les difficultés. Je remercie également mon père, pour toute son aide, ses conseils, son inquiétude et son amour.

# Abstract

Intensity Modulation and Direct Detection (IM/DD) systems with vertical-cavity surface-emitting lasers (VCSELs) provide a cost effective solution for high data rate short-range optical communications. A possible approach to maximize the data rate per wavelength, is to employ the high spectral efficiency discrete multitone (DMT) modulation. Many DMT-based unipolar techniques compatible with IM/DD systems have been proposed to match the light source characteristic. DC biased optical OFDM (DCO-OFDM) and asymmetrically clipped optical OFDM (ACO-OFDM) are the most popular. The power consumption and cost of optical OFDM are still the major obstacles to its market development. The work presented in this thesis mainly focuses on optimizing the power consumption and cost of optical OFDM. The high power consumption stems essentially from the high computational power of the digital signal processor employed to generate digital OFDM waveforms. Indeed, all the proposed DFT-based unipolar OFDM techniques deal with the Hermitian symmetry property to generate real OFDM signals, thus increasing the power consumption and the system cost. To address this issue, we have first developed novel techniques permitting to discard the use of Hermitian symmetry in DMT modulations. These techniques consist in generating a conventional complex OFDM signal and juxtaposing the real and imaginary parts in the time domain to obtain a real OFDM signal. The proposed techniques offer a gain up to 75% in computation complexity, thus significantly reducing the power consumption and the system cost. Several works aiming to improve the optical power efficiency of IM/DD systems have been proposed in the literature, namely Hybrid techniques. However, the obtained gain comes at the expense of increased system complexity and cost. To overcome this issue, we have proposed an asymmetric linear companding algorithm permitting to reduce the optical power of conventional DCO-OFDM modulation with a moderate complexity. The proposed technique is shown

to offer a gain of about 4dB in optical power over conventional DMT techniques. VCSELS have been shown to be cost effective electrical to optical converters for IM/DD systems. VCSELS have particular heating properties as compared to conventional light sources, especially for large dynamic signals. To take into account the particular heating properties of VCSELS, we have developed a new VCSEL behavioral model based on the use of the VCSEL quasi-static characteristic to accurately evaluate the VCSEL impact on DMT modulations. Most of the works concerned with DMT modulation schemes for IM/DD systems are based on computer simulations. In this work, we have built an experimental system to experimentally validate our techniques. Thus, the experimental results show that companded DCO-OFDM offers a gain up to 4.75dB in SNR over conventional DMT modulations. The impact of the optical link on the DMT signal was also measured. The simulation results based on the use of the new VCSEL model are shown to perfectly fit the measurements.

# Resumé

Les systèmes en modulation d'intensité et détection directe (IM/DD) basés sur les VCSEL (Vertical-Cavity Surface-Emitting Lasers) présentent une solution à bas coût pour les communications à courte distance et haut débit. Une approche pour augmenter le débit par longueur d'onde, est d'utiliser la modulation DMT (Discrete Multitone) à haute efficacité spectrale. Plusieurs techniques DMT compatibles avec les systèmes IM/DD ont été proposées dans la littérature. DCO-OFDM (DC biased optical OFDM) et ACO-OFDM (Asymmetrically Clipped optical OFDM) sont le plus courantes. La consommation en puissance et le coût de l'OFDM optique sont les obstacles majeurs qui freinent son industrialisation. Le travail présenté dans cette thèse se focalise principalement sur l'optimisation de la consommation en puissance et le coût de l'OFDM optique. La consommation en puissance élevée résulte essentiellement de la puissance élevée des processeurs requise pour la génération des signaux OFDM. En effet, toutes les modulations OFDM optiques utilisent la propriété de la symétrie Hermitienne pour générer des signaux OFDM réels, ce qui augmente la consommation en puissance et le coût du système. Pour palier ce problème, nous avons tout d'abord développé des nouvelles techniques permettant d'exclure la symétrie Hermitienne des modulations DMT. Ces techniques consistent à générer un signal OFDM complexe et juxtaposer les parties réelle et imaginaire dans le domaine temporel afin d'obtenir un signal réel. Les techniques proposées permettent de réduire la complexité de 75%, réduisant ainsi considérablement la consommation en puissance et le coût du système. Plusieurs travaux visant à réduire la puissance optique des systèmes IM/DD ont été présentés dans la littérature, à savoir les systèmes dits hybrides. Néanmoins, le gain en puissance est obtenu au détriment de la complexité et le coût du système. Pour remédier à ce problème, nous avons proposé un algorithme de compression linéaire asymétrique permettant de réduire la puissance optique de la modulation DCO-OFDM avec une



complexité modérée. Cette technique permet d'atteindre un gain de 4dB en puissance optique en comparaison avec les techniques classiques. L'utilisation des VCSEL dans les systèmes IM/DD permet une conversion électro-optique à bas coût. Les VCSEL ont des propriétés d'échauffement particulières en comparaison avec les autres sources de lumière, notamment pour des signaux à large dynamique. Afin de prendre en compte ses propriétés particulières, nous avons développé un nouveau modèle comportemental du VCSEL basé sur la caractéristique quasi-statique, permettant de simuler avec précision l'impact du VCSEL sur les modulations DMT. La majorité des travaux s'intéressant aux modulations DMT dédiées aux systèmes IM/DD sont basés sur des simulations. Dans ce travail de thèse, nous avons monté un banc de test afin de valider expérimentalement les techniques que nous avons proposées. Ainsi, les résultats de mesures ont montré que la DCO-OFDM avec compression permet d'améliorer le SNR de 4.75 dB en comparaison avec les modulations DMT classiques. L'impact de la non-linéarité du VCSEL sur le signal DMT a été également mesuré. Les résultats de simulations basés sur le nouveau modèle comportemental sont en parfaite cohérence avec les mesures.

# Contents

<b>Acknowledgments</b>	<b>iii</b>
<b>Abstract</b>	<b>v</b>
<b>Resumé</b>	<b>vii</b>
<b>List of Figures</b>	<b>xi</b>
<b>List of Tables</b>	<b>xiii</b>
<b>List of Acronyms</b>	<b>1</b>
<b>General introduction</b>	<b>3</b>
Context . . . . .	3
Thesis contributions . . . . .	4
Thesis structure . . . . .	5
<b>1 Optical OFDM in future optical networks</b>	<b>7</b>
1.1 OFDM principles . . . . .	7
1.1.1 Mathematical description . . . . .	7
1.1.2 Digital implementation of OFDM . . . . .	9
1.1.2.1 System model . . . . .	9
1.1.2.2 Cyclic prefix for OFDM . . . . .	10
1.2 OFDM for optical communications . . . . .	11
1.3 OFDM in short-range optical fiber communications . . . . .	14
1.3.1 Passive optical network . . . . .	14
1.3.1.1 Definition . . . . .	14
1.3.1.2 OFDM for NGPON2 . . . . .	16
1.3.2 Local area network . . . . .	19
1.3.2.1 Definition . . . . .	19
1.3.2.2 History and challenges for optical LANs . . . . .	19
1.3.2.3 Multimode solutions for low-cost networks . . . . .	22
1.3.2.4 Light sources for low-cost networks . . . . .	24
1.3.2.5 OFDM for next generation LANs . . . . .	26
1.4 Discrete multitone modulation . . . . .	27
1.5 Challenges for OFDM in optical networks . . . . .	29
<b>2 Fundamentals of optical OFDM theory</b>	<b>33</b>
2.1 DMT-based IM/DD system model . . . . .	34

2.2	Unipolar OFDM schemes for IM/DD systems . . . . .	38
2.2.1	DCO-OFDM . . . . .	38
2.2.2	ACO-OFDM . . . . .	41
2.2.3	PAM-DMT . . . . .	46
2.2.4	BER performance . . . . .	49
2.2.5	Optical power efficiency . . . . .	50
<b>3</b>	<b>Hermitian symmetry free optical OFDM</b>	<b>55</b>
3.1	Hermitian symmetry in optical OFDM . . . . .	55
3.2	DHT-based optical OFDM . . . . .	58
3.3	Flip-OFDM . . . . .	60
3.4	Hermitian symmetry free OFDM . . . . .	63
3.4.1	System model . . . . .	63
3.4.2	PAPR and BER performance . . . . .	66
3.4.2.1	PAPR . . . . .	66
3.4.2.2	Signal to noise ratio . . . . .	69
3.4.2.3	Bit error rate . . . . .	74
3.4.3	Channel equalization . . . . .	75
3.4.3.1	Flip-OFDM . . . . .	76
3.4.3.2	HSF-OFDM . . . . .	77
3.4.4	Computational complexity . . . . .	78
3.5	Hermitian symmetry free Flip-OFDM . . . . .	80
3.5.1	System model . . . . .	80
3.5.2	Bit error rate . . . . .	82
<b>4</b>	<b>Asymmetrically Companded DCO-OFDM</b>	<b>85</b>
4.1	Overview of optical power efficient DMT systems . . . . .	86
4.1.1	Asymmetrically clipped DC biased optical OFDM . . . . .	86
4.1.1.1	Transmitter model . . . . .	86
4.1.1.2	Receiver model . . . . .	88
4.1.2	Hybrid asymmetrically clipped optical OFDM . . . . .	91
4.1.3	Pilot-assisted modulation . . . . .	92
4.1.4	Discussion and conclusion . . . . .	93
4.2	The companding concept in OFDM systems . . . . .	94
4.3	Asymmetrically companded DCO-OFDM . . . . .	98
4.3.1	System model . . . . .	98
4.3.2	Companding function . . . . .	100
4.4	Simulation results . . . . .	102
4.4.1	Clipping noise reduction . . . . .	103
4.4.2	BER as a function of $E_{b(elec)}/N_0$ . . . . .	104
4.4.3	Optical power efficiency . . . . .	107
<b>5</b>	<b>Experimental investigation of DMT for cost-sensitive networks</b>	<b>109</b>
5.1	VCSEL characterization and modeling . . . . .	110
5.1.1	Static characteristic . . . . .	110
5.1.2	Quasi-static characteristic . . . . .	111
5.1.3	VCSEL nonlinearity modeling . . . . .	112

5.2	Simulation results . . . . .	115
5.2.1	Optical link model . . . . .	115
5.2.2	Optical noise components . . . . .	116
5.2.3	Nonlinearity and clipping distortions . . . . .	118
5.3	Measurements . . . . .	121
5.3.1	Back to back measurements . . . . .	121
5.3.1.1	Inverse sinc compensation . . . . .	122
5.3.1.2	Channel equalization . . . . .	124
5.3.2	Optical link characterization . . . . .	126
5.3.3	Experimental validation of VCSEL non-linear model . . . . .	127
5.3.4	Companded DCO-OFDM . . . . .	129
	<b>General conclusion</b>	<b>133</b>
	<b>Appendix A The AWG impact on the DMT signal</b>	<b>137</b>
A.1	AWG without interleave function . . . . .	137
A.2	AWG with interleave function . . . . .	139
	<b>List of Publications</b>	<b>145</b>
	<b>French thesis summary</b>	<b>147</b>
	Introduction . . . . .	147
5.3	Fondamentaux de l'OFDM optique . . . . .	150
5.3.1	Système IM/DD . . . . .	150
5.3.2	DCO-OFDM . . . . .	151
5.3.3	ACO-OFDM . . . . .	152
5.3.4	Comparaison des deux techniques . . . . .	153
5.3.4.1	BER . . . . .	153
5.3.4.2	Puissance optique . . . . .	154
5.4	L'OFDM optique sans symétrie hermitienne . . . . .	155
5.4.1	La symétrie hermitienne dans les systèmes OFDM optiques . . . . .	155
5.4.2	HSF-OFDM . . . . .	157
5.4.3	HSF-Flip-OFDM . . . . .	159
5.5	DCO-OFDM asymétriquement compressée . . . . .	160
5.5.1	Principe . . . . .	161
5.5.2	La fonction de companding . . . . .	163
5.5.3	Résultats de simulations . . . . .	164
5.5.3.1	BER . . . . .	164
5.5.3.2	Puissance optique . . . . .	165
5.6	Exploration expérimentale de la DMT pour les réseaux à bas coût . . . . .	166
5.6.1	L'impact du VCSEL sur la modulation DMT . . . . .	166
5.6.1.1	La caractérisation quasi-statique du VCSEL . . . . .	166
5.6.1.2	Résultats de simulation . . . . .	168
5.6.1.3	Validation expérimentale . . . . .	170
5.6.2	DCO-OFDM compressée . . . . .	171
	Conclusion . . . . .	173
	<b>Bibliography</b>	<b>175</b>



# List of Figures

1.1	The block diagram of a basic OFDM system . . . . .	8
1.2	Spectra of an OFDM signal with five subcarriers . . . . .	10
1.3	Illustration of ISI caused by dispersive channels [7] . . . . .	11
1.4	IP traffic growth by application type . . . . .	12
1.5	Point-to-point and point-to-multipoint topologies [20] . . . . .	15
1.6	Evolution of PONs [22] . . . . .	15
1.7	An example of OFDM-based PON architecture for NG-PON2 [26] . . . . .	17
1.8	Fiber types in worldwide campus building [36] . . . . .	21
1.9	Evolution of related multimode and single mode components costs [38] . . . . .	23
1.10	Cost comparison of multimode and single mode 100Gb/s links [39] . . . . .	23
1.11	Comparison between VCSELs, LEDs and EELs [40] . . . . .	25
2.1	The block diagram of a general based optical system . . . . .	34
2.2	Time-domain DMT waveforms: (a) real part (b) imaginary part . . . . .	36
2.3	Illustration of the clipping noise in intensity modulated systems [4] . . . . .	37
2.4	Time domain waveforms as function of $K_b$ (a) 0dB (b) 5dB (c) 7dB (d) 13dB . . . . .	39
2.5	Impact of the clipping noise on the constellation diagram: (a) 5dB (b) 7dB (c) 10dB (d) 13dB . . . . .	40
2.6	Time domain waveforms of ACO-OFDM: (a) before clipping (b) after clipping . . . . .	43
2.7	Frequency symbols recovered from the clipped and unclipped DMT signals (a) real part (b) imaginary part . . . . .	45
2.8	The ACO-OFDM signal constellation after clipping . . . . .	46
2.9	Time domain waveforms of PAM-DMT: (a) before clipping (b) after clipping [19] . . . . .	48
2.10	4-PAM-DMT constellation (a) before clipping (b) after clipping . . . . .	48
2.11	DCO-OFDM BER as function of $E_{b(elec)}/N_0$ for 4-QAM, 16-QAM and 256-QAM with DC bias of 7dB and 13dB . . . . .	49
2.12	ACO-OFDM BER as function of $E_{b(elec)}/N_0$ for 4-QAM, 16-QAM, 256-QAM and 1024-QAM . . . . .	50
2.13	Comparison of PAM-DMT and ACO-OFDM performance in a Gaussian channel response (a) bit-loading efficiency (b) achievable bit-rate as function of $N$ [19] . . . . .	51
2.14	Normalized $E_{b(opt)}/N_0$ as function of bit rate to normalized bandwidth ratio for $BER = 10^{-3}$ . . . . .	52
3.1	EVM as function of (a) FFT bit precision (b) IFFT bit precision, for FFT/IFFT sizes varying form 32 to 1024 [54] . . . . .	56

3.2	Computational Complexity of split-radix FFT algorithm on complex input data as function of the FFT size . . . . .	57
3.3	The area and power consumption of 25Gb/s DMT ASIC transceivers for different FFT sizes. . . . .	58
3.4	Clipping effects on IFHT-based ACO-OFDM signal (a) Time domain (b) Frequency domain . . . . .	60
3.5	Block diagrams of Flip-OFDM transmitter and receiver [58] . . . . .	61
3.6	Illustration of the Flip-OFDM concept . . . . .	62
3.7	Block diagrams of HSF-OFDM transmitter and receiver . . . . .	63
3.8	Illustration of the HSF-OFDM approach . . . . .	65
3.9	Effects of HSF-OFDM on the unipolar OFDM signal power . . . . .	68
3.10	The CCDF curves of the conventional DCO-OFDM and the proposed HSF-OFDM techniques for different signal lengths . . . . .	70
3.11	Block scheme of SNR analysis . . . . .	70
3.12	The BER as function of $E_{b(elec)}/N_0$ of ACO-OFDM and HSF-OFDM . . . . .	76
3.13	Illustration of the HSF-flip-OFDM mechanism . . . . .	81
4.1	Block diagram of ADO-OFDM transmitter [50] . . . . .	87
4.2	Constellation diagram: (a) Only even subcarriers are modulated (b) ACO-OFDM on odd subcarriers and DCO-OFDM on even subcarriers . . . . .	88
4.3	Block diagram of ADO-OFDM receiver [50] . . . . .	89
4.4	Profiles of LNST and LCT companding transforms [62] . . . . .	96
4.5	The block diagram of asymmetrically companded DCO-OFDM . . . . .	99
4.6	Profile of the proposed linear companding transform . . . . .	101
4.7	Time domain waveforms: (a) Conventional DC-biased OFDM signal (b) Companded DC-biased OFDM signal . . . . .	103
4.8	Comparison of the received constellation points for conventional and companded DCO-OFDM schemes for different constellation sizes . . . . .	105
4.9	BER as function of $E_{b(elec)}/N_0$ for different constellations of the conventional (Conv) and the companded (Comp) DCO-OFDM techniques . . . . .	106
4.10	BER as function of $E_{b(opt)}/N_0$ of conventional ACO-OFDM, DCO-OFDM and companded DCO-OFDM . . . . .	107
5.1	The static characteristic of the Finisar Photonics VCSEL . . . . .	110
5.2	The static and quasi-static characteristics of the Finisar Photonics VCSEL for different bias currents . . . . .	112
5.3	Comparison of second-order polynomial and Rapp models for the VCSEL static characteristic . . . . .	115
5.4	Block scheme for simulations . . . . .	116
5.5	Contribution of the different noise components (RIN, shot and thermal) to the total noise power as function of the detected photocurrent ( $R_L = 50\Omega$ ) . . . . .	117
5.6	Comparison of the static and quasi-static EVM simulation results as function of the VCSEL bias current . . . . .	119
5.7	Illustration of the frequency response correction using the inverse sinc pre-compensation . . . . .	123
5.8	Effect of the zero-forcing equalizer on the amplitude and the phase of the received QAM constellation . . . . .	125

5.9	Measured $S_{21}$ transmission characteristics of the used optical link for different bias currents . . . . .	126
5.10	Correction of the amplitude and phase distortions due to the optical channel using ZF equalization . . . . .	127
5.11	Measured EVM versus the static and quasi-static EVM simulation results as function of the VCSEL bias current . . . . .	128
5.12	Static characteristic of the DBF laser . . . . .	130
5.13	Measured EVM of conventional and companded DCO-OFDM techniques for different bias currents using 64 – QAM modulation . . . . .	130
5.14	SNR as function of bias current of conventional and companded DCO-OFDM for a 64-QAM modulation . . . . .	131
A.1	Illustration of the zero-order hold conversion . . . . .	138
A.2	The ZOH impact on the DMT signal spectrum . . . . .	139
A.3	The model of a time-interleaved DAC structure using two digital to analog converters . . . . .	140
A.4	Time domain waveforms of a time-interleaved DAC with two parallel paths	141
A.5	Spectra of a time-interleaved DAC with two parallel paths . . . . .	142





# List of Tables

1.1	Requirements for the use of optics at long and short distances [9] . . . . .	12
1.2	Comparison of candidate technologies for NG-PON2 [25] . . . . .	17
1.3	Multimode fiber standards [36] . . . . .	20
1.4	10Gb/s standards for short transmission distances over MMF . . . . .	21
1.5	40Gb/s and 100Gb/s standards for short transmission distances over MMF	22
3.1	Comparison of powers at different stages of each scheme . . . . .	75
3.2	The computational complexity performance of ACO-OFDM, Flip-OFDM and HSF-OFDM for a transmitted signal length of 256 . . . . .	79
4.1	Computational complexity performance of Hybrid optical OFDM and conventional optical OFDM for $N = 256$ . . . . .	94



# List of Acronyms

**OFDM** Orthogonal Frequency-Division Multiplexing

**IP** Internet Protocol

**IM/DD** Intensity Modulated Direct Detection

**DMT** Discrete MultiTone

**ADSL** Asymmetric Digital Subscriber Line

**VDSL** Very-high-data-rate Digital Subscriber Line

**DCO-OFDM** DC Biased Optical OFDM

**ACO-OFDM** Asymmetrically Clipped Optical OFDM

**HSF-OFDM** Hermitian Symmetry Free Optical OFDM

**VCSELs** Vertical-Cavity Surface-Emitting Lasers

**DAB** Digital Audio Broadcasting

**DVB-T** Digital Video Broadcasting-Terrestrial

**3GPP-LTE** 3GPP-Long-Term Evolution

**FDM** Frequency-Division Multiplexing

**DSPs** Digital Signal Processors

**QAM** Quadrature Amplitude Modulation

**PSK** Phase Shift Keying

**DACs** Digital to Analog Converters

<b>ISI</b>	Intersymbol Interference
<b>ICI</b>	Intercarrier Interference
<b>CO-OFDM</b>	Coherent Optical OFDM
<b>MMF</b>	Multimode Fiber
<b>LANs</b>	Local Area Networks
<b>MZM</b>	Mach-Zehnder Modulator
<b>PONs</b>	Passive Optical Networks
<b>OLT</b>	Optical Line Terminal
<b>CO</b>	Central Office
<b>ONUs</b>	Optical Network Units
<b>AON</b>	Active Optical Networks
<b>P2P</b>	point-to-point
<b>P2MP</b>	pointto-multipoint
<b>POS</b>	passive optical splitter
<b>RN</b>	remote node
<b>NG-PONs</b>	Next-generation passive optical networks
<b>SMFs</b>	Single mode fibers
<b>LED</b>	light emitting diode
<b>EEL</b>	edge emitting laser
<b>SNR</b>	signal to noise ratio
<b>PAPR</b>	peak to average power ratio
<b>DFB</b>	Distributed Feedback
<b>PAM-DMT</b>	pulse-amplitude-modulated discrete multitone modulation
<b>ADO-OFDM</b>	Asymmetrically clipped DC biased optical OFDM

**HACO-OFDM** hybrid asymmetrically clipped optical OFDM

**BER** bit error rate

**AWGN** Additive White Gaussian Noise

**EVM** error vector magnitude

**ASICs** Application Specific Integrated Circuits

**DHT** discrete Hartley transform

**IFHT** inverse fast Hartley transform

**FHT** fast Hartley transform

**CCDF** complementary cumulative distribution function

**RIN** relative intensity noise

**AWG** arbitrary wave generator

**ZOH** zero-order hold

**TIDAC** time-interleaved DAC



# General introduction

## Context

The explosive demand for broadband applications has led to a huge growth of Internet Protocol (IP) traffic. To meet the drastically increasing demand for high-bandwidth services, networks have to be upgraded to support higher data rates. Copper-based systems that have reached a point of saturation in capacity and reach, are not capable of providing high capacities with the aggregated transmission distances. Fiber/photonics systems have emerged as a natural alternative of copper-based systems to provide an ultra wide bandwidth medium of transmission.

For short range optical communications, such as rack to rack interconnections in local area networks, Intensity Modulated Direct Detection (IM/DD) systems are preferred to complex coherent detection based systems to lower the overall system cost. In IM/DD systems, data rate is limited by the bandwidth of electrical to optical and optical to electrical interfaces. Thus, when basic on-off keying modulation is employed over a single optical wavelength, the overall data rate is limited to a few tens of gigabits per second. A possible approach to maximize the data rate per wavelength, is to implement high spectral efficiency modulation schemes.

Orthogonal Frequency-Division Multiplexing (OFDM) is a kind of multicarrier modulation that has been incorporated in many wireless standards due to its several advantages including: robustness against frequency-selective fading channels, simple one-tap equalization, high spectral efficiency and easy digital modulator/demodulator implementation. In IM/DD optical systems, the electrical signal driving the light source must be real and positive. Being complex and bipolar, conventional radio OFDM signals can not be used in IM/DD systems. To make the use of OFDM in IM/DD systems



possible, Discrete MultiTone (DMT) modulation, a real baseband version of OFDM, is commonly used. DMT has been widely employed in commercial copper-based lines such as Asymmetric Digital Subscriber Line (ADSL) and Very-high-data-rate Digital Subscriber Line (VDSL).

Many DMT-based unipolar techniques compatible with IM/DD systems have been proposed to match the light source characteristic. DC Biased Optical OFDM (DCO-OFDM) and Asymmetrically Clipped Optical OFDM (ACO-OFDM) are the most popular. DCO-OFDM consists in adding a DC bias to the real bipolar DMT signal to convert it to an unipolar signal, resulting in an inefficient solution in terms of optical power. In ACO-OFDM, only the odd subcarriers are modulated which results in an antisymmetric time-domain signal. The obtained bipolar signal is then made positive by clipping the entire negative excursion. Since only the positive part is transmitted, ACO-OFDM has more optical power efficiency than DCO-OFDM. However, ACO-OFDM suffers from spectral inefficiency because only odd subcarriers are used to carry data. Hybrid techniques combining two basic schemes have been proposed to improve spectral and power efficiencies of IM/DD systems. However, these techniques have complex architectures, thus increasing the complexity and the cost of IM/DD systems.

DMT modulations have been shown to provide the highest data rate over the highest transmission distance for short-range optical networks. However, the power consumption and cost of optical OFDM are still the major obstacles to its market development.

## Thesis contributions

The work presented in this thesis mainly focuses on optimizing the power consumption and cost of optical OFDM by making the following contributions:

1. *Improvement of digital DMT modulator/demodulator complexity and cost:* All the proposed DFT-based unipolar OFDM techniques deal with the Hermitian symmetry property to generate real OFDM signals. The Hermitian symmetry property is shown to increase the power consumption and the cost of the system. An alternative technique is to generate a conventional complex OFDM signal and juxtapose the real and imaginary parts in the time domain to obtain a real OFDM signal. Thus, real OFDM signals can be generated with no need to constrain the input frequency

- vector to have an Hermitian symmetry property. This technique called Hermitian Symmetry Free Optical OFDM (HSF-OFDM) is investigated in terms of complexity and power consumption and compared to the state-of-art optical OFDM techniques. Another novel technique based on combining HSF-OFDM with Flip OFDM is also introduced.
2. *Improvement of optical power efficiency:* The optical power is one of the main constraints of optical systems. Several works aiming to improve the optical power efficiency of IM/DD systems have been proposed. Hybrid techniques have been shown to provide high optical power efficiency at the expense of system complexity and cost. To overcome this issue, an approach is to employ efficient algorithms inspired from radio communications to reduce the optical power of DMT modulations. Within this context, an asymmetric linear companding algorithm is developed and applied to DCO-OFDM modulation. This technique called asymmetrically companded DCO-OFDM is studied and its performance in terms of power efficiency and complexity are compared to the state-of-art optical power efficient OFDM techniques.
  3. *Reliable modeling of VCSEL characteristics:* Vertical-Cavity Surface-Emitting Lasers (VCSELs) have been shown to be cost effective electrical to optical converters for short-range communications, namely IM/DD systems. However, no reliable modeling taking into account the particular properties of VCSELs has been proposed, especially for large dynamic signals. New model based on the use of the VCSEL quasi-static characteristic is developed, permitting to accurately evaluate the VCSEL impact on DMT modulations.

## Thesis structure

This thesis consists of five chapters covering various topics related to DMT modulations including characteristics, challenges and novel algorithms permitting to improve DMT modulation performance.

In Chapter 1, as a start, a background to DMT modulations and their emergence in optical networks is provided. The advantages of DMT modulations in contemporary short-range communications are next pointed out. The challenges for optical OFDM

in future optical networks are discussed and the necessity to innovate novel schemes of unipolar multicarrier modulation format is highlighted.

In Chapter 2, fundamentals of DMT modulation are described. To fix the issues defined in Chapter 1 and design innovative efficient algorithms, a deep understanding of the concepts of unipolar DMT techniques is required. A detailed mathematical description of unipolar OFDM techniques is then provided.

In Chapter 3, the drawbacks of dealing with the Hermitian symmetry to generate real OFDM signals are underlined. The novel HSF-OFDM technique permitting to generate real OFDM signals with no need to constrain the frequency symbols to have an Hermitian symmetry property is presented and compared to conventional DMT modulations. The technique combining HSF-OFDM with Flip-OFDM is finally described and its advantages in terms of complexity reduction are discussed.

In Chapter 4, asymmetrically companded DCO-OFDM that uses an asymmetric companding to compress the negative part of the real OFDM signal is first described. The proposed technique is then compared to conventional unipolar OFDM schemes in terms of optical power efficiency and system complexity.

Finally, in Chapter 5, the impact of VCSELs on DMT modulations is first investigated. A new modeling based on the VCSEL quasi-static characteristic is presented. In the last part of this thesis, an experimental investigation of DMT modulations, namely the performance of the quasi-static modeling and the asymmetrically companded DCO-OFDM, is provided.

# Chapter 1

## Optical OFDM in future optical networks

### Contents

---

<b>1.1 OFDM principles</b> . . . . .	<b>7</b>
1.1.1 Mathematical description . . . . .	7
1.1.2 Digital implementation of OFDM . . . . .	9
<b>1.2 OFDM for optical communications</b> . . . . .	<b>11</b>
<b>1.3 OFDM in short-range optical fiber communications</b> . . . . .	<b>14</b>
1.3.1 Passive optical network . . . . .	14
1.3.2 Local area network . . . . .	19
<b>1.4 Discrete multitone modulation</b> . . . . .	<b>27</b>
<b>1.5 Challenges for OFDM in optical networks</b> . . . . .	<b>29</b>

---

### 1.1 OFDM principles

Orthogonal frequency-division multiplexing is a kind of multicarrier modulation, where the data signal is transmitted over a number of narrowband subcarriers. The OFDM concept was first proposed in 1966 [1], to maximize the data rate and minimize the interchannel and intersymbol interferences due to frequency-selective channels. OFDM has several advantages over single-carrier modulations including robustness against frequency-selective fading channels, simple effective equalization, efficient

spectrum utilization, flexibility in subcarrier allocation, and adaptability in subcarrier modulation [2]. Due to these features, OFDM has been incorporated in many wireless standards such as Digital Audio Broadcasting (DAB), Digital Video Broadcasting-Terrestrial (DVB-T), wireless local area networks (IEEE 802.11a/g) and 3GPP-Long-Term Evolution (3GPP-LTE).

### 1.1.1 Mathematical description

The block diagram of a very basic OFDM system is depicted in Figure 1.1. The incoming data stream is first partitioned to blocks of  $N$  complex symbols. Each symbol is used to modulate one of the available subcarriers during a symbol period of  $T$ .

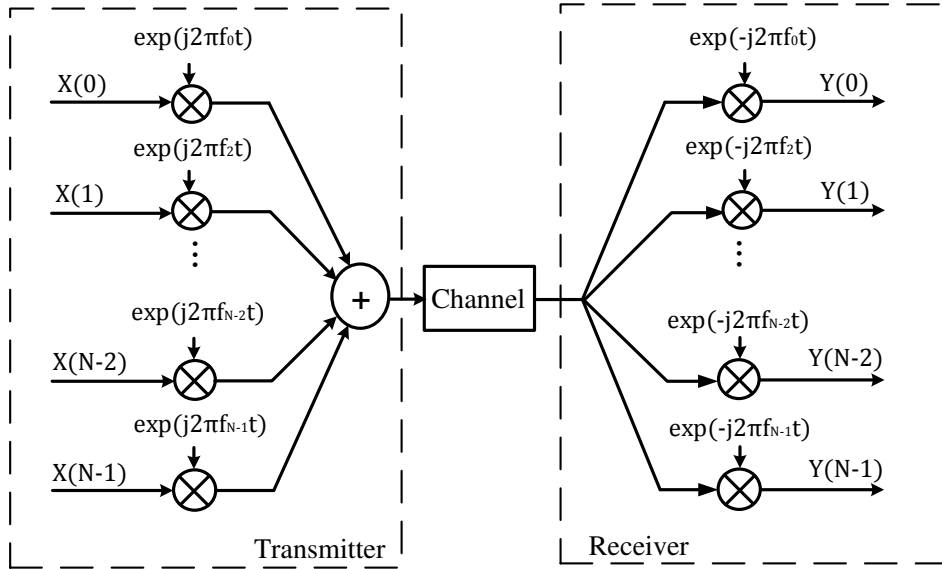


FIGURE 1.1: The block diagram of a basic OFDM system

The modulated subcarriers are then added together to generate a complex OFDM signal as follows,

$$x(t) = \sum_{k=0}^{N-1} X(k) \exp(j2\pi f_k t) \quad (1.1)$$

where  $x(t)$  is the OFDM signal and  $N$  is the number of subcarriers. One prominent advantage of OFDM over the well-known Frequency-Division Multiplexing (FDM) systems lies in the orthogonality between subcarriers. Indeed, in conventional FDM, the separation between subchannels is ensured by inserting guard bands between the different subchannels to keep them far enough from each other. The insertion of guard

bands permits to prevent interferences between subchannels but reduces the overall spectral efficiency. In OFDM transmission, no guard bands are needed to separate the subchannels due to the orthogonal nature of OFDM, thus improving the spectral efficiency. Indeed, subcarriers can be considered to be orthogonal if they are mutually independent. Thus, in the time-domain, subcarriers have to satisfy the orthogonality condition given by,

$$\int_0^T s_i(t)s_j(t)dt = \begin{cases} 1, & \text{if } i = j \\ 0, & \text{if } i \neq j \end{cases} \quad (1.2)$$

This means that if any two different subcarriers among all the subcarriers are multiplied and integrated over a symbol period, the result is equal to zero [3]. In the frequency domain, the orthogonality is ensured if the spacing between subcarriers is a multiple of the inverse of the symbol duration [4]. Thus, two subcarriers are orthogonal if their frequencies satisfy the following condition,

$$f_i - f_j = m \frac{1}{T}, \quad m \in \mathbb{Z}^* \quad \forall i \neq j \quad (1.3)$$

Generally, OFDM systems use several hundred subcarriers so that each subchannel can be considered to be frequency-flat fading channel. Such systems would require a very large number of analog oscillators and multipliers in both the transmitter and receiver, leading to an unreasonably complex and expensive architecture. With the advances in Digital Signal Processors (DSPs), a digital implementation of OFDM using fast Fourier transform (FFT) and its inverse (IFFT) to replace the analog oscillators and demodulator, has been proposed by Weinstein and Ebert [5]. The proposed approach has enabled a low-complexity and cost-effective implementation of OFDM, leading to its adoption in many standards.

## 1.1.2 Digital implementation of OFDM

### 1.1.2.1 System model

The FFT-based OFDM uses IFFT and FFT algorithms to generate and demodulate the OFDM signal. Indeed, as in the case of the analog OFDM, the incoming data stream is first partitioned into blocks of  $N$  symbols. The inverse fast Fourier transform

(IFFT) is then applied to each block of  $N$  symbols to generate a digital OFDM symbol. Considering the orthogonality of subcarriers (i.e.  $f_k = \frac{k}{T}$ ,  $\forall k \in [0, N - 1]$ ), the  $n^{\text{th}}$  sample of  $x(t)$  sampled at  $\frac{T}{N}$  can be expressed as

$$x(n) = \sum_{k=0}^{N-1} X(k) \exp\left(j2\pi \frac{k}{T} \frac{nT}{N}\right) = \sum_{k=0}^{N-1} X(k) \exp\left(j2\pi \frac{kn}{N}\right) \quad (1.4)$$

Note that  $x(n)$  is complex. Contrary to FDM transmission systems, where both analog and digital modulation schemes can be used for each of carriers, OFDM transmission can use only digital modulation schemes. Quadrature Amplitude Modulation (QAM) and Phase Shift Keying (PSK) are commonly employed. Two Digital to Analog Converters (DACs) are next used to convert the real and imaginary parts of  $x(n)$  to the analog domain, before being sent to an I/Q modulator. At the receiver side, the received OFDM signal is demodulated using a fast Fourier transform (FFT) as follows,

$$Y(k) = \sum_{n=0}^{N-1} y(n) \exp\left(-j2\pi \frac{kn}{N}\right) \quad (1.5)$$

In DFT-based OFDM systems, each subcarrier is windowed by a rectangular window of duration  $T$ . The rectangular pulse shape in the time domain leads to a  $\text{sinc}(x)/x$  frequency response in the frequency domain. Since the subcarriers are spaced by  $\frac{1}{T}$ , each subcarrier peak coincides with the nulls of all the other subcarriers, hence, orthogonality between subcarriers is maintained. This is illustrated in Figure 1.2.

### 1.1.2.2 Cyclic prefix for OFDM

Radio channels are not ideal but band-limited channels. The dispersive nature of band-limited channels causes the signal to spread in time, thus introducing the well-known Intersymbol Interference (ISI) distortion. This phenomenon is illustrated in Figure 1.3. In the frequency domain, time-dispersive channels lead to a loss of orthogonality between subcarriers, resulting in Intercarrier Interference (ICI). One straightforward technique to combat ISI and ICI in OFDM systems is the so-called cyclic prefix insertion [6].

This technique consists in copying the last part of the OFDM symbol and appending it to the front of the OFDM symbol. Then, the total length of the transmitted symbol

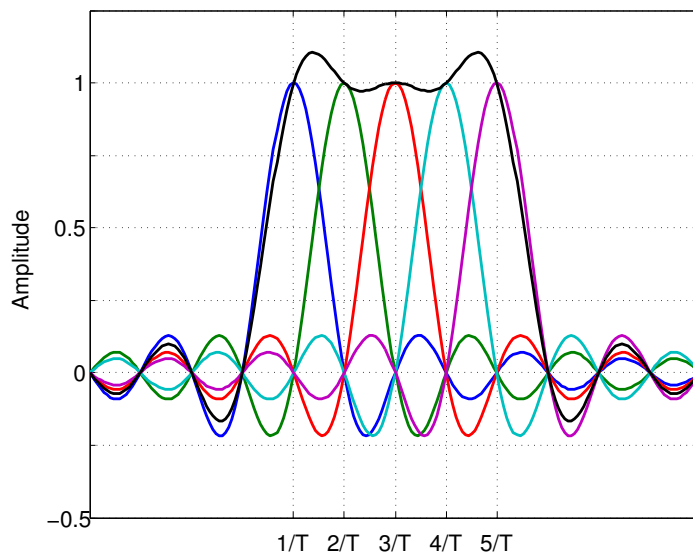


FIGURE 1.2: Spectra of an OFDM signal with five subcarriers

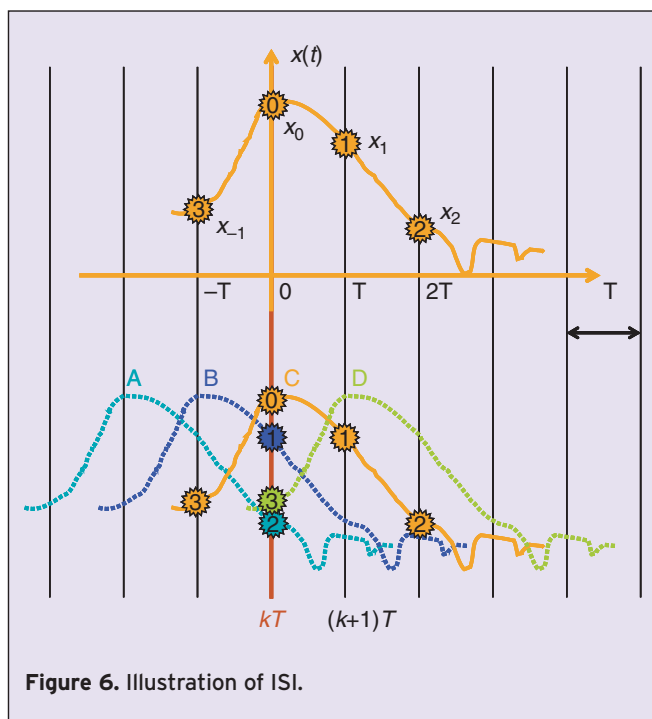


FIGURE 1.3: Illustration of ISI caused by dispersive channels [7]

can be expressed as

$$T_s = T + T_{CP} \quad (1.6)$$

The length of the cyclic prefix  $T_{CP}$  is chosen to be longer than the delay spread of the channel to ensure that all the samples from the previous OFDM symbols fall within



the cyclic prefix duration, thus eliminating intersymbol interferences and maintaining orthogonality between subcarriers [6].

## 1.2 OFDM for optical communications

The explosive growth in the use of broadband applications has drastically increased the IP traffic. Figure 1.3 shows Cisco's forecast for the global IP traffic in Exabyte (EB) per month [8]. According to Cisco's visual networking index (VNI) forecast, the average monthly global traffic is expected to reach 121 EB by 2017, which is equivalent to 37 million DVDs per hour. The global traffic will continue to be dominated by video (business and consumer) applications. Cisco forecasts that global network users will generate 3 trillion Internet video minutes per month.

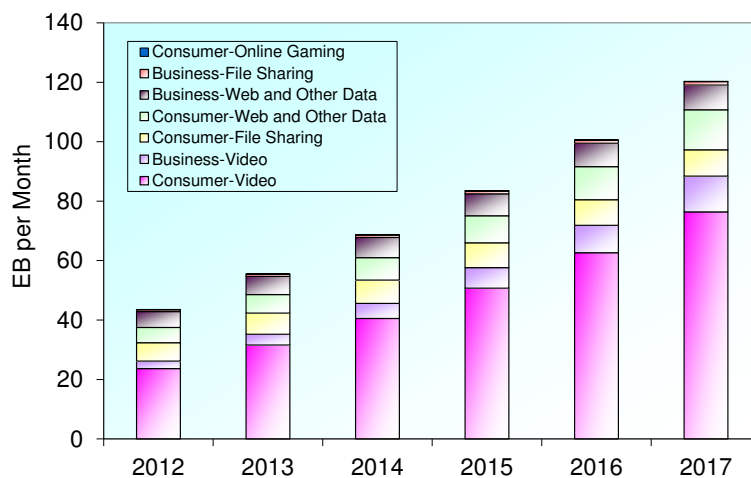


FIGURE 1.4: IP traffic growth by application type

To meet the huge growth in IP traffic and the continuous growth in demand for broadband applications, service providers have to increase the capacity of their networks to support extended data rates. Optical communication systems have emerged as an efficient alternative of copper-based systems that had reached a saturation in capacity and reach [4]. Indeed, the total available bandwidth of standard optical fibers is enormous (i.e. about 20THz), thus providing huge capacities of 100Tb/s and beyond. Table 1.1 summarizes the advantages and requirements for using optics in long and short distance communications.

Long distance	Short distance
Maximum bit/s over longest possible span	Maximum connection density
Longest length of connection	Smallest cross-section for a given bandwidth and length
Total power not critical	Minimize power dissipation
Design for minimum received energy	Design for minimum total energy per bit
Wavelength division multiplexing	Wavelength division multiplexing
Reuse one fiber for many channels. Allow wavelength switching and routing	Give higher density of connections. Allow wavelength switching and routing
	Signal integrity
	Improved timing precision
	Reduced reflections, cross-talk, voltage isolation.

TABLE 1.1: Requirements for the use of optics at long and short distances [9]

However, to take full advantage from the enormous capacity of lightwave systems, the innovation of novel schemes of optical amplification, modulation format and fiber design is required [4]. Two modulation formats can be used in optical communications: single carrier or multicarrier modulations. Optical OFDM has been shown to have several advantages as compared to single-carrier modulation format [4], [10, 11]. These advantages include:

- *Ease of signal processing*: straightforward channel estimation and phase estimation can be performed in OFDM transmission, by inserting pilot symbols within the OFDM signal. In single-carrier modulations, the channel estimation generally relies on algorithms which are prone to error propagation. Furthermore, an efficient one-tap frequency equalization can be performed in OFDM instead the time equalization commonly used in single-carrier modulations.
- *Bit and power allocation*: Information rate and power are independently adjusted on each subcarrier in accordance with channel conditions, permitting to achieve the desired data rate with the minimal power at the smallest error rate.
- *Computation complexity*: OFDM has less computation complexity than single-carrier systems due to the use of the efficient algorithm FFT/IFFT, reducing the chip design complexity.
- *Adaptability to time-varying channels*: The transmitter updates the transmission parameters according to time-varying channel conditions.

Further the features mentioned above, OFDM has other advantages as compared to single-carrier systems including: spectral efficiency, high order modulation, flexibility and scalability. Two flavors of OFDM transmission have been investigated for optical communications, namely Coherent Optical OFDM (CO-OFDM) [12, 13] and direct detection optical OFDM [14]-[19]. Coherent optical OFDM provides high spectral efficiency, high resistance to fiber chromatic dispersion and receiver sensitivity but requires a complex implementation, making it more suitable for long haul communications. Direct detection OFDM is advantageous for short reach applications because it provides a simple low cost realization. Indeed, the challenge of optical-based short reach communications is to develop cost effective solutions based on the use of fast and low-cost components such as VCSELs and Multimode Fiber (MMF). For cost considerations, IM/DD systems are commonly used in fiber-based short-reach networks such as data centers and Local Area Networks (LANs). For such cost-sensitive networks, CO-OFDM can not be employed because it requires the use of complex architectures and high cost components such as Mach-Zehnder Modulator (MZM) and optical coherent detectors. The use of multimode fiber in short reach networks provides a cost effective solution but it comes at the expense of decreased bandwidth. To overcome the bandwidth limitation due to the multimode fiber intermodal dispersion, an approach is to employ optical OFDM to increase the spectral efficiency of short-reach optical communications. The requirements for optical OFDM in next generation of short reach networks are discussed in the following sections.

## **1.3 OFDM in short-range optical fiber communications**

### **1.3.1 Passive optical network**

#### **1.3.1.1 Definition**

Due to the increasing demand for bandwidth-hungry broadband applications, such as VOIP (Voice over IP), VOD (Video on Demand) and streaming video, Passive Optical Networks (PONs) have been adopted as a cost effective solution to support higher bandwidth capability and provide high speed services to distant users. Copper wire based technologies such as xDSL (x Digital Subscriber Line) can provide a data rate of

100Mb/s over a maximum transmission distance of 300m. By deploying large bandwidth capacity optical fiber transmission lines, passive optical networks can achieve higher data rate (up to 10Gb/s) with larger coverage area (up to 20km). A basic fiber based PON consists of three main components: a) the Optical Line Terminal (OLT) located in the Central Office (CO) where the assignment of traffic to subscribers is managed, b) Optical Network Units (ONUs) located at the subscribers premises c) optical fibers that connect the CO to ONUs. Contrary to Active Optical Networks (AON) where active network elements are used to connect the CO to ONUs, passive optical networks do not need any expensive active components to support services to users, thus reducing the cost of deployment and maintenance.

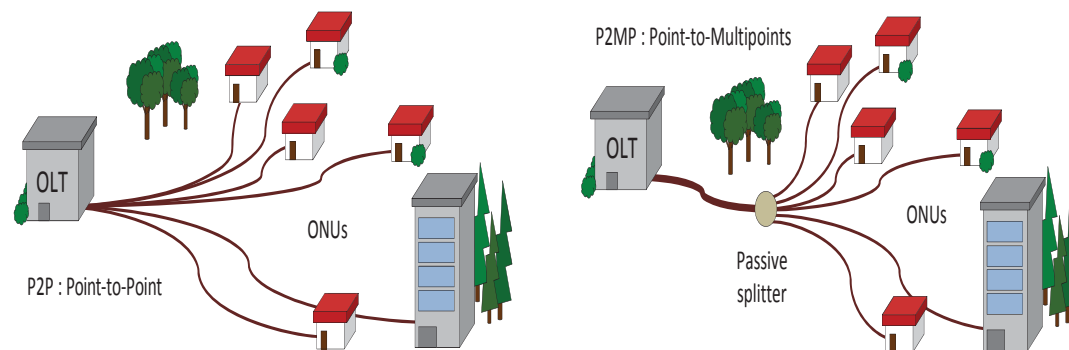


FIGURE 1.5: Point-to-point and point-to-multipoint topologies [20]

The OLT can be interconnected to ONUs using either a point-to-point (P2P) or point-to-multipoint (P2MP) topology. These two topologies are shown in Figure 1.5. In the point-to-point architecture, a dedicated fiber is used to connect each subscriber (ONU) to the central office, with different wavelengths. In the point-to-multipoint topology, the different wavelengths are multiplexed and transmitted over a shared fiber to a passive optical splitter (POS), also called remote node (RN), that splits the optical signal and broadcasts data to all ONUs over separate fibers. Using only one shared fiber, the point-to-multipoint topology of PONs results in additional savings for service providers, making passive optical network one of the dominant broadband access technologies in the access market.

Figure 1.6 shows the evolution of PONs. The most mature PON-based architectures are 10-Gigabit-capable passive optical network (XG-PON) standardized by the international telecommunication union (ITU G.987 series [21]) and 10-Gigabit Ethernet passive optical

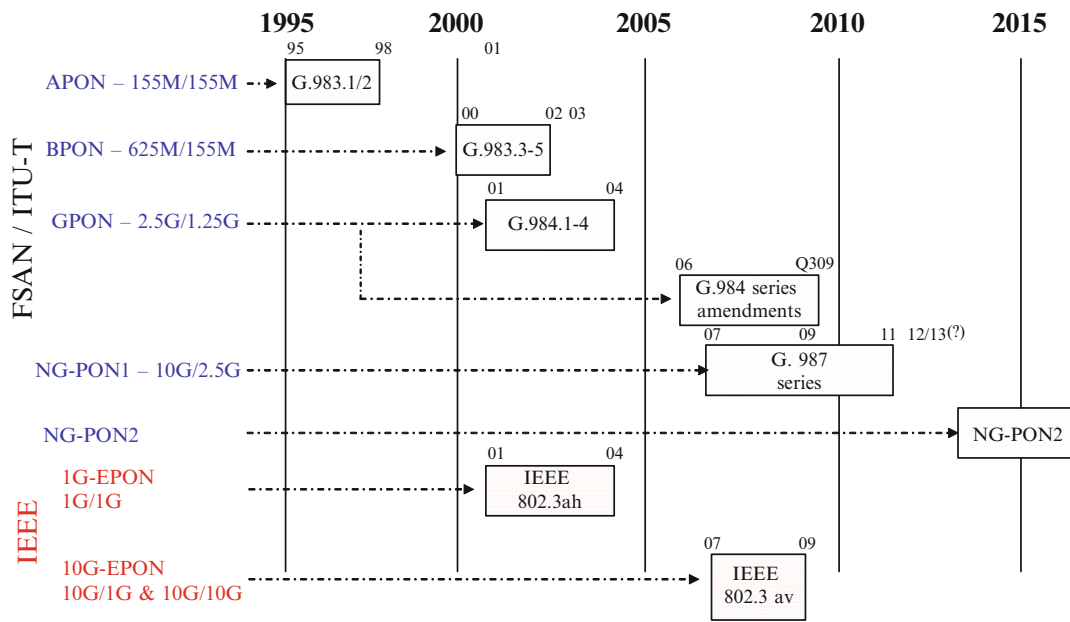


FIGURE 1.6: Evolution of PONs [22]

network (10G-EPON) standardized by the institute of electrical and electronics engineers (IEEE 802.3av [23]). XG-PON1 can provide an asymmetric 10Gb/s downstream and 2.5Gb/s upstream data rates up to 60km physical reach using reach extenders (RE), while 10GE-PON can provide up to 10Gb/s for both downstream and upstream directions with a maximum coverage area of 20km.

### 1.3.1.2 OFDM for NGPON2

The increasing demand for modern applications such as high definition TV, multimedia conferencing, multiplayer online gaming and next-generation 3D TV, has pushed operators worldwide to seek for increased-capacity optical access solutions. Next-generation passive optical networks (NG-PONs) are intensively investigated and emerging as a cost-effective solution to satisfy the growing bandwidth demands fueled by both residential and business applications. A gradual migration strategy from the currently deployed PONs to the next-generation solution is adopted in order to distribute the investment over longer periods of time. The first step of migration to the next generation solution referred to as NG-PON1 has to support coexistence with the deployed Gigabit-capable PONs and reuse the outside plant. In the long term, the second phase of migration referred to as NG-PON2 is required to deliver 40Gb/s downstream

and 10Gb/s upstream up to 60km. The optimal technology permitting to reach NG-PON2 specifications is under discussion. An overview of the candidate technologies for NG-PON2 is given [24, 25]. These technologies include time division multiple access TDMA-PON, wavelength division multiplexed WDM-PON, OFDM access OFDMA-PON, orthogonal code division access OCDM-PON. A combination of two or more of the aforementioned technologies referred to as hybrid technologies can be considered to increase the aggregated capacity. OOFDM is widely considered as one of the most promising technologies for NG-PON2 due to its particular advantages such as immunity to channel impairments, high spectral efficiency, high transmission bit rate and great system scalability. The OFDM-based PON concept was first proposed in [26]. The OFDM-based PON architecture is shown in Figure 1.7.

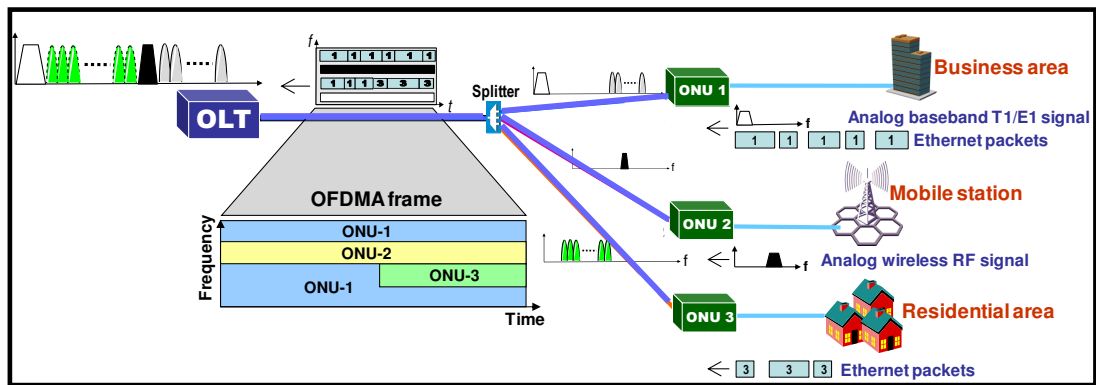


FIGURE 1.7: An example of OFDM-based PON architecture for NG-PON2 [26]

The OFDMA-based PON (OFDMA-PON) is essentially a hybrid technique, that combines OFDM and Time Division Multiple Access (TDMA). Indeed, in OFDMA-PON, the high-bandwidth is divided to  $N$  sub-bands containing each the specific data to each ONU. The OLT broadcasts and transmits the whole sub-bands to ONUs via the passive power splitter, and each ONU selects its specific sub-band with the specific data. One of the distinguishing features of OFDMA-PON is that the number of subcarriers per ONU can be dynamically assigned in different time slots depending on the specific requirements of each user, thus allowing a time and frequency two-dimensional bandwidth allocation. Table 1.2 compares the different candidate technologies for next generation passive optical networks. As can be seen in table 1.2, OFDMA-PON provides the highest upstream and downstream data rates with the highest passive reach, widely outperforming the other technologies. However, the cost and the power consumption of

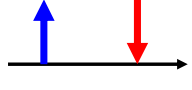

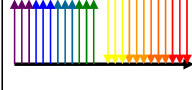
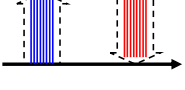
	TDM	TWDM	WDM	OFDM
				
Rate (Down/Up)	40/10G	4x (10/2.5G)	Nx(1/1)G	40/10G
Optical budget	31 dB	37.5 dB	29-43 dB	30-36.5 dB
Split	64 (*)	64 (*)	80	64 (*)
Reach	<40 km (°)	<40 km	<20-60 km	<100 km (°)
System maturity	Research	Development	Development	Research
Cost (L ↔ H)	\$ ↔ \$\$\$	\$ ↔ \$\$	\$\$ ↔ \$\$\$	\$\$ ↔ \$\$\$\$
Power OLT	Low	Low	High	Medium
Power ONU	Medium	Medium	Low	High

TABLE 1.2: Comparison of candidate technologies for NG-PON2 [25]

OFDMA-PON are still high, especially in the ONU which is the most cost-sensitive part of the PON being located at the user side.

The cost-effectiveness of OFDMA-PON can be enabled by combining the exploitation of advanced silicon technologies and sophisticated DSP algorithms tailored to the PON environment:

- The silicon photonic integration, i.e. the integration of chip-scale photonics and electronics in the same semiconductor wafer, is emerging as a promising solution to meet the NG-PON2 requirements in terms of cost, complexity, performance and manufacturing volume [27]. It was shown in [28], that the FDM/FDMA ONU can be integrated in silicon providing low cost and highly manufacturable devices, which allows the use of very low-cost transceivers at the ONU side.
- For practical deployment of cost-effective OFMDA-PONs, IM/DD systems with Directly Modulated Laser (DML) are highly preferred [29, 30]. In addition, VCSELs are a promising solution for IM/DD systems due to several features such as cost-effectiveness, low power consumption and easy packaging and testing. The main drawbacks of VCSELs as compared to single mode lasers are the limited modulation bandwidth, the limited output optical power and the non-linear characteristic [30]. For the upstream direction of PONs, the required modulation bandwidth and output optical power are quite moderate. Thus, the use of VCSELs as intensity modulators at the ONU side, allows the desired transceiver cost target

to be achieved without compromising the NG-PON2 requirements. However, the VCSEL nonlinearity can drastically affect system performance. This issue has to be addressed by researches in order to enable the feasibility of employing VCSELs in OFDMA-PON.

- The aforementioned features allow the mass production of ONU transceivers to meet the mass deployment of NG-PON2. The exploitation of mass-market technologies allows to significantly reduce the cost per unit and achieve the desired cost efficiency [32].

The power consumption of ONUs is still a bottleneck for OFDMA-PON deployment. The high power consumption stems essentially from the high computational power of the DSP to generate OFDM waveforms. The exploitation of advances in complementary metal-oxide-semiconductor (CMOS) can be exploited to reduce the power consumption. However, the use of a very advanced CMOS process can increase the cost per unit [32]. Instead, the exploitation of sophisticated DSP algorithms can significantly reduce the power consumption without considerably increasing the cost of ONU transceivers.

### 1.3.2 Local area network

#### 1.3.2.1 Definition

A local area network (LAN) is a data communication system which interconnects a number of independent data devices such as computers, mass storage devices, workstations and printers, in a moderate sized geographic area such as university campus, office buildings, industrial plants and hospitals [33]. Initially, local area networks (LANs) were only based on copper wire links. With the increased demand in bandwidth and data rate, the limited transmission distance of copper cable has become a real shortcoming of copper-based LANs. Optical fibers have then emerged as an extremely effective solution for high-capacity transmission LANs due to their several advantages over copper wire. These advantages include: large bandwidth, light weight and small diameter, long distance transmission, high security and immunity to electromagnetic interference (EMI) [33, 34].



The LAN architecture may have physical and logical topologies. The physical topology refers to the manner of which the network devices are arranged, while the logical topology refers to how the data is assigned. The three basic topologies are: star, ring and bus. Various combinations of these topologies are possible. The advantages and drawbacks of each combination are detailed in [35].

### 1.3.2.2 History and challenges for optical LANs

With the increasing demand in bandwidth due to the growing number of end user applications, optical LANs had to be upgraded from 1Gb/s to 10Gb/s. 1Gb/s LANs employed some millions kilometers of legacy multi-mode fibers such as Fiber Distributed Data Interface (FDDI), OM1 and OM2. Although the diversity in the already installed fiber types and the difference in their performance and characteristics, the reuse of the existing fiber plant was necessary for a cost-effective upgrade to 10Gb/s. Optical fibers are classified according to two main parameters: the core/cladding diameters and the modal bandwidth that refers to the amount of data the fiber is able to transmit over a certain distance. It is expressed in MHz\*km. Table 1.3 lists various multimode fibers standardized by the Telecommunication Industry Association (TIA), the International Electrotechnical Commission (IEC) and the International Standardization Organization (ISO).

Standard Body	Document	Notes
TIA— Telecommunications Industry Association	492AAAA	62.5 $\mu\text{m}$ fibers with 160/500 MHz.km OFL BW
	492AAAB	50 $\mu\text{m}$ fibers with 500/500 MHz.km OFL BW
	492AAAC	Laser-optimized 50 $\mu\text{m}$ fibers with 2000 MHz.km EMB at 850 nm
IEC—International Electrotechnical Commission	60793-2-10	A1a.1 fiber—50 $\mu\text{m}$ fibers with a range of OFL BW
		A1a.2 fiber—Laser-optimized 50 $\mu\text{m}$ fibers with 2000 MHz.km EMB at 850 nm
		A1b fiber—62.5 $\mu\text{m}$ fibers with a range of OFL BW
ISO—International Standards Organization	11801	OM1 fiber—200/500 MHz.km OFL BW (in practice OM1 fibers are 62.5 $\mu\text{m}$ fibers)
		OM2 fiber—500/500 MHz.km OFL BW (in practice OM2 fibers are 50 $\mu\text{m}$ fibers)
		OM3 fiber—Laser-optimized 50 $\mu\text{m}$ fibers with 2000 MHz.km EMB at 850 nm

OFL: overfilled launch, BW: bandwidth

TABLE 1.3: Multimode fiber standards [36]

The modal bandwidth is mainly limited by the modal dispersion that occurs in multimode fibers. Indeed, multimode fibers contain many propagation modes. When

an optical pulse is launched into a multimode fiber, the modes that constitute the pulse travel at different velocities along the fiber and arrive at different times at the receiving point, causing a temporal spreading of the pulse at the fiber end. This phenomenon is known as modal dispersion and can be assimilated to the well-known multipath phenomenon in radio communications. The temporal spreading depends on the transmission times of the slowest and fastest modes. The modal dispersion increases with the fiber length, limiting the transmission data rate and capacity of MMF-based links. Indeed, the higher the data rate, the shorter the transmission distance limit guaranteeing negligible modal dispersion effects. Figure 1.8 depicts the fiber types in worldwide campus buildings.

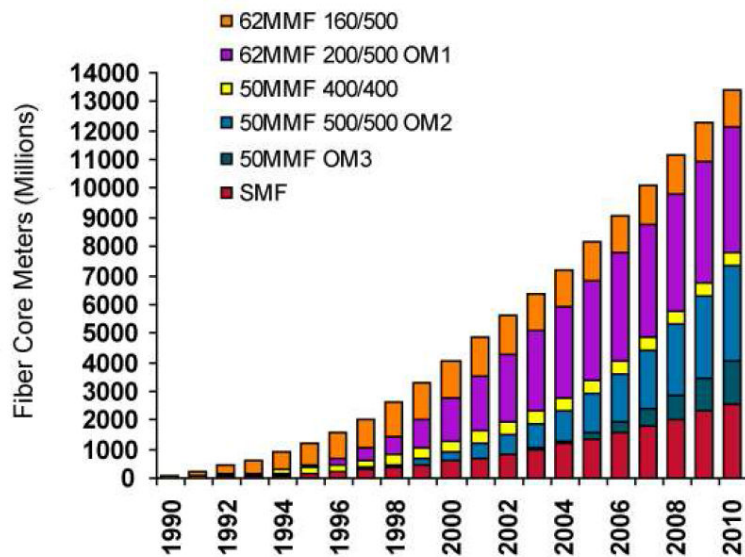


FIGURE 1.8: Fiber types in worldwide campus building [36]

As can be seen in Figure 1.8, traditional OM1 and FDDI represented about 50% of deployed fibers. Hence, the reuse of these fiber types was necessary for a cost-effective deployment of 10Gb/s LANs. Single-mode fibers were also deployed and represented about 20% in 2007. Although Single mode fibers (SMFs) do not suffer from modal dispersion, MMFs have many advantages over SMFs. The large core diameter of MMFs make it easier to align fiber with a laser or another fiber, thus reducing the cost of related components [37] and making easier the installation and the maintenance. Furthermore, the adoption of multimode fibers in 10Gb/s allows the use of low cost VCSELs to transmit data over short transmission distances, thus improving the cost effectiveness of MMF-based LANs. Table 1.4 provides a non-exhaustive list of the existing standards for 10Gb/s over multimode and single mode fibers.

Standard	Wavelength (nm)	Core size	Modal bandwidth	ISO/IEC fiber type	Maximum range (m)
10GBASE-SR (2002)	850	62.5 $\mu$ m	160	FDDI	26
			200	OM1	33
		50 $\mu$ m	400		66
			500	OM2	82
			2000	OM3	300
			4700	OM4	400
10GBASE-LRM (2006)	1310	62.5 $\mu$ m	160	FDDI	220
			200	OM1	220
		50 $\mu$ m	400		100
			500	OM2	220
			2000	OM3	220
10GBASE-USR (2011)	850	62.5 $\mu$ m	200	OM1	10
		50 $\mu$ m	500	OM2	30
			2000	OM3	100

TABLE 1.4: 10Gb/s standards for short transmission distances over MMF

Using the newest Laser-Optimized OM4 with a modal bandwidth of 4700MHz\*km, a transmission distance of up to 400m can be reached. With the emergence of new bandwidth-hungry applications, namely video and social networking, the global internet traffic has reached 12,000 Gigabytes per second in 2012 and forecast to reach 35,000 Gigabytes per second by 2017 [31]. To meet the ongoing growth in internet traffic, local area networks have to be upgraded to support extended data rates of 40Gb/s and beyond. While upgrading local area networks from 1 to 10Gb/s faced the challenge to reuse legacy OM1/OM2 multimode fibers, upgrade LANs to 40Gb/s and beyond will only support Laser-Optimized 50 $\mu$ m multimode fiber OM3 or OM4. The IEEE 802.3ba formed in 2008 and ratified in 2010 specifies two short reach standards employing multimode fibers to deliver data at the aggregated bit rates of 40Gb/s and 100Gb/s: 40GBASE-SR4 and 100GBASE-SR10. Table 1.5 depicts the specifications of these standards.

Standard	Wavelength (nm)	Core size	Modal bandwidth	ISO/IEC fiber type	Maximum range (m)
40GBASE-SR4	850	50 $\mu$ m	2000	OM3	100
			4700	OM4	150
100GBASE-SR10	850	50 $\mu$ m	2000	OM3	100
			4700	OM4	150

TABLE 1.5: 40Gb/s and 100Gb/s standards for short transmission distances over MMF

For both 40Gb/s and 100Gb/s LANs, OM3 provides a transmission distance of 100m while using OM4, a transmission distance of 150m can be reached.

### 1.3.2.3 Multimode solutions for low-cost networks

Single mode fibers are less expensive than multimode fibers. One can use single mode fibers to improve the cost effectiveness of short reach communications. Figure 1.9 depicts the evolution of the relative cost of 10Gb/s transceivers based on single mode components (1330nm) and multimode components (850nm).

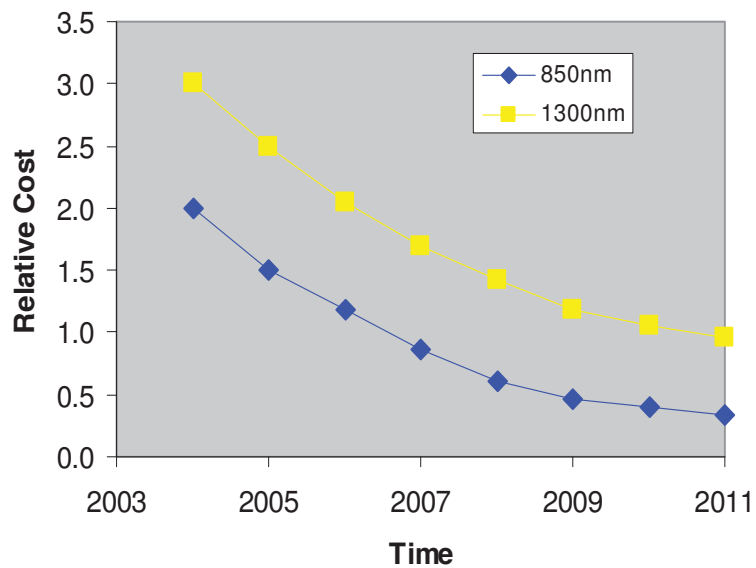


FIGURE 1.9: Evolution of related multimode and single mode components costs [38]

As can be seen in Figure 1.9, both single mode and multimode components relative costs have been divided by about 4 between 2004 and 2011. On the other hand, related single mode components cost 50% higher than multimode components. As a result, the total cost of the SMF-based link is widely higher than that of a MMF-based link, hence multimode fibers are optimal for short distance communications, where the cost is a main constraint and the performance of single mode fibers is not needed. Furthermore, the alignment process of single mode components is delicate and therefore a costly process, thus increasing the cost of the SMF-based link.

Figure 1.10 compares the total cost of various 100Gb/s links at a transmission distance of 250m based on multimode and single mode fibers. Again, the installation of single mode fibers costs more than that of multimode fibers. Indeed, at the same transmission

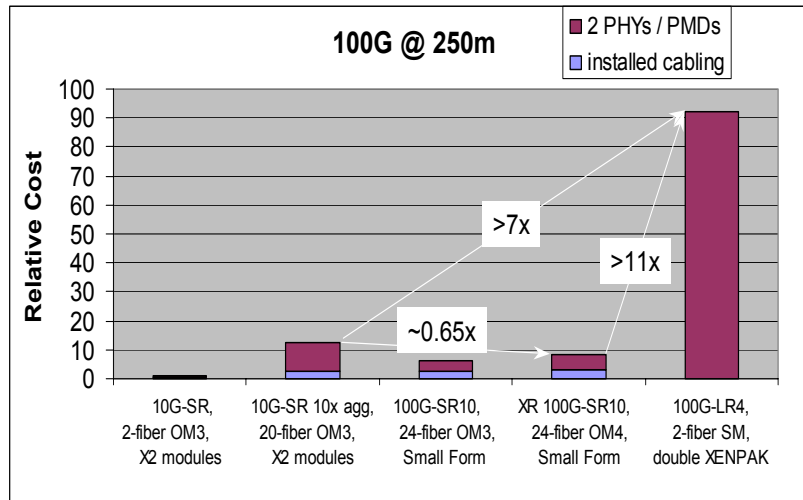


FIGURE 1.10: Cost comparison of multimode and single mode 100Gb/s links [39]

distance (i.e. 250m), the total cost of the SMF-based 100Gb/s link is 11 times higher than that of the OM4-based 100Gb/s link. Multimode solutions based on MMFs and multimode 850nm components are definitely the most cost-effective solutions for 40Gb/s and 100Gb/s links up to 150m.

#### 1.3.2.4 Light sources for low-cost networks

As aforementioned, IM/DD systems offer a cost effective solution for cost-sensitive optical networks. The light source is considered as the active component in IM/DD systems and therefore one of the most important elements that fix optical transceiver performance and cost. Many considerations must be taken into account when choosing the most convenient light source [13]. Spectral bandwidth, reliability, wavelength, launch power and cost are some of the key characteristics of a light source. Three multimode light sources can be used in conjunction with multimode fibers for short-reach communications: light emitting diode (LED), edge emitting laser (EEL) and VCSEL. LEDs are the most common semiconductor light sources, namely for illumination applications. One of the main advantages of typical LEDs is that the output optical power increases almost linearly with the current driving current from 0mA to the saturation current. Hence, the threshold current of an ideal LED is almost equal to zero. LEDs can be only used with multimode fibers, because the emitted beam is quite large and do not couple well with single mode fibers. The light emitted by a LED results from a recombination of an electronic hole pair in a p-n junction due to the

applied bias current (spontaneous emission). The speed of LEDs is then determined by the minority carrier lifetime. Consequently, LEDs can have a maximum bit rate of 622Mb/s and can not be used for high data rate communications. For gigabit systems, one must consider lasers to transmit data at the aggregated bit rates. Either edge-emitting lasers or VCSELs can operate at speeds higher than 10Gb/s. A conventional edge-emitting laser has two mirror facets on opposite edges of a Fabry-Perot cavity. The parallel mirrors are produced by leaving the material along two parallel crystal planes. Edge-emitting lasers emit light from the cleaved edges. Testing of such lasers requires the wafer to be broken into individual laser devices or laser bars, and therefore can not be tested at the wafer level. This testing process results in high manufacturing costs. Vertical cavity surface-emitting lasers were proposed as a cost effective alternative of edge-emitting lasers in several applications, namely high-speed data communications. In VCSEL technology, contrary to edge-emitting lasers, the two reflective mirrors are above and below the active region, thus enabling a light-emitting from the top surface of the wafer. Compared to edge-emitting lasers that require a serial testing, VCSELs can be tested at the wafer level and some parameters can be tested in parallel, resulting in lower manufacturing costs and higher reliability. Figure 1.11 illustrates some benefits of VCSELs versus LEDs and EELs.

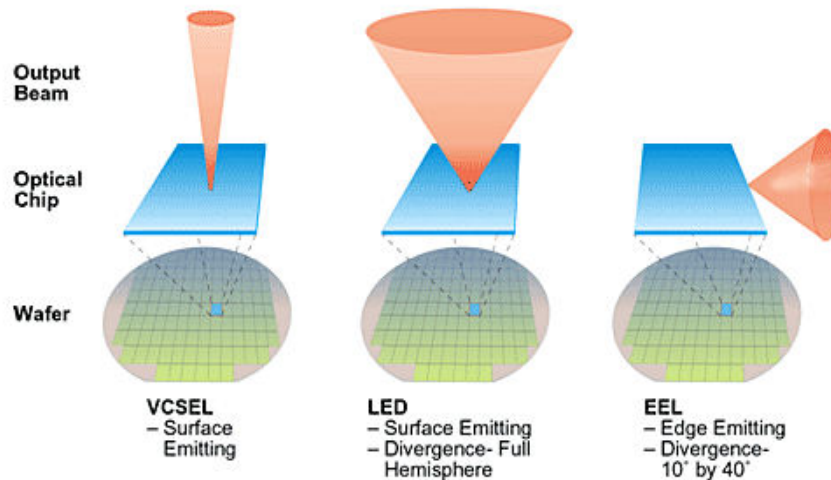


FIGURE 1.11: Comparison between VCSELs, LEDs and EELs [40]

Furthermore, VCSELs have small spot sizes as compared to light emitting diodes, which is one of the major benefits of VCSEL technology. Indeed, the VCSEL's spot size is about  $35\mu\text{m}$ , while LEDs have spot sizes larger than  $100\mu\text{m}$ . Thus, when used in conjunction with a multimode fiber, the LED excites all the modes in the fiber, which results in a

high modal dispersion and therefore in limited bandwidth and data rate. On the other hand, due to its small spot size, the VCSEL excites few modes in the multimode fiber, resulting in less modal dispersion, higher bandwidth and higher data rate ( $> 10\text{Gb/s}$ ). An other key advantage of VCSELs as compared to LEDs and edge-emitting lasers, is the beam quality. Indeed, VCSELs emit a circular beam which considerably reduces the cost of the beam-shaping optics and increases the coupling efficiency to the fiber. A more detailed comparison of these three light sources performance, including the optical power, the spectral width and the beam angle, is given in [41]. It was clearly shown that VCSELs provide the narrowest wavelength over LEDs and standard EELs, have the lowest temperature coefficient and the highest power efficiency. Due to these features, VCSELs have become the choice for several applications and are definitely the optimal choice for next generation of MMF-based optical local area networks.

Advances in multimode fibers and laser technologies have enabled low-cost  $10\text{Gb/s}$  transmission with improved transmission distances. However, multimode solutions still impose some bandwidth limitations for transmission speeds beyond  $10\text{Gb/s}$ . An approach to overcome the bandwidth limitations and increase the capacity of MMF-based LANs is to use discrete multitone modulation [42, 43].

### 1.3.2.5 OFDM for next generation LANs

An attractive technique to improve the spectral efficiency of MMF-based systems, is to use discrete Multitone modulation in combination with IM/DD systems and directly modulated VCSELs [42–44]. Discrete multitone modulation is a real baseband version of the commonly known OFDM modulation that makes it possible to use OFDM in intensity modulated systems. DMT is a promising candidate for next generation of optical LANs due to several particular advantages, including immunity to intersymbol interferences, high spectral efficiency, information rate maximization and simple and cost-effective digital implementation due to the use of fast Fourier transforms (IFFT/FFT). Another key advantage of discrete multitone modulation is the possibility to use power allocation and bit-loading algorithms to approach the channel capacity and improve system performance. These algorithms consist to allocate different power and number of bits to each subcarrier according to the signal to noise ratio (SNR) of each subcarrier [43].

Multicarrier modulations such as OFDM and DMT, unlike constant envelope modulations, suffer from high peak to average power ratio (PAPR). This major disadvantage makes multicarrier modulations very sensitive to nonlinearity. As a result, system performance can be drastically affected by nonlinear components. In radio communications, the nonlinear component that mainly affects OFDM system performance is the power amplifier. In low-cost optical systems such as intensity modulated direct detection systems, the main nonlinear component is the light source. The impact of the LED nonlinearity on optical OFDM performance was widely investigated using both analytical and experimental approaches [45, 46]. Reliable modeling of the LED nonlinearity was developed and validated by measurements and efficient techniques to compensate for LED non-linearities such as the pre-distortion technique, were proposed [46].

The impact of multimode VCSELs on optical OFDM was also investigated and compared to that of single mode Distributed Feedback (DFB) lasers for OFDM-based radio-over-fiber (RoF) applications [47]. It was shown that the use of VCSEL in RoF systems provides a cost effective solution since VCSELs are cheaper to be manufactured than 1310nm DFB lasers. The quality of transmission was investigated by simulations using a simple laser model, while the characteristics of lasers were approximated by a polynomial function. Furthermore, the simulations and measurements were carried for the range of bias currents between threshold and saturation. The approach adopted in [47] does not provide any information of the VCSEL impact when the current is near the threshold or the saturation point.

For multicarrier modulations with high PAPR such as OFDM and DMT, the probability that the signal has peaks lower than threshold and greater than the saturation current is not negligible. Thus, this range of currents is to be considered for reliable and accurate simulations. No sophisticated VCSEL modeling that takes into account both thermal properties of VCSELs and the large dynamic of DMT modulations was proposed in the literature. With the continuous emergence of VCSELs in high-speed transmissions and the need to simulate large-signal behaviors in order to define the optimal modulation conditions, a reliable and accurate VCSEL behavioral modeling with regards to VCSEL characteristics, namely for high bias currents, is of primary importance.



## 1.4 Discrete multitone modulation

Discrete multitone modulation is also based on the use of FFT/IFFT transforms. DMT has been widely employed in copper-based digital subscriber line (DSL) lines, namely in ADSL and VDSL. DMT was adopted in DSL standards because it offers several advantages over single-carrier modulations including: higher performance, immunity to line and noise conditions, simplicity in design and implementation, flexibility and rate adaptation capabilities [48]. On the other hand, as aforementioned in the previous sections, for a low cost approach, IM/DD systems are commonly used in optical short-range communications. To further improve the cost effectiveness of cost-sensitive optical networks, the use of DMT in combination with MMF-based links was advocated to reduce system cost [43, 49]. Indeed, contrary to OFDM, discrete multitone modulation uses real-valued baseband signals instead of complex-valued ones. Therefore, broadband and high-frequency, analog RF components are omitted because no in-phase and quadrature modulation onto an RF carrier is required, reducing system complexity and costs [49].

The application of DMT in MMF-based IM/DD systems, where the electric signal is used to directly modulate the intensity of the light source, is a bit different from copper-based links. Indeed, the electric signal driving the light source must be real and positive. In DMT modulations, time domain signals at the IFFT output are naturally real-valued due to the Hermitian symmetry of the input frequency symbols. Clipping the negative values of the IFFT output signal is a straightforward and basic approach to ensure non-negativity of real-valued DMT signals. However, this method results in a significant noise that can considerably degrade system performance. This noise is commonly referred to as clipping noise. Many techniques were proposed in the literature to reduce the clipping noise. DC biased optical OFDM [14]-[16] and asymmetrically clipped optical OFDM [15]-[18] are commonly used. DCO-OFDM consists in adding a DC bias to the real-valued DMT signal and hard clipping the remaining negative values. This technique is simple to implement but it suffers from optical power inefficiency due to the added DC bias. Moreover, the hard clipping results in a significant clipping noise, especially for low bias levels (7dB) and large constellation sizes. ACO-OFDM was proposed as an optical power efficient alternative of DCO-OFDM. In ACO-OFDM, only odd subcarriers are modulated, resulting in an anti-symmetric time symbols at the IFFT output. The

bipolar signal at the IFFT output is then made positive by clipping the entire negative excursion. Since only the positive part of the anti-symmetric signal is transmitted and no additional DC bias is required, the ACO-OFDM technique exhibits high optical power efficiency. However, the ACO-OFDM technique is spectrally less efficient than DCO-OFDM, due to the fact that half of the subcarriers are off, to prevent distortions arising from the clipping noise. Furthermore, in order to achieve a given bit rate, ACO-OFDM requires higher constellation size because only half of the available subcarriers are used to carry data. For large constellations, the required SNR in each ACO-OFDM subcarrier becomes significant, increasing drastically the required optical power. Therefore, as spectral efficiency increases, DCO-OFDM with large DC bias performs better than ACO-OFDM in terms of optical power.

Another power efficient technique called pulse-amplitude-modulated discrete multitone modulation (PAM-DMT) was proposed in [19]. PAM-DMT consists in modulating all the subcarriers using pulse-amplitude modulation. To obtain an antisymmetric time signal and enable an asymmetric clipping and transmission of only the positive part of the DMT signal as in ACO-OFDM, the real parts of the PAM frequency symbols are set to zero. It was shown in [19], that the restriction to use only odd-numbered subcarriers can degrade system performance in a frequency-selective channel. In PAM-DMT, since all subcarriers are employed, bit-loading can be used to fully adapt the waveform to the channel response and achieve optimum performance. PAM-DMT has the same optical power efficiency of ACO-OFDM but suffers from the same spectral inefficiency, because only the imaginary components of the subcarriers are used to carry data.

To improve spectral and power efficiencies of DMT-based IM/DD systems, hybrid methods based on the combination of two basic techniques were proposed [50, 51]. Asymmetrically clipped DC biased optical OFDM (ADO-OFDM) was first proposed. This technique consists on transmitting simultaneously ACO-OFDM on the odd subcarriers and DCO-OFDM on the even subcarriers. To recover the DCO-OFDM signal, an estimate of the ACO clipping noise on the even subcarriers is performed from the received ACO-OFDM signal. Using the same approach as in ADO-OFDM, hybrid asymmetrically clipped optical OFDM (HACO-OFDM) simultaneously transmits a PAM-DMT signal on the even subcarriers and ACO-OFDM signal on the odd subcarriers. PAM-DMT being more optical power efficient than DCO-OFDM, HACO-OFDM has more optical power efficiency than ADO-OFDM. These techniques have been

shown to provide high power efficiency at the expense of system complexity and cost, which is not suitable for cost-sensitive optical networks.

## 1.5 Challenges for OFDM in optical networks

Optical OFDM is a promising candidate for future high data rate optical communications. Within this context, the strengths and weaknesses of optical OFDM as compared to other candidate technologies were first underlined in the previous sections. Next, IM/DD systems in combination with VCSELs have been shown to provide an optimal cost effective solution for cost-sensitive optical networks. Finally, a short overview of unipolar OFDM techniques compatible with IM/DD systems, summarizing the advantages and drawbacks of each technique, was provided. From the analysis presented above, it can be concluded that:

1. The OFDM techniques compatible with unipolar communications, being basic or hybrid, deal all with the Hermitian symmetry property to generate real OFDM signals. For this purpose, the complex conjugate of the frequency vector is first computed. An Hermitian symmetric vector twice the size of the original vector is then generated and input the IFFT block to generate a real OFDM signal. The Hermitian symmetry constraint results in two major drawbacks: First, the doubled size of the Hermitian symmetric vector requires doubled IFFT/FFT sizes to modulate and demodulate the OFDM signal. The IFFT/FFT blocks with high sizes increase the computational complexity and therefore the power consumption and the occupied chip area, thus increasing the global cost of the chip. Second, the additional resources required to compute the complex conjugate vector increase further the computational complexity and therefore the circuit cost.
2. The OFDM techniques proposed in the literature have more or less spectral and power efficiencies. DCO-OFDM has the highest spectral efficiency but suffers from power inefficiency. ACO-OFDM and PAM-DMT provide high power efficiency at the detriment of the amount of the transmitted data and therefore suffer from spectral inefficiency. To overcome this issue and improve both spectral and power efficiencies, new hybrid methods combining two or more of the aforementioned basic techniques were proposed. These hybrid techniques use three additional FFT/IFFT blocks in the

receiver and one additional IFFT block in the transmitter to generate and recover the transmitted signals. The additional FFT/IFFT blocks result in an excessive circuit complexity, thus greatly increasing the power consumption and the occupied chip area.

The two main factors that influence service providers decisions when upgrading existing networks are the equipment cost and the resulting revenue potential [52]. The migration strategy and technology are chosen to guarantee to service providers a maximum profit with a reduced deployment cost. To fulfill network operators requirements, researchers must provide novel solutions to reduce optical OFDM cost. For this purpose, two areas of research are investigated in this thesis work:

- Develop innovative algorithms to reduce cost and power consumption of optical OFDM systems. To this end, an efficient approach is to develop a new digital signal processing technique that does not deal with the Hermitian symmetry property to generate real OFDM signals. This approach would permit to overcome the drawbacks of the existing real OFDM techniques based on the Hermitian symmetry property and improve system performance in terms of cost and power consumption. On the other hand, develop new power efficient optical OFDM techniques that do not require any additional circuit complexity would provide higher optical and spectral efficiencies, enhancing further the cost efficiency of optical OFDM systems.
- Use cost effective optical components instead the high cost optical devices commonly employed in the existing access networks, and define new models to enhance system performance. A promising approach is to take advantage of the VCSEL technology to replace edge-emitting lasers that are commonly used in high data rate optical communications. The definition of a behavioral model that fits correctly the VCSEL characteristic is then necessary for system simulation and performance evaluation.



## Chapter 2

# Fundamentals of optical OFDM theory

### Contents

---

<b>2.1</b>	<b>DMT-based IM/DD system model . . . . .</b>	<b>34</b>
<b>2.2</b>	<b>Unipolar OFDM schemes for IM/DD systems . . . . .</b>	<b>38</b>
2.2.1	DCO-OFDM . . . . .	38
2.2.2	ACO-OFDM . . . . .	41
2.2.3	PAM-DMT . . . . .	46
2.2.4	BER performance . . . . .	49
2.2.5	Optical power efficiency . . . . .	50

---

As mentioned in the previous chapter, IM/DD systems are a cost-effective solution for cost-sensitive short-range optical communications. On the other hand, the employment of OFDM in MMF-based systems allows to mitigate the bandwidth limitation arising from multimode fibers. Contrary to radio OFDM-based systems that deal with complex signals, only real-valued and positive OFDM signals can be employed in IM/DD systems. Many unipolar DMT techniques compatible with IM/DD systems have been proposed in the literature [15]-[19]. The aim of these techniques is to reduce the so-called clipping noise and improve the optical power efficiency. An overview of basic unipolar DMT techniques with a detailed mathematical description is provided in this chapter. Their performance in terms of bit error rate and optical power efficiency is then analyzed for different constellation sizes. The purpose of the detailed description provided in this

chapter is to gain a deep understanding of fundamentals of DMT modulation with the aim to point out the strengths and weaknesses of each technique. Such understanding is involved to develop new efficient solutions that fulfill the challenging requirements in terms of cost and power consumption.

## 2.1 DMT-based IM/DD system model

Figure 2.1 shows the block diagram of a general DMT-based IM/DD system. As can be seen in this figure, the input serial binary data are first partitioned into  $N$  parallel data and mapped onto frequency samples using a given digital modulation method. Several complex and real modulation forms can be used in conjunction with discrete multitone modulation, quadrature amplitude modulation and pulse amplitude modulation are usually employed.

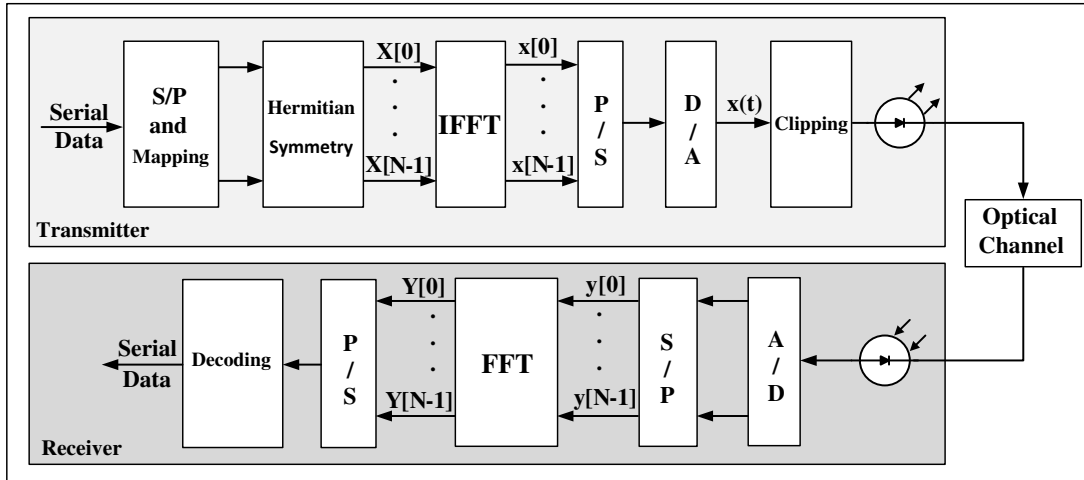


FIGURE 2.1: The block diagram of a general based optical system

To ensure real OFDM signals, the frequency symbols input to the IFFT block are forced to satisfy the Hermitian symmetry constraint,

$$X(N - k) = X^*(k), \quad k = 1, 2, \dots, \frac{N}{2} - 1 \quad (2.1)$$

where  $*$  denotes the complex conjugation. To avoid any DC shift or any residual complex component in the time domain signal, the DC and middle components are set to zero.

$$X(0) = X\left(\frac{N}{2}\right) = 0 \quad (2.2)$$

By performing an IFFT on the frequency symbols,  $X(k)$ , the discrete time signal at the IFFT output can be expressed as,

$$x(n) = \frac{1}{N} \sum_{k=0}^{N-1} X(k) \exp\left(j2\pi \frac{kn}{N}\right) \quad (2.3)$$

Thus,

$$x(n) = \frac{1}{N} \left\{ X(0) + \sum_{k=1}^{\frac{N}{2}-1} X(k) \exp\left(j2\pi \frac{kn}{N}\right) + X\left(\frac{N}{2}\right) \exp\left(j2\pi \frac{N}{2} \frac{n}{N}\right) + \sum_{k=\frac{N}{2}+1}^{N-1} X(k) \exp\left(j2\pi \frac{kn}{N}\right) \right\} \quad (2.4)$$

The DC and middle components being set to zero, the  $n^{\text{th}}$  time-domain sample can be written as,

$$x(n) = \frac{1}{N} \left\{ \sum_{k=1}^{\frac{N}{2}-1} X(k) \exp\left(j2\pi \frac{kn}{N}\right) + \sum_{k=\frac{N}{2}+1}^{N-1} X(k) \exp\left(j2\pi \frac{kn}{N}\right) \right\} \quad (2.5)$$

Let  $k' = N - k$  define a change of variables from  $k$  to  $k'$ . Substituting  $k'$  in (2.5) leads to,

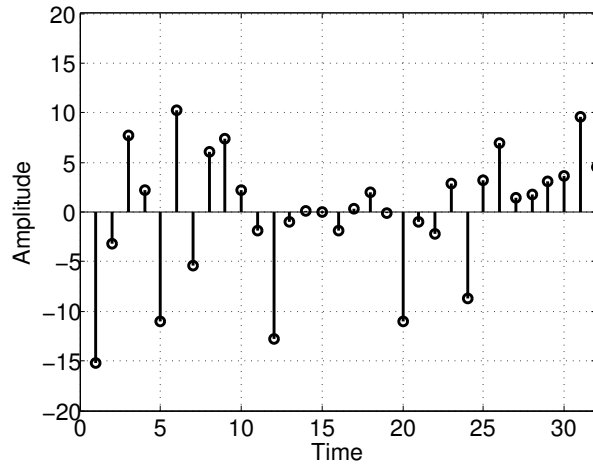
$$x(n) = \frac{1}{N} \left\{ \sum_{k=1}^{\frac{N}{2}-1} X(k) \exp\left(j2\pi \frac{kn}{N}\right) + \sum_{k'=1}^{\frac{N}{2}-1} X(N - k') \exp\left(j2\pi \frac{(N - k')n}{N}\right) \right\} \quad (2.6)$$

Rearranging (2.6) gives,

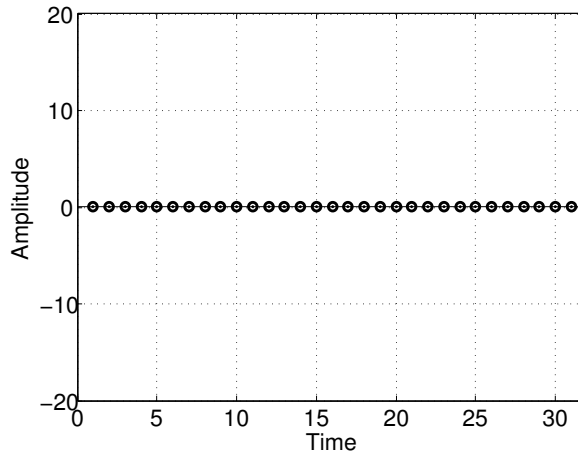
$$\begin{aligned} x(n) &= \frac{1}{N} \left\{ \sum_{k=1}^{\frac{N}{2}-1} X(k) \exp\left(j2\pi \frac{kn}{N}\right) + \sum_{k=1}^{\frac{N}{2}-1} X^*(k) \exp\left(-j2\pi \frac{kn}{N}\right) \right\} \\ &= \frac{1}{N} \sum_{k=1}^{\frac{N}{2}-1} \left\{ 2X_R(k) \cos\left(j2\pi \frac{kn}{N}\right) - 2X_I(k) \sin\left(j2\pi \frac{kn}{N}\right) \right\} \end{aligned} \quad (2.7)$$

where  $X_R(k)$  and  $X_I(k)$  are respectively the real and imaginary components of  $X(k)$ . It has to be noted from (2.7) that due to the Hermitian symmetry of the frequency symbols, the imaginary part of the time domain signal at the IFFT output is equal to zero. Figure 2.2 depicts the real and imaginary parts of the discrete time signal at the IFFT output for a 64-QAM constellation using 32 subcarriers.





(a)



(b)

FIGURE 2.2: Time-domain DMT waveforms: (a) real part (b) imaginary part

The discrete time parallel signal at the IFFT output is converted to a serial signal and input to a digital to analog (D/A) converter to generate a continuous time version,  $x(t)$ . In intensity modulated systems, the DMT signal is used to directly modulate the intensity of the light source (LED or laser). Figure 2.3 illustrates the impact of an ideal light source on a DC biased DMT signal (the impact of the saturation region is also illustrated). As can be seen in this figure, the remaining negative peaks after DC bias addition are clipped at zero, being below the light source threshold. This nonlinear distortion is commonly referred to as clipping noise. In IM/DD systems, to avoid a severe clipping noise penalty, the DMT signal is constrained to be real and positive. The resulting signal at the digital to analog (D/A) converter output is real but bipolar and thus is not compatible with the light source characteristic. To generate an unipolar signal and guarantee non-negativity of the DMT signal, a hard clipping to

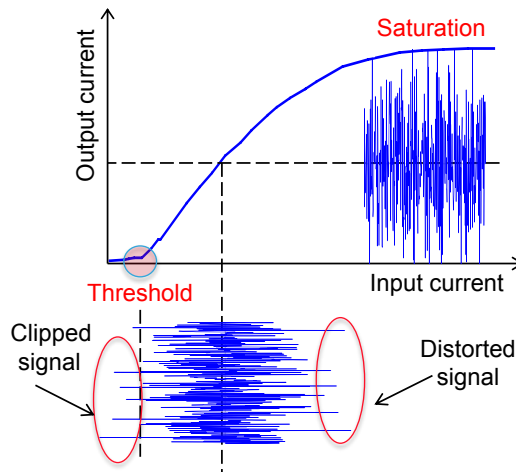


FIGURE 2.3: Illustration of the clipping noise in intensity modulated systems [4]

zero is performed at the digital to analog converter output as follows,

$$x_u(t) = \begin{cases} x(t), & \text{if } x(t) > 0 \\ 0, & \text{if } x(t) \leq 0 \end{cases} \quad (2.8)$$

where  $x_u(t)$  is the generated DMT unipolar signal. At the receiver side, a photodiode is used to detect the received optical signal and convert it to an electric current proportional to the detected optical power. The discrete time serial signal resulting from the analog to digital (A/D) conversion, is converted back to a parallel signal, so that a DMT demodulation using a fast Fourier transform (FFT) can be performed to recover the transmitted frequency symbols,  $Y(k)$ , as follows,

$$Y(k) = \sum_{n=0}^{N-1} y(n) \exp\left(-j2\pi \frac{kn}{N}\right) \quad (2.9)$$

where,  $y(n)$  is the  $n^{\text{th}}$  received time-domain sample. The transmitted bit stream is finally recovered by performing a maximum likelihood detection according to the chosen modulation form.

The Hermitian symmetry (2.1) and the DC (2.2) constraints are necessary to generate a real DMT signal, but this is not without drawbacks. Indeed, these constraints affect the transmission data rate, because only half of the available subcarriers are used to carry useful information. Thus, for  $N$  IFFT points, only  $N/2 - 1$  independent complex frequency symbols are transmitted. The spectral efficiency of real DMT systems is

almost divided by two, compared to conventional complex OFDM systems.

The hard clipping of the negative amplitudes is an irreversible operation, which results in a significant noise that can drastically affect system performance. The reduction of clipping noise was widely investigated in the literature and many techniques more or less efficient were proposed. DC biased optical OFDM [14]-[16], asymmetrically clipped optical OFDM [15]-[18] and pulse-amplitude-modulated discrete multitone modulation [19] are the most popular. The advantages and drawbacks of each of these techniques are detailed in the following section.

## 2.2 Unipolar OFDM schemes for IM/DD systems

### 2.2.1 DCO-OFDM

DC biased optical OFDM is one of the simplest and earliest methods that were proposed to generate unipolar OFDM schemes compatible with IM/DD systems. DC biased optical OFDM consists in adding a DC bias to the bipolar signal to convert it to an unipolar signal. The required DC bias to guarantee non-negativity is equal to the absolute value of the maximum negative amplitude of the bipolar OFDM signal. However, OFDM signals suffer from a high PAPR resulting in a high required bias level to ensure non-negative signals. In practice, for large values of  $N$  (i.e.  $N \geq 64$ ), the OFDM signal amplitude can be approximated by a Gaussian distribution. Therefore, in order to avoid an excessive DC bias and minimize the required optical power, an approach is to use a DC bias  $K_b$  proportional to the root-square of the electric power ( $\sigma$ ),

$$K_b = k\sigma \quad (2.10)$$

where  $k$  is the clipping factor and  $\sigma^2$  is the variance of  $x(t)$  defined as,

$$\sigma^2 = E \{x^2(t)\} \quad (2.11)$$

This is defined in the literature [15] as a bias of  $10 \log_{10}(k^2 + 1)dB$ . The DC-biased time signal,  $x_{DC}(t)$ , is then given by,

$$x_{DC}(t) = x(t) + K_b \quad (2.12)$$

The remaining negative peaks are clipped at zero to ensure non-negativity of the time signal at the optical transmitter input. As aforementioned, the hard clipping results in a clipping noise. Thus, in the case of DCO-OFDM, the unipolar signal can be expressed as,

$$x_{u,DCO}(t) = x(t) + K_b + n_c(K_b), \quad (2.13)$$

where  $n_c(K_b)$  is the clipping noise component. The peak to average power ratio of OFDM signals increases with the number of subcarriers, thus increasing the DC bias required to minimize the clipping noise. On the other hand, the lower the added DC bias, the greater the number of subcarriers affected by the clipping process. As a result, the clipping noise is a function of the added DC bias,  $K_b$ . Figure 2.4 shows the amplitudes

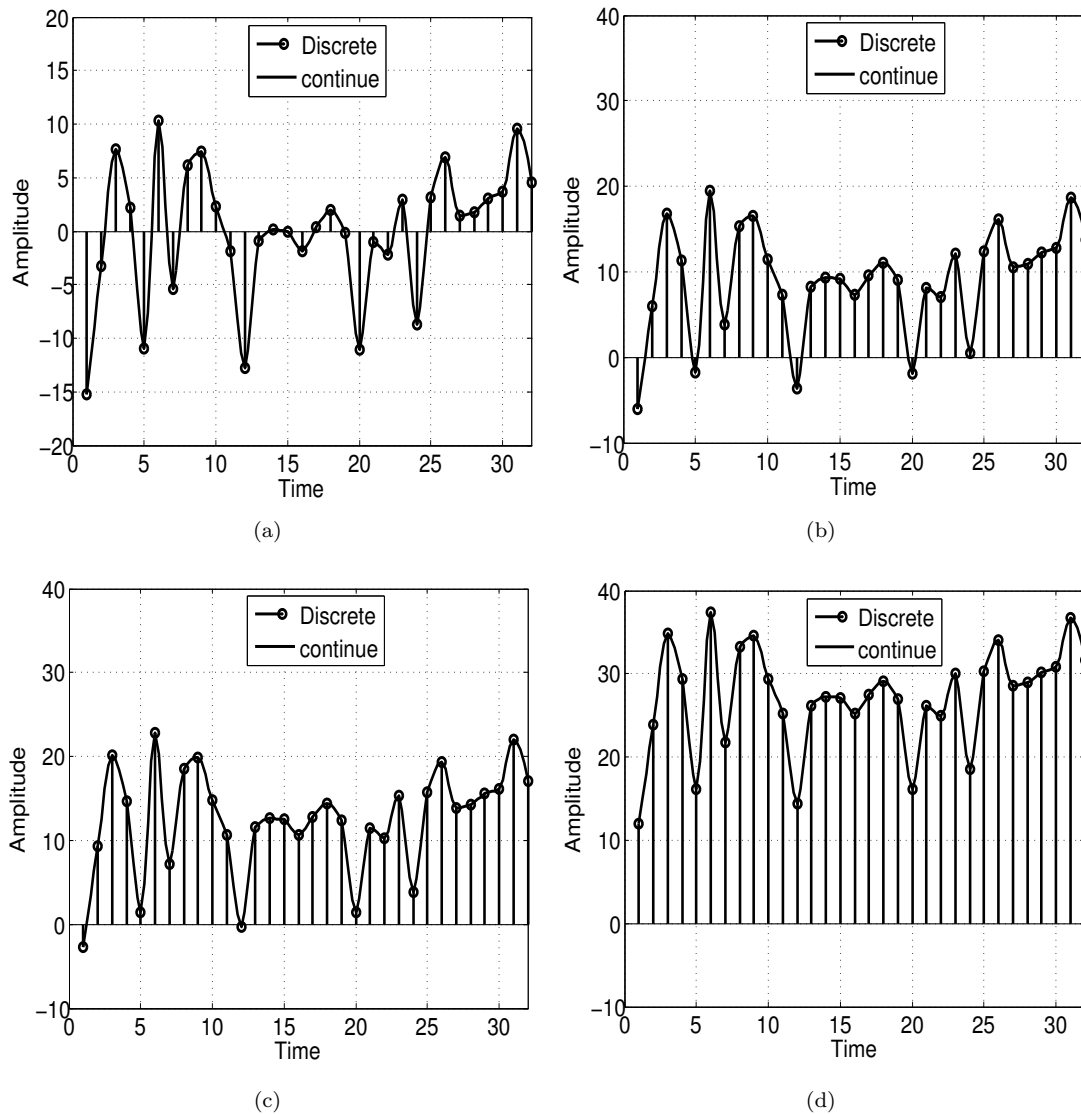


FIGURE 2.4: Time domain waveforms as function of  $K_b$  (a) 0dB (b) 5dB (c) 7dB (d) 13dB

of a real DMT signal for DC offsets of 0dB, 5dB, 10dB and 13dB. As can be seen in this figure, the amount of the remaining negative peaks decreases with the added DC bias level. Thus, as the added DC bias to the bipolar signal increases, less amplitudes are affected by the clipping process.

The impact of the clipping noise as function of the added DC bias can be also investigated using the constellation diagram. Figure 2.5 compares the constellation diagrams before and after the clipping process for different bias levels. The digital modulation considered in this comparison is a 16-QAM constellation.

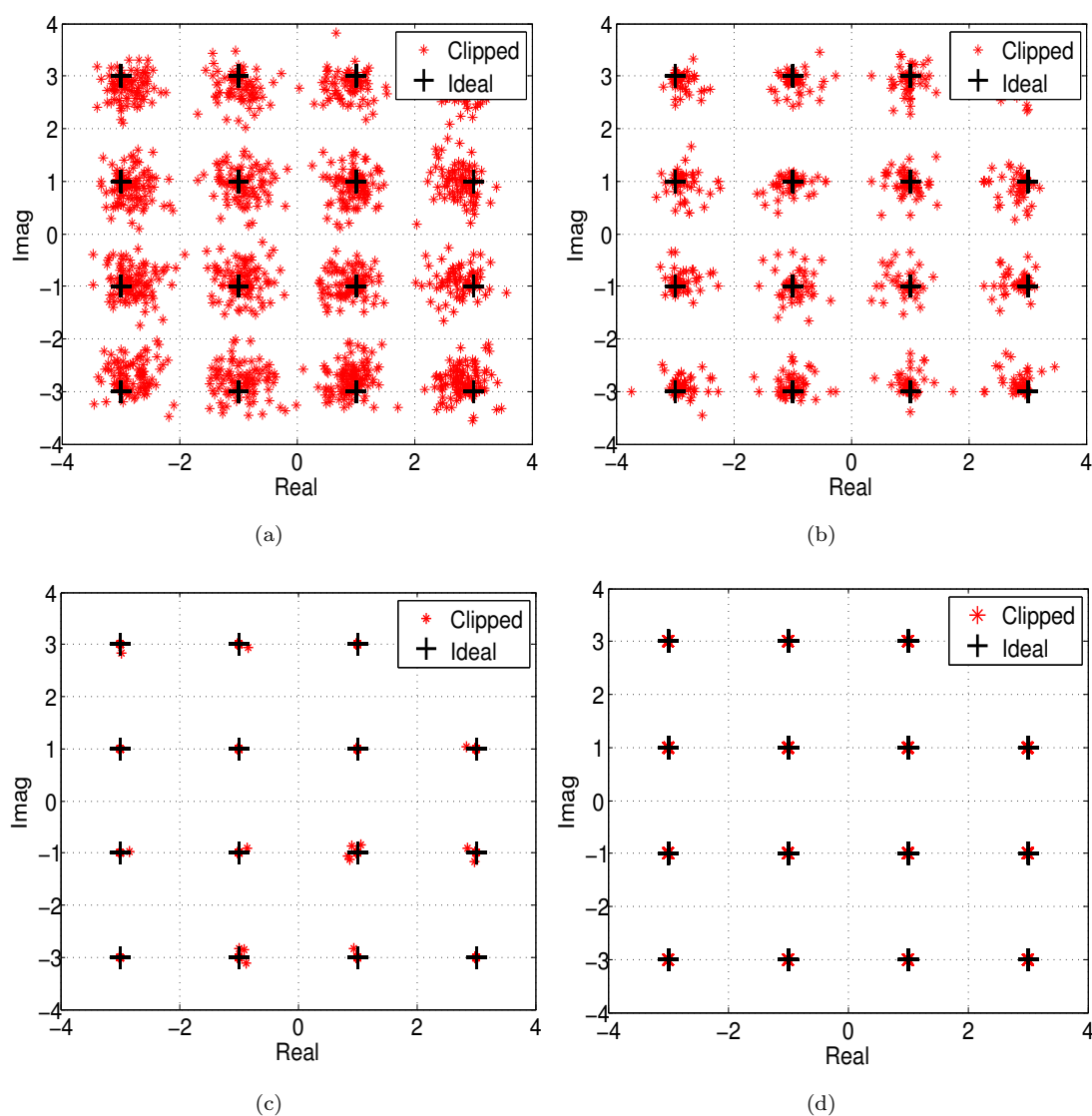


FIGURE 2.5: Impact of the clipping noise on the constellation diagram: (a) 5dB (b) 7dB (c) 10dB (d) 13dB

As can be seen Figure 2.5, for low bias levels, the recovered constellation points after

clipping have small splatter around the ideal constellation due to the clipping noise. The splatter size reflecting the clipping noise decreases with the DC bias levels. For a DC bias as high as 13dB, the clipping noise is negligible and the recovered constellation points are almost equal to the ideal constellation points.

In DCO-OFDM, for  $N$  IFFT points, only  $N/2 - 1$  independent complex symbols are transmitted due to the Hermitian symmetry constraint. Moreover, the electric signal modulates the intensity (not the amplitude) of the optical transmitter. This implies that the required optical power is proportional to the OFDM signal amplitude. As a consequence, the DCO-OFDM technique suffers from an optical power consumption penalty due to the added DC bias.

### 2.2.2 ACO-OFDM

With the aim of improving the power efficiency of optical OFDM systems, an alternative of DCO-OFDM was proposed in [17]. This technique is called asymmetrically clipped optical OFDM and proposes to generate unipolar OFDM signals for IM/DD systems with no need to add a DC bias. This can be achieved by correctly choosing subcarrier frequencies used for data transmission.

In ACO-OFDM, only odd subcarriers are modulated and assigned with Hermitian symmetry. Thus,

$$X(N - k) = \begin{cases} X^*(k), & k \text{ odd} \\ 0, & k \text{ even} \end{cases} \quad (2.14)$$

Using (2.3),  $x(n + \frac{N}{2})$  can be written as,

$$\begin{aligned} x(n + \frac{N}{2}) &= \frac{1}{N} \sum_{k=0}^{N-1} X(k) \exp\left(j2\pi \frac{k}{N} \left(n + \frac{N}{2}\right)\right) \\ &= \frac{1}{N} \sum_{k=0}^{N-1} X(k) \exp\left(j2\pi \frac{kn}{N}\right) \exp(jk\pi) \end{aligned} \quad (2.15)$$

Taking into account that  $\exp(jk\pi) = (-1)^k$ ,  $x(n + \frac{N}{2})$  can be expressed as,

$$x(n + \frac{N}{2}) = \frac{1}{N} \sum_{k=0}^{N-1} X(k) \exp\left(j2\pi \frac{kn}{N}\right) (-1)^k \quad (2.16)$$

In ACO-OFDM, even subcarriers are not modulated. Thus, for  $k$  even,  $X(k) = 0$ . Substituting this constraint in (2.15) leads to,

$$\begin{aligned} x\left(n + \frac{N}{2}\right) &= -\frac{1}{N} \sum_{k=0}^{N-1} X(k) \exp\left(j2\pi \frac{kn}{N}\right) \\ &= -x(n) \end{aligned} \quad (2.17)$$

It can be concluded from (2.17) that the time signal has an antisymmetric property. In ACO-OFDM, the time signal is made positive by hard clipping the entire negative excursion and only the positive part of the bipolar signal is transmitted. The discrete time signal is then given by,

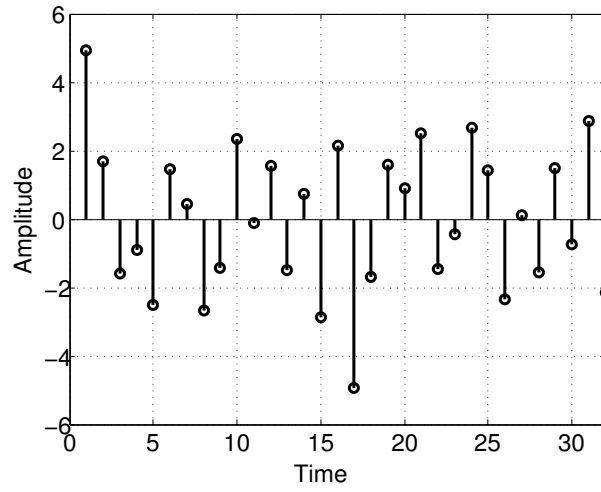
$$x_{u,ACO}(n) = \begin{cases} x(n), & \text{if } x(n) > 0 \\ 0, & \text{if } x(n) \leq 0 \end{cases} \quad (2.18)$$

Figure 2.6 shows the time signal before and after clipping using 16-QAM constellation and 32 subcarriers. As can be seen in this figure, due to the antisymmetric property, for each clipped negative peak, a positive peak with the same absolute value is transmitted. As a result, clipping the negative values does not lead to loss of information and the unclipped time signal can be integrally recovered at the receiver side. The frequency symbols recovered from the unclipped signal can be expressed as,

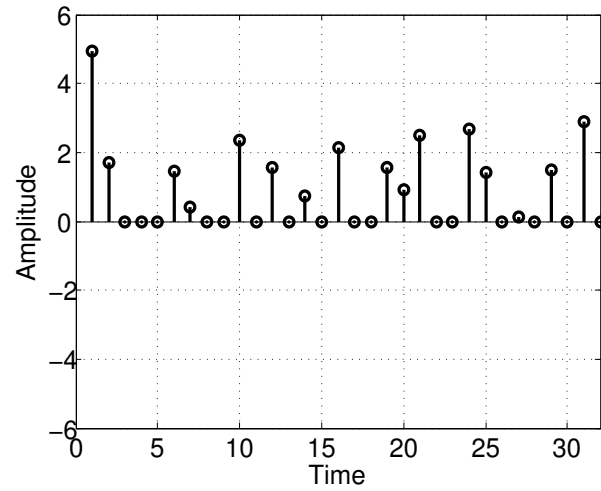
$$\begin{aligned} X(k) &= \sum_{n=0}^{N-1} x(n) \exp\left(-j2\pi \frac{kn}{N}\right) \\ &= \sum_{\substack{n=0 \\ x(n)>0}}^{N-1} x(n) \exp\left(-j2\pi \frac{kn}{N}\right) + \sum_{\substack{n=0 \\ x(n)\leq 0}}^{N-1} x(n) \exp\left(-j2\pi \frac{kn}{N}\right) \end{aligned} \quad (2.19)$$

Let  $X_c(k)$  be the  $k^{\text{th}}$  frequency symbol recovered from the clipped signal,  $x_{u,ACO}(n)$ . Then,  $X_c(k)$  can be expressed as,

$$\begin{aligned} X_c(k) &= \sum_{k=0}^{N-1} x_{u,ACO}(n) \exp\left(-j2\pi \frac{kn}{N}\right) \\ &= \sum_{\substack{n=0 \\ x(n)>0}}^{N-1} x(n) \exp\left(-j2\pi \frac{kn}{N}\right) \end{aligned} \quad (2.20)$$



(a)



(b)

FIGURE 2.6: Time domain waveforms of ACO-OFDM: (a) before clipping (b) after clipping

Substituting (2.20) in (2.19) gives,

$$X(k) = X_c(k) + \sum_{\substack{n=0 \\ x(n) \leq 0}}^{N-1} x(n) \exp\left(-j2\pi \frac{kn}{N}\right) \quad (2.21)$$

Thus,  $X_c(k)$  can be written as,

$$X_c(k) = X(k) - \sum_{\substack{n=0 \\ x(n) \leq 0}}^{N-1} x(n) \exp\left(-j2\pi \frac{kn}{N}\right) = X(k) + N_c(k) \quad (2.22)$$



where  $N_c(k)$  is the clipping noise component in the  $k^{\text{th}}$  subcarrier. Extracting  $N_c(k)$  from (2.22) leads to,

$$N_c(k) = - \sum_{\substack{n=0 \\ x(n) \leq 0}}^{N/2-1} x(n) \exp\left(-j2\pi \frac{kn}{N}\right) - \sum_{\substack{n=N/2 \\ x(n) \leq 0}}^{N-1} x(n) \exp\left(-j2\pi \frac{kn}{N}\right) \quad (2.23)$$

Substituting the antisymmetric property (2.17) in (2.23) gives,

$$N_c(k) = \sum_{\substack{n=0 \\ x(n) > 0}}^{N/2-1} x\left(n + \frac{N}{2}\right) \exp\left(-j2\pi \frac{kn}{N}\right) + \sum_{\substack{n=N/2 \\ x(n) > 0}}^{N-1} x\left(n - \frac{N}{2}\right) \exp\left(-j2\pi \frac{kn}{N}\right) \quad (2.24)$$

Considering a variable change from  $n$  to  $n + \frac{N}{2}$  in the first term and from  $n$  to  $n - \frac{N}{2}$  in the second term gives,

$$\begin{aligned} N_c(k) &= \sum_{\substack{n=N/2 \\ x(n) > 0}}^{N-1} x(n) \exp\left(-j2\pi \frac{k}{N} \left(n - \frac{N}{2}\right)\right) + \sum_{\substack{n=0 \\ x(n) > 0}}^{N/2-1} x(n) \exp\left(-j2\pi \frac{k}{N} \left(n + \frac{N}{2}\right)\right) \\ &= \sum_{\substack{n=N/2 \\ x(n) > 0}}^{N-1} x(n) \exp\left(-j2\pi \frac{kn}{N}\right) \exp(j\pi k) + \sum_{\substack{n=0 \\ x(n) > 0}}^{N/2-1} x(n) \exp\left(-j2\pi \frac{kn}{N}\right) \exp(-j\pi k) \end{aligned} \quad (2.25)$$

For  $k$  odd,  $\exp(j\pi k) = \exp(-j\pi k) = -1$ , then,

$$N_c(k) = -X_c(k) \quad (2.26)$$

Substituting (2.26) in (2.22) gives,

$$X_c(k) = \frac{X(k)}{2} \quad (2.27)$$

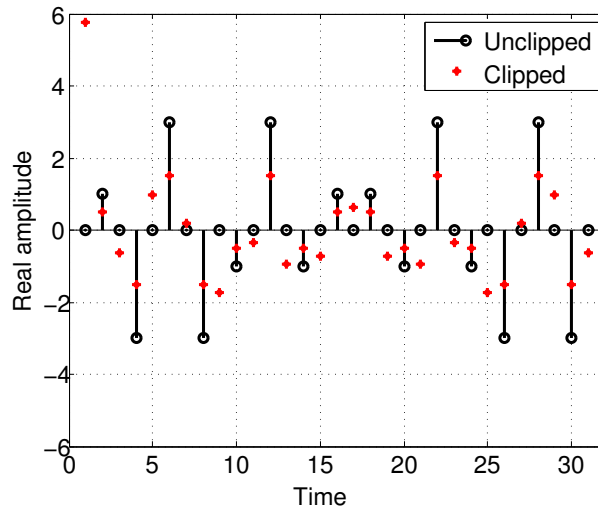
For  $k$  even,  $\exp(j\pi k) = \exp(-j\pi k) = 1$  and  $X(k) = 0$ , then,

$$N_c(k) = X_c(k) \quad (2.28)$$

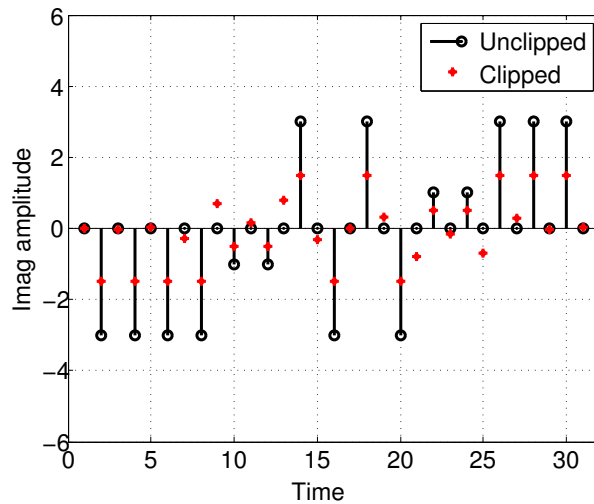
As a result, if only odd subcarriers are modulated, the amplitude of recovered symbols,  $X_c(k)$ , is half of their original values (without clipping). Furthermore, all the clipping noise falls on the even subcarriers. Hence, the data carrying odd subcarriers are not

affected by clipping noise. This is summarized in (2.29).

$$X_c(k) = \begin{cases} \frac{X(k)}{2}, & k \text{ odd} \\ N_c(k), & k \text{ even} \end{cases} \quad (2.29)$$



(a)



(b)

FIGURE 2.7: Frequency symbols recovered from the clipped and unclipped DMT signals  
(a) real part (b) imaginary part

Figure 2.7 shows the clipping effect on the frequency vector when an ACO-OFDM modulation is employed. As expected by the analytical results, only even subcarriers are affected by the clipping noise. On the other hand, the amplitudes of odd subcarriers are divided by two as compared to their original values before the clipping process.

The same results can be seen in Figure 2.8 depicting a 16-QAM constellation diagram recovered from a clipped ACO-OFDM signal.

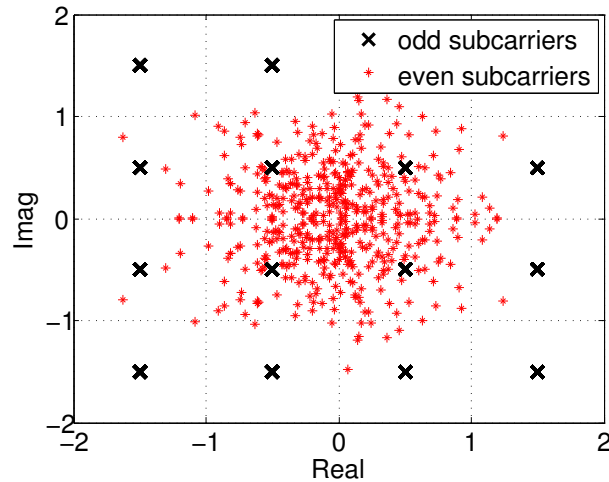


FIGURE 2.8: The ACO-OFDM signal constellation after clipping

In ACO-OFDM, only the positive part is transmitted. Thus, the ACO-OFDM signal amplitude is equal to the half of bipolar OFDM amplitude. Therefore, the ACO-OFDM technique has a high optical efficiency. However, for  $N$  IFFT points, only  $N/4$  subcarriers are used to carry useful data due to Hermitian symmetry and odd subcarriers modulation constraints.

### 2.2.3 PAM-DMT

In ACO-OFDM, only odd-numbered subcarriers are used to carry data, even subcarriers being off to guarantee an anti-symmetric time-domain signal at the IFFT output. This restriction can degrade system performance in frequency-selective channels, namely the performance of bit-allocation algorithm. To overcome the restriction to use only odd-numbered subcarriers and perform an optimal adaptation of the channel frequency response, an alternative to ACO-OFDM called pulse amplitude modulation DMT was proposed in [19]. This technique consists in modulating only the imaginary components of all the available subcarriers to generate an anti-symmetric time-domain signal and enable an asymmetric clipping at zero. Thus, similar to ACO-OFDM, only the positive part is transmitted, resulting in a power efficient technique. However, since all subcarriers are employed to carry data, bit-loading can be used more efficiently to adapt the channel response, thus permitting to achieve better performance in frequency-selective channels as compared to ACO-OFDM.

PAM-DMT uses also the Hermitian symmetry property to generate real OFDM signals. On the other hand, the real components are set to zero to enable an asymmetric clipping at zero. Thus,

$$X(k) = \begin{cases} jC_k, & k = 1, 2, \dots, \frac{N}{2} - 1 \\ X^*(N - k), & k = \frac{N}{2} + 1, \dots, N - 1 \\ 0, & k = 0, \frac{N}{2} \end{cases} \quad (2.30)$$

where  $C_k$  are the symbols containing useful data. Taking into account (2.30), the  $n^{\text{th}}$  time-domain sample can be written as,

$$\begin{aligned} x(n) &= \frac{1}{N} \sum_{k=0}^{N-1} jC_k \exp\left(j2\pi \frac{kn}{N}\right) \\ &= \frac{1}{N} \left[ \sum_{k=1}^{N/2-1} jC_k \exp\left(j2\pi \frac{kn}{N}\right) + \sum_{k=N/2+1}^{N-1} -jC_{N-k} \exp\left(j2\pi \frac{kn}{N}\right) \right] \end{aligned} \quad (2.31)$$

Considering a variable change from  $k$  to  $N - k$  in the second term gives,

$$\begin{aligned} x(n) &= \frac{1}{N} \sum_{k=1}^{N/2-1} \left[ jC_k \exp\left(j2\pi \frac{kn}{N}\right) - jC_k \exp\left(-j2\pi \frac{kn}{N}\right) \right] \\ &= \frac{-2}{N} \sum_{k=0}^{N-1} C_k \sin\left(j2\pi \frac{kn}{N}\right) \end{aligned} \quad (2.32)$$

$x(N - n)$  can be expressed as,

$$\begin{aligned} x(N - n) &= \frac{-2}{N} \sum_{k=0}^{N-1} C_k \sin\left(j2\pi k \frac{(N - n)}{N}\right) \\ &= \frac{-2}{N} \sum_{k=0}^{N-1} C_k \sin\left(2\pi k - \frac{j2\pi kn}{N}\right) \\ &= \frac{-2}{N} \sum_{k=0}^{N-1} C_k \left[ \sin\left(-\frac{j2\pi kn}{N}\right) \right] \end{aligned} \quad (2.33)$$

Finally,

$$x(N - n) = -x(n), \quad n = 1, \dots, \frac{N}{2} - 1 \quad (2.34)$$

As a result, similar to ACO-OFDM, the time-domain signal at the IFFT output has an antisymmetric property. Thus, clipping the entire negative excursion does not lead to loss of information since all necessary information is contained in the positive part. Figure 2.9 shows the time domain PAM-DMT signal before and after clipping.

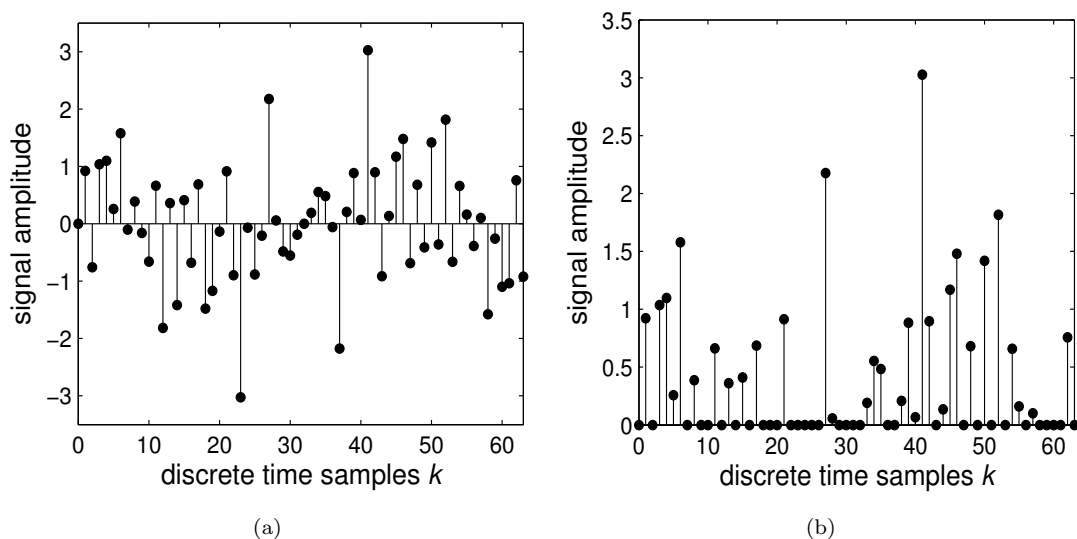


FIGURE 2.9: Time domain waveforms of PAM-DMT: (a) before clipping (b) after clipping [19]

It has been shown in [19] that if PAM modulation is used to modulate the imaginary components of all subcarriers, all the distortion arising from the asymmetric clipping falls on the real parts of the subcarriers and thus is orthogonal to the data. Orthogonality between noise and data is illustrated in Figure 2.10.

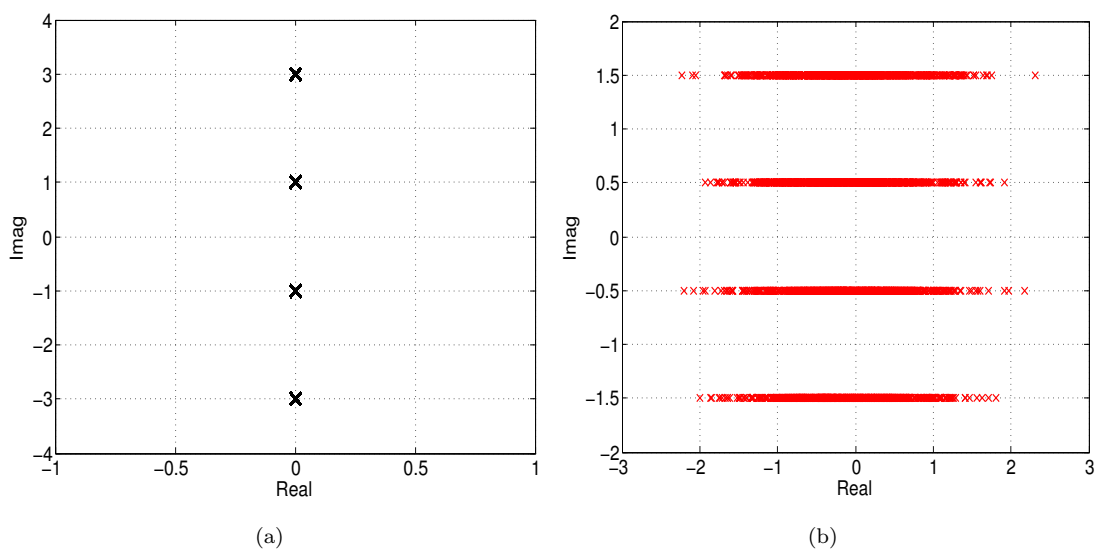


FIGURE 2.10: 4-PAM-DMT constellation (a) before clipping (b) after clipping

In PAM-DMT, all the subcarriers are used to carry useful data, but only half of the quadrature is filled. Thus, PAM-DMT and ACO-OFDM have identical performance in terms of spectral efficiency.

### 2.2.4 BER performance

One robust metric that is commonly used in communications to evaluate system performance is the bit error rate (BER). It is defined as the ratio of error bits to the total number of transmitted bits, thus describing the probability of bit error. The BER depends, inter alia, on the channel noise, the signal power and the considered constellation. In other words, the bit error rate is a function of the signal to noise ratio defined as the ratio of the signal power to the noise power. Analytical expressions of the bit error rate as function of electric energy-per-bit to noise power spectral density,  $E_b(elec)/N_0$ , were early proposed in the literature. The presented analytical formula are strongly limited by the considered channel model and do not provide accurate estimations of system BER performance. With the use of FFT/IFFT transforms, computer simulations are used to provide reliable estimations of BER with an optimized computing time.

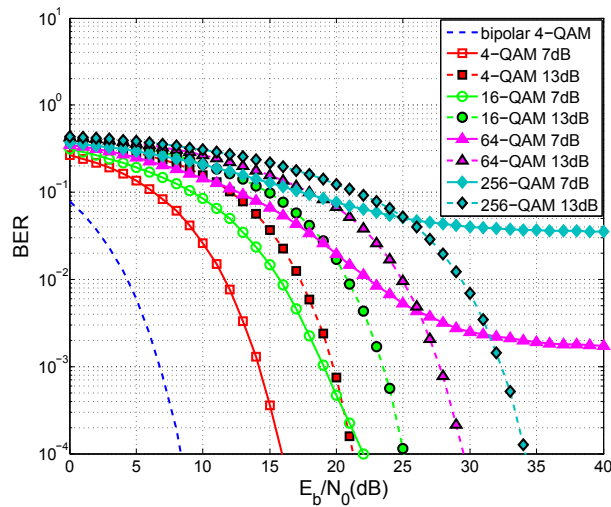


FIGURE 2.11: DCO-OFDM BER as function of  $E_{b(elec)}/N_0$  for 4-QAM, 16-QAM and 256-QAM with DC bias of 7dB and 13dB

Figure 2.11 shows the simulation results of the DCO-OFDM BER as function of electric energy-per-bit to noise power spectral density,  $E_{b(elec)}/N_0$ , in an additive white Gaussian noise Additive White Gaussian Noise (AWGN) channel. The simulated OOFDM frame is formed by 1000 symbols each with 256 subcarriers. In the case of OFDM, an oversampling with an oversampling factor of 4 is to be performed in order to correctly approximate the PAPR of the continuous OOFDM signal [53]. As shown in [15], the performance in an additive white Gaussian noise channel forms a theoretical basis for OOFDM systems from which the results for the more general case of a frequency selective

channel can be found. As can be seen in Figure 2.11, for high bias levels, the clipping noise is not dominant and the required SNR is approximately equal to the bipolar signal SNR plus the added bias (in dB). For lower bias levels and large constellations ( $\geq 64$ ), the clipping noise dominates and the BER graphs plateau.

Figure 2.12 shows the simulation results of the ACO-OFDM BER as function of electric energy-per-bit to noise power spectral density,  $E_{b(\text{elec})}/N_0$ , in an AWGN channel. In ACO-OFDM, the half of the electrical power is wasted on the even subcarriers carrying no useful data. Consequently, for any constellation, ACO-OFDM signals always require 3dB more power than bipolar systems.

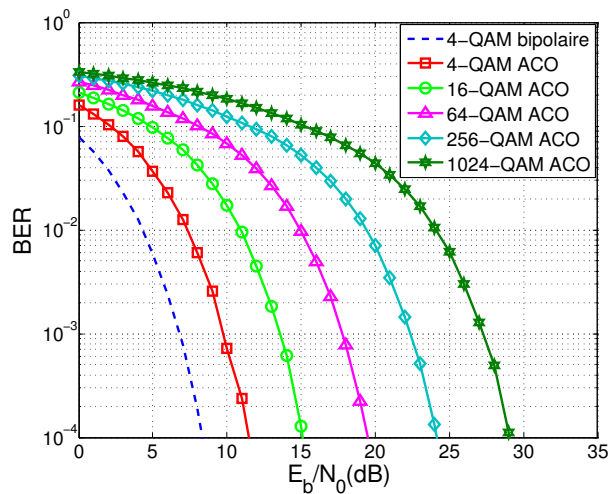


FIGURE 2.12: ACO-OFDM BER as function of  $E_{b(\text{elec})}/N_0$  for 4-QAM, 16-QAM, 256-QAM and 1024-QAM

Finally, it has been shown in [19] that in a flat fading channel and for the same spectral efficiency, PAM-DMT and ACO-OFDM achieve identical BER performance. In a frequency selective channel, since PAM-DMT allows to perform an optimal rate-adaptive bit-loading (Figure 2.13), PAM-DMT can achieve higher bit rates as compared to ACO-OFDM. The gain in bit rate performance decreases with the number of total subcarriers. Thus, for  $N = 32$ , PAM-DMT can achieve up to 1.21 times higher bit rates compared to ACO-OFDM, whereas the reached gain is negligible for  $N \geq 512$ .

### 2.2.5 Optical power efficiency

The BER as a function of  $E_{b(\text{elec})}/N_0$  forms a theoretical basis to compare OFDM schemes. However, in optical systems, the transmitted optical power is the main system

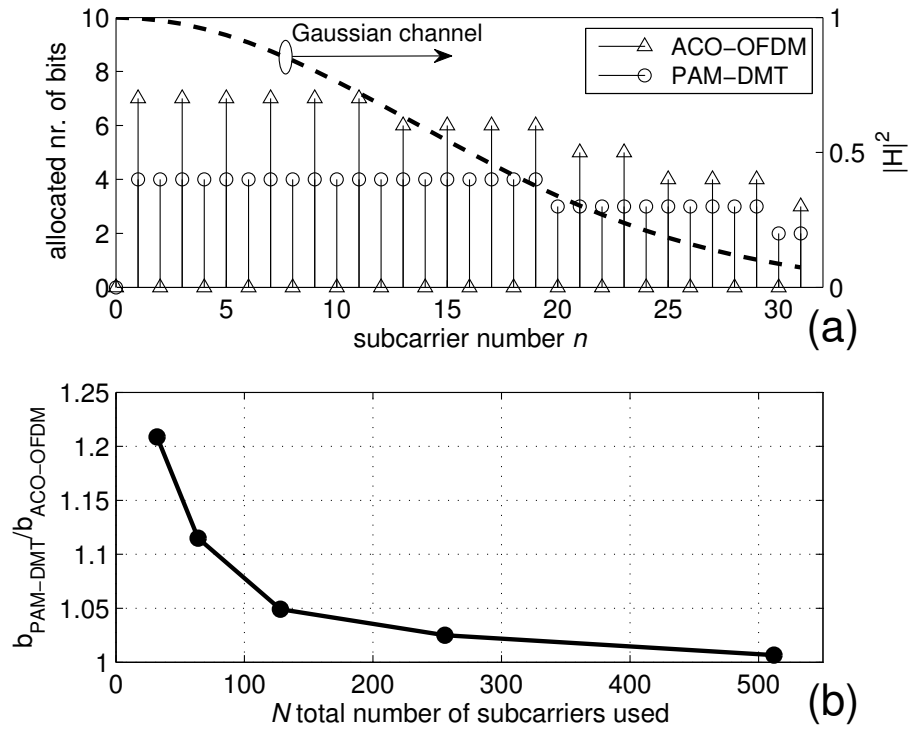


FIGURE 2.13: Comparison of PAM-DMT and ACO-OFDM performance in a Gaussian channel response (a) bit-loading efficiency (b) achievable bit-rate as function of  $N$  [19]

constraint, being one of the main indicators for the system power consumption. Thus, the optical energy-per-bit to noise power spectral density metric,  $E_{b(\text{opt})}/N_0$ , is usually used to evaluate the optical power efficiency of optical systems [15, 18]. Contrary to the electric power, that is proportional to  $x^2(t)$ , the transmitted optical power is equal to the amplitude of the transmitted signal. Thus, the average transmitted optical power can be expressed as

$$P_{\text{opt}} = E\{x\}. \quad (2.35)$$

In ACO-OFDM, only the positive part is transmitted, therefore the optical power of an ACO-OFDM signal can be computed using the formula given in (4.27),

$$P_{\text{opt},\text{ACO}} = E\{x_{u,\text{ACO}}(t)\} = \frac{\sigma}{\sqrt{2\pi}} \quad (2.36)$$

If the DC bias is assumed to be rather large, so that no clipping noise is present in the transmitted signal, the optical power in DCO-OFDM can be expressed as

$$P_{\text{opt},\text{DCO}} = E\{x_{u,\text{DCO}}(t)\} \approx K_b \quad (2.37)$$



For a normalized optical power, the optical energy-per-bit to noise power spectral density is defined as [15],

$$\frac{E_{b(opt)}}{N_0} = \frac{E^2\{x\}}{E\{x^2\}} \frac{E_{b(elec)}}{N_0}, \quad (2.38)$$

where  $E\{x^2\}$  is the average electric power of the transmitted unipolar signal. Figure 2.14 compares the optical power efficiencies of DCO-OFDM and ACO-OFDM as function of bit rate to normalized bandwidth ratio for  $BER = 10^{-3}$ .

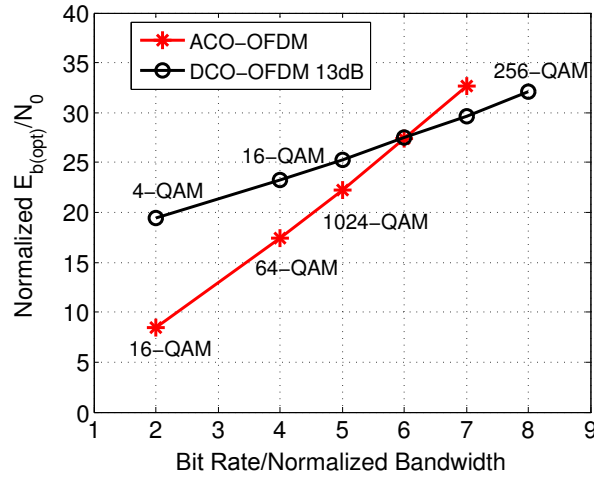


FIGURE 2.14: Normalized  $E_{b(opt)}/N_0$  as function of bit rate to normalized bandwidth ratio for  $BER = 10^{-3}$ .

For the same constellation size, DCO-OFDM achieves twice the data rate as compared to ACO-OFDM. This is due to the fact that ACO-OFDM modulates only odd subcarriers, whereas even subcarriers are set to zero. Thus, to make a fair comparison,  $M$ -QAM DCO-OFDM should be compared to  $M^2$ -QAM ACO-OFDM. To this end, optical power efficiencies of ACO-OFDM and DCO-OFDM are compared for different bit rate/normalized bandwidth values.

As can be seen in Figure 2.14, for bit rate to normalized bandwidth ratios lower than 6, ACO-OFDM requires the lowest optical  $E_{b(opt)}/N_0$ , only the positive part of the bipolar signal being transmitted. For bit rate to normalized bandwidth ratios larger than 6, ACO-OFDM becomes inefficient in terms of optical power as compared to DCO-OFDM. Indeed, the optical signal to noise ratio required to transmit  $M^2$ -QAM on each ACO-OFDM subcarrier becomes significant as compared to the large DC bias required to achieve an acceptable noise clipping penalty in DCO-OFDM.

All the simulation results provided in this chapter are fully compliant with results from literature [15]-[19], which is a good basis to compare our new proposed techniques with the state of the art. To achieve high data rates in optical links, high bit rate to normalized bandwidth ratios are required. Thus, it can be concluded that DCO-OFDM is preferred for high data rate and low-cost optical links, DCO-OFDM providing high optical power efficiency with low complexity. Hence the idea to focus on improving the optical power efficiency of DCO-OFDM rather than ACO-OFDM presented in Chapter 4.



## Chapter 3

# Hermitian symmetry free optical OFDM

### Contents

---

<b>3.1</b>	<b>Hermitian symmetry in optical OFDM . . . . .</b>	<b>55</b>
<b>3.2</b>	<b>DHT-based optical OFDM . . . . .</b>	<b>58</b>
<b>3.3</b>	<b>Flip-OFDM . . . . .</b>	<b>60</b>
<b>3.4</b>	<b>Hermitian symmetry free OFDM . . . . .</b>	<b>63</b>
3.4.1	System model . . . . .	63
3.4.2	PAPR and BER performance . . . . .	66
3.4.3	Channel equalization . . . . .	75
3.4.4	Computational complexity . . . . .	78
<b>3.5</b>	<b>Hermitian symmetry free Flip-OFDM . . . . .</b>	<b>80</b>
3.5.1	System model . . . . .	80
3.5.2	Bit error rate . . . . .	82

---

### 3.1 Hermitian symmetry in optical OFDM

To be employed to drive light sources such as LEDs and Lasers, OFDM signals must be real and positive, so that they are compatible with the light source characteristic. A common approach to generate real time OFDM signals is to constrain the frequency symbols at the IFFT input to have an Hermitian symmetry property. This modulation

technique is also known as Discrete MultiTone modulation. The fast Fourier transform (FFT) and its inverse transform (IFFT) are the key components of an OFDM system. The power consumption and the occupied chip area of the OFDM transceiver increase significantly with the IFFT/FFT sizes. On the other hand, the Hermitian symmetry of the frequency symbols in optical OFDM systems results in a doubled size of the FFT/IFFT blocks. Indeed, to modulate  $N$  frequency symbols,  $2N$ -point IFFT/FFT transforms are needed. The impact of the FFT/IFFT sizes on the optical OFDM transceiver performance was studied in [54]. Figure 3.1 shows the effect of the FFT size on the error vector magnitude (EVM) for an FFT/IFFT sizes varying from 32 to 1024. As shown in [54], increasing the FFT/IFFT sizes increases the number of data

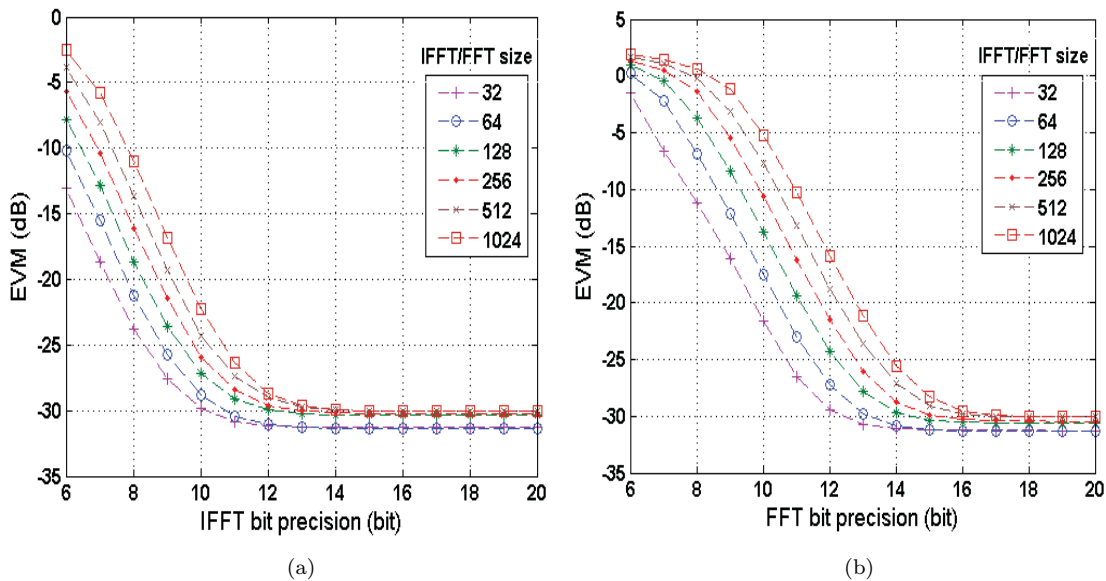


FIGURE 3.1: EVM as function of (a) FFT bit precision (b) IFFT bit precision, for FFT/IFFT sizes varying from 32 to 1024 [54]

subcarriers and therefore the dynamic range of the OFDM signal, which requires higher precision in the arithmetic operations. This phenomenon has a direct impact on the transceiver EVM performance. Indeed, as shown in Figure 3.1, the required FFT/IFFT bit precisions permitting to reach a given EVM, increase with the FFT/IFFT sizes. In other words, for a given FFT/IFFT bit precision, the corresponding EVM reduces as the FFT/IFFT size decreases and vice versa. Thus, for a FFT bit precision of 8 for example, increasing the FFT/IFFT sizes by a factor of two, leads to an EVM penalty of approximately 2dB. It has to be noted that for high FFT/IFFT bit precisions, an EVM floor occurs due to the limited resolution of DAC/ADC (as shown in Figure 3.1). For a radix-2 algorithm [55], the number of multiplications and additions required to compute

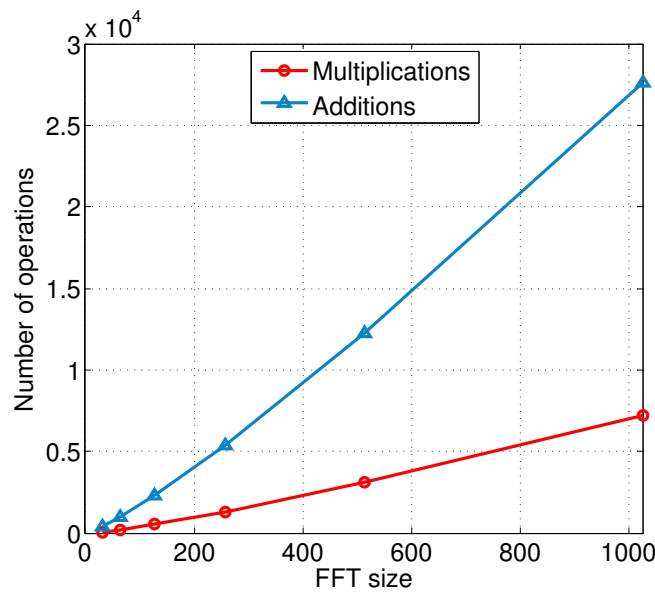
the real-valued FFT is given by,

$$\begin{aligned} P^{FFT} &= N \log_2 N - 3N + 4 \\ A^{FFT} &= 3N \log_2 N - 3N + 4 \end{aligned} \quad (3.1)$$

where  $N$  is the FFT size. The number of multiplications and additions required to compute the FFT transform is also referred to as computational complexity. Figure 3.2 depicts the number of multiplications and additions required to compute the FFT on complex-valued input data using split-radix algorithm for FFT sizes varying from 32 to 1024.

FFT size	Number of Multiplications	Number of Additions
32	64	388
64	196	964
128	516	2308
256	1284	5380
512	3076	12292
1024	7172	27652

(a)



(b)

FIGURE 3.2: Computational Complexity of split-radix FFT algorithm on complex input data as function of the FFT size

It can be clearly seen in Figure 3.2 that the computational complexity of a DMT system increases drastically with the FFT size. Indeed, increasing the FFT size by a factor of two, increases by a factor of  $\sim 2.3$  the number of operations required to compute the

FFT transform. Application Specific Integrated Circuits (ASICs) are commonly used in networking devices to maximize performance [56]. The computational complexity is directly related to the power consumption and the cost of ASIC-based chips. The impact of the FFT size on the power consumption and the cost of ASIC-based DMT transceivers was studied in [54]. For this purpose, for each FFT size from 32 to 1024, a system was designed and synthesized in order to assess the occupied area and power consumption. The FFT/IFFT precisions for each FFT size were determined based on the results presented in Figure 3.1. The results of this study are shown in Figure 3.3 depicting the occupied chip area and power consumption trade-offs for 25Gb/s DMT ASIC transceivers. As shown in [54], the cost and the power consumption of both transmitters and receivers increase considerably with the FFT/IFFT sizes even if the FFT/IFFT precisions are fixed. The increase is observed to be more significant for high FFT/IFFT sizes. Thus, when changing the FFT size from  $N = 512$  to  $N = 1024$ , the occupied chip area increases of approximately 40% while an increase of about 38% in the receiver power consumption is observed. These results can be seen as a direct measure of the Hermitian symmetry impact on the cost and power consumption of DMT transceivers, since the FFT/IFFT blocks are generally the dominating power consumer in DMT systems.

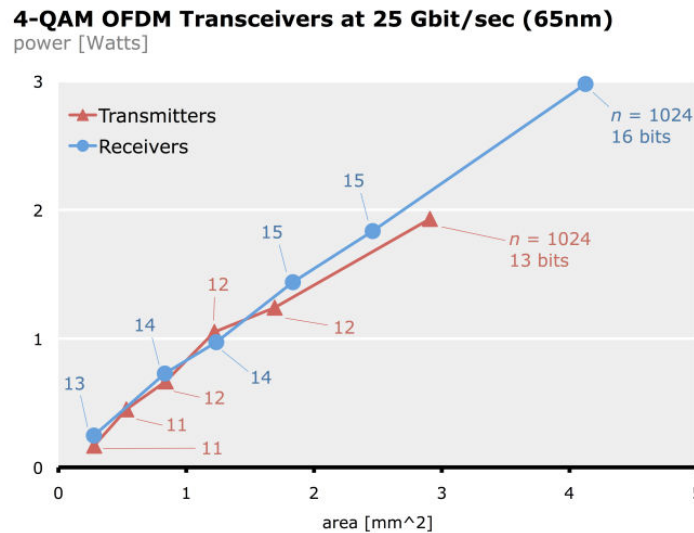


FIGURE 3.3: The area and power consumption of 25Gb/s DMT ASIC transceivers for different FFT sizes.

Furthermore, to generate a frequency vector satisfying the Hermitian symmetry constraint, the complex conjugate of the origin frequency vector is computed at the

IFFT input. This requires additional resources and longer time to compute the FFT transform, thus impacting the latency and the rate of the overall DMT system. As mentioned in Chapter 1, the cost and power consumption of optical OFDM systems are a major obstacle to the mass market adoption of OFDM-based solutions in the next generation of networks. The hardware complexity issue in optical OFDM systems has to be mandatorily resolved to enable the mass market deployment of real OFDM systems. Few techniques aiming to reduce the hardware complexity of optical OFDM systems were proposed in the literature. The advantages and drawbacks of each technique are detailed in the following sections.

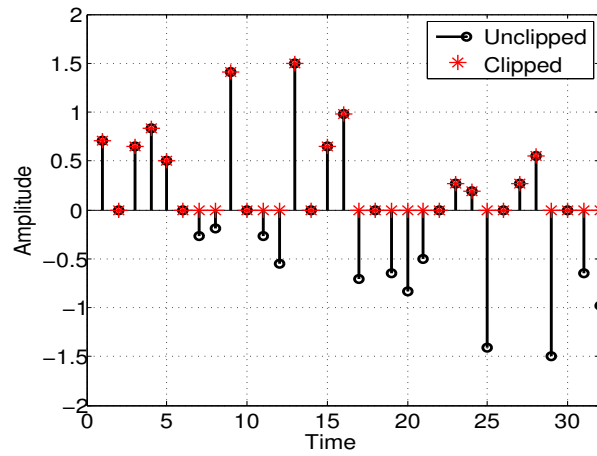
### 3.2 DHT-based optical OFDM

To overcome the Hermitian symmetry drawbacks in DMT systems, a technique based on discrete Hartley transform (DHT) was proposed in [57]. This technique consists in applying the inverse fast Hartley transform (IFHT) to the frequency symbols as follows,

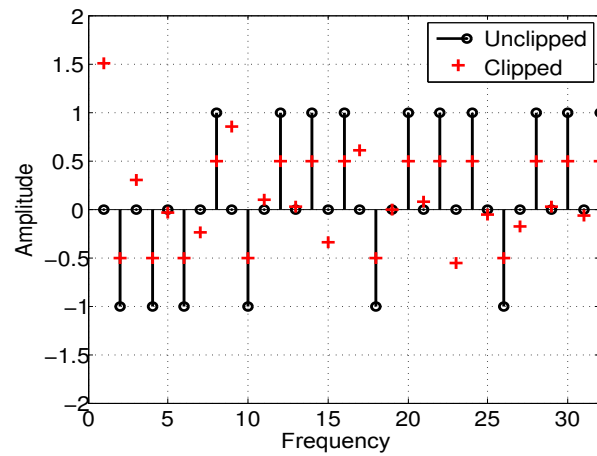
$$x(n) = \frac{1}{\sqrt{N}} \sum_{k=0}^{N-1} X(k) \left[ \cos\left(2\pi \frac{kn}{N}\right) + \sin\left(2\pi \frac{kn}{N}\right) \right] \quad (3.2)$$

The fast Hartley transform (FHT) is used in the receiver to recover the transmitted frequency symbols. It was shown in [57], that if the frequency vector is real (i.e. real constellations such as binary phase shift keying (BPSK) or pulse amplitude modulation (PAM) are used for the bit to symbol mapping), the time-domain signal at the IFHT output has only real values. Consequently, the Hermitian symmetry property of the frequency symbols at the IFHT input is not needed and the additional resources required to compute the complex conjugate can be saved. In FHT-based optical OFDM, all the subcarriers are used to carry non redundant useful data, permitting to transmit the double of independent symbols compared to the conventional FFT-based optical systems. In other words, to transmit a given number of bits using  $N$  subcarriers, optical OFDM system based on fast Hartley transform, requires a lower constellation size. Furthermore, it was clearly shown in [57] that both DCO-OFDM and ACO-OFDM techniques can be applied to the FHT-based DMT, with the same power efficiency of FFT-based DMT. Figure 3.4 shows the clipping effects on the time domain signal and the frequency vector when an IFHT-based ACO-OFDM modulation is applied on a BPSK constellation. In





(a)



(b)

FIGURE 3.4: Clipping effects on IFHT-based ACO-OFDM signal (a) Time domain (b) Frequency domain

FHT-based ACO-OFDM, as in the case of FFT-based ACO-OFDM, the clipping noise affects only the even subcarriers, thus permitting to integrally recover the transmitted data from the clipped signal. Moreover, for a given bit rate, FHT-based optical OFDM permits to transmit the same data with the same power efficiency of optical FFT-based OFDM systems.

However, the use of the Hartley transform to replace the fast Fourier transforms in optical OFDM systems, does not reduce the computational complexity. Indeed, considering a radix-2 algorithm, the FHT-based transform requires the same number of multiplications and  $N - 2$  more additions than the FFT-based algorithm. Finally, although the use of the Hartley transform in OFDM-based optical systems permits to save the additional resources required to compute the complex conjugate, it increases the computational

complexity which increases in turn the cost and the power consumption of ASIC-based DMT transceivers as compared to FFT-based algorithms.

### 3.3 Flip-OFDM

To reduce the computational complexity of optical OFDM systems, an alternative approach of ACO-OFDM called Flip-OFDM with the same performance and different hardware complexity was proposed in [58]. The block diagrams of Flip-OFDM transmitter and receiver are depicted in Figure 3.5.

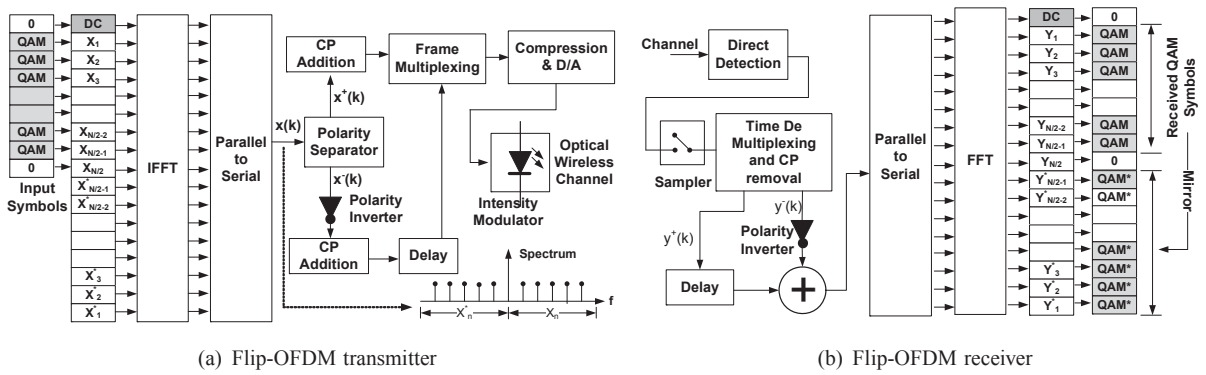


FIGURE 3.5: Block diagrams of Flip-OFDM transmitter and receiver [58]

Contrary to the conventional ACO-OFDM, where only odd subcarriers are modulated, Flip-OFDM modulates all the subcarriers and uses the Hermitian symmetry property to generate a real bipolar OFDM signal. The resulting real bipolar time signal given by (2.3), is considered as the sum of a positive part,  $x^+(n)$ , and a negative part,  $x^-(n)$ ,

$$x(n) = x^+(n) + x^-(n) \quad (3.3)$$

where the positive and negative parts are respectively given by,

$$x^+(n) = \begin{cases} x(n), & \text{if } x(n) \geq 0 \\ 0, & \text{otherwise} \end{cases} \quad (3.4)$$

$$x^-(n) = \begin{cases} x(n), & \text{if } x(n) < 0 \\ 0, & \text{otherwise} \end{cases} \quad (3.5)$$

In order to convert the bipolar signal,  $x(n)$ , to an unipolar signal, the positive part is transmitted in the first OFDM subframe and the flipped negative part, is transmitted in the second OFDM subframe as follows,

$$x_{2N,Flip}(n) = \begin{cases} x^+(n), & n = 0, \dots, N-1 \\ -x^-(n-N), & n = N, \dots, 2N-1 \end{cases} \quad (3.6)$$

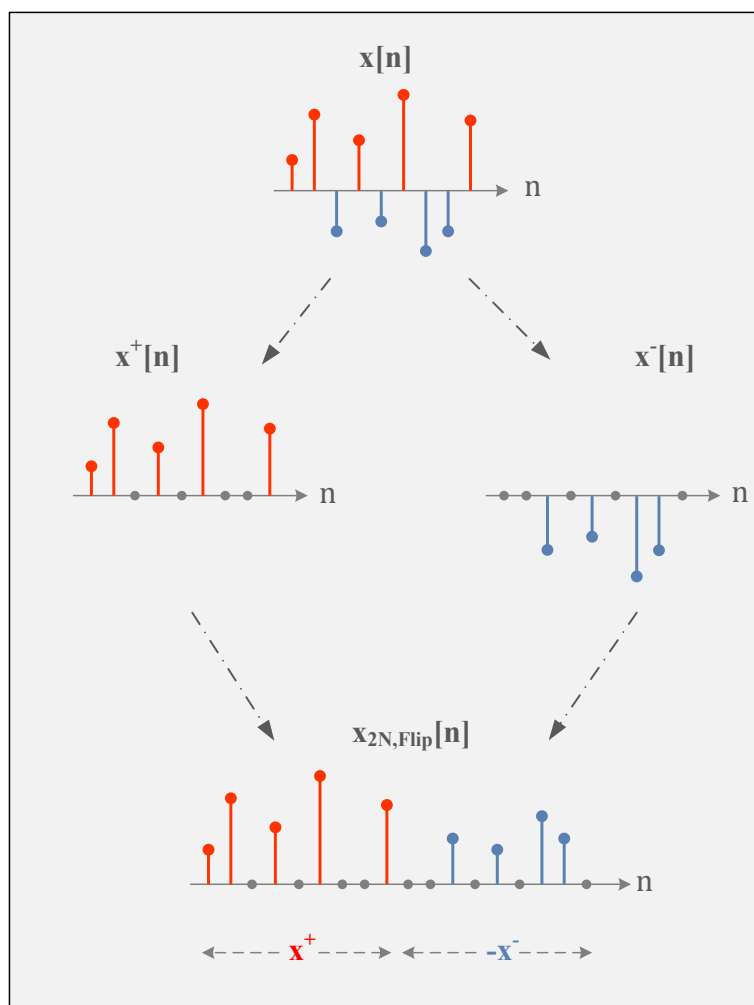


FIGURE 3.6: Illustration of the Flip-OFDM concept

Figure 3.6 illustrates the process of generating an ACO-OFDM signal at the transmitter side using the Flip-OFDM approach. At the receiver side, the real bipolar OFDM signal,  $y(k)$ , is recovered as follows,

$$y(n) = y^+(n) - y^-(n) \quad (3.7)$$

where  $y^+(n)$  and  $y^-(n)$  represent respectively the first and second subframes of the received OFDM signal. The transmitted frequency vector is then recovered by performing a conventional OFDM demodulation. It was clearly shown in [58], that Flip-OFDM and ACO-OFDM have the same performance in terms of spectral efficiency, signal to noise ratio and bit error rate. Furthermore, considering  $N$ -point IFFT/FFT blocks, Flip-OFDM transmits twice as many information as ACO-OFDM. Consequently, Flip-OFDM offers a saving of 50% in the receiver hardware complexity as compared to ACO-OFDM. However, Flip-OFDM has two main drawbacks: first, Flip-OFDM deals with the Hermitian symmetry property to generate real OFDM signals, leading to an increase of power consumption and an enlargement of occupied chip area. Second, Flip-OFDM permits to generate only ACO-OFDM signals and therefore can not be applied to the recently proposed optical power efficient techniques based on DCO-OFDM [50].

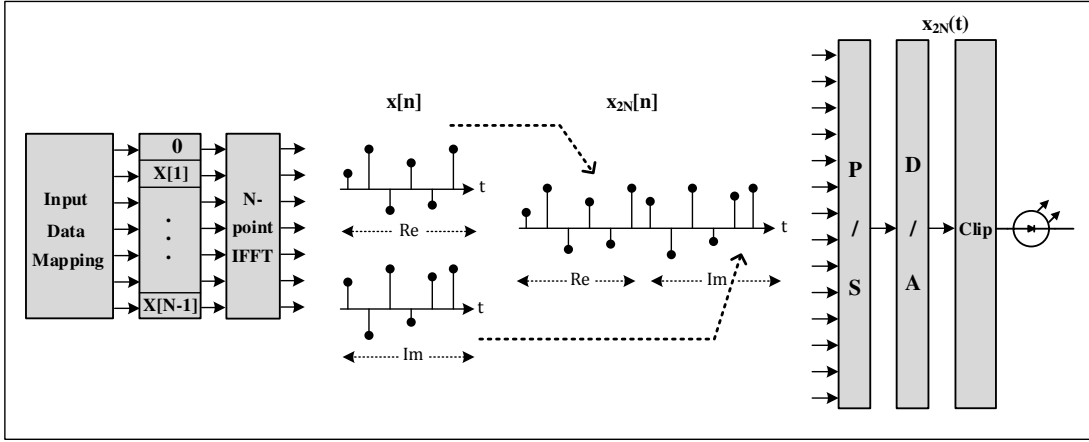
## 3.4 Hermitian symmetry free OFDM

### 3.4.1 System model

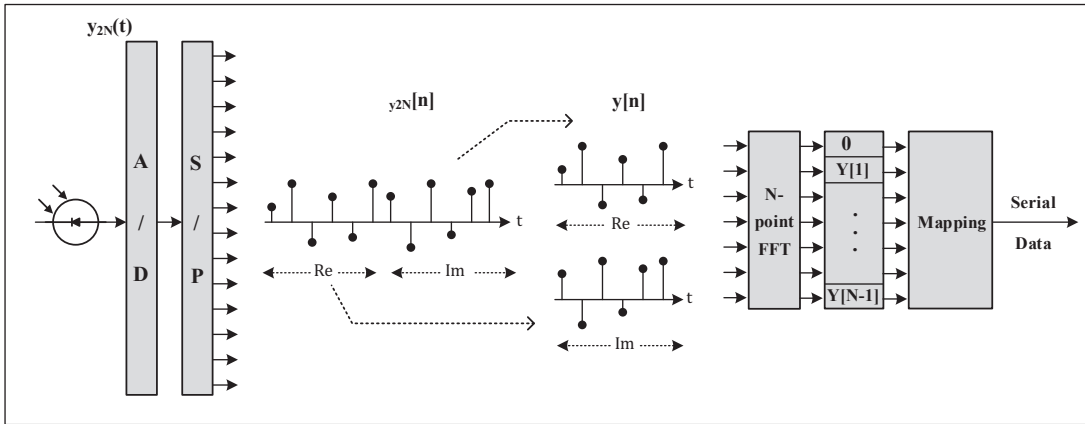
To overcome the drawbacks of the techniques presented above, we propose a novel technique permitting to improve the hardware complexity with no need to constrain the frequency symbols to have an Hermitian symmetry property. We call this technique Hermitian symmetry free OFDM. The block diagrams of HSF-OFDM transmitter and receiver are depicted in Figure 3.7.

Indeed, HSF-OFDM is based on applying the IFFT transform to a frequency vector that does not satisfy the Hermitian symmetry constraint, which results in a complex OFDM signal at the IFFT output. The complex signal is then converted to a real OFDM signal using a novel specific signal processing method. Indeed, the frequency vector,  $X(k)$ , is directly input to an  $N$ -point IFFT block as in conventional complex OFDM systems. Since no Hermitian symmetry constraint is imposed, the IFFT output signal is complex and can be formulated as follows,

$$x(n) = \sum_{k=0}^{N-1} (X_R(k) + jX_I(k)) \exp(j2\pi \frac{kn}{N}) \quad (3.8)$$



(a) Transmitter block diagram



(b) Receiver block diagram

FIGURE 3.7: Block diagrams of HSF-OFDM transmitter and receiver

where  $X_R(k)$  and  $X_I(k)$  are respectively the real and imaginary components of  $X(k)$ . To avoid any DC shift, the DC component,  $X(0)$ , is set to zero. The complex time signal,  $x(n)$ , can be written as,

$$x(n) = x_R(n) + jx_I(n), \quad n = 1, 2, \dots, N - 1 \quad (3.9)$$

where  $x_R(n)$  and  $x_I(n)$  are respectively the real and the imaginary components of  $x(n)$ . To generate a  $2N$ -point real OFDM signal, the real and imaginary parts of the  $N$ -point complex OFDM signal are juxtaposed in the time-domain as follows,

$$x_{2N}(n) = \begin{cases} x_R(n), & n=0, \dots, N-1 \\ x_I(n - N), & n=N, \dots, 2N-1 \end{cases} \quad (3.10)$$

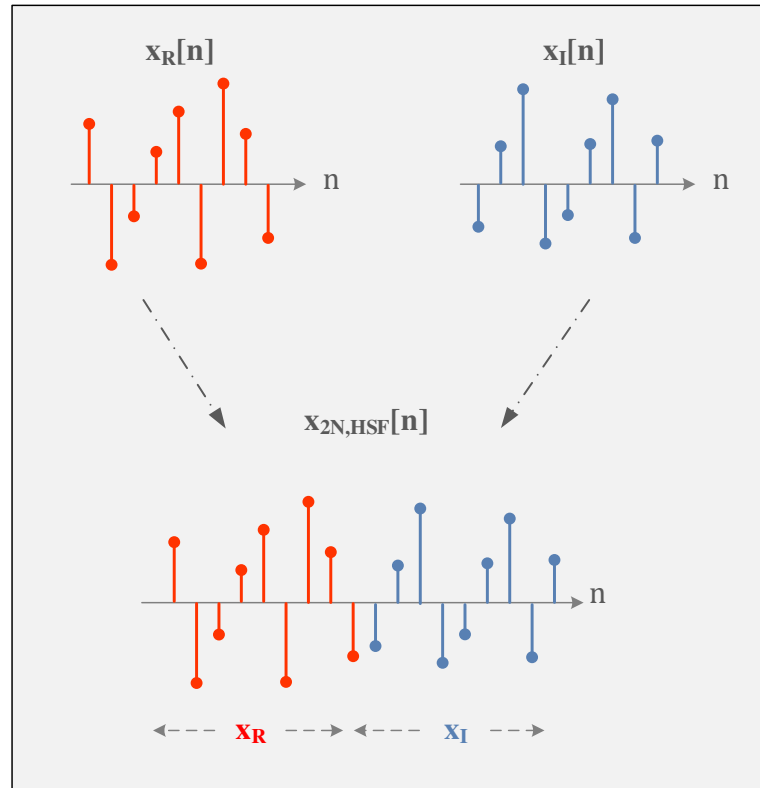


FIGURE 3.8: Illustration of the HSF-OFDM approach

Figure 3.8 illustrates the approach of generating a real OFDM signal using HSF-OFDM. At the receiver side, the  $2N$ -point real-valued signal,  $y_{2N}(n)$ , is first converted to an  $N$ -point complex signal as follows,

$$\begin{cases} y_R(n) = y_{2N}(n), & n=0,\dots,N-1 \\ y_I(n) = y_{2N}(N+n), & n=0,\dots,N-1 \end{cases} \quad (3.11)$$

where  $y_R(n)$  and  $y_I(n)$  are respectively the real and the imaginary components of  $y(n)$ . The resulting complex signal is then demodulated as in conventional complex OFDM systems. The recovered frequency vector,  $Y(k)$ , can be written as

$$\begin{aligned} Y(k) &= \sum_{k=0}^{N-1} y(n) \exp\left(-j2\pi \frac{kn}{N}\right) \\ &= \sum_{k=0}^{N-1} (y_R(n) + jy_I(n)) \exp\left(-j2\pi \frac{kn}{N}\right) \\ &= Y_R(k) + jY_I(k) \end{aligned} \quad (3.12)$$

where  $Y_R(k)$  and  $Y_I(k)$  are respectively the real and imaginary parts of the received

frequency vector. It has to be noted that HSF-OFDM has a considerable advantage as compared to Flip-OFDM. Indeed, contrary to Flip-OFDM, HSF-OFDM provides the possibility to generate a multitude of unipolar OFDM signals, namely the commonly known DCO-OFDM and ACO-OFDM. HSF-OFDM can be then successfully applied to DCO-OFDM-based hybrid techniques, such as ADO-OFDM [50].

### 3.4.2 PAPR and BER performance

#### 3.4.2.1 PAPR

Despite their numerous advantages, namely their total immunity to inter symbol interferences, OFDM schemes suffer from a high peak to average power ratio. The main drawbacks of signals with high PAPR are the distortions due to the nonlinearity of nonlinear electric components such as power amplifiers, D/A and A/D converters, and nonlinear optical components such as LEDs, photodiodes and optical fibers [59, 60]. The PAPR of an OFDM signal,  $x(n)$ , is defined as,

$$PAPR = \frac{\max\{|x(n)|^2\}}{E\{|x(n)|^2\}}. \quad (3.13)$$

In OFDM systems, the OFDM signal amplitude has random values. In practice, for large values of  $N$ , i.e.  $N \geq 64$ , the amplitude of the complex OFDM signal can be modeled as a Gaussian random process with zero mean and a variance  $\sigma^2$  equal to the total power of the complex time signal. The probability density function of the complex OFDM signal,  $x(n)$ , is given by

$$p(x) = \frac{1}{\sigma\sqrt{2\pi}} \exp\left\{-\frac{x^2}{2\sigma^2}\right\} \quad (3.14)$$

The amplitudes of the real and imaginary parts of  $x(n)$ , can be then approximated by Gaussian distributions with zero mean and a variance  $\sigma^2/2$ . Consequently, the variance of the  $2N$ -point real signal,  $\sigma_{2N}^2$ , is given by

$$\begin{aligned} \sigma_{2N}^2 &= E\{|x_{2N}(n)|^2\} = \frac{1}{2N} \sum_{n=0}^{2N-1} |x_{2N}(n)|^2 \\ &= \frac{1}{2} \left\{ \frac{1}{N} \sum_{n=0}^{N-1} |x_R(n)|^2 + \frac{1}{N} \sum_{n=N}^{2N-1} |x_I(n-N)|^2 \right\} \end{aligned} \quad (3.15)$$

where  $E\{\cdot\}$  is the expectation operator. Let  $n' = n - N$  define a change of variables from  $n$  to  $n - N$ . Substituting  $n'$  in (3.15) leads to

$$\begin{aligned}\sigma_{2N}^2 &= \frac{1}{2} \left\{ \frac{1}{N} \sum_{n=0}^{N-1} |x_R(n)|^2 + \frac{1}{N} \sum_{n'=0}^{N-1} |x_I(n')|^2 \right\} \\ &= \frac{1}{2} \left\{ \frac{\sigma^2}{2} + \frac{\sigma^2}{2} \right\} = \frac{\sigma^2}{2}\end{aligned}\quad (3.16)$$

On the other hand, the maximum power of  $x(n)$  can be computed as follows,

$$\max\{|x(n)|^2\} = \max\{x_R(n)^2 + x_I(n)^2\} \quad (3.17)$$

To simplify the analysis, let us assume

$$\max\{x_R(n)^2\} = \max\{x_I(n)^2\} = K^2 \quad (3.18)$$

This leads to,

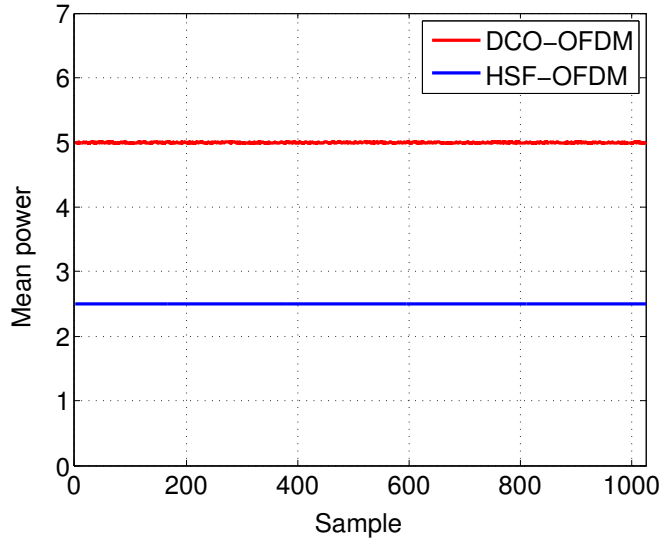
$$\max\{|x(n)|^2\} = 2K^2 \quad (3.19)$$

The maximum power of  $x_{2N}(n)$  is given by

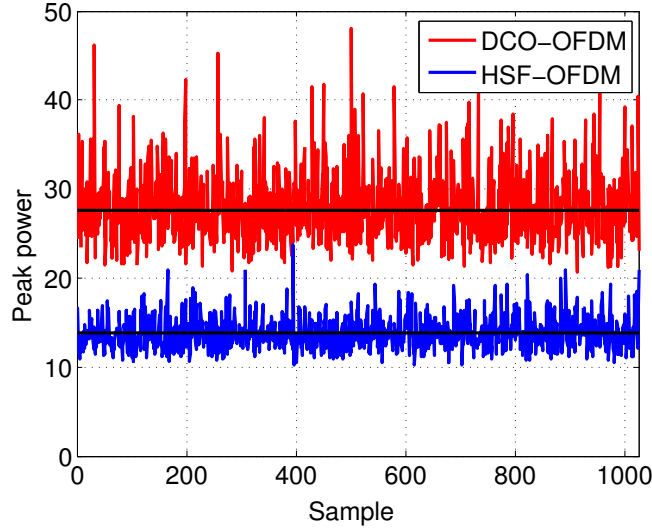
$$\begin{aligned}\max\{|x_{2N}(n)|^2\} &= \max\{\max\{x_R(n)^2\}, \max\{x_I(n)^2\}\} \\ &= K^2 = \frac{\max\{|x(n)|^2\}}{2}\end{aligned}\quad (3.20)$$

It has to be concluded from (3.16), (3.19) and (3.20), that HSF-OFDM divides by two both mean and peak powers as compared to conventional unipolar OFDM techniques. These analytical conclusions are compliant with the simulation results shown in Figure 3.9, depicting the mean and peak powers of two DCO-OFDM signals generated using conventional DCO-OFDM and HSF-OFDM. The simulation is carried out for 1024 DCO-OFDM symbols, each with 1024 samples and a 16-QAM constellation. It has to be noted that in case of conventional DCO-OFDM technique, 1024-point FFT/IFFT blocks are required to generate and demodulate a 1024-point DCO-OFDM symbol. On the contrary, in HSF-OFDM, the same signal can be obtained using only 512-point FFT/IFFT blocks. As can be seen in Figure 3.9, the mean power of the DCO-OFDM signal generated using HSF-OFDM is equal to half the mean power of the conventional





(a) Mean power



(b) Peak power

FIGURE 3.9: Effects of HSF-OFDM on the unipolar OFDM signal power

DCO-OFDM signal. On the other hand, the peak powers fluctuate around a given mean value. Indeed, since the peak power of an OFDM signal is a random variable, the assumption (3.18) is not always satisfied. However, for a large number of DCO-OFDM symbols, the mean value of the peak powers satisfy the equality (3.18). The PAPR of the  $N$ -point complex signal,  $x(n)$ , can be expressed as

$$PAPR\{x(n)\} = \frac{\max\{|x(n)|^2\}}{E\{|x(n)|^2\}} = \frac{2K^2}{\sigma^2} \quad (3.21)$$

The PAPR of the  $2N$ -point real signal,  $x_{2N}(n)$ , is given by

$$\begin{aligned} PAPR\{x_{2N}(n)\} &= \frac{\max\{|x_{2N}(n)|^2\}}{E\{|x_{2N}(n)|^2\}} = \frac{K^2}{\sigma^2/2} = \frac{2K^2}{\sigma^2} \\ &= PAPR\{x(n)\} \end{aligned} \quad (3.22)$$

As aforementioned, the HSF-OFDM technique divides by two both the mean and the peak powers of the transmitted OFDM signal compared to conventional real OFDM techniques, thus resulting in no PAPR increase. As a result, the HSF-OFDM technique conclusively permits to generate unipolar OFDM signals with the same PAPR as conventional unipolar OFDM techniques. It has to be noted that the analytical analysis presented in this section is conducted for DCO-OFDM signals. The same approach can be employed for other unipolar approaches. Considering the ACO-OFDM technique for example and taking into account the odd subcarriers modulation constraint, the power of the transmitted ACO-OFDM signal, is equal to  $\sigma^2/4$ , while the power of the transmitted signal in HSF-OFDM is equal to  $\sigma^2/8$ .

In OFDM modulations, the high peaks occur randomly. Consequently, to statistically characterize the PAPR, the complementary cumulative distribution function (CCDF) is commonly used. The CCDF function is defined as the probability (Pr) that PAPR exceeds a particular value of  $PAPR_0$ .

$$CCDF = Pr(PAPR > PAPR_0) \quad (3.23)$$

Figure 3.10 shows the CCDF curves of real OFDM signals generated using HSF-OFDM and conventional DCO-OFDM. These curves are obtained for a 16-QAM constellation and a signal length varying from  $L = 128$  to  $L = 1024$ . As can be seen in Figure 3.10, for all the considered signal lengths, the CCDF curves of conventional DCO-OFDM and HSF-OFDM are superposed. Indeed, the PAPR of the generated real OFDM signal is not impacted by the used technique, but depends only on the signal length.

### 3.4.2.2 Signal to noise ratio

Another decisive metric to evaluate and validate the proposed HSF-OFDM technique is the signal to noise ratio defined as the ratio of the signal power to the noise power.

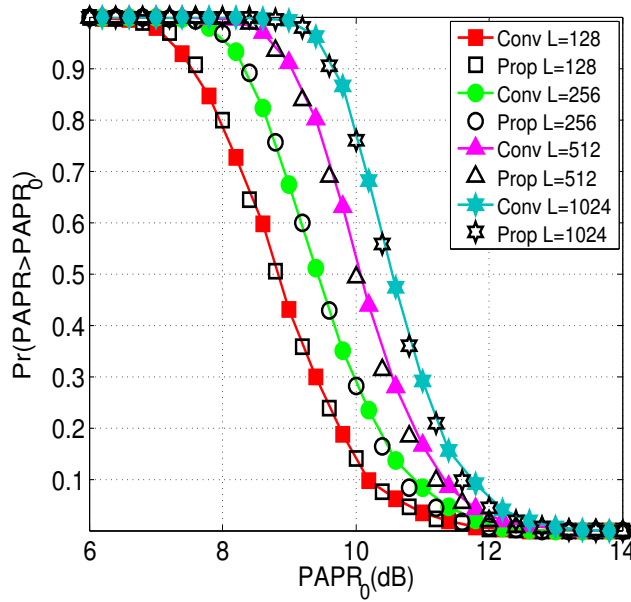


FIGURE 3.10: The CCDF curves of the conventional DCO-OFDM and the proposed HSF-OFDM techniques for different signal lengths

To simplify analysis, we consider the ACO-OFDM technique to ensure non-negativity of the generated real time OFDM signals, so that the performance of HSF-OFDM and Flip-OFDM in terms of SNR can be fairly compared. Furthermore, in order to simply clarify the approach adopted to computing the SNR of each technique and avoid any confusion of notations, let us consider the block scheme depicted in Figure 3.11 as a basis of SNR analysis. In this scheme, the transmitter output signal,  $x(n)$ , is transmitted through an AWGN channel with an impulse response  $h(n)$ . In the case of an AWGN channel, the noise added to the signal is a zero mean Gaussian noise with a variance of  $\sigma_z^2$  (i.e.  $\sim \mathcal{N}(0, \sigma_z^2)$ ).

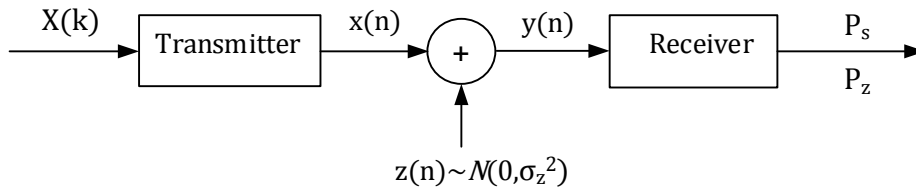


FIGURE 3.11: Block scheme of SNR analysis

The received time sample at the receiver input,  $y(n)$ , is given by

$$y(n) = h(n) * x(n) + z(n) \quad (3.24)$$

where  $*$  denotes convolution and  $z(n)$  is the channel noise. The received frequency symbol,  $Y(k)$ , can be expressed as

$$Y(k) = H(k)X(k) + Z(k) \quad (3.25)$$

where  $H(k)$  is the frequency response of the AWGN channel. The signal to noise ratio at the receiver output is then given by,

$$SNR = \frac{P_s}{P_z} = \frac{E\{|X(k)|^2\}}{E\{|Z(k)|^2\}} \quad (3.26)$$

where  $P_s$  and  $P_z$  are the signal and noise powers at the receiver output. Using Parseval's theorem, the signal to noise ratio can be also expressed as,

$$SNR = \frac{E\{|x(n)|^2\}}{E\{|z(n)|^2\}} \quad (3.27)$$

Let  $\sigma_x^2$  be the power of the transmitted signal (i.e. the power of  $x(n)$  at the transmitter output). To simplify analysis, we consider  $H(k) = 1$ .

#### a) ACO-OFDM

In case of conventional ACO-OFDM, no signal processing is performed at the receiver side and the frequency symbols are directly recovered from the clipped signal. As a result, the SNR at the ACO-OFDM receiver output is given by,

$$SNR_{ACO} = \frac{\sigma_x^2}{\sigma_z^2} \quad (3.28)$$

#### b) Flip-OFDM

In Flip-OFDM, a bipolar real signal is first generated and converted to an unipolar signal by transmitting the positive part in the first OFDM subframe and the flipped negative part in the second OFDM subframe. Let  $z^+(n)$  and  $z^-(n)$  be respectively the channel noise components added to the first and the second OFDM subframes (3.7). Then, the two received OFDM subframes can be formulated as follows,

$$\begin{aligned} y^+(n) &= x^+(n) + z^+(n) \\ y^-(n) &= -x^-(n) + z^-(n) \end{aligned} \quad (3.29)$$

The power of the transmitted signal (i.e. the signal at the transmitter output),  $\sigma_{x,Flip}^2$ , can be expressed as

$$\sigma_{x,Flip}^2 = \frac{1}{2N} \left\{ \sum_{n=0}^{N-1} |x^+(n)|^2 + \sum_{n=N}^{2N-1} |x^-(n)|^2 \right\} \quad (3.30)$$

Similarly, the noise power at the receiver input,  $\sigma_{z,Flip}^2$ , can be expressed as

$$\sigma_{z,Flip}^2 = \frac{1}{2N} \left\{ \sum_{n=0}^{N-1} |z^+(n)|^2 + \sum_{n=N}^{2N-1} |z^-(n)|^2 \right\} \quad (3.31)$$

In Flip-OFDM, the positive and negative parts are combined in the receiver to recover the bipolar OFDM signal (3.7). As a result, the power of the N-point bipolar time signal at the receiver output can be expressed as,

$$P_{s,Flip} = \frac{1}{N} \left\{ \sum_{n=0}^{N-1} |x^+(n) - x^-(n)|^2 \right\} \quad (3.32)$$

It can be concluded from (3.3), (3.4) and (3.5) that

$$|x^+(n) - x^-(n)| = \begin{cases} x^+(n), & \text{if } x(n) > 0 \\ x^-(n), & \text{if } x(n) < 0 \end{cases} \quad (3.33)$$

Substituting (3.33) in (3.32) leads to,

$$\begin{aligned} P_{s,Flip} &= \frac{1}{N} \left\{ \sum_{n=0}^{N-1} |x^+(n)|^2 + \sum_{n=0}^{N-1} |x^-(n)|^2 \right\} \\ &= 2\sigma_x^2 \end{aligned} \quad (3.34)$$

Similarly, the noise power after the combination process can be formulated as,

$$\begin{aligned} P_{z,Flip} &= \frac{1}{N} \left\{ \sum_{n=0}^{N-1} |z^+(n) + z^-(n)|^2 \right\} \\ &= \frac{1}{N} \left\{ \sum_{n=0}^{N-1} |z^+(n)|^2 + \sum_{n=0}^{N-1} |z^-(n)|^2 \right\} = 2\sigma_z^2 \end{aligned} \quad (3.35)$$

As a consequence, the SNR at the Flip-OFDM receiver output can be written as,

$$SNR_{Flip} = \frac{\sigma_{x,Flip}^2}{\sigma_{z,Flip}^2} = \frac{2\sigma_x^2}{2\sigma_z^2} = SNR_{ACO} \quad (3.36)$$

Indeed, contrary to ACO-OFDM, all the subcarriers are used to transmit useful data. Consequently, the equivalent electrical energy per symbol is twice the amount of ACO-OFDM, where half of the energy is wasted in the even subcarriers carrying no data. Hence, ACO-OFDM and Flip-OFDM have the same performance in terms of signal to noise ratio.

c) HSF-OFDM

In HSF-OFDM, a complex time signal is first generated and converted to a real signal by juxtaposing the real and imaginary parts in the time domain. Let  $z_R(n)$  and  $z_I(n)$  be respectively the channel noise components added to the first and the second OFDM subframe (3.10). Then, the two received OFDM subframes can be formulated as follows,

$$\begin{aligned} y_R(n) &= x_R(n) + z_R(n) \\ y_I(n) &= x_I(n) + z_I(n) \end{aligned} \quad (3.37)$$

The power of the transmitted signal (i.e. the signal at the transmitter output),  $\sigma_{x,HSF}^2$ , can be expressed as

$$\sigma_{x,HSF}^2 = \frac{1}{2N} \left\{ \sum_{n=0}^{N-1} |x_R(n)|^2 + \sum_{n=N}^{2N-1} |x_I(n)|^2 \right\} \quad (3.38)$$

Similarly, the noise power at the receiver input,  $\sigma_{z,HSF}^2$ , can be expressed as

$$\sigma_{z,HSF}^2 = \frac{1}{2N} \left\{ \sum_{n=0}^{N-1} |z_R(n)|^2 + \sum_{n=N}^{2N-1} |z_I(n)|^2 \right\} \quad (3.39)$$

In HSF-OFDM, the complex OFDM signal is recovered in the receiver from the received real and imaginary parts (3.7). As a result, the power of the  $N$ -point complex time signal at the receiver output can be expressed as,

$$P_{s,HSF} = \frac{1}{N} \left\{ \sum_{n=0}^{N-1} |x_R(n)|^2 + \sum_{n=0}^{N-1} |x_I(n)|^2 \right\} = 2\sigma_x^2 \quad (3.40)$$

Similarly, the noise power of the resulting complex noise, can be formulated as

$$P_{z,HSF} = \frac{1}{N} \left\{ \sum_{n=0}^{N-1} |z_R(n)|^2 + \sum_{n=0}^{N-1} |z_I(n)|^2 \right\} = 2\sigma_z^2 \quad (3.41)$$

The combination of the real and imaginary parts to recover the complex transmitted signal in the receiver, doubles both signal and noise powers. As a consequence, the SNR at the HSF-OFDM receiver output can be written as,

$$SNR_{HFS} = \frac{\sigma_{x,HFS}^2}{\sigma_{z,HFS}^2} = \frac{2\sigma_x^2}{2\sigma_z^2} = SNR_{ACO} \quad (3.42)$$

Let  $\sigma_X^2$  be the power of the frequency vector,  $X(k)$ , at the transmitter input. In ACO-OFDM, only the odd subcarriers are modulated to transmit useful data. As a result, the power of the frequency vector at the IFFT input is divided by two and therefore it is equal to  $\sigma_X^2/2$ . Furthermore, the clipping process of the time signal at the IFFT output divides by two the signal power. Consequently, the transmitted signal has a power of  $\sigma_X^2/4$ . In Flip-OFDM, contrary to ACO-OFDM, all subcarriers are used to transmit useful data. Thus, the power of the time signal at the IFFT output is equal to  $\sigma_X^2/2$ . The bipolar to unipolar conversion (i.e. the juxtaposition of positive and negative parts in the time-domain) divides by two the signal power. However, no clipping process is needed to convert the bipolar signal to an unipolar signal. As a consequence, the mean power of the transmitted signal is equal to  $\sigma_X^2/2$ . In HSF-OFDM, the odd subcarriers modulation constraint is also required to generate an antisymmetric signal. Thus, the complex time signal at the IFFT output has a power of  $\sigma_X^2/2$ . Furthermore, the juxtaposition of real and imaginary parts to convert the complex signal to a real signal, divides by two the signal power. As a result, the power of the transmitted unipolar signal is equal to  $\sigma_X^2/8$ , due to the clipping process.

Let  $E_s$  denote the energy per symbol information at the transmitter input. For sufficiently large FFT size,  $N$ , the total energy of the frequency vector,  $X(k)$ , is equal to  $NE_s$ . In order to transmit the same power, i.e.  $NE_s/2$ , the energy per symbol information is set to  $2E_s$  in ACO-OFDM,  $E_s$  in Flip-OFDM and  $4E_s$  in HSF-OFDM. The evolution of the signal power at the different stages of each technique is summarized in table 3.1.

### 3.4.2.3 Bit error rate

The probability of generating an error is a pragmatic indicator of system performance. The bit error rate is a practical measure of probability of error, that permits to assess link quality. In an AWGN channel, the theoretical expression of the probability of error

	ACO-OFDM	Flip-OFDM	HSF-OFDM
Frequency vector	$2NE_s$	$NE_s$	$4NE_s$
Odd subcarriers modulation constraint	$NE_s$	NA	$2NE_s$
Complex to real	NA	NA	$NE_s$
Bipolar to unipolar	$NE_s/2$	$NE_s/2$	$NE_s/2$
Combination process	NA	$NE_s$	$NE_s$
$P_z$	$\sigma_z^2$	$2\sigma_z^2$	$2\sigma_z^2$
SNR	$NE_s/2\sigma_z^2$	$NE_s/2\sigma_z^2$	$NE_s/2\sigma_z^2$

NA: not applicable

TABLE 3.1: Comparison of powers at different stages of each scheme

is a function of the signal to noise ratio. For a square M-QAM constellation and Gray mapping, the bit probability error is given by,

$$P_b = \frac{2}{\log_2 M} \left(1 - \frac{1}{\sqrt{M}}\right) \operatorname{erfc} \left( \sqrt{\frac{3}{2(M-1)} \operatorname{SNR}} \right) \quad (3.43)$$

where  $M$  is the constellation size and  $\operatorname{erfc}(\cdot)$  is the complementary error function. As mentioned in the previous paragraph, HSF-OFDM exhibits the same SNR performance as that of ACO-OFDM. Since the probability of error given by (3.43) depends only on the signal to noise ratio, HSF-OFDM and ACO-OFDM would exhibit the same performance in terms of bit error rate. To validate this theoretical conclusion, a simulation of the BER as function of SNR was conducted for different QAM constellation sizes. Figure 3.12 depicts the BER performance of HSF-OFDM and ACO-OFDM as a function of  $E_{b(\text{elec})}/N_0$  in an AWGN channel for constellation sizes varying from 4-QAM to 256-QAM. As can be seen in Figure 3.12, the simulation results are fully compliant with analytical conclusions. Indeed, for a given M-QAM constellation, HSF-OFDM permits to generate ACO-OFDM signals with the same BER performance as that of the conventional ACO-OFDM technique. Note that similar analysis can be conducted for any other unipolar OFDM technique, namely DCO-OFDM and PAM-DMT.

### 3.4.3 Channel equalization

The main advantage of OFDM modulation over single-carrier modulations is its ability to cope with dispersive channels using a simple equalization. To this end, the last part of the OFDM signal is copied and inserted at the beginning of the OFDM signal. This



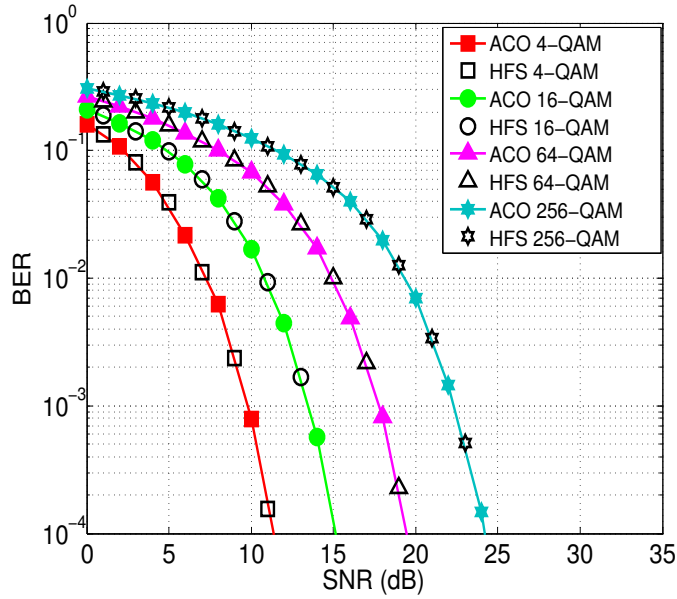


FIGURE 3.12: The BER as function of  $E_{b(elec)}/N_0$  of ACO-OFDM and HSF-OFDM

technique is known as cyclic prefix insertion (Section 1.1.2.2). The purpose of Flip-OFDM and HSF-OFDM is to generate real OFDM signals with the same characteristics as those of conventional unipolar OFDM techniques. Thus, the cyclic prefix insertion approach is obviously compatible with both Flip-OFDM and HSF-OFDM techniques. Furthermore, cyclic prefix insertion enables a very simple frequency domain channel equalization [16], that consists in using one complex multiplication per subcarrier to correct the distortion caused by the dispersive channel.

### 3.4.3.1 Flip-OFDM

In Flip-OFDM, the received frequency symbol can be formulated as,

$$Y(k) = Y^+(k) - Y^-(k) \quad (3.44)$$

where  $Y^+(k)$  and  $Y^-(k)$  are respectively the fast Fourier transforms of  $y^+(n)$  and  $y^-(n)$ .  $Y^+(k)$  and  $Y^-(k)$  can be expressed as,

$$\begin{aligned} Y^+(k) &= H^+(k)X^+(k) + Z^+(k) \\ Y^-(k) &= H^-(k)X^-(k) + Z^-(k) \end{aligned} \quad (3.45)$$

where  $H^+(k)$  and  $H^-(k)$  are the channel responses of the  $k^{\text{th}}$  OFDM subcarrier over the first and the second OFDM subframes respectively, and  $Z^+(k)$  and  $Z^-(k)$  are the fast Fourier transforms of  $z^+(n)$  and  $z^-(n)$  respectively. As shown in [58], under slow fading characteristics, the channel can be assumed to be constant over two consecutive OFDM symbols. This leads to,

$$H^+(k) = H^-(k) \cong H(k) \quad (3.46)$$

Substituting (3.45) in (3.44) and taking into account (3.46), the received frequency symbol can be written as,

$$Y(k) = H(k)X(k) + Z^+(k) + Z^-(k) \quad (3.47)$$

Consequently, the transmitted data can be recovered from the received symbol using a single tap equalization as follows,

$$\hat{X}(k) = \frac{Y(k)}{H(k)} = X(k) + \frac{Z^+(k) + Z^-(k)}{H(k)} \quad (3.48)$$

As a result, similarly to conventional OFDM schemes, a single tap equalization can be used in Flip-OFDM to correct the channel distortion and recover the transmitted data.

### 3.4.3.2 HSF-OFDM

In HSF-OFDM, the received frequency symbol is given by (3.12). The real and imaginary parts of  $Y(k)$  can be expressed as,

$$\begin{aligned} Y_R(k) &= H_R(k)X_R(k) + Z_R(k) \\ Y_I(k) &= H_I(k)X_I(k) + Z_I(k) \end{aligned} \quad (3.49)$$

where  $H_R(k)$  and  $H_I(k)$  are the channel responses of the  $k^{\text{th}}$  OFDM subcarrier over the first and the second OFDM subframes respectively, and  $Z_R(k)$  and  $Z_I(k)$  are respectively the fast Fourier transforms of  $z_R(n)$  and  $z_I(n)$ . As in the case of Flip-OFDM, the assumption that the channel is constant over two consecutive OFDM symbols implies,

$$H_R(k) = H_I(k) \cong H(k) \quad (3.50)$$

Substituting (3.49) in (3.12) and taking into account (3.50) leads to,

$$Y(k) = H(k)X(k) + Z_R(k) + jZ_I(k) \quad (3.51)$$

Then, the transmitted data can be recovered from the received symbol as follows,

$$\hat{X}(k) = \frac{Y(k)}{H(k)} = X(k) + \frac{Z_R(k) + jZ_I(k)}{H(k)} \quad (3.52)$$

Consequently, HFS-OFDM enables a single tap equalization to recover the transmitted data, thus preserving one of the enabling advantages of OFDM (i.e. simple channel equalization).

#### 3.4.4 Computational complexity

It has been clearly shown in the previous sections that HSF-OFDM permits to generate real OFDM signals with the same PAPR and BER performance as that of the conventional DCO-OFDM and ACO-OFDM techniques. In this section, the performance in term of computational complexity of the different techniques presented in the previous section is investigated, the purpose of HSF-OFDM being the reduction of circuit complexity. DHT-based optical OFDM permits admittedly to generate real OFDM signals with no need to constrain the frequency symbols to have an Hermitian symmetry property. However, no gain in the number of operations required to compute the real-valued signal is reached, since the FHT-based transform requires the same number of multiplications and  $N - 2$  more additions than the FFT-based algorithm. Even if the FHT improved version [57] is considered, FHT-based DMT still requires two more additions than FFT-based algorithms. On the other hand, Flip-OFDM uses only  $N$ -point IFFT/FFT transform to generate a  $2N$ -point ACO-OFDM signal. Thus, Flip-OFDM offers a 50% saving in hardware complexity compared to ACO-OFDM. However, as shown in Section 3.3, Flip-OFDM deals with the Hermitian symmetry property to generate real OFDM signals which requires additional resources to compute the complex conjugate, thus resulting in a longer time to compute the OFDM signal. Furthermore, considering the optimized IFFT operation taking into account the fact that half of subcarriers are set to zero in ACO-OFDM [58], Flip-OFDM and ACO-OFDM are found to have the same computation complexity at the transmitter side. As a result,

the improvement in hardware complexity achieved using Flip-OFDM is concerned only with the receiver and no improvement is reached in the transmitter. Contrary to Flip-OFDM, HSF-OFDM permits to generate both DCO-OFDM and ACO-OFDM signals, using only  $N$ -point IFFT/FFT blocks to generate and demodulate a  $2N$ -point real OFDM signal. Consequently, HSF-OFDM offers a 50% saving in hardware complexity compared conventional real OFDM techniques. Furthermore, HSF-OFDM modulates only the odd subcarriers to generate an ACO-OFDM signal. Thus, the aforementioned optimized IFFT operation in ACO-OFDM can be applied as well to HSF-OFDM. As a result, contrary to Flip-OFDM, HSF-OFDM offers a 50% saving in hardware complexity in both transmitter and receiver. Concretely, let consider the radix-2 algorithm to compute the FFT transform. The number of operations required to compute an  $N$ -point real OFDM signal using the conventional techniques is given by (3.1). The FHT improved version requires two more additions to generate a DMT signal compared to the FFT-based real OFDM. Flip-OFDM and HSF-OFDM use  $N/2$ -point IFFT block to demodulate an  $N$ -point real OFDM signal in the receiver, the number of operations required to compute the FFT transform in the receiver is then given by,

$$\begin{aligned} P^{FFT} &= \frac{N}{2} \log_2 \left( \frac{N}{2} \right) - 3 \frac{N}{2} + 4 \\ A^{FFT} &= 3 \frac{N}{2} \log_2 \left( \frac{N}{2} \right) - 3 \frac{N}{2} + 4 \end{aligned} \quad (3.53)$$

where  $P^{FFT}$  and  $A^{FFT}$  are respectively the number of multiplications and additions. Finally, it has to be noted that HSF-OFDM can take advantage of the optimized IFFT operation(3.53) to lower transmitter complexity, whereas, Flip-OFDM does not provide any improvement in complexity at the transmitter side. A concrete example comparing the computational complexity of ACO-OFDM, Flip-OFDM and HSF-OFDM for a transmitted signal length of 256 is given in Table 3.2.

	Conventional OOFDM	Flip-OFDM	HSF-OFDM
Hermitian symmetry	Required	Required	Not required
Transmitter complexity	$P^{FFT} = 1284$ $A^{FFT} = 5380$	$P^{FFT} = 1284$ $A^{FFT} = 5380$	$P^{FFT} = 516$ $A^{FFT} = 2308$
Receiver complexity	$P^{FFT} = 1284$ $A^{FFT} = 5380$	$P^{FFT} = 516$ $A^{FFT} = 2308$	$P^{FFT} = 516$ $A^{FFT} = 2308$

TABLE 3.2: The computational complexity performance of ACO-OFDM, Flip-OFDM and HSF-OFDM for a transmitted signal length of 256

Note that for ACO-OFDM and HSF-OFDM, the number of operations required for calculating the IFFT transform is computed using the optimized IFFT operation taking into account the fact that half of subcarriers are set to zero. As can be seen in table 3.2, Flip-OFDM offers savings of about 60% in the number of multiplications and about 57% in the number of additions in the receiver, but almost no gain is achieved in the transmitter. On the contrary, HSF-OFDM offers the same savings in both transmitter and receiver as compared to ACO-OFDM.

## 3.5 Hermitian symmetry free Flip-OFDM

### 3.5.1 System model

To further improve the computational complexity reduction of HSF-OFDM and increase the energy efficiency of unipolar OFDM systems, we propose a new technique combining the low complexity HSF-OFDM and Flip-OFDM to generate real-valued OFDM signals. This technique will be named as HSF-Flip-OFDM. In this technique, the Hermitian symmetry and odd subcarriers modulation constraints are not required. The time OFDM signal at the IFFT output is then complex and does not have any anti-symmetric property. As in HSF-OFDM, the complex OFDM signal is made real by juxtaposing real and imaginary parts in the time domain (3.10). The resulting  $2N$ -point bipolar signal can also be considered as the sum of a positive part,  $x_{2N}^+(n)$ , and a negative part,  $x_{2N}^-(n)$ , that can be expressed as,

$$x_{2N}^+(n) = \begin{cases} x_{2N}(n), & \text{if } x(n) \geq 0 \\ 0, & \text{otherwise} \end{cases} \quad (3.54)$$

$$x_{2N}^-(n) = \begin{cases} x_{2N}(n), & \text{if } x(n) < 0 \\ 0, & \text{otherwise} \end{cases} \quad (3.55)$$

In order to convert the bipolar signal to an unipolar signal, the positive part and the flipped negative part are juxtaposed in the time domain as follows,

$$x_{4N}(n) = \begin{cases} x_{2N}^+(n), & n = 0, \dots, 2N - 1 \\ -x_{2N}^-(n - N), & n = 2N, \dots, 4N - 1 \end{cases} \quad (3.56)$$

The mechanism of generating an unipolar signal using HSF-Flip-OFDM is illustrated in Figure 3.13. At the receiver side, the  $4N$ -point unipolar signal,  $y_{4N}(n)$ , is first converted to a  $2N$ -point bipolar signal as follows,

$$y_{2N}(n) = y_{4N}(n) - y_{4N}(2N + n) \quad n = 0, \dots, 2N - 1, \quad (3.57)$$

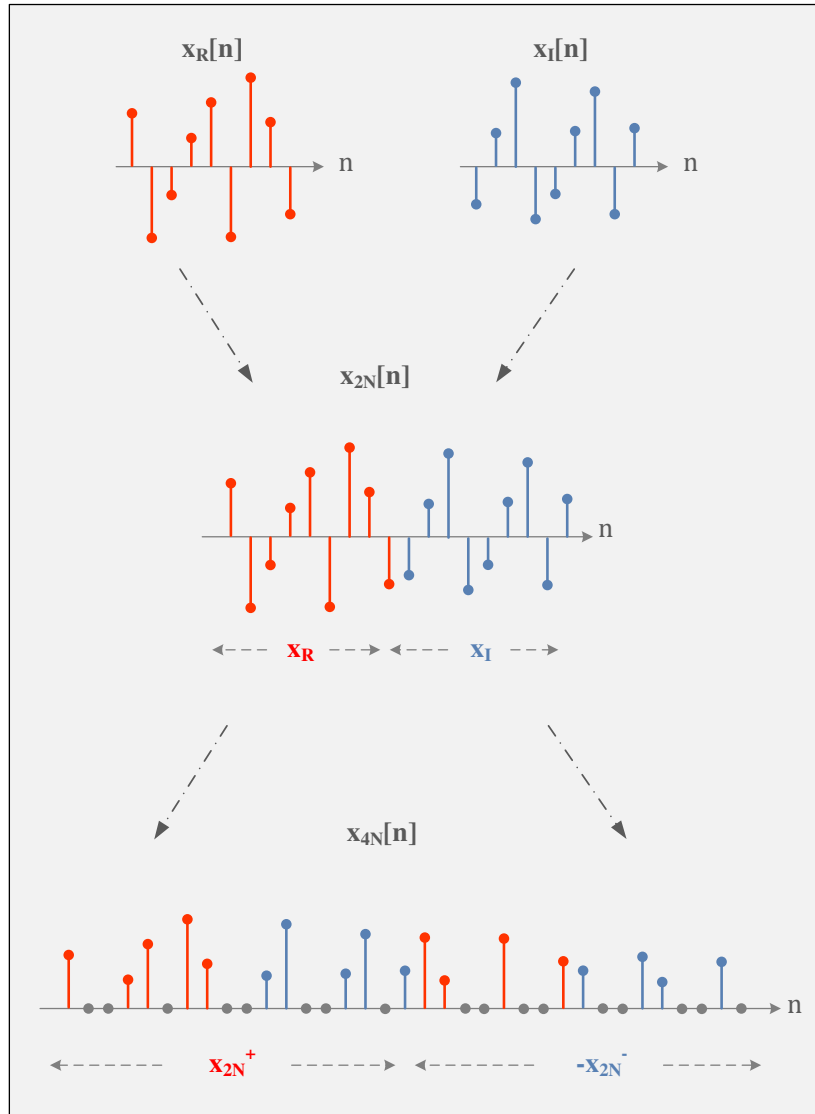


FIGURE 3.13: Illustration of the HSF-flip-OFDM mechanism

The real signal,  $y_{2N}(n)$ , is then converted to an  $N$ -point complex signal by extracting the real part,  $y_R(n)$ , and imaginary part,  $y_I(n)$ , from the real signal as follows,

$$\begin{cases} y_R(n) = y_{2N}(n), & n = 0, \dots, N - 1 \\ y_I(n) = y_{2N}(N + n), & n = 0, \dots, N - 1 \end{cases} \quad (3.58)$$

HSF-Flip-OFDM uses  $N$ -point IFFT/FFT blocks to generate a  $4N$ -point unipolar signal and transmit  $N - 1$  information symbols. In other words, to generate an  $N$ -point ACO-OFDM signal,  $N$ -point IFFT/FFT blocks are needed in ACO-OFDM, while only  $\frac{N}{4}$ -point IFFT/FFT blocks are required in HSF-Flip-OFDM to transmit almost the same amount of information. As a result, the proposed HSF-Flip-OFDM divides by four the needed FFT/IFFT sizes, thereby offering 75% savings in hardware complexity compared to ACO-OFDM. Considering the radix-2 algorithm for computing the FFT/IFFT transforms, the number of operations required to generate a  $N$ -point unipolar OFDM signal using HSF-Flip-OFDM is given by,

$$\begin{aligned} P^{FFT} &= \frac{N}{4} \log_2 \left( \frac{N}{4} \right) - 3 \frac{N}{4} + 4 \\ A^{FFT} &= 3 \frac{N}{4} \log_2 \left( \frac{N}{4} \right) - 3 \frac{N}{4} + 4 \end{aligned} \quad (3.59)$$

Considering the example given in table 3.2, the number of multiplications required to generate a 256-point signal using HSF-Flip-OFDM is equal to 196, while the number of additions is equal to 964. As a result, HSF-Flip-OFDM offers savings of about 85% in the number of multiplications and 82% in the number of additions as compared to ACO-OFDM.

### 3.5.2 Bit error rate

Let consider the approach and the block scheme presented in Section 3.4.2.2 for computing the theoretical signal to noise ratio of HSF-Flip-OFDM. Indeed, as in Flip-OFDM, in HSF-Flip-OFDM, the combination of the positive and flipped negative parts to recover the bipolar signal,  $y_{2N}(n)$ , doubles both signal and channel noise powers. In this stage, the signal to noise ratio can be expressed as,

$$SNR_{y_{2N}} = \frac{\sigma_{x,Flip}^2}{\sigma_{z,Flip}^2} = \frac{2\sigma_x^2}{2\sigma_z^2} \quad (3.60)$$

Moreover, as in HSF-OFDM, the combination of the real and imaginary parts to recover the complex transmitted signal, further doubles both signal and noise powers. As a consequence, the SNR at the HSF-Flip-OFDM receiver output can be written as,

$$SNR_{HSF-Flip} = \frac{4\sigma_x^2}{4\sigma_z^2} = SNR_{ACO} \quad (3.61)$$

As a result, HSF-Flip-OFDM permits to generate unipolar OFDM signals with the same signal to noise ratio performance as that of conventional ACO-OFDM and a significantly reduced hardware complexity.

To validate this theoretical conclusion, the HSF-Flip-OFDM BER as function of  $E_{b(elec)}/N_0$  was simulated for constellation sizes varying from 4-QAM to 256-QAM. The obtained simulation results are identical to those of HSF-OFDM (Figure 3.12). It can be concluded that HSF-Flip-OFDM and ACO-OFDM have the same BER performance for all the considered QAM constellations. Consequently, to reach a given BER, HSF-Flip-OFDM and ACO-OFDM require the same SNR, which is fully compliant with the theoretical analysis conducted above.





## Chapter 4

# Asymmetrically Companded DCO-OFDM

### Contents

---

<b>4.1</b>	<b>Overview of optical power efficient DMT systems . . . . .</b>	<b>86</b>
4.1.1	Asymmetrically clipped DC biased optical OFDM . . . . .	86
4.1.2	Hybrid asymmetrically clipped optical OFDM . . . . .	91
4.1.3	Pilot-assisted modulation . . . . .	92
4.1.4	Discussion and conclusion . . . . .	93
<b>4.2</b>	<b>The companding concept in OFDM systems . . . . .</b>	<b>94</b>
<b>4.3</b>	<b>Asymmetrically companded DCO-OFDM . . . . .</b>	<b>98</b>
4.3.1	System model . . . . .	98
4.3.2	Companding function . . . . .	100
<b>4.4</b>	<b>Simulation results . . . . .</b>	<b>102</b>
4.4.1	Clipping noise reduction . . . . .	103
4.4.2	BER as a function of $E_{b(elec)}/N_0$ . . . . .	104
4.4.3	Optical power efficiency . . . . .	107

---

The optical power efficiency of optical OFDM systems has been widely discussed in the literature and many approaches aiming to improve the optical power efficiency of unipolar communications were proposed. First, the well known ACO-OFDM has been proposed as an optical power efficient alternative of DCO-OFDM.

However, as aforementioned in the previous chapters, only odd subcarriers are modulated in ACO-OFDM, thus penalizing the spectral efficiency of the overall system. Furthermore, to achieve a given bit rate, ACO-OFDM requires higher constellation size than DCO-OFDM because only half of the available subcarriers are used to carry data. For large constellations, the required SNR in each ACO-OFDM subcarrier becomes significant, thus drastically increasing the required optical power to transmit an ACO-OFDM signal. Consequently, as spectral efficiency increases, DCO-OFDM with large DC bias becomes more efficient than ACO-OFDM in terms of optical power [15].

In order to improve the optical power efficiency without penalizing the spectral efficiency, new hybrid approaches combining two conventional techniques were proposed in the literature [50, 51]. Asymmetrically clipped DC biased optical OFDM was first proposed in [50]. ADO-OFDM consists in simultaneously transmitting ACO-OFDM on the odd subcarriers and DCO-OFDM on the even subcarriers. To recover the DCO-OFDM signal, an estimate of the ACO-OFDM clipping noise on the even subcarriers is performed from the received ACO-OFDM signal. The noisy estimate of the clipping noise results in doubled channel noise on DCO-OFDM components, thus penalizing the optical power efficiency of the overall system. The same approach was adopted in the Hybrid asymmetrically clipped optical OFDM technique proposed in [51]. HACO-OFDM consists in transmitting ACO-OFDM on the odd subcarriers and PAM-DMT on the imaginary parts of the even subcarriers. As in the case of ADO-OFDM, the clipping noise on even subcarriers is estimated from the received ACO-OFDM signal. HACO-OFDM was shown to provide more optical power efficiency than ADO-OFDM. However, both ADO-OFDM and HACO-OFDM require one additional IFFT block in the transmitter and three additional FFT/IFFT blocks in the receiver to generate and recover the transmitted hybrid signal. These additional blocks result in an excessive circuit complexity, thus considerably increasing the power consumption and the occupied chip area. To improve spectral and optical power efficiencies with a moderate circuit complexity, an approach is to take advantage of the spectral efficiency of DCO-OFDM and develop an appropriate signal processing to overcome the optical power efficiency limitation caused by the clipping noise and the excessive DC bias required in conventional DCO-OFDM systems. To this end, a solution is to use an asymmetric companding transformation, inspired from linear companding techniques [61]-[63] that are generally used in radio communications to reduce the peak to average power ratio of radio OFDM

signals. The approach and the advantages of this technique are the purpose of this chapter.

## 4.1 Overview of optical power efficient DMT systems

### 4.1.1 Asymmetrically clipped DC biased optical OFDM

#### 4.1.1.1 Transmitter model

To improve optical power performance of optical OFDM systems without degrading the spectral efficiency, an asymmetrically clipped DC biased optical OFDM was proposed in [50]. This technique consists in simultaneously transmitting DCO-OFDM on the even subcarriers and ACO-OFDM on the odd subcarriers. To this end, two paths with two IFFT blocks are used to separately generate ACO-OFDM and DCO-OFDM signals in the transmitter. The block diagram of the ADO-OFDM transmitter is shown in Figure 4.1.

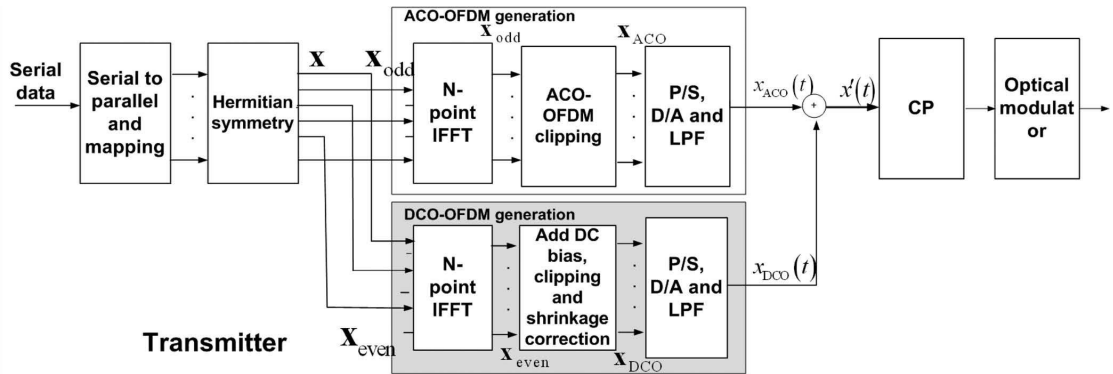


FIGURE 4.1: Block diagram of ADO-OFDM transmitter [50]

The input vector  $X$  that satisfies the Hermitian symmetry property is first partitioned onto even and odd components. The  $N$ -point vectors  $X_{odd}$  and  $X_{even}$  containing odd and even data are then generated as follows,

$$\begin{aligned} X_{odd} &= 0, X_1, 0, X_3, \dots, 0, X_{N-1} \\ X_{even} &= X_0, 0, X_2, 0, \dots, X_{N-2}, 0 \end{aligned} \quad (4.1)$$

It has to be noted that  $X_{odd}$  and  $X_{even}$  obviously satisfy the Hermitian symmetry constraint.  $X_{odd}$  and  $X_{even}$  are then input to two  $N$ -point IFFT blocks to produce

respectively the ACO-OFDM signal,  $x_{ACO}$ , and the DCO-OFDM signal,  $x_{DCO}$ . Finally, the resulting ACO-OFDM and DCO-OFDM signals are added together to generate the time signal,  $x'$ , that will be transmitted through the optical channel. The transmitted real-valued signal can be expressed as,

$$x' = x_{DCO} + x_{ACO} \quad (4.2)$$

As discussed above, the clipping process in ACO-OFDM divides by two the amplitude of the bipolar signal and transforms the remaining part on a clipping noise (that falls on the even subcarriers). The ACO-OFDM signal can be then expressed as,

$$x_{ACO} = \frac{1}{2}x_{odd} + n_{ACO} \quad (4.3)$$

where  $x_{odd}$  is the unclipped signal at the IFFT output and  $n_{ACO}$  is the ACO clipping noise. On the other hand, the clipped DCO-OFDM signal can be expressed as,

$$x_{DCO} = x_{even} + K_b + n_{DCO} \quad (4.4)$$

where  $x_{even}$  is the unclipped signal at the IFFT output,  $n_{DCO}$  is the DCO clipping noise and  $K_b$  is the added DC bias.

It was clearly shown in [50] that all ACO-OFDM clipping noise falls on the even subcarriers and therefore no clipping noise is present on odd subcarriers. The impact of the ACO clipping noise on the even subcarriers is illustrated in Figure 4.2, depicting the constellation diagram of the transmitted signal when a 16-QAM constellation is used for both even and odd components.

As can be seen in Figure 4.2, when only even subcarriers are modulated, the constellation points recovered from the clipped signal have small splatter around the ideal constellation points, due to the DCO clipping noise. On the other hand, if the ACO-OFDM and DCO-OFDM signals are simultaneously transmitted, the constellation recovered from the DCO-OFDM signal (i.e. even subcarriers) is considerably deteriorated due to the presence of the ACO clipping noise that integrally falls on the even subcarriers.

Note that in Figure 4.2(b), the odd frequency symbols recovered from the clipped signal were multiplied by two to highlight the ideal 16-QAM constellation.

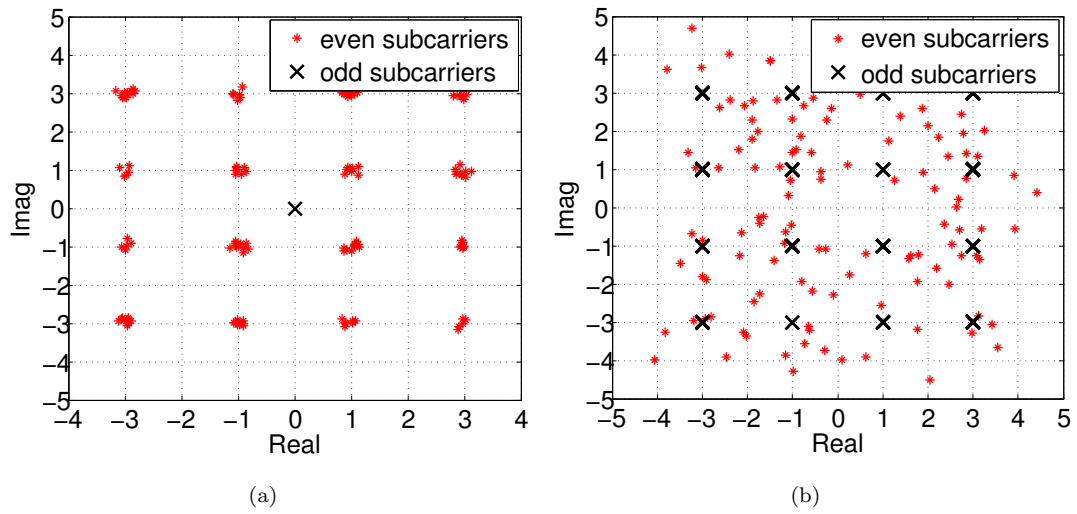


FIGURE 4.2: Constellation diagram: (a) Only even subcarriers are modulated (b) ACO-OFDM on odd subcarriers and DCO-OFDM on even subcarriers

#### 4.1.1.2 Receiver model

The block diagram of the ADO-OFDM receiver is shown in Figure 4.3. Assuming an AWGN channel, the time-domain received signal at the receiver input can be expressed as,

$$y = x_{ACO} + n_{odd,AWGN} + x_{DCO} + n_{even,AWGN} \quad (4.5)$$

where  $n_{even,AWGN}$  is the channel noise on the even subcarriers and  $n_{odd,AWGN}$  the channel noise on the odd subcarriers. Substituting (4.3) and (4.4) in (4.5) leads to

$$y = \frac{1}{2}x_{odd} + n_{ACO} + x_{even} + K_b + n_{DCO} + n_{odd,AWGN} + n_{even,AWGN} \quad (4.6)$$

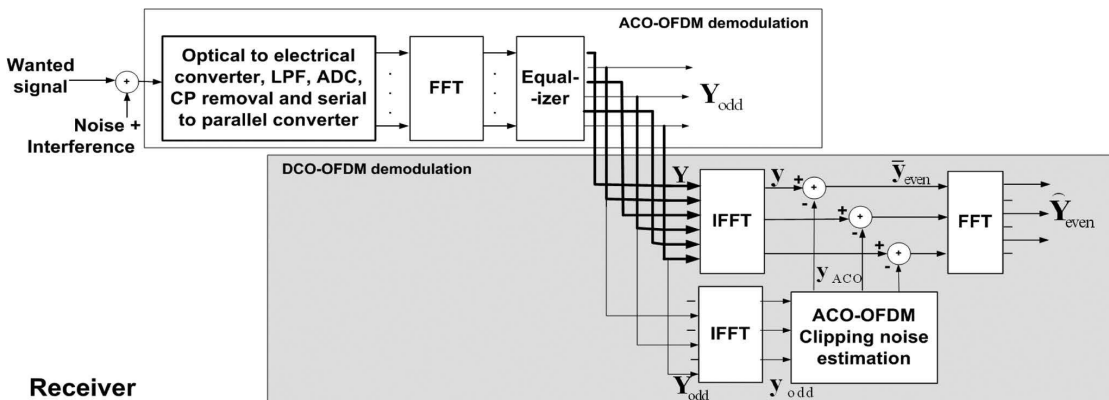


FIGURE 4.3: Block diagram of ADO-OFDM receiver [50]

To recover the transmitted data, a first  $N$ -point FFT block is used to demodulate the time-domain OFDM signal. The recovered frequency symbols resulting from applying the FFT to (4.6) can be expressed as,

$$Y = \frac{1}{2}X_{odd} + N_{ACO} + X_{even} + K_b + N_{DCO} + N_{odd,AWGN} + N_{even,AWGN} \quad (4.7)$$

The recovered frequency vector is then separated into odd and even components. As discussed above, both the DCO and ACO clipping noises fall on the even subcarriers. As a result, in ADO-OFDM, odd subcarriers are only affected by the channel noise as in conventional ACO-OFDM systems. Consequently, the data transmitted on odd subcarriers,  $Y_{odd}$ , can be directly recovered from the FFT output vector with the same performance as that of conventional ACO-OFDM schemes,

$$Y_{odd} = \frac{1}{2}X_{odd} + N_{odd,AWGN} \quad (4.8)$$

On the other hand, the even subcarriers at the FFT output,  $Y_{even}$ , comprise three noise components: DCO clipping noise, the AWGN noise added to the even subcarriers and ACO clipping noise resulting from the ACO-OFDM path. The even vector,  $Y_{even}$ , can be then written as follows,

$$Y_{even} = X_{even} + K_b + N_{DCO} + N_{even,AWGN} + N_{ACO} \quad (4.9)$$

To recover the data transmitted on even subcarriers, an estimate of the clipping noise is computed from the received odd subcarriers. To this end,  $Y_{odd}$  is input to an  $N$ -point IFFT block to generate a discrete time signal,  $y_{odd}$ , which is then multiplied by two and clipped at zero to generate an estimate of the transmitted ACO-OFDM signal. The resulting discrete time signal before clipping,  $\hat{x}_{odd}$ , can be expressed as

$$\hat{x}_{odd} = x_{odd} + 2n_{ACOodd,AWGN} \quad (4.10)$$

The clipping process permitting to generate the estimate of the ACO clipping noise results in equal total power in odd and even subcarriers. Thus, the estimate of the ACO-OFDM signal,  $y_{ACO}$ , can be written as,

$$y_{ACO} = \frac{1}{2}x_{odd} + n_{ACOodd,AWGN} + n_{ACO} + n_{ACOeven,AWGN} \quad (4.11)$$

It has to be noted that  $n_{ACOodd,AWGN}$  and  $n_{ACOeven,AWGN}$  have equal average noise power. In parallel, an additional  $N$ -point IFFT block is used to generate, from the equalized symbols at the FFT output, an estimate of the transmitted signal,  $y$ , comprising DCO-OFDM and ACO-OFDM signals. The estimate of the ACO-OFDM signal (4.11) is then subtracted from  $y$  in the time domain to generate an estimate of the DCO-OFDM signal. Finally, the resulting signal is input to an  $N$ -point FFT block to recover the data transmitted on even subcarriers. The resulting even subcarriers,  $\hat{Y}_{even}$ , can be expressed as,

$$\hat{Y}_{ACO} = X_{even} + K_b + N_{DCO} + N_{ACOeven,AWGN} + N_{even,AWGN} \quad (4.12)$$

As a consequence, the resulting even subcarriers  $\hat{Y}_{even}$  consist of three noise components: DCO clipping noise, the AWGN noise added to even subcarriers and the AWGN noise added to odd subcarriers. Therefore, the effective AWGN power is doubled for the DCO-OFDM component.

In [50], the performance in term of BER of DCO-OFDM and ACO-OFDM components was analyzed. It was shown that, for low constellations, the BER curves of the DCO-OFDM component are 3dB worse than the original DCO-OFDM due to the noisy estimate of the ACO clipping noise. For larger constellations, the DCO clipping noise becomes dominant and the 3dB shift becomes less visible. For the ACO-OFDM component, the BER curves are identical to those of conventional ACO-OFDM systems, because the clipping noise does not affect odd subcarriers.

The purpose of ADO-OFDM is to reduce the optical power of OFDM-based IM/DD systems. To outperform the conventional unipolar techniques in term of optical power efficiency, three factors were varied to find out the optimal optical power for a given bit rate to normalized bandwidth ratio ( $R_b/BW$ ). These factors include: the proportion of the total optical power allocated to ACO-OFDM, the DC-bias level of DCO-OFDM and the constellation sizes on odd and even subcarriers. As shown in [50], for a bit rate/normalized bandwidth ratio ranging from 4 to 6, ADO-OFDM provides a gain of about 1.9dB in optical power over conventional unipolar techniques. For  $R_b/BW < 4$ , ACO-OFDM outperforms both DCO-OFDM and ADO-OFDM in terms of optical power, whereas for  $R_b/BW > 6$ , DCO-OFDM provides more optical power efficiency than ADO-OFDM.



### 4.1.2 Hybrid asymmetrically clipped optical OFDM

To further improve the optical power efficiency of unipolar DMT-based systems, a hybrid asymmetrically clipped optical OFDM was proposed in [51]. This technique uses the same approach and architecture of ADO-OFDM to simultaneously transmit a PAM-DMT signal on the even subcarriers and an ACO-OFDM signal on the odd subcarriers. At the receiver side, an estimate of the ACO-OFDM clipping noise on the even subcarriers is computed and subtracted from the received signal, to recover the PAM-DMT signal using a signal processing similar to that of ADO-OFDM. It was clearly shown in [51] that HACO-OFDM offers better optical power efficiency than ADO-OFDM. This is due to the fact that PAM-DMT has the same optical power efficiency as ACO-OFDM, which reduces the optical power required to transmit the hybrid OFDM signal. The optical power performance of HACO-OFDM as function of bit rate/normalized bandwidth ratio was analyzed in [51] and compared to that of ADO-OFDM. Thus, it was shown that the gain in optical power efficiency that achieves HACO-OFDM over ADO-OFDM is more significant for low bit rate/normalized bandwidth values (i.e.  $R_b/BW < 4$ ). The maximum gain is reached for an average bit rate to normalized bandwidth of 2, where HACO-OFDM requires 5dB less optical power than ADO-OFDM to achieve a BER of  $10^{-3}$ . For  $R_b/BW \geq 4$  and a BER of  $10^{-3}$ , the maximum gain is about 1dB.

### 4.1.3 Pilot-assisted modulation

In [64], a pilot symbol is embedded in the original OFDM frame to reduce the PAPR of an intensity-modulated optical wireless system. Assuming the pilot symbol to have an amplitude of  $A_p(k)$  and a phase of  $\theta_p(k)$ , pilot-assisted PAPR reduction technique consists in rotating the phase of each data subcarrier by  $\theta_p(k)$  and scaling its amplitude by a factor of  $A_p(k)$ , to avoid coherent addition of the subcarriers as much as possible. The resulting subcarrier,  $\tilde{X}^u(k)$ , can be expressed as,

$$\tilde{X}^u(k) = X^u(k) \times A_p e^{j\theta_p(k)} \quad (4.13)$$

where  $k = 1, 2, \dots, N_{sub}$  and  $u = 1, 2, \dots, U$ .  $N_{sub}$  being the number of data carrying subcarriers and  $U$  the number of OFDM symbols per OFDM frame. The  $(U + 1)^{th}$

time symbol is the pilot symbol. The phase of the pilot symbol is chosen based on the selected mapping (SLM) algorithm and an effective maximum likelihood (ML) is used in the receiver to recover the pilot signal.

To achieve a minimum PAPR, an optimization algorithm is employed. First, different iterations of the pilot symbol with a randomly phase sequence are generated. The PAPR of each iteration,  $r$ , is then evaluated. Finally, among all the different iterations, the iteration that guarantees a minimum PAPR is found out as follows,

$$\tilde{r} = \underset{1 \leq r \leq R}{\operatorname{argmin}}(\operatorname{PAPR}^r) \quad (4.14)$$

where  $R$  is the total number of iteration. The pilot symbol corresponding to the optimal iteration,  $\tilde{r}$ , is chosen as the desired pilot symbol. The pilot signal amplitude is set to unity to preserve the electrical power of the data signal.

At the receiver side, the phase of the received pilot signal,  $Y^{U+1}$ , is first estimated using a maximum likelihood criterion to avoid data recovery errors due to the presence of noise on the pilot symbol. An estimate of the transmitted data is then obtained by dividing all received data subcarriers by the pilot symbol. The estimate of the  $k^{\text{th}}$  subcarrier of the  $u^{\text{th}}$  OFDM symbol can be written as,

$$\hat{X}^U(k) = \frac{Y^u(k)}{Y^{U+1}(k)} \quad (4.15)$$

As shown in [64], for large constellation sizes (i.e.  $M > 4$ ), the pilot-assisted PAPR reduction technique is more efficient than the classical SLM [65]. For a constellation of 16-QAM and a CCDF of  $10^{-4}$ , the pilot-assisted technique offers a gain of 0.9dB in PAPR reduction compared to the conventional SLM technique. Further the PAPR reduction capabilities, the pilot-assisted technique does not degrade system error performance, thus providing a BER performance nearly identical to that of the basic OFDM with no PAPR reduction. The purpose of the pilot-assisted technique is to reduce the PAPR of OFDM-based intensity-modulated systems and therefore the amount of the DC bias required to avoid signal clipping. As mentioned in [64], for a 64-QAM constellation and 127 data carrying subcarriers, the pilot-assisted optical OFDM technique reduces of about 0.15V the required DC bias, thereby offering a saving of over 1.3dB in transmitted average optical power as compared to the basic OFDM system.

#### 4.1.4 Discussion and conclusion

The optical OFDM techniques presented in this section perform better than conventional optical OFDM schemes for a range of average bit rate/normalized bandwidth values. However, the gain in optical power efficiency comes to the detriment of very remarkable computational complexity. In the case of ADO-OFDM and HACO-OFDM, four additional IFFT/FFT blocks are needed to simultaneously transmit two different signals. Indeed, one additional IFFT block is needed in the transmitter to generate the OFDM signal and three IFFT/FFT blocks are required in the receiver to estimate the ACO clipping noise on the even subcarriers. These additional IFFT/FFT blocks result in an excessive complexity, thus significantly increasing the power consumption and the occupied chip area. Table 4.1 compares the computational complexity performance of Hybrid optical OFDM with that of conventional unipolar techniques.

	Conventional OOFDM	Hybrid OOFDM
Transmitter complexity	$P^{FFT} = 1284$ $A^{FFT} = 5380$	$P^{FFT} = 2568$ $A^{FFT} = 10760$
Receiver complexity	$P^{FFT} = 1284$ $A^{FFT} = 5380$	$P^{FFT} = 5136$ $A^{FFT} = 21520$

TABLE 4.1: Computational complexity performance of Hybrid optical OFDM and conventional optical OFDM for  $N = 256$

As can be seen in table 4.1, hybrid OFDM transmitters have twice the computational complexity of conventional OOFDM transmitters. Whereas, to demodulate and recover the transmitted data, hybrid OOFDM techniques require four times the number of operations needed in conventional ACO-OFDM and DCO-OFDM receivers. For pilot-assisted modulation, the IFFT and the PAPR of the OFDM signal are computed for each iteration. Thus, the computational complexity in the transmitter increases with the total number of iterations. Furthermore, each subcarrier is multiplied by the pilot symbol, thus increasing the computational complexity and therefore the power consumption of the whole system. To avoid the excessive increase in circuit complexity arising from the use of hybrid OFDM techniques, an approach is to use an efficient signal processing with a moderate complexity to reduce the optical power of the spectrally efficient DCO-OFDM modulation.

## 4.2 The companding concept in OFDM systems

Multicarrier modulations such as OFDM are known to have a high dynamic range and therefore a high peak to average power ratio. In radio communications, the high PAPR results in performance degradation due to the nonlinearity of electrical components, namely power amplifiers and data (D/A or A/D) converters. Many techniques aiming to reduce the PAPR of OFDM signals have been proposed in the literature. A simple technique based on the clipping concept to reduce the PAPR of OFDM signals was first proposed [66]. This technique consists in simply limiting the amplitude excursions to a given value called the clipping threshold. To this end, a nonlinear clipping function is applied to the OFDM signal as follows,

$$x_c(t) = \begin{cases} A, & \text{if } x(t) \geq A \\ x(t), & \text{if } |x(t)| < A \\ -A, & \text{if } x(t) \leq -A \end{cases} \quad (4.16)$$

where  $x(n)$  is the OFDM signal,  $x_c(n)$  is the clipped signal and  $A$  is the clipping threshold. The clipping method permits to considerably reduce the PAPR of OFDM signals, namely for large clipping thresholds. However, the clipping function being itself nonlinear and non injective, it results in a considerable loss of information, thus drastically degrading the BER performance. Other algorithms with more or less complexity and efficiency, such as selected mapping (SLM) [65] and tone reservation (TR) [67], have been proposed in the literature. Among all the proposed algorithms, companding methods have been shown to provide a good trade off between complexity and PAPR reduction efficiency. The companding concept consists in applying a companding function to the OFDM signal to compress large amplitudes and enlarge small amplitudes, thus reducing the PAPR of the baseband signal. The companding approach in radio communications was inspired from speech processing, where the companding process is widely used to compress the speech signal. Logarithmic-based companding transforms such as  $\mu$ -law [68] and  $A$ -law [69] were first employed. These techniques reduce PAPR by increasing the average signal power and keeping the peak power unchanged, resulting in modest improvements in PAPR performance. Linear companding transforms such as linear nonsymmetrical transform (LNST) [61] and linear companding transform (LCT) [62] have been shown to provide better performance in

terms of PAPR reduction and BER, with less hardware complexity than logarithmic-based transforms. The LNST transfer function is given by,

$$x_c(n) = \begin{cases} \frac{1}{u}x(n), & \text{if } |x(n)| \leq \nu \\ ux(n), & \text{if } |x(n)| > \nu \end{cases} \quad (4.17)$$

where  $x_c(n)$  is the companded signal,  $0 \leq u \leq 1$  and  $0 \leq \nu \leq \max|x(n)|$ . A new linear companding transform (LCT) with two inflexion points was proposed in [62]. The LCT transfer function is given by,

$$x_c(n) = \begin{cases} u_1x(n), & \text{if } |x(n)| \leq \nu_1 \\ u_2x(n), & \text{if } \nu_1 < |x(n)| \leq \nu_2 \\ u_3x(n), & \text{if } |x(n)| > \nu_2 \end{cases} \quad (4.18)$$

where  $u_1 > 1$  and  $u_3 < 1$  and  $u_2$  is generally set to unity to reduce the undesired effect of noise transformation in the receiver. Figure 4.4 shows the profiles of LNST and LCT transfer functions.

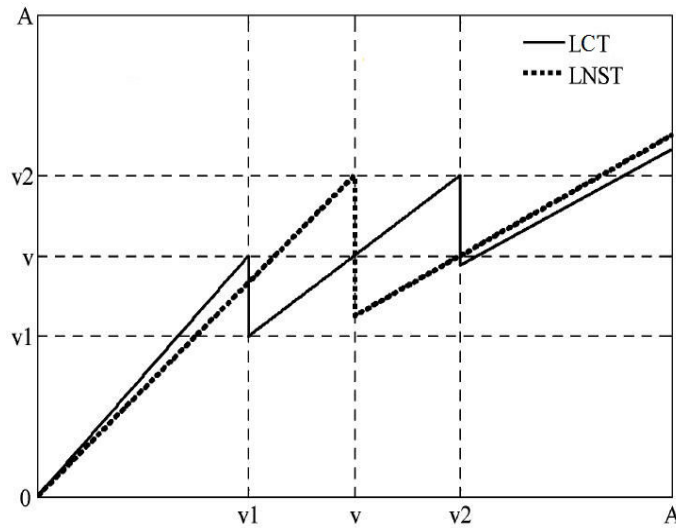


FIGURE 4.4: Profiles of LNST and LCT companding transforms [62]

In both LNST and LCT, the inverse companding function is applied to the received signal in order to recover the uncompanded transmitted OFDM signal. It was clearly shown in [62] that LCT has better PAPR reduction and BER performance than LNST with better power spectral density (PSD) and design flexibility.

Despite their numerous advantages, conventional linear transforms have in general one or more discontinuities as can be seen in Figure 4.4. As shown in [70], the discontinuities in companding transforms have two drawbacks. First, the companding transforms with discontinuities are non-injective. Thus, some elements of the companded signal are mapped to distinct elements of the original signal (i.e. one-to-one mapping is not satisfied), which results in an erroneous recovery of the transmitted signal in the receiver. Second, the abrupt jumps degrade the power spectral density due to the presence of unwanted high frequency components in the companded signal. Furthermore, side information is required to be transmitted to compute the inverse transforms in the receiver, thus decreasing the bit rate performance. Moreover, side information is not ideal due to the channel noise, which further degrades the BER performance. To overcome these drawbacks, a two-piecewise companding (TPWC) transform that compresses large signal amplitudes and expands small ones with no inflexion points was proposed in [63]. The TPWC transfer function is given by,

$$x_c(n) = \begin{cases} u_1 |x(n)| \cdot \text{sgn}(x(n)), & \text{if } |x(n)| \leq \nu \\ (u_2 |x(n)| + s) \cdot \text{sgn}(x(n)), & \text{if } |x(n)| > \nu \end{cases} \quad (4.19)$$

where  $u_1 > 1$ ,  $u_2 < 1$  and  $s > 0$ . It was shown in [63] that by carefully choosing the transform parameters (i.e.  $u_1$  and  $u_2$ ), a good trade-off between PAPR reduction and BER performance can be achieved with low computational complexity. Furthermore, since the TPWC transform has no discontinuities, TPWC can achieve a good power spectral density (PSD) performance and does not need any additional side information, contrary to conventional linear transforms that have one or more discontinuities, for which side information is of critical importance.

The companding technique has been also investigated for optical OFDM. In [71], a  $\mu$ -law transformation is applied to coherent optical OFDM to reduce its PAPR. It has been shown that  $\mu$ -law companding and de-companding can work successfully in the CO-OFDM transmission system. Furthermore, it has been demonstrated that  $\mu = 1$  provides the optimal trade off between PAPR reduction and channel noise amplification. In [72], a  $\mu$ -law companding combined with Hadamard transform was applied to reduce the PAPR of the optical OFDM signal with the aim of remedying the nonlinear effect of the Mach-zehnder modulator and data converters (DAC/ADC). As shown in [72],

the use of the Hadamard algorithm to reduce the OFDM signal PAPR increases neither the error probability nor the complexity of the system, the Hadamard transform being implemented by a butterfly structure in the FFT process. It has been experimentally demonstrated that the hybrid transform combining the Hadamard transform and the companding technique has better performance in terms of PAPR reduction and BER.

The use of linear companding transforms in optical OFDM systems, to the best of our knowledge, has never been investigated in the literature. As aforementioned, linear companding transforms provide a good trade off between PAPR reduction, complexity and BER performance. Furthermore, It has been shown in the literature that logarithmic-based companding transforms such as  $\mu$ -law can be successfully applied to optical OFDM signals to reduce their PAPR. To overcome the drawbacks of logarithmic-based companding transforms and improve the system performance in terms of complexity and BER, one can use linear companding transforms in optical OFDM systems. The overview of linear companding transforms provided in this section, has highlighted the advantages and drawbacks of the different companding transforms proposed in the literature. These advantages and drawbacks, namely the discontinuities effects, should be taken into consideration when designing the companding transform in order to take full advantage of applying linear companding to OFDM-based IM/DD systems.

The approach aiming to improve optical power performance and hardware complexity of IM/DD systems by applying an asymmetric linear companding to the conventional DCO-OFDM, is presented in the following section. We call this technique Asymmetrically companded DCO-OFDM. A detailed description of the system model with detailed analysis are provided. The improvement in optical power and BER performance is then discussed.

## 4.3 Asymmetrically companded DCO-OFDM

### 4.3.1 System model

The block diagram of asymmetrically companded DCO-OFDM is shown in Figure 4.5. First, the DC bias  $K_b$  is computed from the real discrete time signal at the IFFT output,

$x(n)$ .

$$K_b = k\sqrt{E\{x^2(n)\}}. \quad (4.20)$$

In conventional DCO-OFDM systems, the DC bias is directly added to the continuous signal at the DAC output and a hard clipping is performed to set to zero the remaining negative amplitudes. However, the dynamic range of the bipolar real OFDM signal increases with the spectral efficiency (i.e. the constellation size). Thus, if a moderate DC bias is used, more negative peaks are clipped, resulting in a significant clipping noise penalty (Figure 4.5). As a result, for large constellation sizes (i.e.  $M \geq 64$ ), the DCO-OFDM technique becomes inefficient in terms of bit error rate. To overcome this inefficiency, an approach is to increase the added DC bias [15], so that less negative peaks remain after DC bias addition, thus reducing the clipping noise penalty. However, this approach results in an increase of the optical power required to transmit the unipolar signal, which impacts the optical power efficiency of DCO-OFDM systems.

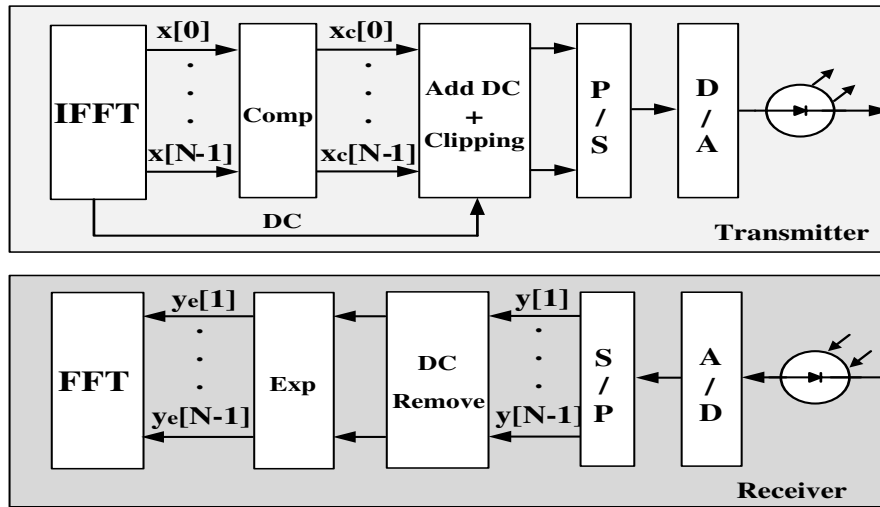


FIGURE 4.5: The block diagram of asymmetrically companded DCO-OFDM

To minimize the clipping impact and overcome the optical power inefficiency of conventional DCO-OFDM systems, a technique based on the companding concept can be employed to reduce the dynamic range of the DCO-OFDM signal, so that the DC bias required to ensure non-negativity of the transmitted signal is not excessive. To this end, an asymmetric companding transform is applied to the time signal at the IFFT output, so that the negative part is compressed and less negative peaks are clipped even



if a moderate DC bias is used. The discrete time companded signal can be expressed as,

$$x_c(n) = \begin{cases} x(n), & \text{if } x(n) > \nu \\ \alpha x(n), & \text{if } x(n) \leq \nu \end{cases} \quad (4.21)$$

where  $\alpha \in [0, 1]$  and  $\nu \in [\min\{x(n)\}, 0]$ . The DC bias computed from the IFFT output signal is next added to the companded signal as follows,

$$x_{DC}(n) = x_c(n) + K_b, \quad n = 0, 1, \dots, N - 1. \quad (4.22)$$

The remaining negative amplitudes in the resulting DC-biased companded signal,  $x_{DC}(n)$ , are hard clipped at zero to ensure non-negativity of the electric signal at the optical transmitter input. At the receiver side, to correctly recover the transmitted data, the DC component is first removed from the received DC-biased signal. To recover the transmitted bipolar signal, the received companded signal is expanded using the inverse companding transform as follows,

$$y_e(n) = \begin{cases} y(n), & \text{if } y(n) > \nu \\ \frac{1}{\alpha} y(n), & \text{if } y(n) \leq \nu \end{cases} \quad (4.23)$$

The resulting expanded signal is then demodulated using the FFT transform and the transmitted data is recovered as in conventional DCO-OFDM systems.

### 4.3.2 Companding function

In this work, the companding concept is used to reduce the clipping noise caused by optical sources in IM/DD systems. For this purpose, a new asymmetric linear companding transform is designed in order to compress the negative part of the real-valued OFDM signal. The proposed linear companding transform is shown in Figure 4.6. Indeed, the proposed companding transform is a linear function with two degrees of freedom,  $\alpha$  and  $\nu$ . As aforementioned, the companding functions with one or more discontinuities degrade the BER performance and the power spectral density of the OFDM signal. To overcome these drawbacks, the proposed companding function was designed so that the companded signal exhibits no discontinuities.

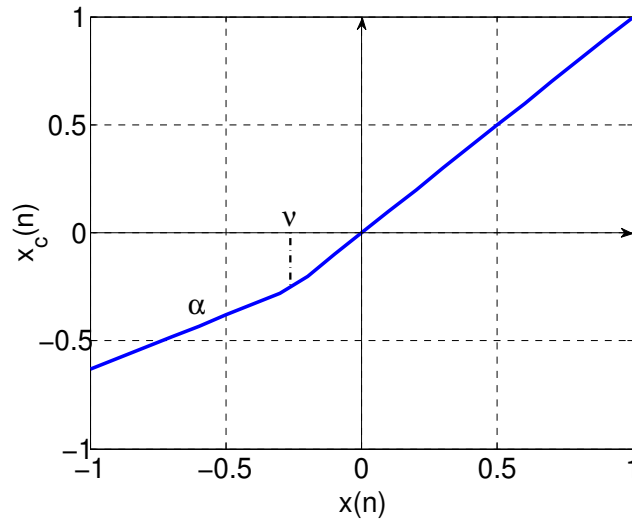


FIGURE 4.6: Profile of the proposed linear companding transform

In conventional companding transforms, the companding function parameters are either once fixed in the transmitter and the receiver or adaptive. When they are fixed, the companding process is independent of the OFDM signal statistical characteristics and the parameters are not optimized to provide better performance. In adaptive companding transforms [73], the parameters are computed adaptively so that the companding process provides optimal performance in terms of PAPR and BER. However, this technique results in data rate degradation, because the updated parameters need to be transmitted to the receiver in order to update the inverse companding transform.

In this work, the companding function parameters,  $\alpha$  and  $\nu$ , are defined according the statistical properties of the OFDM signal. Indeed, as mentioned in the previous chapters, the real-valued bipolar OFDM signal,  $x(n)$ , can be approximated by a Gaussian distribution with zero mean and a variance  $\sigma^2$ . The probability density function of  $x(n)$  is then given by,

$$p(x) = \frac{1}{\sigma\sqrt{2\pi}} \exp\left(\frac{-x^2}{2\sigma^2}\right) \quad (4.24)$$

As in Flip-OFDM (Section 3.3), the bipolar signal can be considered as the sum of a positive part,  $x^+(n)$ , and a negative part,  $x^-(n)$ , that can be respectively expressed as,

$$x^+(n) = \begin{cases} x(n), & \text{if } x(n) \geq 0 \\ 0, & \text{otherwise} \end{cases}, \quad (4.25)$$

$$x^-(n) = \begin{cases} x(n), & \text{if } x(n) < 0 \\ 0, & \text{otherwise} \end{cases}. \quad (4.26)$$

The positive and the negative parts can be approximated by one-sided Gaussian distributions. The means of the positive part,  $\mu^+$ , and the negative part,  $\mu^-$ , are respectively given by,

$$\begin{aligned} \mu^+ &= E[x^+(n)] \\ &= \frac{1}{\sigma\sqrt{2\pi}} \int_0^\infty t \exp\left(\frac{-t^2}{2\sigma^2}\right) dt = \frac{\sigma}{\sqrt{2\pi}}, \end{aligned} \quad (4.27)$$

$$\begin{aligned} \mu^- &= E[x^-(n)] \\ &= \frac{1}{\sigma\sqrt{2\pi}} \int_{-\infty}^0 t \exp\left(\frac{-t^2}{2\sigma^2}\right) dt = \frac{-\sigma}{\sqrt{2\pi}}. \end{aligned} \quad (4.28)$$

In the proposed companding function, the parameter  $\nu$  is set equal to the mean of the negative part of the bipolar signal, i.e.  $\nu = \mu^-$ . Furthermore, it can be concluded from (4.27) and (4.28), that

$$|\mu^-| = |\mu^+|. \quad (4.29)$$

Moreover, since the positive part is not modified by the companding process, the means of the positive part before and after the companding transformation are identical. On the other hand, in wired IM/DD systems, the intensity modulation is commonly performed by employing laser diodes such as Distributed Feedback lasers or VCSELs. Both these lasers exhibit a linear behavior above the laser threshold current (Chapter 5). As mentioned in [74], the laser is the major source of nonlinearity in optical fiber communication systems. Thus, if the laser diode has a linear behavior above the threshold, the nonlinearity distortion affects only the negative peaks of the bipolar signal, the clipping of the positive peaks is then negligible. As a result, the mean of the positive part is neither affected by the companding transformation nor by the clipping distortion. Thus, since  $\nu = \mu^-$  and  $\mu^- = -\mu^+$ , the parameter  $\nu$  in the receiver can be directly extracted from the received companded signal (i.e.  $\nu = -\mu^+$ ). On the other hand, the parameter  $\alpha$  is fixed according to the used constellation, so that an optimal clipping noise reduction is performed. Thus, the companding function parameters in the

receiver, can be directly computed from the received companded signal and according to the used constellation. As a result, an adaptive companding process can be performed with no need to transmit any additional data.

## 4.4 Simulation results

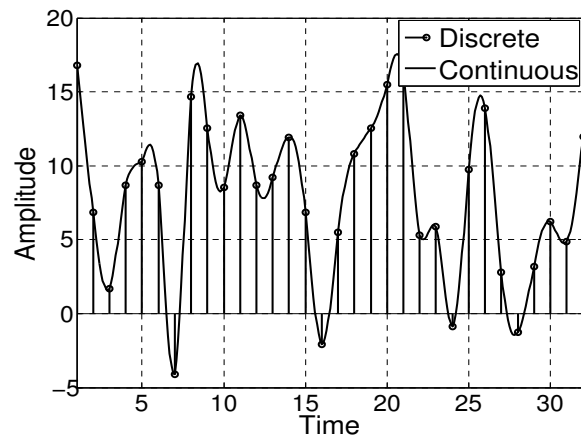
To evaluate the linear asymmetric companding performance in optical OFDM systems, several simulations were conducted for different signal lengths and constellations. The obtained simulation results are provided in this section. The simulation parameters are adjusted according to the performance to simulate (i.e. clipping noise reduction, bit error rate or optical power).

### 4.4.1 Clipping noise reduction

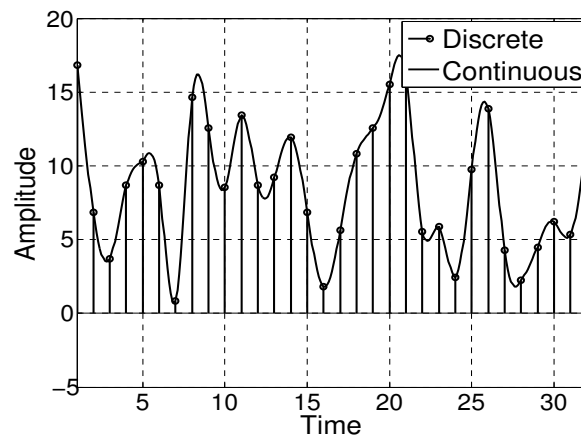
The proposed asymmetric companding aims to compress the negative part of the bipolar OFDM signal, so that after DC bias addition, the DC-biased companded signal has fewer negative peaks. The capability of the asymmetric companding function to reduce the remaining negative peaks after DC bias addition was first simulated in time and frequency domains. Figure 4.7 shows the amplitudes of a conventional DC-biased OFDM signal and a companded DC-biased OFDM signal. In the two cases, the simulated OFDM signal has 32 points and the added DC bias is equal to 5dB.

It can be clearly seen that using the companding technique, the remaining negative peaks are significantly reduced. Therefore, the companded OFDM signal will be less affected by the clipping noise, with no need to add an excessive DC bias. Contrary to the clipping, the proposed companding transformation is injective and reversible. As a result, the negative amplitudes, which are in general clipped in the conventional DCO-OFDM technique, are not lost in the proposed technique and can be efficiently recovered in the receiver using the inverse companding transform.

The clipping noise reduction can be also seen on the constellation recovered from the clipped OFDM signal. Figure 4.8 shows the received constellation points of conventional and companded DCO-OFDM schemes for different constellation sizes (i.e. 16-QAM, 32-QAM and 64-QAM). For each constellation size, the constellation points are



(a)



(b)

FIGURE 4.7: Time domain waveforms: (a) Conventional DC-biased OFDM signal (b) Companded DC-biased OFDM signal

compared to their ideal positions (black points). For companded DCO-OFDM, the inverse companding transformation is applied to the clipped OFDM signal to recover the uncompanded signal. In all cases, the added DC bias is equal to 7dB and the channel noise is not considered, so that only the clipping noise is present.

In the case of conventional DCO-OFDM, the recovered constellation points after clipping have small splatter around the ideal constellation points, due to the clipping noise. In companded DCO-OFDM, the recovered constellation points are very close to the ideal constellation points. As a result, the clipping noise is considerably reduced and the performance in terms of BER would be mainly affected by the channel noise contrary to conventional DCO-OFDM schemes, where the clipping noise is the dominant noise, namely for constellations larger than 16-QAM. Furthermore, as aforementioned, the

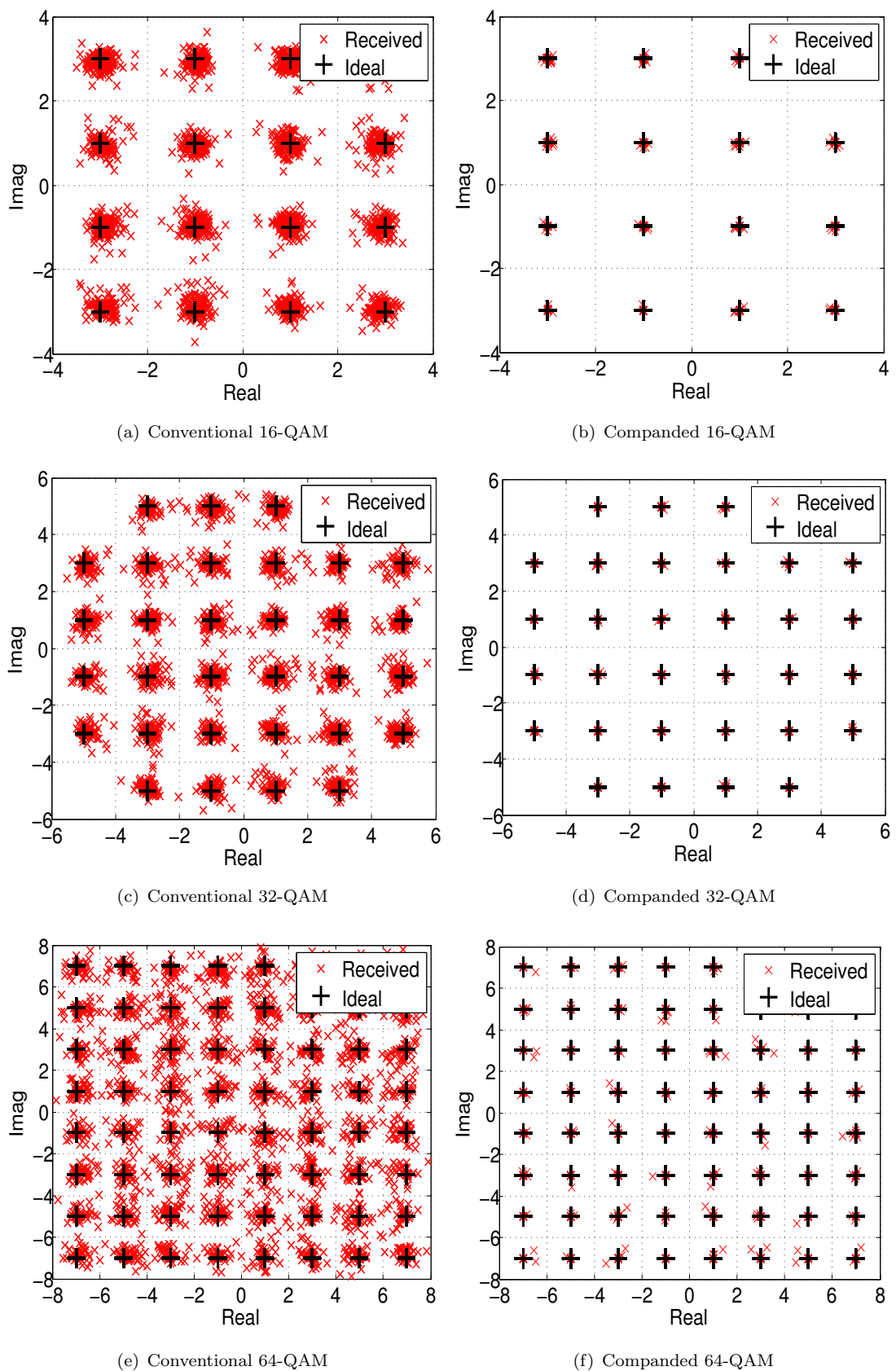


FIGURE 4.8: Comparison of the received constellation points for conventional and companded DCO-OFDM schemes for different constellation sizes

dynamic range of the OFDM signal increases with the constellation size, thus increasing the clipping noise, the needed DC bias to ensure non-negativity of the signal and the optical power required to transmit the OFDM signal. Consequently, the performance of the asymmetric companding technique in terms of clipping noise reduction increases with the constellation size. This effect will be clearly demonstrated in the following sections, but can be already seen on the constellation diagrams.

#### 4.4.2 BER as a function of $E_{b(elec)}/N_0$

Figure 4.9 compares the BER performance of companded DCO-OFDM to that of conventional DCO-OFDM as a function of electric energy-per-bit to noise power spectral density,  $E_{b(elec)}/N_0$ . The simulated OOFDM frame is formed by 1000 symbols each with 256 subcarriers. Furthermore, an oversampling with an oversampling factor of 4 is performed in order to correctly approximate the PAPR of the continuous OOFDM signal [53]. To simplify analysis, the optical channel is modeled as an AWGN channel with a frequency non-selective fading. Thus, no guard interval is used.

As shown in [15], the performance in an additive white Gaussian noise channel forms a theoretical basis for OOFDM systems from which the results for the more general case of a frequency selective channel can be found. Thus, for the theoretical analysis, we consider an AWGN channel, so that the performance of companded DCO-OFDM can be judiciously compared to the simulation results proposed in the literature, where an AWGN channel is commonly considered. The comparison is performed for a DC bias of 7dB and constellation sizes from 4-QAM to 256-QAM.

In conventional DCO-OFDM systems, for low constellation size (i.e. 4-QAM), the time OFDM signal has a small dynamic range which results in a negligible clipping noise. Since the dynamic range of the time OFDM signal increases with the constellation size, the clipping noise becomes significant for 16-QAM and dominant for larger constellation sizes. Consequently, as can be seen in Figure 4.9, the BER curves reach a BER floor for constellation sizes larger than 16-QAM [15, 16]. In companded DCO-OFDM, since the clipping noise is negligible for 4-QAM constellation, the parameter  $\alpha$  is set equal to 1, so that the channel noise, which is the dominant noise, is not amplified in the receiver. For larger constellation sizes, the companding transformation, with  $\alpha < 1$ , reduces significantly the remaining negative amplitudes and therefore the clipping noise.

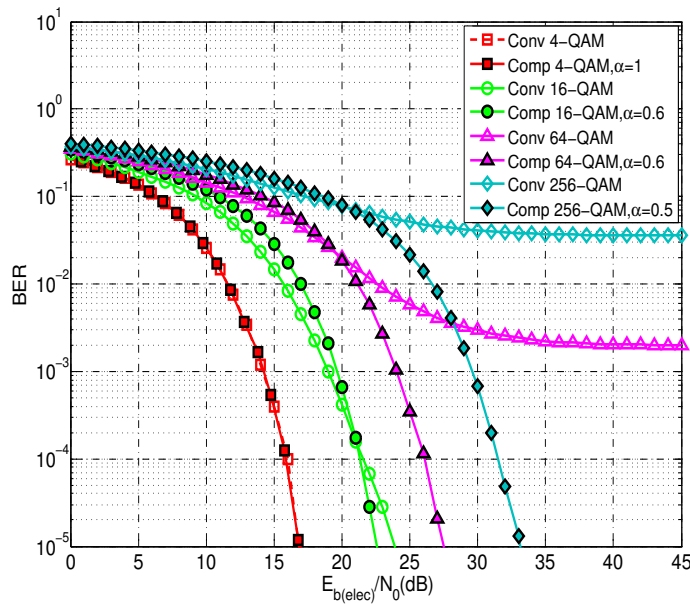


FIGURE 4.9: BER as function of  $E_{b(elec)}/N_0$  for different constellations of the conventional (Conv) and the companded (Comp) DCO-OFDM techniques

Furthermore, the proposed companding function was designed so that a small part of the time signal is amplified in the receiver. Consequently, the amplification of the channel noise is less significant compared to the clipping noise cancellation. As a result, the BER curves are not limited by a BER floor and very low BER levels can be reached using only a moderate DC bias (i.e. 7dB) even for large constellation sizes (i.e.  $M \geq 64$ ).

#### 4.4.3 Optical power efficiency

Figure 4.10 compares the optical power efficiency of companded DCO-OFDM to that of conventional ACO-OFDM and DCO-OFDM schemes. To make a judicious comparison, different sets of particular modulations, having the same bit rate/normalized bandwidth,  $R_b/BW$ , are used. For bit rate/normalized bandwidth  $R_b/BW$  of 5, 32-QAM companded DCO-OFDM is compared to 1024-QAM ACO-OFDM, conventional ACO-OFDM being more efficient than conventional DCO-OFDM in term of optical power. For  $R_b/BW \geq 6$ , conventional DCO-OFDM is shown to have more optical power efficiency than ACO-OFDM. Thus, for  $R_b/BW \geq 6$ , companded DCO-OFDM is compared to conventional DCO-OFDM. To achieve high data rate, either DCO-OFDM with a large DC-bias (13dB) or ACO-OFDM with larger constellation size ( $M^2$ ) in each ACO-OFDM subcarrier can be used. Both these schemes require a high optical power to transmit the OFDM signal and the optical power penalty increases as the constellation size increases.



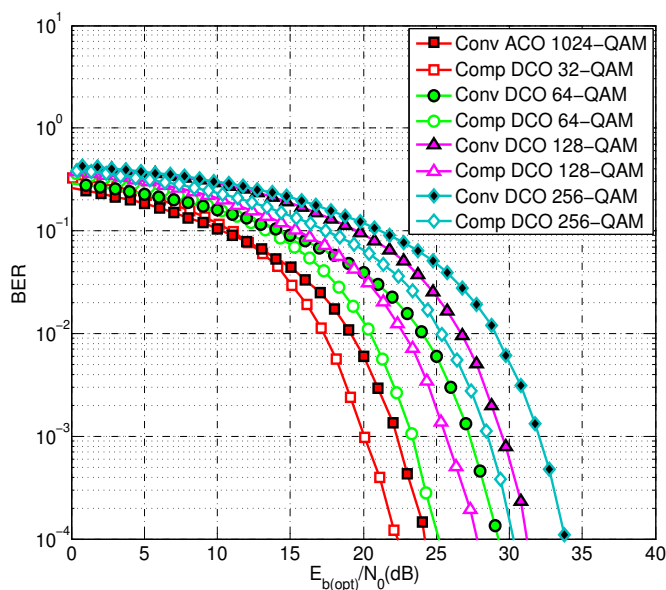


FIGURE 4.10: BER as function of  $E_{b(opt)}/N_0$  of conventional ACO-OFDM, DCO-OFDM and companded DCO-OFDM

As can be seen in figure Figure 4.10, companded DCO-OFDM permits to reach high data rate using lower DC bias (7dB) than conventional DCO-OFDM and lower constellation size than conventional ACO-OFDM. As a result, companded DCO-OFDM requires the lowest  $E_{b(opt)}/N_0$ . For  $R_b/BW = 5$  and  $BER = 10^{-4}$ , a gain of 2dB in optical power over conventional ACO-OFDM is reached, while for  $R_b/BW \geq 6$  (i.e.  $M \geq 64$ ), a gain of about 4dB over conventional DCO-OFDM is achieved.

## Chapter 5

# Experimental investigation of DMT for cost-sensitive networks

### Contents

---

<b>5.1</b>	<b>VCSEL characterization and modeling . . . . .</b>	<b>110</b>
5.1.1	Static characteristic . . . . .	110
5.1.2	Quasi-static characteristic . . . . .	111
5.1.3	VCSEL nonlinearity modeling . . . . .	112
<b>5.2</b>	<b>Simulation results . . . . .</b>	<b>115</b>
5.2.1	Optical link model . . . . .	115
5.2.2	Optical noise components . . . . .	116
5.2.3	Nonlinearity and clipping distortions . . . . .	118
<b>5.3</b>	<b>Measurements . . . . .</b>	<b>121</b>
5.3.1	Back to back measurements . . . . .	121
5.3.2	Optical link characterization . . . . .	126
5.3.3	Experimental validation of VCSEL non-linear model . . . . .	127
5.3.4	Companded DCO-OFDM . . . . .	129

---

As mentioned in the previous chapters, VCSELs have many advantages over the edge-emitting laser diodes including: low threshold currents, high fiber-coupling efficiency, easy two-dimensional integration due to the surface-normal emission and the possibility of testing during the fabrication process. Thanks to these features, VCSELs represent an attractive solution for high data-rate, low cost and low power communication systems.

However, the VCSEL exhibits a nonlinear behavior, especially for high bias currents, due to the internal heating. Multicarrier modulations, such as OFDM and DMT have a large dynamic range making them more vulnerable to nonlinearities. To simulate and evaluate the impact of the VCSEL nonlinearity on DMT modulations, the VCSEL static characteristic is commonly used [75]. The static characteristic represents the optical power at the VCSEL output as function of the DC driving current.

However, in [76], it has been reported that 1 – dB compression point was found to increase with the bias current, which is inconsistent with the VCSEL static L-I characteristic. A quasi-static VCSEL characterization was then proposed to investigate the VCSEL nonlinearity and a new VCSEL quasi-static characteristic that is more consistent with VCSEL properties was derived [76]. The quasi-static approach consists in using a dynamic signal to modulate the VCSEL around the DC bias and reporting the measured optical power as function of bias current amplitudes to plot the quasi-static characteristic. OFDM and DMT signals being dynamic, it is more appropriate to use the VCSEL quasi-static characteristic for evaluating the impact of VCSEL nonlinearity on DMT modulations. This approach is being investigated in this chapter and the obtained results will be compared to those of the static approach that is more commonly used to describe the VCSEL nonlinearity. To this end, the VCSEL nonlinear behavior is first described using an appropriate modeling. The developed models are then employed to simulate and evaluate the VCSEL impact on DMT modulations. The simulation results are finally compared to measurements with the aim of evaluating the accuracy of using the VCSEL quasi-static characteristic to evaluate DMT modulation performance.

## 5.1 VCSEL characterization and modeling

### 5.1.1 Static characteristic

The light source considered in this study is a low-cost VCSEL from Finisar photonics with an emitting wavelength of 850nm and a 3dB bandwidth from 5GHz to 7GHz for a range of DC bias currents from 3mA to 15mA. Figure 5.1 shows the measured output optical power as a function of the DC driving current. The VCSEL static characteristic is measured over a range of bias currents from 0 to 15mA, 15mA being the absolute maximum driving current for an ambient temperature of around 25°C as indicated in

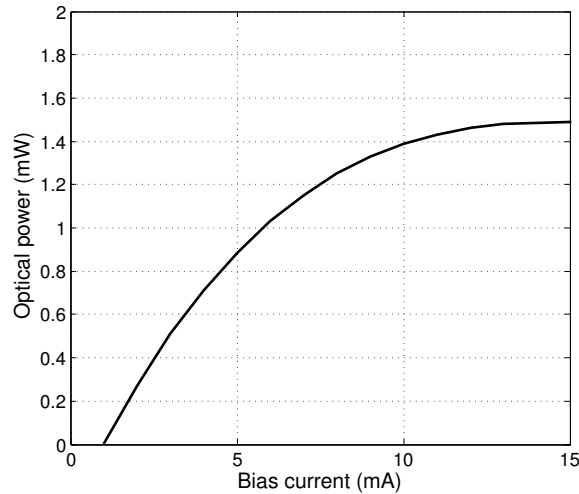


FIGURE 5.1: The static characteristic of the Finisar Photonics VCSEL

the datasheet. As can be seen in Figure 5.2, the VCSEL works with low driving currents, which could be advantageous for low-cost optical links. The threshold current of the VCSEL is equal to 1.2mA. For low driving currents, the L-I curve is almost linear with a slope efficiency of 0.22W/A. For bias currents greater than 6mA, the static characteristic exhibits a considerable nonlinearity. The nonlinear effect significantly increases with the bias current until saturation occurs at a bias current of 12mA.

### 5.1.2 Quasi-static characteristic

As discussed in [76], VCSELs suffer from poor heat dissipation and consequently can exhibit strong thermally dependent behavior. In order to describe the thermal dependence of the VCSEL L-I characteristic, thermal models have been developed using modified laser rate equations [77] or multidimensional thermal heating analysis [78]. The presented models permit to accurately simulate the VCSEL's small-signal and transient behaviors, with more or less excessive levels of complexity. However, these models are valid for bias currents below the VCSEL's rollover point ( $I_{RO}$ ) and therefore can not be used to simulate the VCSEL's behavior when the bias current is near the rollover point.

Motivated by the need to simulate the large-signal behavior in order to define the optimal modulation conditions, a quasi-static approach has been presented in [76]. The VCSEL quasi-static characterization consists in directly modulating the VCSEL using a sinusoidal signal at a given RF power,  $P_{RF}$ . For a given bias current and a given RF power, the minimum and maximum photodetected currents corresponding to the

minimum and the maximum of the modulating sinusoidal signal are measured. The corresponding optical powers are then computed using the photodiode transfer function, i.e. the photodetected current as function of the input optical power. Thus, varying the RF power of the modulating signal, and therefore the current amplitude around the bias current, a new quasi-static L-I curve permitting to describe the VCSEL large-signal behavior, can be derived. Figure 5.2 compares the static and quasi-static characteristics of the Finisar Photonics VCSEL. The quasi-static curves are measured for three Bias currents: 4mA, 6mA and 8mA.

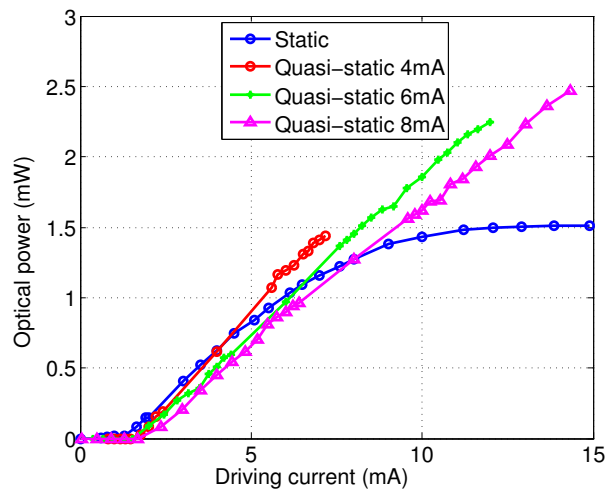


FIGURE 5.2: The static and quasi-static characteristics of the Finisar Photonics VCSEL for different bias currents

If the VCSEL driving current is a DC current (the static curve on Figure 5.2), the device temperature increases with the applied DC current causing an output optical power saturation (saturation region in Figure 5.2). For DC currents higher than the rollover current ( $I_{RO} \approx 15mA$ ), the output optical power is expected to decrease with the DC current, which corresponds to the rollover region [77, 79]. This region is not shown in Figure 5.2 due to the VCSEL maximum driving current (i.e. 15mA). On the other hand, if a dynamic signal is used to modulate the VCSEL around the DC bias current, the dynamic optical power response as function of the VCSEL driving current is almost a linear function (the quasi-static curves in Figure 5.2). Indeed, when a dynamic signal is modulating the VCSEL around the DC operating current, peak amplitudes occur for a short time compared to the VCSEL semiconductor thermal time constant [80]. Consequently, the VCSEL does not undergo any severe additional heating from the RF signal compared to the DC thermal contribution.

It can be noticed as well that the quasi-static VCSEL threshold,  $I_{th,QS}$ , is found to be slightly higher than the static VCSEL threshold,  $I_{th}$ . This is due to the fact that the VCSEL operating current induces an increase in VCSEL temperature, thus impacting the laser threshold in the dynamic regime.

### 5.1.3 VCSEL nonlinearity modeling

A simple way to model the VCSEL nonlinearity and predict its impact on a DMT system using computer simulations is the behavioral modeling approach. It consists in developing a mathematical model of the VCSEL transfer function from the measured characteristics. Contrary to the equivalent circuit modeling, the behavioral modeling approach does not require a deep knowledge of the low level circuit layout and significantly optimizes the simulation time [81]. Memory-less polynomial modeling is commonly used to describe the VCSEL nonlinear behavior [45, 82]. The accuracy of the simulation results depends on the polynomial degree. As demonstrated in [82], a second-order polynomial can provide a satisfying model for nonlinear behaviors. However, as shown in [83], the polynomial modeling with a reasonable complexity is not suitable for strong nonlinearities and the model does not accurately represent the saturation region. This issue has been widely discussed in radio communications, where the power amplifier exhibits a nonlinear behavior similar to that of VCSELs, thus impacting the performance of radio OFDM systems. Several models were proposed in the literature to properly describe the nonlinear behavior of power amplifiers. Saleh [84], Ghorbani [85] and Rapp [86] models have been extensively reported in the literature. First, Saleh has proposed two-parameter formulas to model the AM-AM (amplitude) and AM-PM (phase) conversions of traveling-wave tube (TWT) amplifiers. In [85], Ghorbani has adapted Saleh's model for solid state power amplifiers (SSPAs) by adding two more fitting elements to better fit the AM-AM and AM-PM conversions of SSPAs, especially in the small signal region, where SSPAs tend to exhibit more linear performance than TWTs. In [86], assuming that the AM-PM conversion of the SSPA is small enough, so that it can be neglected, a new analytical expression for the AM-AM conversion was proposed. As mentioned in [86], for large inputs the amplitude function of SSPA tends to a maximum value called saturation level whereas TWTs present a 'roll-over' effect beyond the saturation level. Thus, it was shown that the Rapp model provides a

better approximation for the SSPA measured AM-AM characteristic, especially in the saturation region.

To properly model the nonlinearity of VCSELs, one can adapt one of the aforementioned models to describe the VCSEL nonlinear transfer function. Contrary to SSPAs, VCSELs exhibit two main nonlinearities that considerably affect OFDM modulation performance. Indeed, further the saturation and rollover regions that occur for large input currents, the VCSEL exhibit a power jump near the threshold current below which the VCSEL's output is dominated by spontaneous emission rather than simulated emission. This phenomenon causes the signal amplitude lower than the VCSEL threshold to be clipped, thus drastically impacting the system performance in small-signal region. Consequently, to derive an appropriate model for VCSEL nonlinearity, the VCSEL threshold should be taken into account when formulating the VCSEL behavior model. Furthermore, since the signal driving the VCSEL is a real signal, the AM-PM conversion is not required to be described. Based on these considerations, the Rapp model is found to provide a better approximation for the VCSEL AM-AM conversion. Within this context, a modified Rapp model taking into account the VCSEL nonlinearity in the small-signal region was developed. The modified Rapp model is given by,

$$P_{out} = \begin{cases} G \frac{I - I_{th}}{\left(1 + \left|\frac{I - I_{th}}{P_{sat}/G}\right|^{2p}\right)^{1/2p}}, & \text{if } I > I_{th} \\ 0, & \text{if } I \leq I_{th} \end{cases} \quad (5.1)$$

where  $P_{out}$  represents the output optical power,  $I$  is the driving current,  $G$  is the linear gain,  $P_{sat}$  is the output saturation level and  $p$  is the smoothness factor. The model parameters are extracted from the measured input-output characteristic. The parameter  $p$  permits to describe the hardness of the nonlinear characteristic. If the factor  $p$  is rather low, the Rapp model produces a smooth transition from the linear region to the limiting region. In contrast, when  $p$  approaches infinity, the Rapp model converges to a hard-limiter model.

Note that the DMT modulation signal bandwidth is assumed to be smaller than the VCSEL 3dB bandwidth for any DC driving current in the range 3mA to 15mA. Consequently, the VCSEL frequency limitation can be discarded in this model.

To simply model the VCSEL nonlinearity, one can use a memory-less polynomial modeling. The N-order polynomial model of the VCSEL transfer function can be expressed as,

$$P_{out} = \sum_{n=0}^N b_n I^n \quad (5.2)$$

The second-order polynomial model and the Rapp model of the VCSEL static characteristic are reported in Figure 5.3.

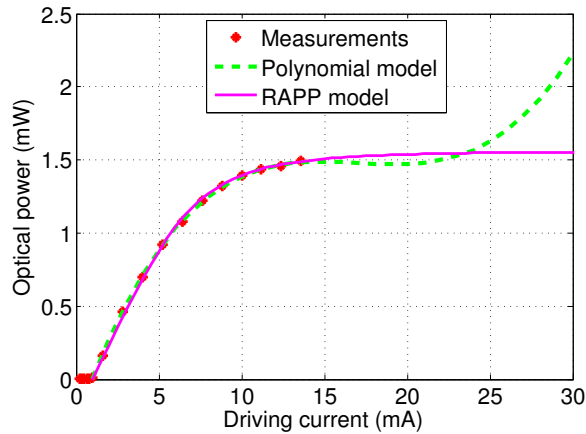


FIGURE 5.3: Comparison of second-order polynomial and Rapp models for the VCSEL static characteristic

As can be seen in Figure 5.3, both of the considered models fit correctly the measured static characteristic in the linear region. However, when the bias current exceeds the measurement range, the polynomial model increases significantly, whereas Rapp model is kept flat, simulating the saturation level. Thus, as expected, the Rapp model provides better extrapolation of the static characteristic in the saturation region than the polynomial model. As shown in Figure 5.2, the VCSEL quasi-static characteristics are almost linear. Thus, a first-order polynomial can provide a satisfying model for the quasi-static transfer function.

## 5.2 Simulation results

### 5.2.1 Optical link model

In this section, the impact of the VCSEL transfer function on DMT modulation performance is investigated. The simulations are based on the simulation model shown



in Figure 5.4 and are carried out using Matlab software. First, a DMT modulator is used to generate a real DMT signal using a given number of subcarriers. The VCSEL is then biased at a bias  $I_{DC}$  and directly modulated using the generated DMT signal with an electric power  $P_{RF}$ . The resulting signal at the VCSEL output is then passed through an optical fiber and converted back to an electric signal using a PIN photodiode with a responsivity of 0.55A/W. The photodiode is assumed to have a linear behavior, which is a common assumption for fiber-optic communication systems. The DMT demodulator at the photodiode output is used to demodulate the DMT signal and recover the transmitted QAM symbols. The VCSEL is approximated by either the static or quasi-static models presented in Figure 5.2. The optical fiber is a standard MMF OM3 glass fiber with 50/125 $\mu\text{m}$  core/cladding diameters. The fiber is assumed to be quite short (i.e.  $\approx 1\text{m}$ ), so that its impact can be neglected (i.e. no intermodal dispersion is considered).

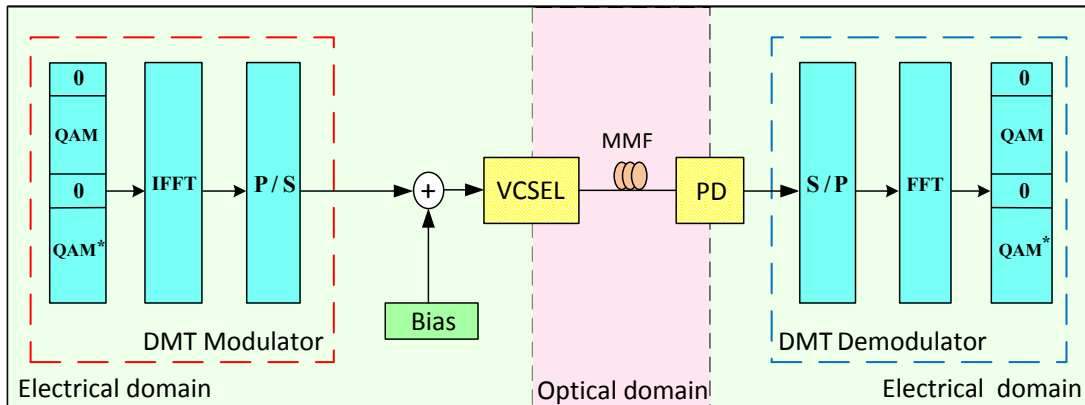


FIGURE 5.4: Block scheme for simulations

Concretely, the DMT signal has 256 subcarriers with a 16-QAM constellation. Furthermore, an oversampling with an oversampling factor of 4 is performed in order to correctly approximate the PAPR of the continuous DMT signal [53]. The EVM metric [90] is used to evaluate the quality of the optical link.

## 5.2.2 Optical noise components

The main noise sources in the considered optical link are the relative intensity noise (RIN) due to the spontaneous emission in the VCSEL, the shot noise due to the photodetection process and the thermal noise. The variances of the photocurrent induced

by the optical noise components are given by,

$$\langle i^2 \rangle_{RIN} = RIN \cdot I_0^2 \cdot \Delta f \quad (5.3)$$

$$\langle i^2 \rangle_{shot} = 2qI_0 \cdot \Delta f \quad (5.4)$$

$$\langle i^2 \rangle_{th} = \frac{4kT\Delta f}{R_L} \quad (5.5)$$

where  $I_0$  is the average detected photocurrent,  $\Delta f$  is the signal bandwidth,  $RIN$  is the relative intensity noise,  $q$  is the electron charge,  $T(K)$  is the actual temperature,  $k$  is Boltzmann's constant and  $R_L$  is the load resistance. Note that the transimpedance amplifier (TIA) integrated with the photodiode is supposed to be noiseless. The total noise power at the optical receiver output can be expressed as,

$$P_{noise} = (RIN \cdot I_0^2 + 2qI_0) \Delta f \cdot R_L + 4kT\Delta f \quad (5.6)$$

Figure 5.5 shows the contribution of each noise component to the total noise power as a function of the detected photocurrent. For simplicity, the RIN noise is assumed to be a white noise with a constant value of  $-125\text{dB}/\text{Hz}$ , and the dark current is negligible.

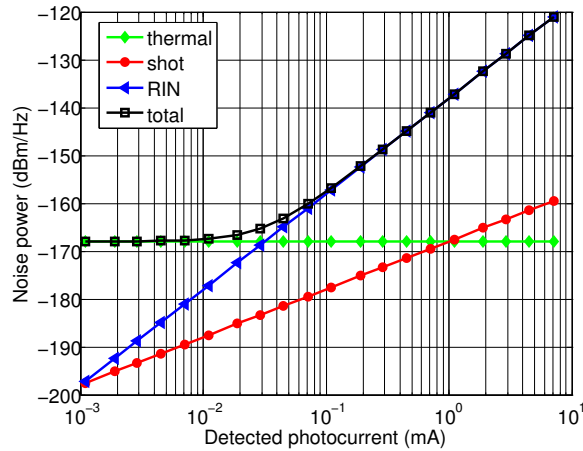


FIGURE 5.5: Contribution of the different noise components (RIN, shot and thermal) to the total noise power as function of the detected photocurrent ( $R_L = 50\Omega$ )

Thermal noise is a constant contribution versus the detected photocurrent. Shot noise has a slope of one decade/10dB and RIN noise has a slope of about two decades/10dB. Two main regions can be defined from the results shown in Figure 5.5: the first region corresponds to  $I_0 < 0.01\text{mA}$ , where the total noise power is dominated by the thermal

noise. In the second region (i.e.  $I_0 > 0.07\text{mA}$ ), the RIN is the dominant noise power contribution over the remaining noise components.

In practice, relative intensity noise is not white noise. Furthermore, the RIN spectral density depends on the VCSEL bias current. The considered DMT signal has a bandwidth of 500MHz. The measurements of the RIN noise in the VCSEL under test, have shown that the RIN spectral density does not exhibit important variations on the considered bandwidth. To take into account the dependence of the RIN noise on the frequency and the bias current, an approach is to consider the RIN mean value on the signal bandwidth for the different considered bias currents. When assuming the RIN to be the dominant noise, which is the case for the considered bias currents in this study, then the signal to noise ratio at the receiver output can be expressed as,

$$SNR_{noise} = \frac{P_{RFout}}{RIN \cdot I_0^2 \cdot \Delta f \cdot R_L} \quad (5.7)$$

where  $P_{RFout}$  is the electric power at the receiver output.

### 5.2.3 Nonlinearity and clipping distortions

In order to simulate the impact of the VCSEL nonlinearity on the DMT modulation, a real DMT signal is first generated using Matlab software and a DC bias current is then added to the generated DMT signal. The nonlinear models given in Figure 5.2 are next applied to the DC biased DMT signal in order to simulate the electrical-to-optical conversion. Since the fiber impact and the photodiode nonlinearity are negligible, the receiver can be modeled by a linear function with a slope equal to the photodiode responsivity. The QAM data at the DMT demodulator output is finally compared to the transmitted QAM data in order to compute the EVM assessing the nonlinearity and the clipping contributions to the total SNR. The relationship between EVM and SNR is given by [90]

$$SNR \approx \frac{1}{EVM^2} \quad (5.8)$$

The SNR taking into account the VCSEL nonlinearity impact and the noise contribution, can be computed using (5.7) as follows,

$$SNR = \frac{P_{RFout}}{P_{noise} + P_{NLD}} \quad (5.9)$$

Rearranging (5.9) leads to,

$$\frac{1}{SNR} = \frac{1}{SNR_{noise}} + \frac{1}{SNR_{NLD}} \quad (5.10)$$

where  $P_{NLD}$  is the nonlinear distortions power and  $SNR_{NLD}$  represents the nonlinear distortion contribution to the SNR.

Let  $EVM_{noise}$  and  $EVM_{NLD}$  be respectively the EVMs due to the noise components and the nonlinear distortion. Using (5.8),  $EVM_{noise}$  and  $EVM_{NLD}$  can be expressed as,

$$EVM_{noise} = \sqrt{\frac{1}{SNR_{noise}}} \quad (5.11)$$

$$EVM_{NLD} = \sqrt{\frac{1}{SNR_{NLD}}} \quad (5.12)$$

Substituting (5.11) and (5.12) in (5.10), the total error  $EVM$  can be written as,

$$EVM = \sqrt{EVM_{noise}^2 + EVM_{NLD}^2} \quad (5.13)$$

It has to be noted that  $EVM_{noise}$  is evaluated using the theoretical formula given by (5.7), whereas  $EVM_{NLD}$  is the simulation result of the VCSEL nonlinearity impact on the transmitted constellation based on the VCSEL static and quasi-static models defined in Section 5.1. Figure 5.6 shows the EVM simulation results whether the VCSEL nonlinearity is modeled by the static or the quasi-static characteristics.

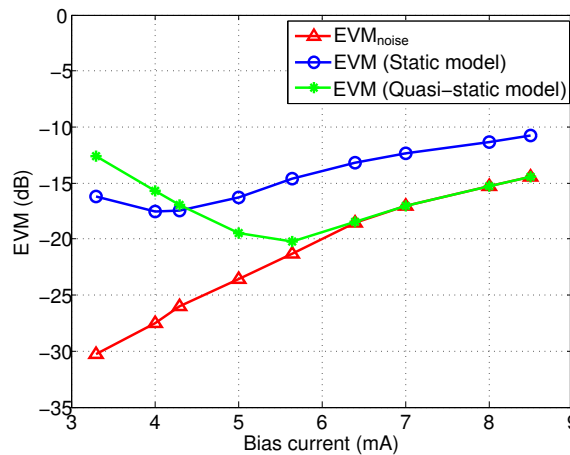


FIGURE 5.6: Comparison of the static and quasi-static EVM simulation results as function of the VCSEL bias current

As can be seen in Figure 5.6, when the static characteristic is used to model the VCSEL nonlinear behavior, the static EVM curve can be divided into two regions. The first region corresponds to  $I_0 < 4.2\text{mA}$ , where the clipping noise is the dominant noise. The second region corresponds to  $I_0 > 4.2\text{mA}$ , where the optical noise and the nonlinear distortions due to the saturation and roll-over regions are dominant over the clipping noise. On the other hand, when the quasi-static characteristic is used to model the VCSEL nonlinear behavior, the quasi-static EVM is either impacted by the clipping noise ( $I_0 > 5.6\text{mA}$ ) or the optical noise ( $I_0 > 5.6\text{mA}$ ). Thus, for  $I_0 > 5.6\text{mA}$ , the EVM curve arising from the quasi-static model and the EVM curve resulting from the optical noise components ( $EVM_{noise}$ ) are found to be superposed. Indeed, since the quasi-static characteristic is almost linear for bias currents larger than the quasi-static threshold, no nonlinearity distortions are impacting the quasi-static EVM performance. Note that in the case of the quasi-static model, the clipping noise contribution is more significant and spread out over larger bias currents. This is due to the fact that the quasi-static threshold is larger than the static one. The optimum bias current minimizing the EVM is found to be remarkably different for static and quasi-static models. For a given DMT signal with a current excursion,  $\Delta I$ , the optimal driving current can be defined as the lowest DC bias that guarantees a minimum clipping noise. Infinitely increasing the DC bias, will minimize the clipping noise at the cost of an increased detected photocurrent and therefore an increased optical noise power (5.6). The optimal driving current,  $I_{DC,opt}$ , that satisfies a good trade-off between the clipping noise and the optical noise can be expressed as,

$$I_{DC,opt} - \Delta I \cong I_{th} \quad (5.14)$$

The considered DMT signal in both simulations and measurements has a mean power of  $P_{rms} = 0.158\text{mW}$ , a peak power of  $P_{peak} = 1.8\text{mW}$  and a PAPR (i.e.  $P_{rms}/P_{peak}$ ) of 10.56dB. The corresponding mean current,  $I_{rms}$ , and peak current,  $I_{peak}$ , are given by

$$I_{rms} = \sqrt{P_{rms}/R_{in}} = 1.8\text{mA} \quad (5.15)$$

$$I_{peak} = \sqrt{P_{peak}/R_{in}} = 6\text{mA} \quad (5.16)$$

where  $R_{in} = 50\Omega$  is the VCSEL input resistance. The current excursion,  $\Delta I$ , is then given by

$$\Delta I = I_{peak} - I_{rms} = 4.2\text{mA} \quad (5.17)$$

Considering the static model, the optimal current is equal to 4mA for a minimum EVM of  $-17$ dB. Substituting this current in (5.14) leads to

$$I_{DC,opt} - \Delta I = -0.2\text{mA} \ll I_{th} \quad (5.18)$$

The optimal driving current resulting from the use of the static model does not guarantee a minimum clipping noise, which provides an erroneous estimation of the optimal driving current. The quasi static model expects an optimal driving current of 5.65mA for a minimum EVM of  $-20$ dB. Substituting this current in (5.14) leads to

$$I_{DC,opt} - \Delta I = 1.45\text{mA} \cong I_{th,QS} \quad (5.19)$$

Equation (5.19) means that after adding the DC bias to the DMT signal, no peaks lower than the quasi-static threshold will remain at the VCSEL input. As a result, no clipping noise will be introduced by the VCSEL device. It has to be noted that the quasi-static approach could be used for larger bandwidths, provided that the RIN spectral density variations on the considered bandwidth are taken into account.

### 5.3 Measurements

In Chapter 4, a companded DCO-OFDM permitting to improve the optical power performance of OFDM-based optical systems was presented. Several simulation results comparing DCO-OFDM performance to that of conventional schemes in both time and frequency domains were provided. In the first part of Chapter 5, a new approach based on the use of the quasi-static characteristic to evaluate the VCSEL impact on DMT modulations was presented. To experimentally validate these analytical results, a test system was built. The experimental setup consists in generating a DCO-OFDM signal using Matlab software and uploading the obtained signal on a Tektronix arbitrary wave generator (AWG) in order to generate a continuous signal with the desired bit data rate. The continuous time signal at the AWG output is injected to the light source RF input and a DC bias is added using a DC supply. The resulting DC biased optical signal is next passed through the optical channel and a photodiode is used to detect the optical signal and convert it back to an electric signal. At the photodiode output, an Agilent oscilloscope is used to measure the received electric OFDM signal. Finally, an OFDM

demodulation is performed using Matlab software in order to recover the transmitted data from the measured OFDM signal. To carry out the different measurements and correctly evaluate the transmission performance, the channel must be characterized, estimated and equalized. To this end, a back-to-back testing is first performed to evaluate the effects of the AWG and oscilloscope on the transmitted DCO-OFDM signal. The back-to-back testing is detailed in the following section.

### 5.3.1 Back to back measurements

The back-to-back configuration consists in directly connecting the AWG to the oscilloscope using a coaxial cable. A sample clock synchronization that consists in connecting the AWG 10MHz reference output to the oscilloscope 10MHz input, is used to synchronize the two equipments. The AWG is a TEKTRONIX 7122B [91] with two output channels, each with a sample rate of up to 12GS/s. A maximum sample rate of 24GS/s can be reached thanks to the “interleave” function. The oscilloscope is a digital sampling oscilloscope AGILENT DSO 54855A [92] with a bandwidth of 6GHz, four channels and a sample rate of up to 20GS/s on all four channels simultaneously.

The impact of the AWG on the DMT signal whether the “interleave” function is used or not is discussed in AppendixA. Indeed, the AWG leads to a sinc distortion whose frequency response depends on the use or not of the “interleave” function. To overcome the magnitude droop, the spectrum must be compensated for the sinc distortion stemmed from the AWG’s zero-order hold (ZOH) converter.

#### 5.3.1.1 Inverse sinc compensation

An approach to compensate for the sinc distortion, is to use a digital filter whose frequency response is the inverse of the ZOH transfer function to achieve frequency response correction. Such filter is called “compensation filter”. To accomplish the sinc compensation, one can apply a post-compensation filter to the received frequency data. However, the post-compensation does not only amplify the channel noise in the receiver, but significantly complicates the design of the post compensation filter [93]. To recover the transmitted data with no amplitude distortion, an alternative approach is to apply the sinc compensation filter prior to the DAC operation. This technique is

known as DAC equalization. In OFDM modulations, the DAC equalization, consists in applying the inverse sinc filter to the frequency subcarriers before the inverse fast Fourier transformation operation [94]. The inverse sinc compensation filter is a linear phase filter whose frequency response is given by,

$$H(f) = \frac{wT_s/2}{\sin(wT_s/2)} = 1/\text{sinc}(f/f_s) \quad (5.20)$$

Figure 5.7 compares the transmitted and received spectrum of the same DMT signal with and without pre-compensation. In the two cases, the frequency sampling is 10GHz. As can be seen in Figure 5.7(d), the received spectrum is almost flat due to the inverse sinc pre-compensation that negates the effects of the DAC on the signal magnitude. The inverse sinc compensation has two main weaknesses. First, the use of the inverse sinc filter compensates only for the amplitude distortion, thus providing no phase correction. Second, different pre-compensation filters have to be applied whether the “interleave” function is used or not. Indeed, in the case of time-interleaved DAC, the sinc frequency response “rolls off” to zero at half the sampling frequency, whereas the ZOH frequency response of a simple DAC “rolls off” to zero at the sampling frequency. To overcome these drawbacks, an alternative approach is to use a zero-forcing equalizer.

### 5.3.1.2 Channel equalization

The purpose of channel equalization is to reduce amplitude and phase distortions due to channel imperfections. One of the main advantages of OFDM systems is its low-complexity equalization that can be performed in the frequency domain, which is much less complex than the time-domain equalization required in single-carrier modulations. Indeed, multicarrier modulations decompose the frequency selective channel into several flat channels, thereby enabling low complexity per-tone equalization that consists in applying 1-tap frequency-domain equalizer (FEQ) per tone, to compensate for channel amplitude and phase effects [95]. A straightforward and simple way to perform one-tap channel equalization is to divide the received frequency symbols by the frequency-domain channel taps. This is referred to as zero-forcing (ZF) equalization [96]. To this end, an estimation of the channel frequency taps is first performed and the equalizer coefficients are then computed using the channel estimate. To estimate the channel taps, one can insert known training symbols prior or within the OFDM symbols. The training symbols



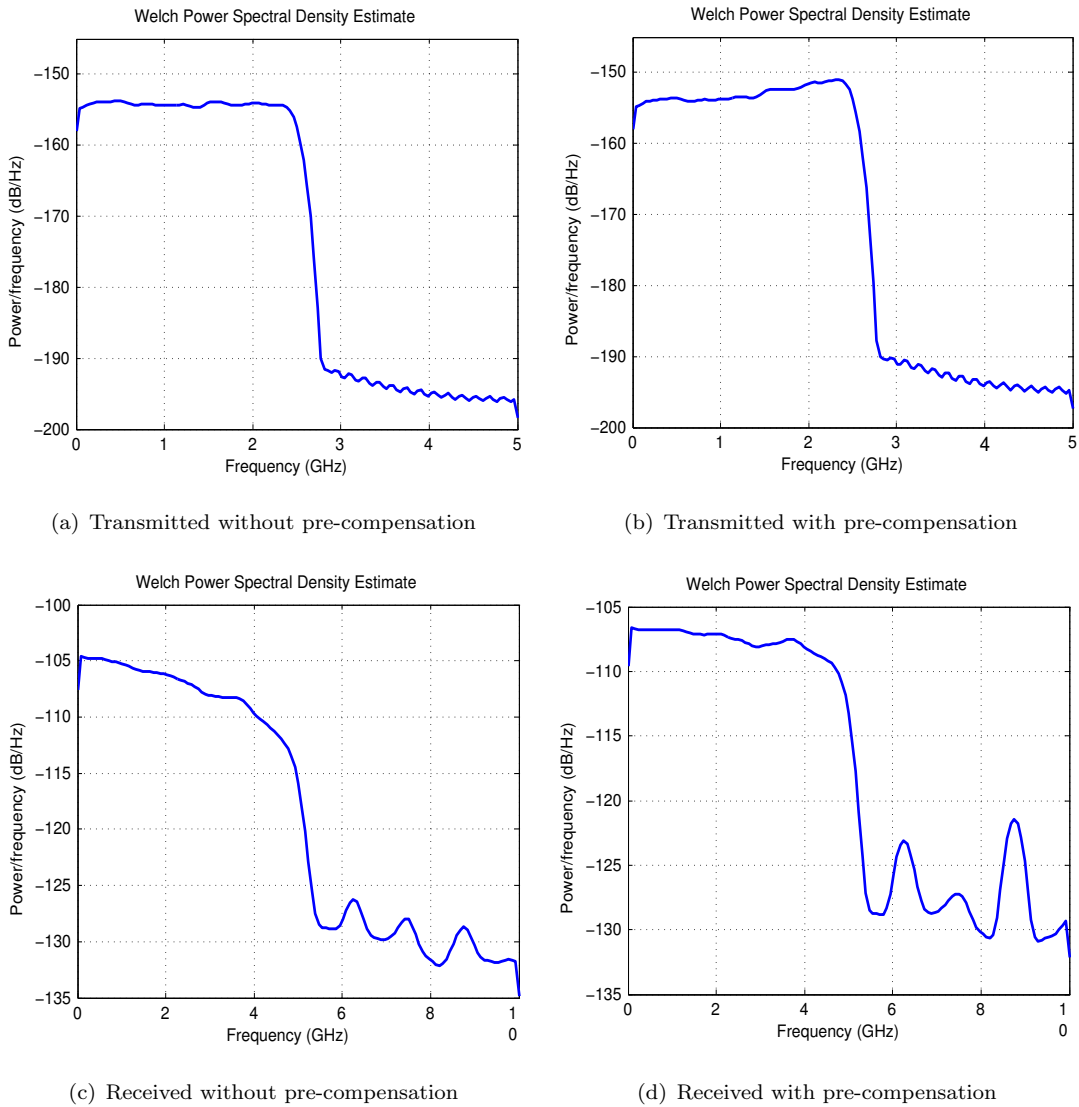


FIGURE 5.7: Illustration of the frequency response correction using the inverse sinc pre-compensation

are also referred to as pilot symbols. The quality of channel estimation depends on the number and arrangement of pilot symbols. The larger the number of pilot symbols, the more accurate the estimation. However, the number of pilot symbols should be chosen to provide a best trade-off between channel estimation accuracy and bit rate degradation. Thus, a large number of pilot symbols would provide an accurate channel estimation at the expense of a decreased bit rate. On the other hand, two types of pilot arrangement are possible whether the channel is slow fading or time-varying [97]. Indeed, in the case of slow fading channels, where the channel characteristics do not change rapidly, the channel estimation is commonly performed by inserting pilot symbols into all of the

subcarriers at the beginning of the OFDM frame. This is commonly known as block-type arrangement. Assuming that the channel characteristics do not change within the OFDM frame, free-error channel estimation can be performed. On the contrary, in the case of time varying channels, the channel characteristics vary rapidly and the channel can not be assumed to be constant within an OFDM frame. To perform an accurate channel estimation and therefore an optimal channel equalization, pilot tones should be inserted into each OFDM symbol, so that the receiver can update the equalizer coefficients according to the channel characteristics for each OFDM symbol. This is referred to as Comb-type arrangement.

Wired optical channels being almost time-invariant channels, block-type arrangement can be used to perform an optimal zero-forcing equalization. An advantage of block-type based channel estimation, is that only one OFDM symbol is used to perform channel estimation. The remaining OFDM symbols are all used to carry useful data and no more subcarriers are wasted to estimate the channel. Once the channel taps are estimated, the zero-forcing equalizer coefficients are computed and applied to the received symbols.

The  $k^{th}$  coefficient of the zero-forcing equalizer is then given by,

$$C(k) = \frac{1}{\hat{H}(k)} \quad (5.21)$$

The  $k^{th}$  equalized frequency symbol of the  $n^{th}$  OFDM symbol can be expressed as,

$$\hat{X}(n, k) = \frac{Y(n, k)}{\hat{H}(k)} = X(n, k) + \frac{Z(k)}{\hat{H}(k)} \quad (5.22)$$

where  $Y(n, k)$  is the  $k^{th}$  received frequency symbol of the  $n^{th}$  OFDM symbol,  $Z(k)$  the channel noise and  $\hat{H}(k)$  the estimated channel frequency tap. Figure 5.8 shows the received QAM constellation before and after the zero-forcing equalization.

The improvement resulting from the one-tap equalization can be evaluated using the EVM metric. Indeed, if no channel equalization is applied to the received constellation, then the EVM is equal to 29.2%. After applying the one-tap equalizer to the received constellation, the EVM is found to be equal to 13.22%.

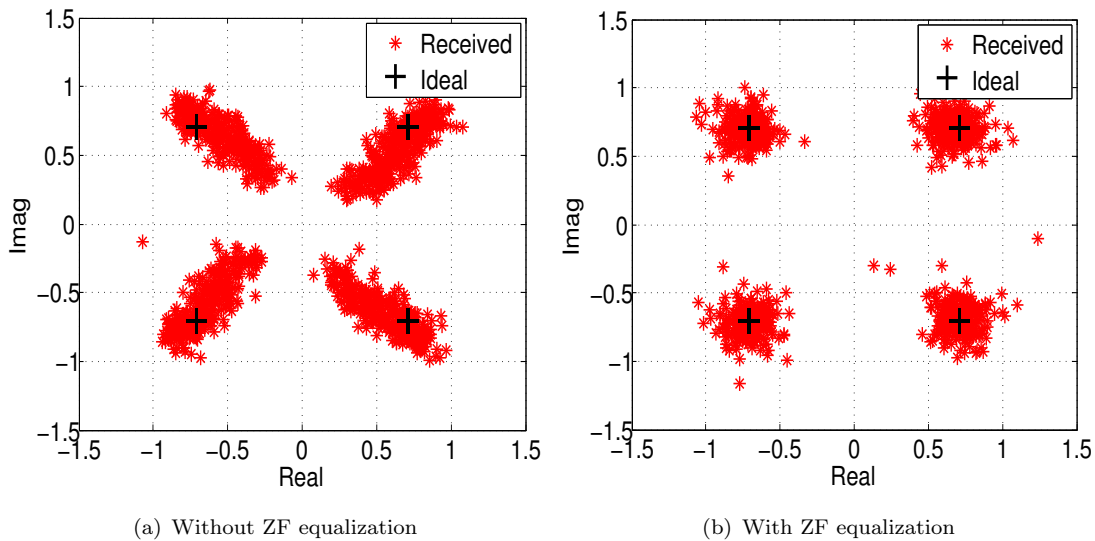


FIGURE 5.8: Effect of the zero-forcing equalizer on the amplitude and the phase of the received QAM constellation

### 5.3.2 Optical link characterization

In the previous section, a back-to-back testing was performed to study the effects of electronic equipments on the DMT signal. In this section, the impact of the whole optical link including the light source, the optical fiber and the photodiode is being evaluated. The used optical link consists of a multimode VCSEL from Finisar, a standard MMF OM2 glass fiber and a PIN photodiode. The fiber is quite short ( $\sim 1m$ ), so that its impact in terms of fiber attenuation and intermodal dispersion is negligible. The photodiode has a typical bandwidth of about 9GHz. Figure 5.4 shows the  $S_{21}$  parameter of the considered optical link for different bias currents, measured with a vector network analyzer (VNA) HP8510C.

It may be noted from Figure 5.4 that the coherence bandwidth of the optical link,  $B_c$ , is about several hundreds MHz. The overall delay spread of the channel, that is approximately equal to the reciprocal of the coherence bandwidth (5.23), is then about few nanoseconds.

$$\tau_d = \frac{1}{B_c} \quad (5.23)$$

To evaluate the impact of the optical link on DMT modulations, the continuous time signal at the AWG output is used to drive the Finisar VCSEL. At the photodiode output, the oscilloscope is used to measure the continuous time signal and convert it to a digital

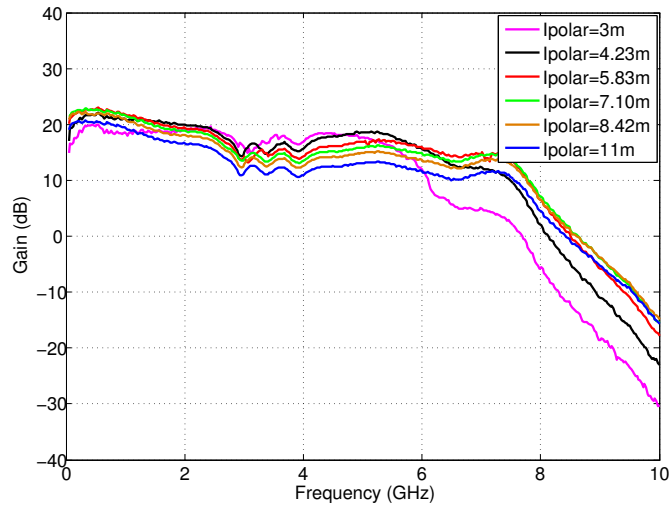


FIGURE 5.9: Measured  $S_{21}$  transmission characteristics of the used optical link for different bias currents

signal. The DMT signal is demodulated off-line and a zero-forcing equalizer is used to compensate for the channel distortions. Figure 5.10 depicts the received constellation

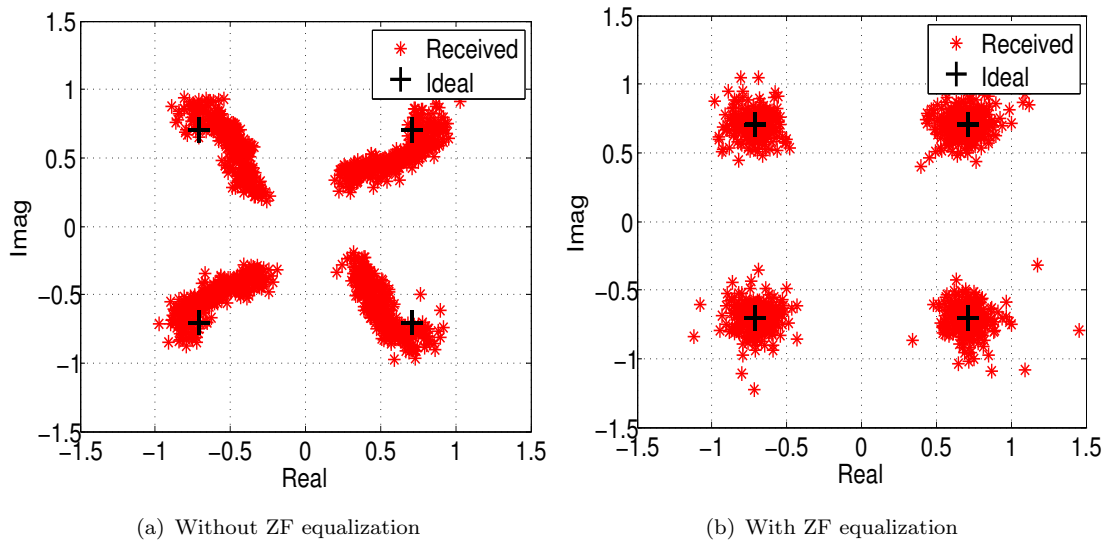


FIGURE 5.10: Correction of the amplitude and phase distortions due to the optical channel using ZF equalization

before and after applying the zero-forcing equalization. As can be seen in Figure 5.10, contrary to the back-to-back testing, both the amplitude and the phase of the received symbols are impacted by the optical channel distortions. This is due to the fact that low and high frequencies are not similarly impacted by the channel frequency response, thus resulting in both a rotation and a spread of the transmitted constellation.

### 5.3.3 Experimental validation of VCSEL non-linear model

The experimental setup permitting to evaluate the impact of VCSEL nonlinearity on DMT modulations is based on the system model shown in Figure 5.4. The DMT frame is formed by one training symbol and four data symbols each with 256 subcarriers. An oversampling with an oversampling factor of 4 is as well performed. Indeed, the considered oversampling reduces the noise timing jitter due to nonideal sampling clocks [87, 88]. The sample rate of the AWG is 3GS/s, which corresponds to a useful bandwidth of 500MHz, due to the oversampling and the Hermitian symmetry constraints. Then, the subcarrier frequency spacing can be expressed as,

$$\delta f = \frac{\Delta f}{N} = \frac{500MHz}{256} = 1.93MHz \quad (5.24)$$

It can be concluded from (5.24) that the bandwidth per subcarrier is sufficiently smaller than the coherence bandwidth of the channel, thus each subcarrier can be considered to experience a flat fading. As a result, the frequency-selective fading is substantially reduced, thereby no ISI occurs. In this scenario, a simple one-tap frequency equalization can be employed to compensate for channel impairments. On the other hand, the time duration of an OFDM symbol can be expressed as,

$$T_u = \frac{1}{\delta f} = 512ns \quad (5.25)$$

It can be concluded from (5.25) that the OFDM symbol duration is much larger than the spread delay of the channel. For these reasons, a simplified approach, where no guard interval is used, is considered in this study.

Figure 5.11 compares the measured EVM with the simulation results of the static and quasi-static EVMs. As can be seen in this figure, the measured and the quasi-static EVM curves are almost superposed. Indeed, as expected by the theoretical analysis, modeling the VCSEL nonlinearity by the static characteristic when a large dynamic signal is used to modulate the VCSEL device, leads to inaccurate estimations of the nonlinear distortions. On the contrary, the use of the quasi-static characteristic provides a reliable estimate of optical DMT modulation performance. The optimal driving current expected by the quasi-static model is equal to the measured optimal current (i.e. 5.65mA).

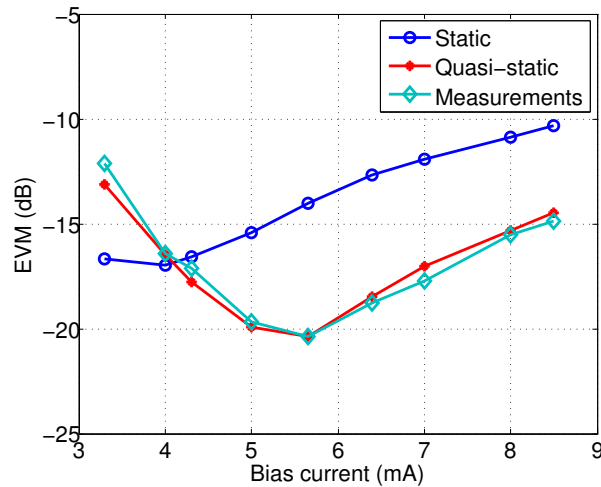


FIGURE 5.11: Measured EVM versus the static and quasi-static EVM simulation results as function of the VCSEL bias current

### 5.3.4 Companded DCO-OFDM

The experimental setup permitting to evaluate the performance of companded DCO-OFDM is also based on the system model shown in Figure 5.4. However, the used optical link consists of a Distributed Feedback laser, a 1m OM2 glass fiber and a PIN photodiode. Indeed, the DFB is used to take advantage of the small RIN of the laser source (around  $-145\text{dB/Hz}$ ), permitting to precisely quantify the impact of the optical link distortion on companded DCO-OFDM performance. The DMT frame has the same characteristics as those detailed in the previous section. The oversampling with an oversampling factor of 4, the channel estimation and the zero-forcing equalization are also applied to correctly transmit and recover data.

The major works dealing with DMT-based IM/DD systems presented in the literature consider a hard clipping at zero for both theoretical analysis and simulations [15]-[18]. Indeed, in those works, the light source threshold is assumed to be equal to zero. This assumption is suitable for LED-based systems, where the light source threshold current is effectively equal to zero. However, as mentioned in Chapter 1, LEDs have a limited speed and thus can not be used in high data rate communications. Instead, laser-based light sources such as DFBs and VCSELs are usually employed to build high data rate interconnects. Such devices do not exhibit an ideal behavior and therefore do not have a threshold current equal to zero. Figure 5.12 shows the AM-AM characteristic of the DFB employed in this work.

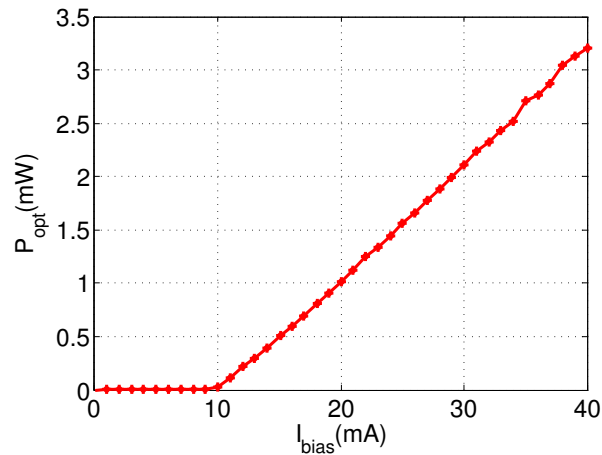


FIGURE 5.12: Static characteristic of the DBF laser

As can be seen from the AM-AM characteristic, the DFB laser has a linear behavior with a slope efficiency of  $0.18\text{W/A}$  and a threshold of about  $11\text{mA}$ . For a given working point  $(I_{bias}, P_{opt})$ , the biased OFDM peaks whose amplitudes are lower than the DFB threshold, are clipped. The clipping effect decreases with the bias current. On the other hand, since the average optical power is equal to the mean of the transmitted signal, the optical power increases with the bias current. To reduce the clipping noise and improve system performance in terms of BER, one can increase the bias current of the DFB component. However, this approach will increase the optical power required to transmit the DCO-OFDM signal. An alternative solution to improve BER performance without degrading the optical power efficiency of the system is to employ companded DCO-OFDM instead of the conventional optical power inefficient DCO-OFDM. Figure 5.13 compares the measured EVM performance of companded DCO-OFDM to that of conventional DCO-OFDM for different bias currents and a  $64\text{-QAM}$  modulation. In this proof of concept experiment, the useful signal bandwidth is  $500\text{MHz}$ , leading to a data rate of  $3\text{Gb/s}$ .

As can be seen in Figure 5.13, for both conventional and companded DCO-OFDM, the EVM decreases with the bias current. Indeed, the lower the bias current, the higher the clipping noise and the worse the EVM. On the other hand, for high bias currents, the number of subcarriers affected by the clipping process is negligible and the dominant noise is the channel noise. Thus, for bias currents larger than  $18\text{mA}$ , the parameter  $\alpha$  is set equal to 1, so that the channel noise is not amplified in the receiver and the EVM is not deteriorated.

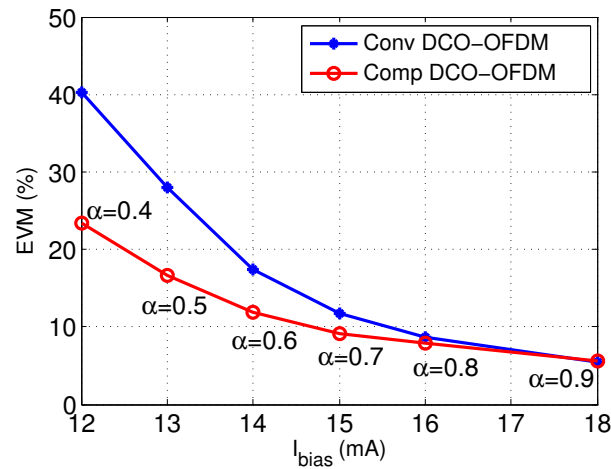


FIGURE 5.13: Measured EVM of conventional and companded DCO-OFDM techniques for different bias currents using 64-QAM modulation

For low bias currents, the clipping noise is the dominant noise. Thus, to improve EVM performance, the companding transformation, with  $\alpha < 1$ , is used to significantly reduce the peaks affected by the clipping process. Furthermore, the companding function was designed so that a small part of the time signal is amplified in the receiver. Therefore, the amplification of the channel noise is negligible compared to the clipping noise cancellation, thus significantly improving the EVM performance. As a result, for a DC bias current of 12mA, a gain of about 17% in EVM is achieved, permitting to reach an EVM as low as 23% (i.e. free error system).

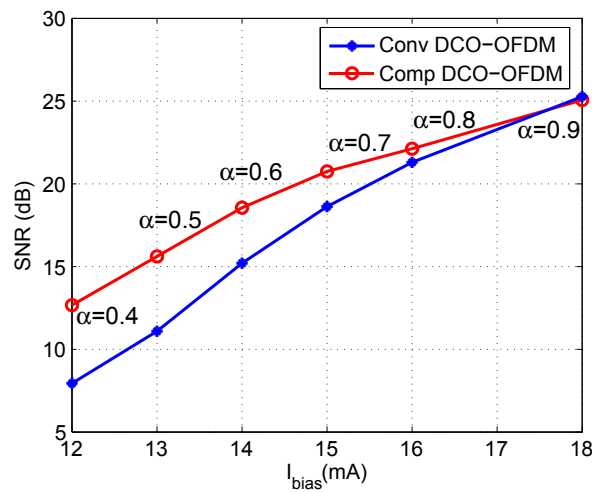


FIGURE 5.14: SNR as function of bias current of conventional and companded DCO-OFDM for a 64-QAM modulation

The EVM metric is usually used to practically approximate the BER performance through SNR. Indeed, the SNR can be computed from the measured EVM for each



bias current using (5.8). The results are reported in Figure 5.14 that compares the SNR performance of companded and conventional DCO-OFDM schemes for different bias currents and a 64-QAM constellation. As can be seen in this figure, companded DCO-OFDM offers a gain up to 4.75dB in SNR. This gain is reached by simply employing a companding transformation with a very moderate complexity and with no need to increase neither the DC bias nor the circuit complexity, as is the case with hybrid techniques and pilot-assisted modulation.

# General conclusion

To meet the huge demand of bandwidth-hungry broadband applications, networks have to be upgraded to support higher data rates. Several technologies with more or less efficiency are currently competing for future optical systems. Among the candidate technologies, optical OFDM appears to be a promising solution for future optical communications. Within this context, we have shown in the first chapter that direct detection optical OFDM provides a cost-effective solution for short range optical systems such as NGPON2 access networks and 100Gb/s local area networks. Indeed, optical OFDM has been shown to provide the highest data rate over the longest reach. However, we have highlighted that the power consumption and cost of optical OFDM are still the major obstacles to its large scale deployments. We have concluded that these issues have to be addressed to fulfill service providers requirements in terms of cost and potential revenue. On the other hand, we have shown that cost effective laser sources such as VCSELS, must be used in IM/DD systems to lower the overall system cost. Finally, we have shown that reliable and accurate modeling of the electrical to optical interface is required to correctly simulate and evaluate the light source impact on DMT modulations.

An overview of unipolar OFDM techniques with a detailed mathematical description of each technique was provided in Chapter 2. Indeed, three basic unipolar OFDM schemes, namely DCO-OFDM, ACO-OFDM and PAM-DMT were presented and compared to each other based on different metrics (i.e. BER, clipping noise and optical power efficiency). This chapter aimed at developing a deeper understanding of optical OFDM basics, in order to arise the issues concerned with the high cost and power consumption of unipolar OFDM systems.

Two main conclusions have been made from the analysis provided in the first and second chapters. First, all DFT-based unipolar techniques deal with the Hermitian

symmetry property to generate real OFDM signals, increasing the complexity of DMT-based IM/DD systems. Second, hybrid techniques provide high spectral and power efficiencies at the expense of circuit complexity, thus further increasing the system cost.

In Chapter 3, we have first shown that the Hermitian symmetry constraint results in doubled FFT/IFFT sizes which considerably increases the power consumption and cost of DMT systems. We have proposed a new Hermitian symmetry free OFDM technique that permits to overcome the Hermitian symmetry drawbacks. The proposed technique has been shown to achieve a 50% saving in hardware complexity in both the transmitter and the receiver, thus significantly reducing the power consumption and the occupied chip area. To further improve system performance, we proposed a new technique combining HSF-OFDM and Flip-OFDM. This technique has been shown to divide by four the FFT/IFFT sizes required to generate and demodulate ACO-OFDM signals, thus offering 75% savings in hardware complexity as compared to the conventional ACO-OFDM modulation.

The optical power is one of the main constraints of optical systems and a leading parameter for DMT-based systems power consumption. Several techniques have been proposed to improve the spectral and power efficiencies of IM/DD systems. An overview of power efficient DMT techniques was first provided in Chapter 4. We have shown that the reached improvement comes at the expense of an increased system complexity due to the use of additional FFT/IFFT blocks. To overcome this issue, we have proposed a new power efficient DCO-OFDM scheme based on the use of an asymmetric linear companding to reduce the DC bias required to guarantee an acceptable clipping noise penalty. The proposed companded DCO-OFDM has been shown to provide a gain up to  $4dB$  in optical power over conventional DMT techniques.

In chapters from 1 to 4, theoretical analysis of DMT modulations and algorithms permitting to improve the performance of IM/DD systems were presented. An experimental investigation of these topics was provided in Chapter 5. We first investigated the impact of VCSELs on DMT modulations. We derived a new model for the VCSEL static characteristic based on the use of RAPP model inspired from radio communications. Using the proposed model, we demonstrated that the non-linear VCSEL modeling based on the static characteristic is not suitable for DMT modulations. We then proposed to use the quasi-static characteristic to model the VCSEL behavior

and simulate its impact on DMT modulations. The simulation results based on the quasi-static characteristic have been shown to perfectly fit EVM measurements. Experimental results of asymmetrically companded DCO-OFDM were provided in the last part of Chapter 5. The measurements have shown that companded DCO-OFDM offers a gain up to  $4.75\text{dB}$  in SNR over conventional DCO-OFDM.

Several computer simulations and experimental results proving the feasibility and evaluating the performance of the proposed techniques and models are provided in this manuscript. Nevertheless, further analytical and experimental investigations should be performed to complete the work presented in this thesis.

- *Time multiplexer/demultiplexer architectures:* Digital models of HSF-OFDM and HSF-Flip-OFDM, namely the block permitting to extract and juxtapose the real and imaginary parts in the time-domain are provided in this thesis. These models allowed to validate and compare the proposed schemes with conventional optical OFDM techniques. To enable a real-time implementation of HSF-OFDM and HSF-Flip-OFDM algorithms, the architecture of the time-multiplexer (time-demultiplexer) permitting the complex to real (real to complex) conversion should be designed.
- *Real-time validation and silicon implementation of HSF-OFDM:* The simulation results presented in this thesis provide an estimation of HSF-OFDM and HSF-Flip-OFDM performance in terms of BER and PAPR in an AWGN channel. However, no concrete estimate of circuit complexity and power consumption is obtained. To experimentally validate the proposed algorithms under more realistic conditions, FPGA-based real-time implementation is required. Once the FPGA-based prototyping is complete and verified, an ASIC-based design and implementation of the proposed algorithms are envisioned in order to accurately evaluate the gain in complexity and power consumption.
- *Compatibility with photonic integration:* All theoretical and experimental results provided in this thesis are based on the use of discrete electrical and optical components. As mentioned in Chapter 1, the silicon photonic integration is widely emerging as a promising solution for enhancing performance of optical communications. The performance of the proposed algorithms and models when photonic and electronic components are integrated in the same wafer, should be studied.



## Appendix A

# The AWG impact on the DMT signal

### A.1 AWG without interleave function

The digital signal input to the AWG is first converted to an analog signal using the AWG's converter. To this end, the discrete samples injected to the AWG are first converted to a sequence of impulses by multiplying  $x(n)$  with a train of unit impulses as follows,

$$x_s(t) = \sum_{n=-\infty}^{\infty} x(nT_s)\delta(t - nT_s) \quad (\text{A.1})$$

where  $x(nT_s)$  is the discrete time signal,  $T_s$  is the sampling interval and  $\delta(t)$  is the Dirac delta function. A zero-order hold conversion is next used to transform the resulting succession of impulses to a staircase function. The ZOH conversion consists in holding each sample value constant until the next sample arrives. Thus, the zero order hold impulse response can be expressed as,

$$h(t) = \begin{cases} 1, & \text{if } 0 \leq t \leq T_s \\ 0, & \text{otherwise} \end{cases} \quad (\text{A.2})$$

The resulting staircase function at the ZOH output can be written as,

$$y(t) = \sum_{n=-\infty}^{\infty} x(n)h(t - nT_s) \quad (\text{A.3})$$

Figure A.1 illustrates the zero-order hold process that permits to produce the staircase-function signal from the input digital samples.

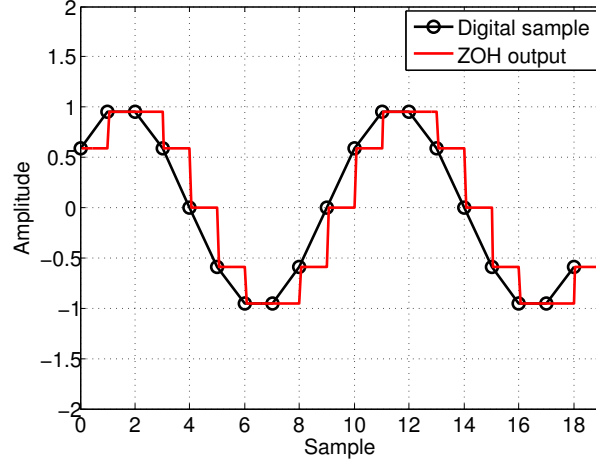


FIGURE A.1: Illustration of the zero-order hold conversion

In the frequency domain, the ZOH conversion can be regarded as the multiplication of the input spectrum by the ZOH transfer function,

$$\begin{aligned}
 Y(f) &= \frac{1}{T_s} \sum_{n=-\infty}^{\infty} X\left(f - \frac{n}{T_s}\right) H(f) \\
 &= \sum_{n=-\infty}^{\infty} X\left(f - \frac{n}{T_s}\right) \frac{\sin(\omega T_s/2)}{\omega T_s/2} e^{-j\omega T_s/2}
 \end{aligned} \tag{A.4}$$

where  $X(f)$  is the input spectrum and  $H(f)$  is the ZOH transfer function. It can be concluded from (A.4), that the input spectrum is first replicated over the entire frequency axis with period  $f_s = 1/T_s$ , due to the sampling process. The entire replicated spectrum is next filtered by the zero-order hold filter, thus introducing some distortion of the desirable spectrum, i.e. the portion of the signal spectrum that lies within the Nyquist interval  $[-f_s/2, f_s/2]$ . Indeed, both the fundamental signal spectrum and its images are attenuated by the ZOH transfer function. The attenuation introduced by the zero-order hold is referred to as sinc distortion. Figure A.2 illustrates the ZOH impact on the DMT signal spectrum sampled at a frequency sampling of 10GHz.

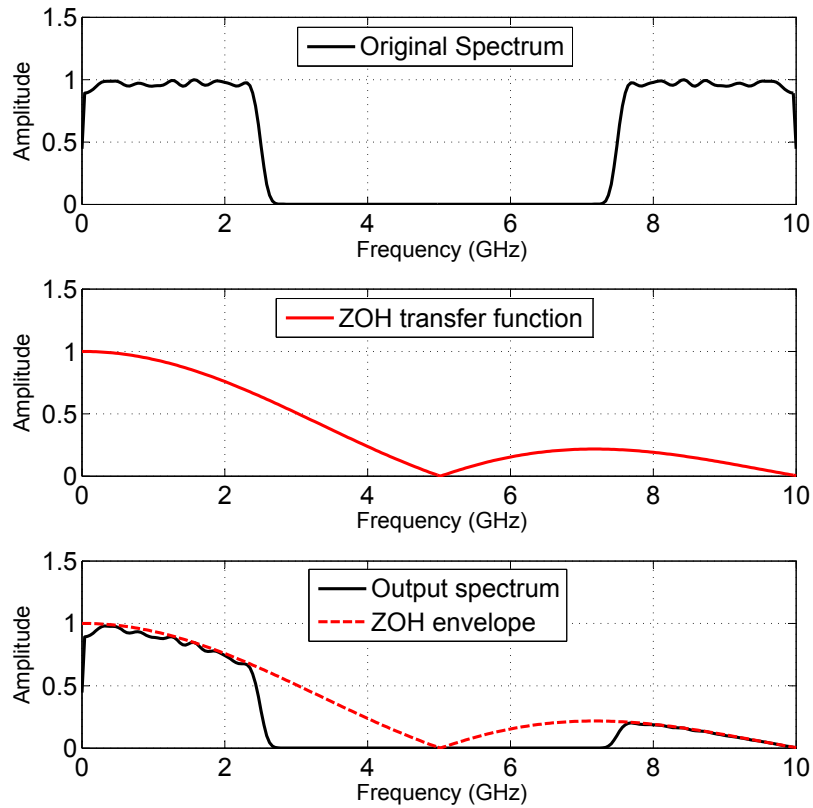


FIGURE A.2: The ZOH impact on the DMT signal spectrum

## A.2 AWG with interleave function

As aforementioned, the TEKTRONIX 7122B AWG provides a sample rate up to 24GS/s thanks to the “interleave” function. Indeed, the AWG has two DACs, providing each a sample rate up to 12GS/s. To reach a data rate higher than 12GS/s, the input digital signal is fed across to the two DACs, both clocked at the same speed but with two different clock phases. The outputs of the two digital to analog converters are next added together, thereby enabling an effective sample rate twice the sample rate of each DAC. This is known as time-interleaved architecture which is commonly used to built data converters with high date rate [98]. The model of a time-interleaved DAC (TIDAC) is shown Figure A.3.

As can be seen in Figure A.3, the time interleaved DAC architecture consists of two paths, providing each a sample rate up to 12GS/s. First, two sampling pulses are used to sample the input digital signal with a sampling period of  $T_s$ .  $p_1(t)$  has a 180 degrees (i.e.  $T_s/2$ ) delay than  $p_2(t)$  to deliver interleaved digital data samples.



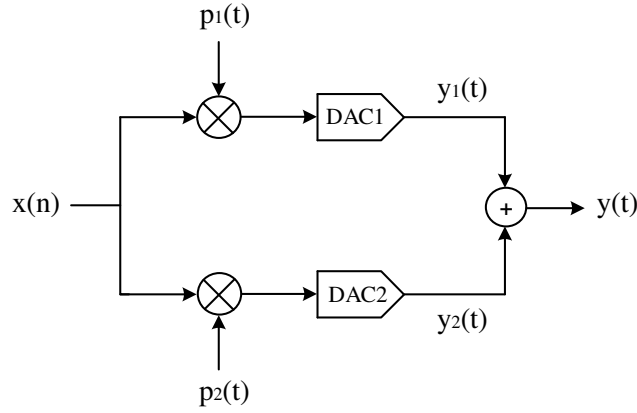


FIGURE A.3: The model of a time-interleaved DAC structure using two digital to analog converters

The two sampling pulses can be respectively expressed as,

$$\begin{aligned}
 p_1(t) &= \sum_{n=-\infty}^{\infty} \delta(t - nT_s) \\
 p_2(t) &= \sum_{n=-\infty}^{\infty} \delta\left(t - nT_s - \frac{T_s}{2}\right)
 \end{aligned} \tag{A.5}$$

The outputs of the two DACs are respectively given by

$$\begin{aligned}
 y_1(t) &= \sum_{n=-\infty}^{\infty} x(n)\delta(t - nT_s) * h(t) \\
 y_2(t) &= \sum_{n=-\infty}^{\infty} x(n)\delta\left(t - nT_s - \frac{T_s}{2}\right) * h(t)
 \end{aligned} \tag{A.6}$$

where  $*$  denotes the convolution operator and  $h(t)$  is the ZOH impulse response. Finally, the TIDAC output can be expressed as,

$$y(t) = \sum_{n=-\infty}^{\infty} \left[ x(n)h(t - nT_s) + x(n)h\left(t - nT_s - \frac{T_s}{2}\right) \right] \tag{A.7}$$

It can be noted from (A.7) that the continuous time signal at the time-interleaved DAC is the sum of two interleaved staircase functions, both with a sampling period of  $T_s$ . The use of time-interleaving concept to achieve high rate sample, using sub-DACs with low sample rate is illustrated in Figure A.4. As can be seen in Figure A.4, the outputs of the sub-DACs are staircase functions, each with a period of  $T_s$ , whereas the TIDAC output is a staircase function with a period of  $T_s/2 = 2f_s$ . In the frequency domain, the

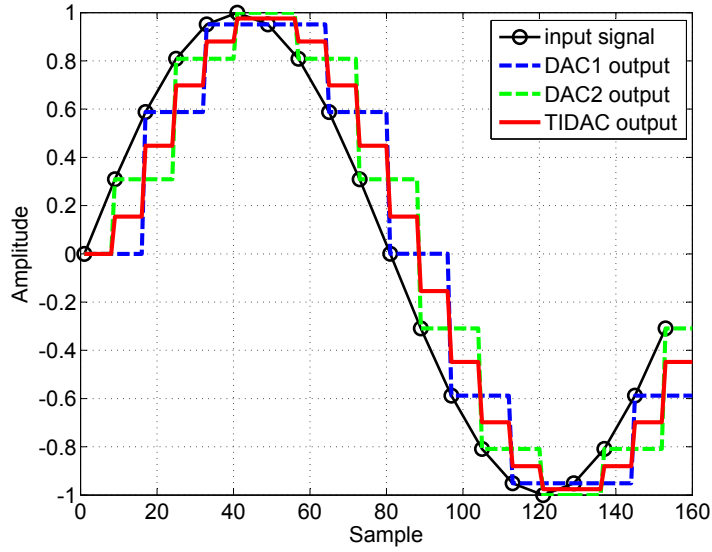


FIGURE A.4: Time domain waveforms of a time-interleaved DAC with two parallel paths

outputs of the two sub-DACs can be respectively expressed as,

$$\begin{aligned}
 Y_1(f) &= \frac{1}{T_s} \sum_{n=-\infty}^{\infty} X\left(f - \frac{n}{T_s}\right) H(f) \\
 Y_2(f) &= \frac{1}{T_s} \sum_{n=-\infty}^{\infty} X\left(f - \frac{n}{T_s}\right) e^{-jn\pi} H(f)
 \end{aligned} \tag{A.8}$$

where  $H(f)$  is the ZOH frequency response and  $X(f)$  is the FFT of the input digital symbols. The output of the time-interleaved DAC can be then written as,

$$Y(f) = \frac{1}{T_s} \sum_{n=-\infty}^{\infty} X\left(f - \frac{n}{T_s}\right) [1 + e^{-jn\pi}] H(f) \tag{A.9}$$

Considering the odd and even cases for  $n$ , the output of the time-interleaved DAC can be formulated as follows,

$$Y(f) = \begin{cases} \frac{2}{T_s} \sum_{n=-\infty}^{\infty} X\left(f - \frac{n}{T_s}\right) H(f), & \text{if } n = 2k, \quad k \in \mathbb{Z} \\ 0, & \text{if } n \neq 2k, \quad k \in \mathbb{Z} \end{cases} \tag{A.10}$$

The output of each sub-DAC consists of the desired signal and replicated images at frequencies  $nF_s$ . The replicated images of the two sub-DACs have the same phase for  $n$  odd and opposite phases for  $n$  even. By summing the two sub-DACs outputs (A.10),

even components that have opposite phases are canceled. As a result, the TIDAC output spectrum contains replicated images that occur at  $2nF_s$  instead  $nF_s$ , thus providing twice the sampling frequency of each sub-DAC. The output spectrum of a time-interleaved DAC with two parallel paths is depicted in Figure A.4. The input digital signal is an OFDM signal with 512 subcarriers and 4-QAM constellation. The time interleaved DAC provides a sampling frequency of 20GHz using two sub-DACs delivering each a sampling frequency of 10GHz.

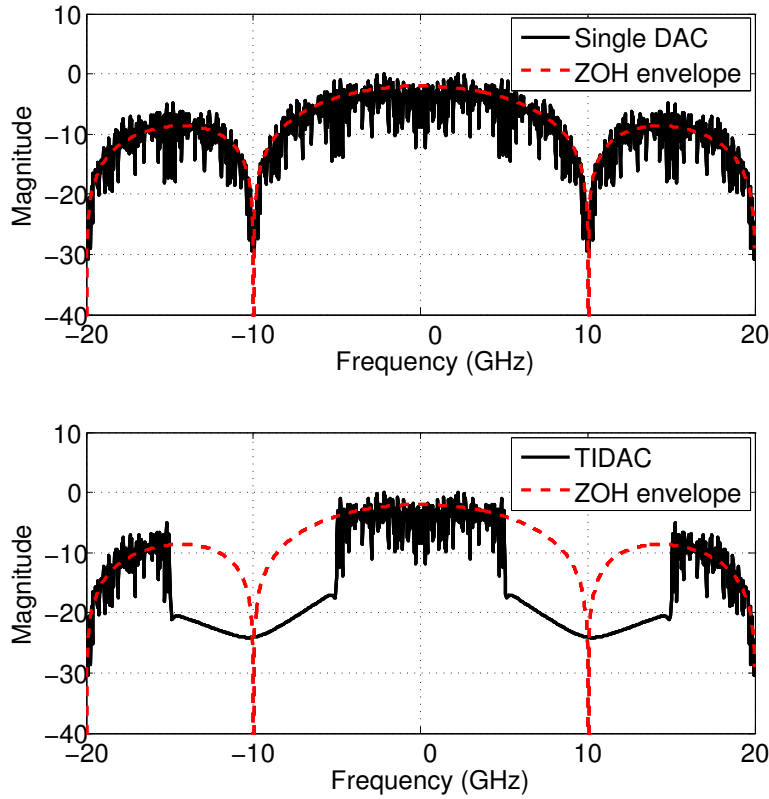


FIGURE A.5: Spectra of a time-interleaved DAC with two parallel paths

Note that, in the two cases, the spectrum waveforms have a sinc roll-off up to 10GHz. Indeed, if a faster DAC is used to deliver a sampling frequency of 20GHz without time-interleaving, the spectrum would have a sinc roll-off up to 20GHz. On the other hand, being the sum of two sub-DACs outputs, each with a sinc roll-off up to 10GHz, the spectrum of a time-interleaved DAC exhibits a sinc roll-off up to 10GHz. Finally, the frequency response of the time-interleaved DAC can be expressed as,

$$Y(f) = \begin{cases} \frac{2}{T_s} \sum_{n=-\infty}^{\infty} X\left(f - \frac{n}{T_s}\right) \frac{\sin(\omega T_s/2)}{\omega T_s/2} e^{-j\omega T_s/2}, & \text{if } n = 2k, \quad k \in \mathbb{Z} \\ 0, & \text{if } n \neq 2k, \quad k \in \mathbb{Z} \end{cases} \quad (\text{A.11})$$

The study presented above was conducted to analyze and evaluate the impact of the AWG “interleave” function on the DMT signal. However, time-interleaved DACs are commonly used to meet the high data rate requirements of broadband applications. Thus, the analysis conducted above can be useful to study the impact of real TI-DACs on DMT modulation performance.



# List of Publications

- **A novel FFT/IFFT size efficient technique to generate real time optical OFDM signals compatible with IM/DD systems.** Fatima Barrami, Yannis Le Guennec, Emil Novakov, Jean-Marc Duchamp and Pierre Busson. In *IEEE European Microwave Conference (EuMC 2013)*, pp. 1247-1250, Nuremberg, Germany.
- **An Optical Power Efficient Asymmetrically Companded DCO-OFDM for IM/DD Systems.** Fatima Barrami, Yannis Le Guennec, Emil Novakov and Pierre Busson. In *IEEE Wireless and Optical Communication Conference (WOCC 2014)*, pp. 1-6, Newark, USA.
- **Impact of VCSEL Nonlinearity on Discrete MultiTone Modulation: Quasi-static Approach.** Fatima Barrami, Yannis Le Guennec, Emil Novakov and Pierre Busson. In *IEEE International Conference on Telecommunications (ICT 2014)*, pp. 1-6, Lisbon, Portugal.
- **Comparaison des modulations DCO-OFDM et ACO-OFDM dans un canal optique réel.** Fatima Barrami, Yannis Le Guennec, Emil Novakov, Jean-Marc Duchamp and Pierre Busson. In *Journées Nationales Microondes (JNM2013)*, Paris, France.
- **Real time OFDM transmission system.** Fatima Barrami. *Patent*.
- Other scientific publications are ongoing.



# Systemes OFDM optiques à détection directe à complexité réduite pour les communications à haut débit

## Introduction

La demande croissante en applications à large bande passante a induit à l'explosion de la demande d'accès au très haut débit. Pour faire face à cette demande, les réseaux de prochaine génération (Next generation networks NGN) devront supporter des débits supérieurs à 40Gb/s. Les technologies basées sur les câbles de cuivre ayant atteint un point de saturation en débit et en distance de transmission, leur utilisation est limitée aux courtes distances (une dizaine de mètres). Pour des distances plus longues, la fibre a émergé comme une alternative efficace en débit et en coût aux technologies traditionnelles basées sur le cuivre.

Dans les communications optiques à courte distance telles que les cœurs de réseau dans les réseaux locaux, une des contraintes principales est le coût. Ainsi, les systèmes IM/DD (Intensity Modulated Direct Detection) sont largement employés pour réduire le coût total du réseau. Dans les systèmes IM/DD, le débit total est limité par la bande passante des convertisseurs électrique-optique et optique-électrique. Lorsqu'une modulation basique telle que l'OOK (On-Off-Keying) est employée pour moduler la porteuse optique, le débit total atteint est limité à quelques dizaine de gigabits par seconde. Pour augmenter le débit par longueur d'onde, une approche est d'employer des



modulations sophistiquées à grande efficacité spectrale telle que l'OFDM (Orthogonal Frequency-Division Multiplexing). En effet, l'OFDM a été adaptée dans plusieurs standards de communication sans fil grâce à ses nombreux avantages à savoir : l'immunité aux interférences entre symboles, une égalisation du canal simple et robuste et une implémentation digitale simplifiée due à l'utilisation des transformées de Fourier.

Les signaux OFDM étant complexes et bipolaires, ils ne peuvent pas être utilisés dans les systèmes optiques IM/DD, où l'intensité de l'émetteur optique est directement modulée par le signal RF. Afin de générer des signaux OFDM réels, une symétrie hermitienne est imposée aux données fréquentielles à l'entrée de l'IFFT (Inverse Fast Fourier Transform). Plusieurs techniques compatibles avec les systèmes IM/DD basées sur la symétrie hermitienne ont été proposées dans la littérature. Dans la DCO-ODFM (DC-biased Optical OFDM) [14]-[16], un offset est ajouté au signal réel et les résidus négatifs sont forcés à zéro afin d'obtenir un signal unipolaire. Si l'offset ajouté est faible, le forçage à zéro résulte en un bruit significatif. Dans l'ACO-OFDM (Asymmetrically Clipped Optical OFDM) [15]-[18], seules les sous porteuses impaires sont modulées. Ainsi, le bruit résultant du forçage à zéro, n'affecte que les porteuses paires. Néanmoins, seules les sous porteuses impaires étant employées pour transmettre de l'information utile, l'ACO-OFDM est spectralement inefficace.

Bien qu'elles permettent d'atteindre un débit très élevée, notamment dans le cas des réseaux optiques à courte distance, les modulations OFDM optiques souffrent de deux inconvénients majeurs : la consommation en puissance et le coût. Pour que la modulation OFDM puisse être adoptée dans les réseaux de prochaine génération, les problèmes liés au coût et à la consommation doivent être résolus. Le travail présenté dans cette thèse s'est focalisé sur ces deux thématiques via les contributions suivantes :

1. Réduction de la complexité du modulateur/démodulateur OFDM : toutes les techniques basées sur la transformée de Fourier, ont recours à imposer une symétrie Hermitienne aux données fréquentielles afin de générer un signal OFDM réel. La symétrie Hermitienne a pour inconvénient d'augmenter le coût et la consommation en puissance du système. Une nouvelle technique permettant de générer des signaux OFDM réels sans avoir à imposer la symétrie Hermitienne aux données fréquentielles a été proposée dans ce travail de thèse. Les performances de cette

technique en termes de coût et de consommation en puissance sont explorées et comparées à l'état de l'art.

2. Amélioration de l'efficacité en puissance optique : La puissance optique est une contrainte principale dans les systèmes optiques. Plusieurs travaux visant à réduire la puissance optique des systèmes IM/DD ont été proposés dans la littérature. Les systèmes dits hybrides permettent d'avoir une meilleure efficacité en puissance optique au détriment de la complexité du circuit et par la suite le coût du système. Pour remédier à ce problème, une nouvelle technique permettant de réduire la puissance optique de la modulation OFDM a été proposée dans cette thèse. Cette technique emploie un companding linéaire asymétrique pour réduire l'offset de la modulation DCO-OFDM. Le gain en puissance optique apporté par cette technique est évalué et comparé à l'état de l'art.
3. Modélisation fiable de la caractéristique du VCSEL : Les VCSEL présentent une solution à bas coût pour les communications optique à courte distance, notamment les systèmes IM/DD. Néanmoins, aucune modélisation prenant en compte les propriétés particulières du VCSEL n'a été proposée. Un nouveau modèle basé sur la caractéristique quasi-statique a été développé, permettant une évaluation fiable de l'impact du VCSEL sur les performances des modulations OFDM optiques.

## 5.3 Fondamentaux de l'OFDM optique

### 5.3.1 Système IM/DD

La FIGURE 5.6 représente le schéma de principe d'un système IM/DD basé sur la modulation OFDM. Dans ce système, un modulateur binaire/M-aire convertit la suite binaire en une suite de symboles à  $n$  bits. Les modulations QAM (Quadrature Amplitude Modulation) et PAM (Pulse Amplitude Modulation) sont souvent utilisées. Pour que

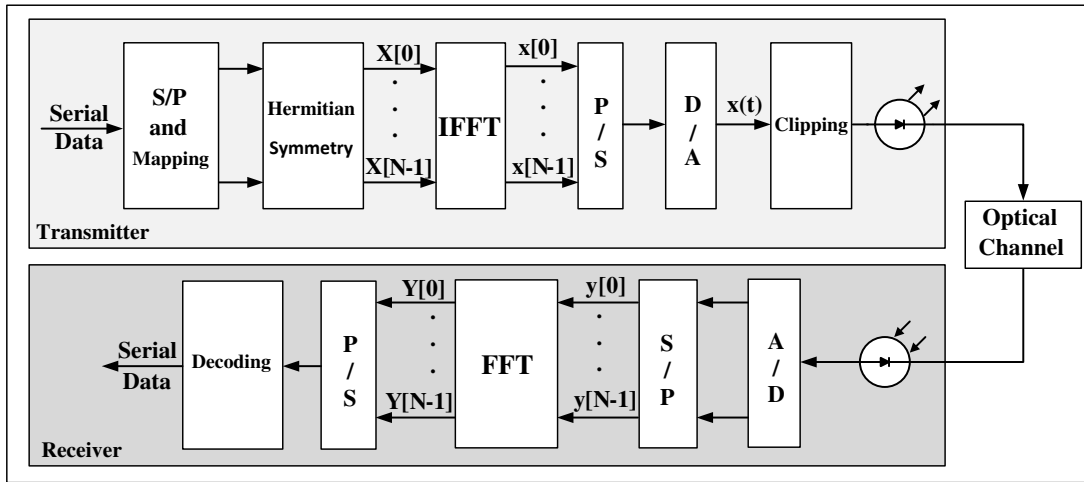


FIGURE 5.6: Schéma bloc d'un système IM/DD basé sur la modulation OFDM

le signal OFDM soit réel, les symboles fréquentiels en entrée de l'IFFT doivent être symétriquement hermitiens :

$$X(N - k) = X^*(k), \quad k = 1, 2, \dots, \frac{N}{2} - 1 \quad (5.12)$$

où  $N$  est la taille de l'IFFT et  $*$  représente le complexe conjugué. Pour éviter toute modification de la composante DC et l'apparition des résidus complexes, une contrainte supplémentaire est imposée :

$$X(0) = X\left(\frac{N}{2}\right) = 0 \quad (5.13)$$

Le signal temporel discret en sortie de l'IFFT a donc pour expression :

$$x(n) = \frac{1}{N} \sum_{k=0}^{N-1} X(k) \exp\left(j2\pi \frac{kn}{N}\right) \quad (5.14)$$

En sortie du convertisseur numérique analogique (D/A), les valeurs négatives du signal sont forcées à 0, on parle de «clipping à zéro». L'amplitude du signal unipolaire, contenant uniquement des valeurs positives, peut donc être utilisée pour moduler l'intensité de l'émetteur optique (LED, Laser...). En réception, une photodiode détecte le signal optique et le convertit en un signal électrique. En sortie du convertisseur analogique numérique (A/D), le signal temporel discret est démodulé à l'aide d'une FFT (Fast Fourier Transform) et la suite binaire émise est finalement restituée à l'aide d'une détection à maximum de vraisemblance. Pour réduire le bruit de clipping, deux techniques sont couramment utilisées : la DCO-OFDM et l'ACO-OFDM.

### 5.3.2 DCO-OFDM

Dans la DCO-OFDM [14]-[16], un offset  $K_b$  est ajouté au signal. La valeur de l'offset permettant d'obtenir un signal positif est égale à la valeur absolue du minimum du signal bipolaire. Pour  $N \geq 64$ , l'amplitude du signal  $x(n)$  peut être approximée par une distribution gaussienne centrée. Ainsi, pour éviter des offsets excessifs, la valeur de  $K_b$  est exprimée en fonction de la moyenne quadratique du signal temporel continu,  $x(t)$ .

$$K_b = k\sigma \quad (5.15)$$

où  $k$  est le facteur de clipping et  $\sigma^2$  est la variance de  $x(t)$ . Les résidus négatifs sont ensuite supprimés par un clipping à zéro, ce qui résulte en un bruit de clipping. Le signal écrêté à zéro peut être écrit sous la forme :

$$x_{u,DCO}(t) = x(t) + K_b + n_c(K_b), \quad (5.16)$$

où  $n_c(K_b)$  est le bruit de clipping. Ce dernier dépend de la valeur de l'offset ajouté. Si  $K_b$  est assez grand, alors le nombre de pics négatifs résidus après l'ajout de l'offset est faible et le bruit de clipping est négligeable. Si par contre la valeur de  $K_b$  est faible, le bruit de clipping devient très significatif et donc déterminant vis-à-vis des performances de la DCO-OFDM en termes de BER (Bit Error rate). Le bruit de clipping dépend également de la constellation utilisée. En effet, la dynamique du signal OFDM est d'autant plus large que la taille de la constellation est grande. Par conséquent, les résidus négatifs et par la suite le bruit de clipping croissent avec la taille de la constellation utilisée. Dans

la DCO-OFDM,  $N/2 - 1$  données indépendantes sur  $N$  points IFFT sont transmises dû à la symétrie hermitienne. En outre, le signal RF modulant directement l'intensité de l'émetteur optique, la puissance optique est une fonction linéaire de l'amplitude du signal. Ainsi, l'ajout d'un offset élevé dégrade considérablement l'efficacité en puissance optique de la technique DCO-OFDM.

### 5.3.3 ACO-OFDM

Dans l'ACO-OFDM [15]-[18], seules les porteuses impaires sont modulées :

$$X(N - k) = \begin{cases} X^*(k), & k \text{ impair} \\ 0, & k \text{ pair} \end{cases} \quad (5.17)$$

Comme il a été montré dans [17], le signal obtenu à partir de (5.17) est antisymétrique par rapport à  $N/2$ ,

$$\begin{aligned} x\left(n + \frac{N}{2}\right) &= -\frac{1}{N} \sum_{k=0}^{N-1} X(k) \exp\left(j2\pi \frac{kn}{N}\right) \\ &= -x(n) \end{aligned} \quad (5.18)$$

Cela signifie que pour tout symbole négatif forcé à zéro, un symbole positif de la même valeur absolue est conservé dans le signal transmis. En conséquence, le clipping de la partie négative n'entraînera aucune perte d'information et les données binaires transmises pourront être intégralement restituées au récepteur. L'excursion négative étant entièrement supprimée avant la transmission, l'expression du signal continu ACO-OFDM est donnée par,

$$x_{u,ACO}(n) = \begin{cases} x(n), & \text{si } x(n) > 0 \\ 0, & \text{si } x(n) \leq 0 \end{cases} \quad (5.19)$$

La FIGURE 5.7 représente la partie réelle d'une suite de symboles fréquentiels 16-QAM restituée à partir du signal unipolaire donné par (5.19). Si seules les porteuses impaires sont modulées, tout le bruit de clipping est contenu dans les porteuses paires et aucun bruit n'est présent sur les porteuses impaires portant toute l'information. Néanmoins,

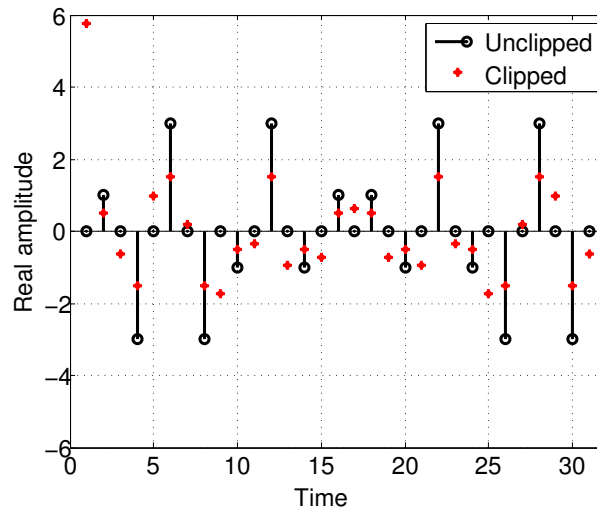


FIGURE 5.7: Symboles fréquentiels ACO-OFDM

l'amplitude des données fréquentielles est divisée par deux à cause du clipping.

$$X_c(k) = \frac{X(k)}{2}, k \text{ impair} \quad (5.20)$$

où  $X_c(k)$  est le symbole ACO-OFDM transmis à la fréquence discrète  $k$ . Dans l'ACO-OFDM, seule la partie positive du signal temporel est transmise et aucun offset n'est ajouté au signal. En outre, l'amplitude du signal ACO-OFDM est deux fois moins grande que celle d'un signal OFDM bipolaire. En conséquence, la technique ACO-OFDM permet d'avoir une bonne efficacité en puissance optique. En contrepartie, sur  $N$  points IFFT, seules  $N/4$  sous-porteuses portent de l'information, vu que seules les porteuses impaires sont modulées.

### 5.3.4 Comparaison des deux techniques

#### 5.3.4.1 BER

La FIGURE 5.8 représente les courbes de BER en fonction de  $E_{b(elec)}/N_0$  des deux techniques DCO-OFDM et ACO-OFDM dans un canal AWGN. Pour des faibles constellations, la dynamique du signal DCO-OFDM n'est pas très large et le bruit de clipping est négligeable. Le rapport signal à bruit SNR (Signal to Noise Ratio) requis pour transmettre le signal DCO-OFDM est donc égal à celui d'un signal bipolaire plus l'offset ajouté (en dB). Pour des constellations plus larges (i.e. 64-QAM), et des faibles offsets (i.e. 7dB), la dynamique du signal devient plus large et le bruit de clipping est

dominant. En conséquence, les courbes de BER en fonction du rapport énergie binaire à la densité spectrale du bruit,  $E_b/N_0$ , stagnent. Dans l'ACO-OFDM, la moitié de la

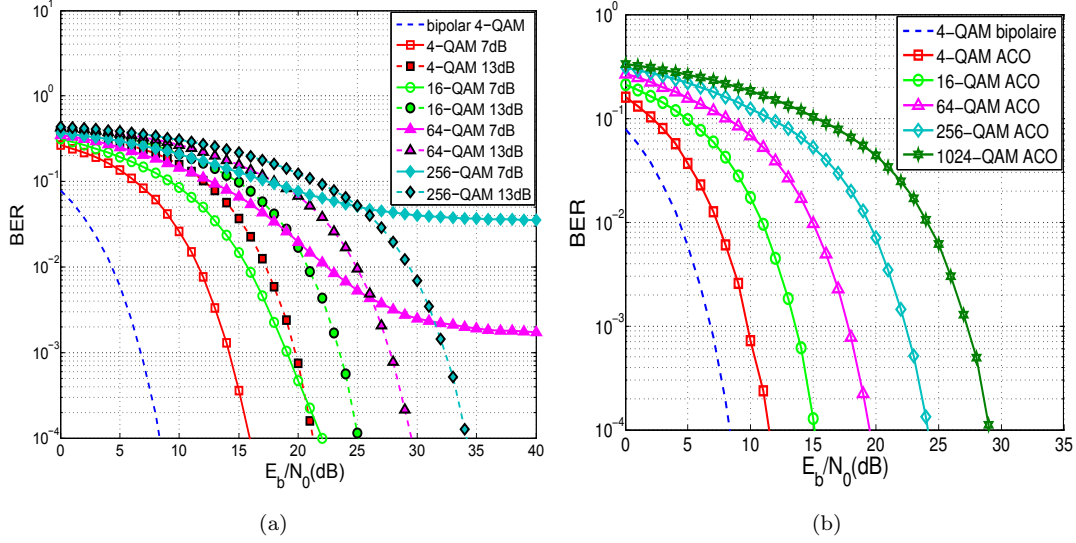


FIGURE 5.8: BER en fonction de  $E_{b(elec)}/N_0$  dans un canal AWGN pour différentes constellations (a) DCO-OFDM pour des offsets de 7dB et 13dB (b) ACO-OFDM

puissance électrique est utilisée par les porteuses paires ne portant aucune information. Ainsi, quelque soit la constellation utilisée, le signal ACO-OFDM nécessite 3dB de plus de puissance qu'un signal OFDM bipolaire.

### 5.3.4.2 Puissance optique

Le BER en fonction de  $E_{b(elec)}/N_0$  permet de comparer théoriquement des différents types de modulation. Néanmoins, cette métrique ne fournit aucune indication sur la puissance optique, qui est une contrainte principale dans les systèmes optiques. Pour ce faire, une approche est d'utiliser le rapport énergie binaire optique à la densité spectrale du bruit,  $E_{b(opt)}/N_0$ . Pour une puissance optique normalisée, le facteur  $E_b/N_0$  optique est donné par,

$$\frac{E_{b(opt)}}{N_0} = \frac{E^2\{x\}}{E\{x^2\}} \frac{E_{b(elec)}}{N_0}, \quad (5.21)$$

La FIGURE 5.9 compare les efficacités en puissance optique des deux modulations DCO-OFDM et ACO-OFDM en fonction du rapport débit binaire à bande passante normalisée,  $R_b/BW$ . Les résultats présentés correspondent à un  $BER = 10^{-3}$  et une puissance optique normalisée.

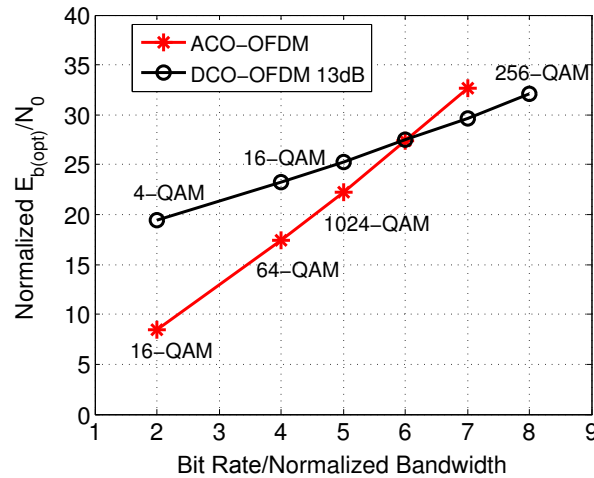


FIGURE 5.9:  $E_{b(opt)}/N_0$  normalisé en fonction du rapport débit binaire à bande passante normalisée pour  $BER = 10^{-3}$

A constellation égale, la DCO-OFDM permet de transmettre deux fois le débit binaire de l'ACO-OFDM. Ainsi, pour faire une comparaison judicieuse à efficacité spectrale égale,  $M$ -QAM DCO-OFDM doit être comparé à  $M^2$ -QAM ACO-OFDM. De ce fait, les efficacités en puissance optique sont comparées pour différents rapports débit binaire à bande passante normalisée. Comme le montre la FIGURE 5.9, pour un rapport  $R_b/BW \leq 6$ , la modulation ACO-OFDM requiert une puissance optique moins élevée, étant donné que seule la partie positive du signal temporel est transmise. Pour un rapport  $R_b/BW > 6$ , la DCO-OFDM devient plus efficace en puissance que l'ACO-OFDM, dû au fait que l'ACO-OFDM requiert  $M^2$ -QAM pour transmettre la même quantité d'information qu'une modulation  $M$ -QAM DCO-OFDM.

Tous les résultats de simulation présentés dans cette section sont en parfaite cohérence avec l'état de l'art. Ce qui permettra de comparer judicieusement les nouvelles techniques présentées dans ce travail avec l'état de l'art.

## 5.4 L'OFDM optique sans symétrie hermitienne

### 5.4.1 La symétrie hermitienne dans les systèmes OFDM optiques

Pour générer un signal OFDM réel, une approche communément employée est d'imposer la symétrie hermitienne aux données fréquentielles à l'entrée de l'IFFT. Cette technique est aussi connue sous le nom de DMT (Discrete Multitone). La symétrie hermitienne a



pour conséquence d'augmenter d'un facteur de 2 la taille de la transformée de Fourier nécessaire à générer le signal OFDM optique, ce qui impacte la consommation en puissance et la surface en silicium du système IM/DD, notamment dans le cas d'un circuit ASIC. L'impact de la taille de l'IFFT sur les circuits ASIC a été étudié dans [54]. Il a été démontré expérimentalement que l'augmentation de la taille des blocs FFT/IFFT par un facteur de 2, peut augmenter de 38% la consommation en puissance et de 40% la surface en silicium du circuit ASIC.

Comme il a été évoqué précédemment, la consommation en puissance et le coût élevés constituent deux obstacles majeurs devant l'adoption et l'industrialisation de l'OFDM optique. En effet ces deux facteurs sont fortement liés aux processeurs permettant d'effectuer les différents calculs nécessaires à la génération du signal OFDM, et par la suite au nombre d'opérations requises pour le calcul des transformées de Fourier. Le nombre d'opérations dépend de la taille de l'IFFT. En effet, augmenter la taille de l'IFFT d'un facteur de 2, peut augmenter de  $\sim 2.3$  le nombre d'opérations (additions, multiplications) nécessaires au calcul de l'IFFT.

Pour réduire la consommation en puissance et le coût des systèmes OFDM optiques, une approche est de développer de nouvelles techniques permettant de générer des signaux OFDM réels sans avoir recours à employer la symétrie hermitienne, permettant ainsi de réduire la complexité du circuit. Dans ce cadre, une technique basée sur la transformée de Hartley a été proposée dans [57]. Il a été démontré que si le vecteur de données à l'entrée de la DHT (Discrete Hartley Transform) est réel, le signal OFDM en sortie de la DHT est également réel.

La contrainte de la symétrie hermitienne n'étant pas requise, le calcul du complexe conjugué n'est pas nécessaire, ce qui permet de réduire le besoin en ressources de calcul. Néanmoins, il a été démontré dans [57], que pour générer un signal OFDM réel de  $N$  points, la transformée de Hartley nécessite plus d'opérations que la transformée de Fourier (i.e. le même nombre de multiplications et  $N - 2$  plus d'additions). Par conséquent, l'emploi de la transformée de Fourier dans les systèmes OFDM optiques, a pour effet d'augmenter la complexité du circuit, et par la suite le coût et la consommation en puissance des systèmes IM/DD basés sur la technologie ASIC.

Pour réduire la complexité liée au nombre d'opérations nécessaires à générer un signal OFDM réel, une alternative à l'ACO-OFDM appelée Flip-OFDM a été proposée dans

[58]. Cette technique consiste à moduler toutes les porteuses, contrairement à l'ACO-OFDM, pour générer un signal OFDM réel. Le signal bipolaire résultant ne présente aucune propriété d'antisymétrie. Pour le convertir en un signal unipolaire, la partie positive,  $x^+(n)$ , et l'opposé de la partie négative,  $-x^+(n)$ , sont juxtaposées dans le domaine temporel comme suit,

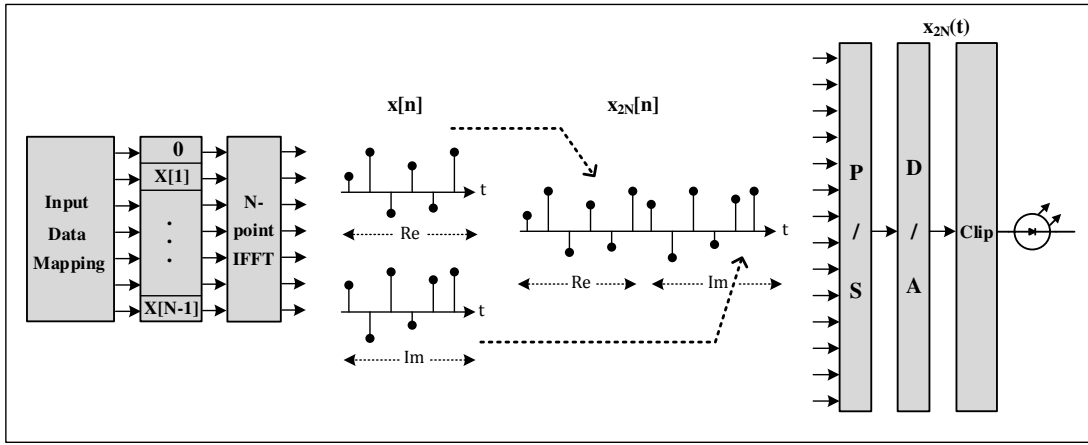
$$x_{2N,Flip}(n) = \begin{cases} x^+(n), & n = 0, \dots, N - 1 \\ -x^+(n - N), & n = N, \dots, 2N - 1 \end{cases} \quad (5.22)$$

où  $x_{2N,Flip}(n)$  est le signal unipolaire résultant. Il a été démontré dans [58] que la Flip-OFDM permet de diviser par deux les tailles des blocks IFFT/FFT nécessaire à générer/démoduler le signal ACO-OFDM, fournissant un gain de 50% en complexité. Lorsque la version optimisée de l'ACO-OFDM, prenant en compte le fait que la moitié des sous-porteuses sont mises à zéro, est considérée, la Flip-OFDM présente la même complexité que l'ACO-OFDM au niveau de l'émetteur. Par conséquent, seul le récepteur est concerné par le gain apporté par la technique Flip-OFDM. De plus, la Flip-OFDM est basée sur l'utilisation de la symétrie Hermitienne, ce qui a pour inconvénient d'augmenter considérablement la complexité du circuit. D'autre part, la Flip-OFDM ne permet de générer que des signaux ACO-OFDM, et n'est donc pas compatible avec les autres types de modulations optiques, telles que la DCO-OFDM.

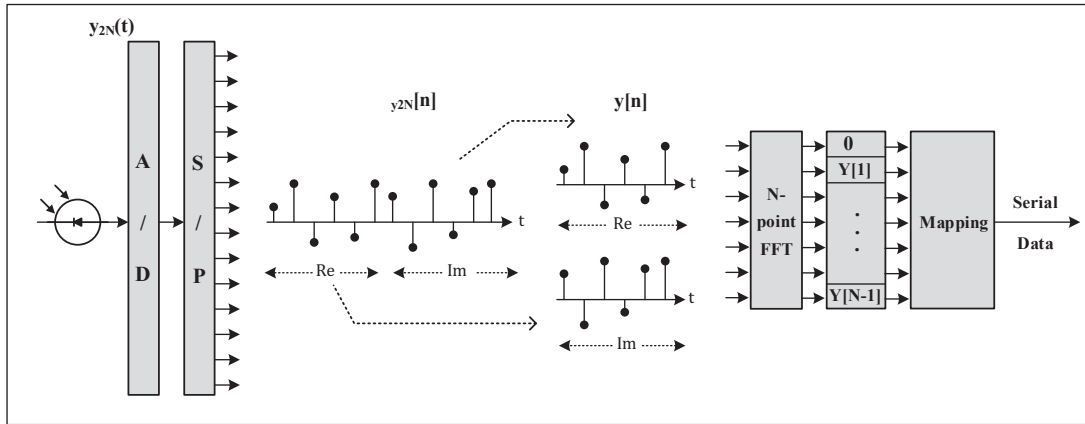
#### 5.4.2 HSF-OFDM

Pour pallier les inconvénients des techniques présentées dans la section précédente, nous avons proposé une nouvelle technique permettant de générer plusieurs types de signaux OFDM réels sans contraindre les données fréquentielles à satisfaire la propriété de la symétrie hermitienne. Nous avons appelé cette technique la HFS-OFDM (Hermitian symmetry free OFDM). La FIGURE 5.10 présente le schéma bloc de cette technique. En effet, un signal OFDM complexe est tout d'abord généré comme dans le cas de des systèmes OFDM radio. En sortie de l'IFFT, les parties réelle et imaginaire du signal complexe généré sont juxtaposées dans le temps afin de le convertir en un signal réel,  $x_{2N}(n)$ ,

$$x_{2N}(n) = \begin{cases} x_R(n), & n=0,\dots,N-1 \\ x_I(n - N), & n=N,\dots,2N-1 \end{cases} \quad (5.23)$$



(a) Émetteur



(b) Récepteur

FIGURE 5.10: Schéma bloc des émetteur et récepteur HSF-OFDM

où  $x_R(n)$  et  $x_I(n)$  présentent respectivement les parties réelle et imaginaire du signal complexe en sortie de l'IFFT. Au niveau du récepteur, les parties réelle et imaginaire sont tout d'abord extraites du signal OFDM réel reçu,  $y_{2N}(n)$ ,

$$\begin{cases} y_R(n) = y_{2N}(n), & n=0, \dots, N-1 \\ y_I(n) = y_{2N}(N+n), & n=0, \dots, N-1 \end{cases} \quad (5.24)$$

où  $y_R(n)$  et  $y_I(n)$  présentent respectivement les parties réelle et imaginaire du signal complexe,  $y(n)$ , en entrée de la transformée de Fourier. Une démodulation OFDM classique est ensuite appliquée au signal complexe afin de restituer les données fréquentielles transmises,  $Y(k)$ . Il est à remarquer que la technique proposée peut être appliquée aux différents types de modulations optiques, notamment la DCO-OFDM et l'ACO-OFDM.

La symétrie Hermitienne n'est pas requise dans la technique HSF-OFDM, ce qui permet de diviser par deux les tailles des blocs IFFT/FFT nécessaires à générer/démoduler le signal OFDM optique. De plus, le calcul du complexe conjugué n'est pas requis, permettant de réduire davantage la complexité du système.

Contrairement à la Flip-OFDM, la HSF-OFDM module uniquement les porteuses impaires pour générer un signal ACO-OFDM de  $2N$  points. Ainsi, la version optimisée de l'ACO-OFDM, prenant en compte le fait que la moitié des sous-porteuses sont mises à zéro, peut être également appliquée à la HSF-OFDM. Par conséquent, quel que soit le type du signal optique à générer, la HSF-OFDM fournit un gain de 50% en complexité au niveau de l'émetteur et du récepteur. Un exemple concret est donné au tableau 5.1 qui compare les techniques ACO-OFDM, Flip-OFDM et HSF-OFDM en termes de nombre d'opérations nécessaires à générer un signal ACO-OFDM de 256 points. L'algorithme considéré pour le calcul de la transformée de Fourier est un radix-2 [55].

	ACO-OFDM	Flip-OFDM	HSF-OFDM
Symétrie Hermitienne	Requise	Requise	Non requise
Emetteur complexité	$P^{FFT} = 1284$ $A^{FFT} = 5380$	$P^{FFT} = 1284$ $A^{FFT} = 5380$	$P^{FFT} = 516$ $A^{FFT} = 2308$
Récepteur complexité	$P^{FFT} = 1284$ $A^{FFT} = 5380$	$P^{FFT} = 516$ $A^{FFT} = 2308$	$P^{FFT} = 516$ $A^{FFT} = 2308$

TABLE 5.1: Comparaison de la complexité des techniques ACO-OFDM, Flip-OFDM et HSF-OFDM pour un signal transmis de 256 points

### 5.4.3 HSF-Flip-OFDM

Pour réduire davantage la complexité des systèmes IM/DD, nous avons proposé une nouvelle technique basée sur la combinaison de la HSF-OFDM et la Flip-OFDM pour générer des signaux ACO-OFDM avec une complexité réduite, comme l'illustre la FIGURE 5.11. Cette technique appelée HSF-Flip-OFDM consiste à moduler toutes les porteuses pour générer un signal complexe comme dans le cas des systèmes OFDM radio. Le signal complexe est ensuite converti en un signal réel à l'aide de la technique HSF-OFDM. Toutes les porteuses ayant été modulées, le signal réel résultant ne présente aucune propriété d'antisymétrie. Il est donc converti en un signal unipolaire en employant

le même algorithme que la Flip-OFDM. La technique HSF-Flip-OFDM permet de réduire de  $\sim 75\%$  la complexité des récepteurs IM/DD basés sur la modulation OFDM.

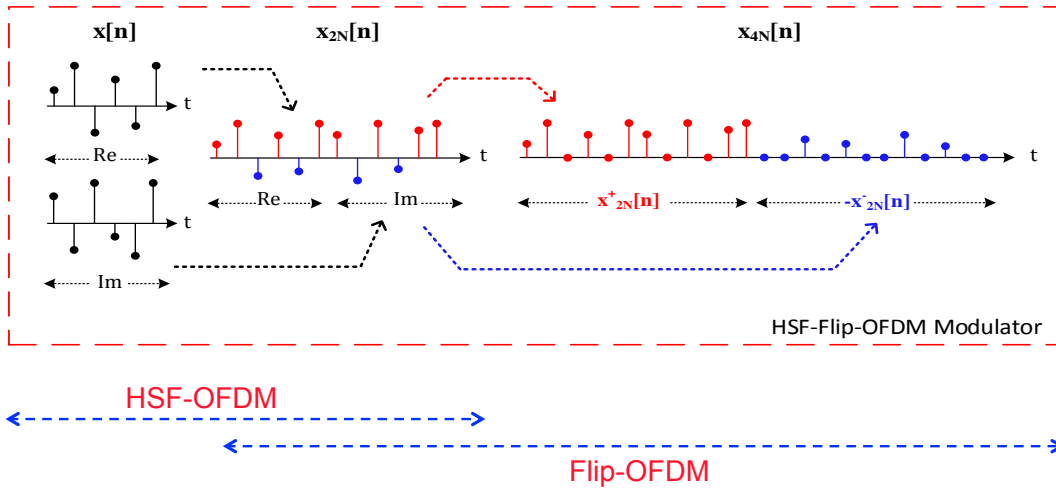


FIGURE 5.11: Illustration du principe de la technique HSF-flip-OFDM

Les techniques proposées HSF-OFDM et HSF-Flip-OFDM permettent de réduire considérablement la complexité des systèmes OFDM optiques sans dégrader leurs performances. En effet, les deux techniques proposées ont les mêmes performances en BER, PAPR et égalisation du canal que les systèmes OFDM optiques classiques.

## 5.5 DCO-OFDM asymétriquement compressée

L'efficacité en puissance des systèmes OFDM optiques a été largement évoquée dans la littérature et plusieurs approches ont été proposées dans le but de réduire la puissance optique des systèmes OFDM unipolaires. Tout d'abord, l'ACO-OFDM a été proposé comme une alternative efficace en puissance optique à la DCO-OFDM. Cependant, l'ACO-OFDM dégrade considérablement l'efficacité spectrale, la moitié des sous-porteuses étant mises à zéro. De plus, à efficacité spectrale égale, l'ACO-OFDM devient moins efficace en puissance si le débit envisagé est élevé.

Pour améliorer l'efficacité en puissance sans dégrader l'efficacité spectrale des systèmes OFDM unipolaires, des techniques dites hybrides ont été proposées [50, 51]. Ces techniques sont basées sur la transmission simultanée de deux types de modulations. L'ADO-OFDM (Asymmetrically clipped DC biased optical OFDM) consiste à transmettre de l'ACO-OFDM sur les porteuses impaires et la DCO-OFDM sur les

porteuses paires, tandis que la HACO-OFDM (Hybrid asymmetrically clipped optical OFDM) remplace la DCO-OFDM par la PAM-DMT () qui fournit la même efficacité en puissance que l'ACO-OFDM.

Dans ces deux modulations hybrides, le bruit de clipping introduit par la composante ACO-OFDM est estimé au récepteur et soustrait des porteuses paires afin de restituer les données transmises. Les techniques hybrides permettent d'améliorer considérablement l'efficacité en puissance des systèmes DMT. Néanmoins, la génération du signal OFDM hybride, ainsi que l'estimation du bruit de clipping au récepteur nécessite 4 blocs IFFT/FFT supplémentaires, ce qui augmente excessivement la complexité temporelle et spatiale du système.

Dans le but d'améliorer l'efficacité en puissance des systèmes OFDM optiques, sans dégrader l'efficacité spectrale et/ou augmenter excessivement la complexité du circuit, nous avons proposé une nouvelle technique basée sur l'utilisation d'un companding asymétrique afin de réduire la puissance optique de la DCO-OFDM. En effet, la technique de companding est très largement employée dans les systèmes OFDM radio afin de réduire la dynamique du signal et prévenir des distorsions liées aux composants non linéaire, notamment l'amplificateur de puissance. Diverses fonctions de companding ont été proposées dans la littérature. Tout d'abord, les fonctions logarithmiques telles que la loi  $\mu$  et la loi A ont été appliquées pour compresser le signal de la parole. Ces fonctions ont été par la suite adaptées aux signaux OFDM radio. En effet, ces techniques sont basées sur l'augmentation de la puissance moyenne afin de réduire le facteur crête du signal OFDM. La puissance maximale étant maintenue constante, ces techniques ont une efficacité modérée en termes de réduction du PAPR.

Les fonctions de compression linéaires telles que la loi LNST (linear nonsymmetrical transform) [61] et la loi LCT (linear companding transform) [62] permettent d'avoir une meilleure performance en termes de réduction du PAPR et BER avec une complexité réduite.

### 5.5.1 Principe

La FIGURE 5.12 représente le schéma bloc de la technique DCO-OFDM asymétriquement compressée. Tout d'abord l'offset est calculé en fonction de la variance du signal discret

en sortie de l'IFFT,  $x(n)$ .

$$K_b = k\sqrt{E\{x^2(n)\}}. \quad (5.25)$$

Dans les systèmes DCO-OFDM classiques, l'offset est directement ajouté au signal continu en sortie du convertisseur numérique analogique (D/A) et un écrêtage à zéro est appliqué afin de forcer à zéro les amplitudes négatives persistantes. Comme il a été

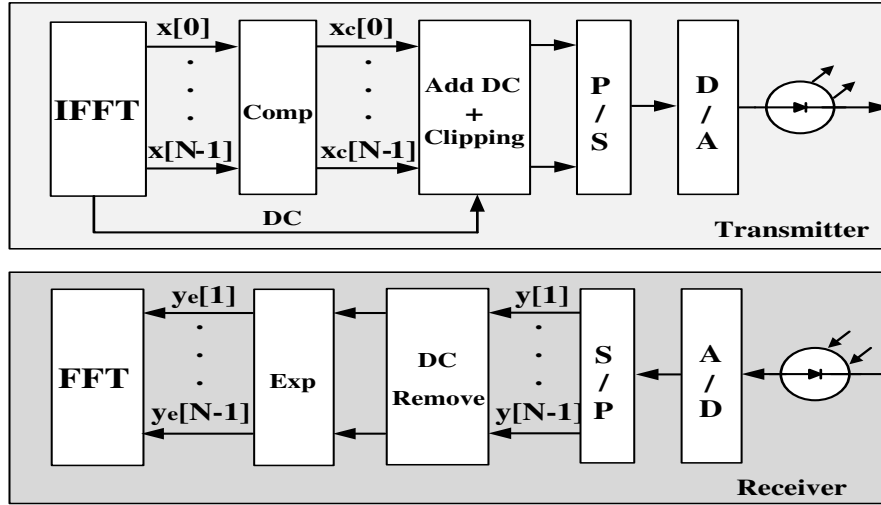


FIGURE 5.12: Le schéma de principe de la DCO-OFDM asymétriquement compressée

évoqué précédemment, le bruit de clipping augmente avec la constellation utilisée. Par conséquent, l'offset garantissant un bruit de clipping acceptable devient excessif pour des constellations supérieures ou égales à 64-QAM, ce qui affecte considérablement l'efficacité en puissance du système. Pour réduire l'offset requis, une approche est d'appliquer une fonction de companding linéaire au signal OFDM en sortie de l'IFFT afin de réduire sa dynamique, et par la suite l'impact de l'écrêtage à zéro. Le signal compressé peut être exprimé par,

$$x_c(n) = \begin{cases} x(n), & \text{if } x(n) > \nu \\ \alpha x(n), & \text{if } x(n) \leq \nu \end{cases} \quad (5.26)$$

où  $\alpha \in [0, 1]$  et  $\nu \in [\min\{x(n)\}, 0]$ . L'offset donné par (5.25) est ensuite ajouté au signal compressé comme suit,

$$x_{DC}(n) = x_c(n) + K_b, \quad n = 0, 1, \dots, N - 1. \quad (5.27)$$

Les valeurs négatives persistantes sont finalement mises à zéro afin de générer un signal électrique unipolaire. Au niveau du récepteur, le DC est tout d'abord soustrait du

signal discret reçu afin de restituer le signal compressé transmis. La transformation de companding inverse est ensuite appliquée au signal compressé afin de restituer le signal bipolaire avant companding comme suit,

$$y_e(n) = \begin{cases} y(n), & \text{if } y(n) > \nu \\ \frac{1}{\alpha}y(n), & \text{if } y(n) \leq \nu \end{cases} \quad (5.28)$$

Une démodulation OFDM est finalement appliquée au signal résultant et les données fréquentielles sont restituées comme dans le cas des systèmes DCO-OFDM classiques.

### 5.5.2 La fonction de companding

Dans ce travail, le concept de compression (companding) est employé afin de réduire le bruit de clipping dû au courant de seuil de l'émetteur optique. A cette fin, une nouvelle fonction de compression linéaire asymétrique a été conçue, pour réduire la partie négative du signal bipolaire en sortie de l'IFFT. L'allure de cette fonction est représentée à la FIGURE 5.13.

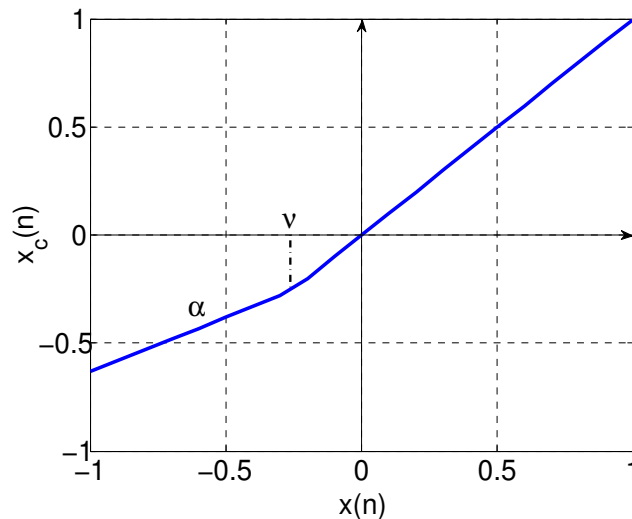


FIGURE 5.13: Allure de la fonction de companding linéaire asymétrique proposée

En effet, la fonction de companding proposée est une fonction linéaire avec deux degrés de liberté,  $\alpha$  et  $\nu$ . Cette fonction a deux avantages : 1/ La fonction n'ayant aucune discontinuité, elle ne génère aucune dégradation au niveau de la densité spectrale de puissance (PSD) du signal compressé ou du BER. 2/ Le paramètre  $\alpha$  est fixé en fonction de la constellation utilisée, tandis que le paramètre  $\nu$  est égal à la valeur moyenne de la



partie négative du signal bipolaire. Dans les cas de figure considérés dans ce travail (DFB ou VCSEL), les paramètres de la fonction  $\alpha$  et  $\nu$  peuvent être directement extraits du signal reçu. Cette approche innovante permet d'adapter dynamiquement les paramètres de la fonction aux caractéristiques statistiques du signal, fournissant ainsi une efficacité optimale en termes de réduction du bruit de clipping. Les paramètres adaptatifs n'étant pas transmis au récepteur, aucune dégradation du débit n'est introduite.

### 5.5.3 Résultats de simulations

#### 5.5.3.1 BER

Plusieurs simulations ont été réalisées afin d'évaluer les performances de la DCO-OFDM compressée pour différentes constellations. La FIGURE 5.14 représente les résultats de simulation du BER en fonction de  $E_{b(\text{elec})}/N_0$  de la technique DCO-OFDM avec et sans companding dans un canal AWGN. La comparaison est faite pour un offset de  $7\text{dB}$  et des constellations allant de 4-QAM à 256-QAM.

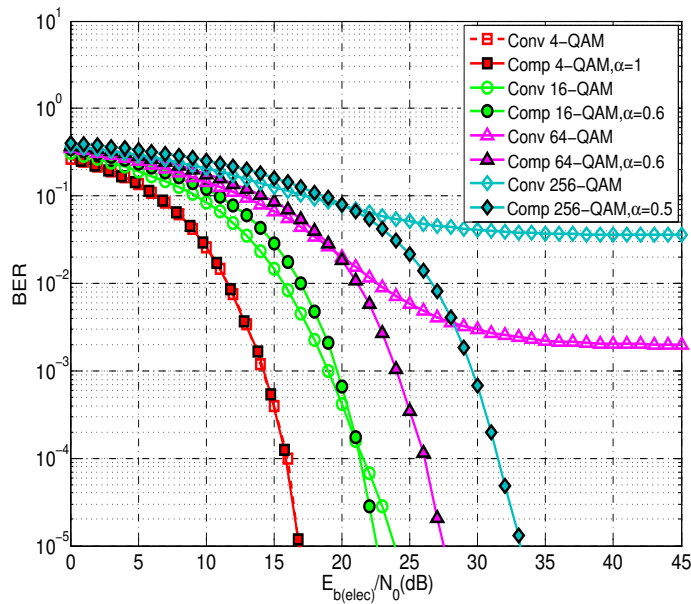


FIGURE 5.14: BER en fonction de  $E_{b(\text{elec})}/N_0$  pour différentes des deux techniques DCO-OFDM conventionnelle (Conv) et compressée (Comp)

Dans le système DCO-OFDM classique, pour des petites constellations (i.e. 4-QAM), le bruit de clipping est négligeable. Pour des constellations plus larges, le bruit de clipping devient dominant et les courbes de BER stagnent. Dans le système DCO-OFDM avec companding, le bruit de clipping étant négligeable pour une constellation

de 4-QAM, le paramètre  $\alpha$  est fixé à 1 afin de ne pas amplifier le bruit du canal qui est le bruit dominant. Pour des constellations plus larges, la fonction de companding avec un paramètre  $\alpha < 1$ , permet de réduire les amplitudes négatives persistantes à l'ajout de l'offset et par la suite le bruit de clipping. De plus, la fonction de companding a été conçue pour n'amplifier qu'une petite partie du signal au récepteur. Ainsi, l'amplification du bruit du canal n'est pas significative vis-à-vis le gain dû à la réduction du bruit de clipping. Par conséquent, les courbes de BER ne stagnent pas et des valeurs de BER assez faibles peuvent être atteintes même lorsqu'un offset modéré (i.e. 7dB) est employé.

### 5.5.3.2 Puissance optique

La FIGURE 5.15 compare l'efficacité en puissance optique des techniques DCO-OFDM, ACO-OFDM et DCO-OFDM compressée. Pour que la comparaison soit concluante, un ensemble de modulations particulières ayant le même rapport débit binaire à bande passante normalisée,  $Rb/BW$ , ont été considérées.

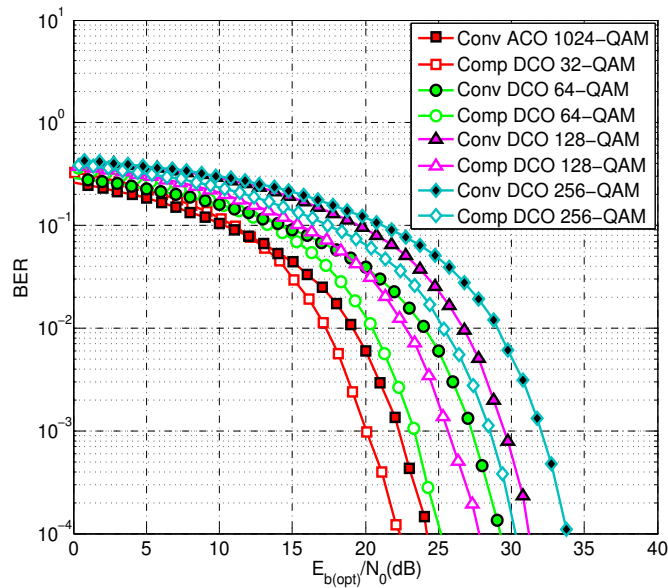


FIGURE 5.15: BER en fonction de  $E_{b(opt)}/N_0$  des techniques ACO-OFDM, DCO-OFDM and DCO-OFDM compressée

Pour un rapport  $Rb/BW = 5$ , 32-QAM DCO-OFDM compressée est comparée à 1024-QAM ACO-OFDM, l'ACO-OFDM étant plus efficace en puissance optique que la DCO-OFDM classique. Pour  $Rb/BW \geq 6$ , la DCO-OFDM conventionnelle a une meilleure efficacité en puissance que l'ACO-OFDM. Ainsi, pour  $Rb/BW \geq 6$ , la DCO-OFDM compressée est comparée à la DCO-OFDM classique.

Pour atteindre un haut débit, deux approches sont possibles : la DCO-OFDM avec un offset élevé ( $13dB$ ) ou l'ACO-OFDM avec une large constellation ( $M^2$ -QAM). Ces deux modulations nécessitent une puissance optique élevée pour transmettre le signal OFDM. La DCO-OFDM compressée, permet d'atteindre le même débit avec un offset modéré ( $7dB$ ). Par conséquent, pour un  $BER = 10^{-4}$  et  $Rb/BW = 5$ , un gain de  $2dB$  en puissance optique peut être atteint. Pour une efficacité spectrale plus élevée (i.e.  $Rb/BW \geq 6$ ), un gain de  $4dB$  en puissance optique est atteint.

## 5.6 Exploration expérimentale de la DMT pour les réseaux à bas coût

Tous les résultats présentés dans les sections précédentes sont basés sur une analyse théorique complétée et validée par les simulations. Dans cette section, une exploration expérimentale des performances de la modulation DMT est présentée. En effet, tout d'abord l'impact du VCSEL sur les modulations OFDM est analysé, modélisé et validé par les mesures. Ensuite, les performances de la modulation DCO-OFDM asymétriquement compressée sont expérimentalement évaluées.

### 5.6.1 L'impact du VCSEL sur la modulation DMT

#### 5.6.1.1 La caractérisation quasi-statique du VCSEL

Le VCSEL a plusieurs avantages par rapport à l'EEL (Edge Emitting Laser) à savoir : un courant de seuil très bas, un couplage efficace et aisé avec la fibre, un haut degré d'intégration dû à la cavité verticale et l'émission de la lumière par la surface, réduisant ainsi le coût de fabrication. Grâce à ces multiples avantages, entre autres, les VCSEL procurent une solution attractive pour les systèmes à haut débit, bas coût et basse consommation en puissance.

La caractéristique statique est communément employée pour modéliser le comportement non linéaire du VCSEL. Néanmoins, il a été démontré dans [76], que le point de compression  $1 - dB$  augmente avec le courant de polarisation, ce qui est incohérent avec la caractéristique statique. Une caractérisation quasi-statique prenant en compte

les propriétés particulières du VCSEL, notamment pour les signaux à large dynamique, a été proposé dans [76]. Une approche permettant d'évaluer l'impact du VCSEL sur la modulation DMT, est d'employer la caractéristique quasi-statique pour modéliser le VCSEL.

Le VCSEL considéré dans cette étude est un Finisar photonics avec une longueur d'onde de  $850nm$  et un bande passante de  $5GHz$  à  $7GHz$  pour des courants de polarisation allant de  $3mA$  à  $15mA$ . La FIGURE 5.16 représente les caractéristiques statique et quasi-statiques du VCSEL en fonction du courant de polarisation.

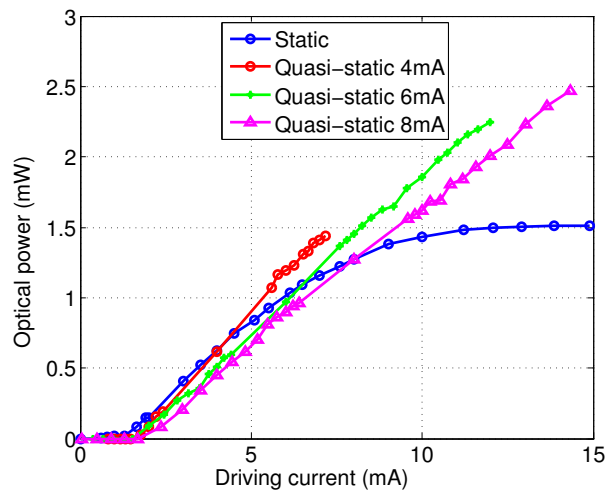


FIGURE 5.16: Les caractéristiques statique et quasi-statique du VCSEL Finisar Photonics pour différents courants de polarisation

Il est à remarquer que le VCSEL fonctionne avec des courants assez bas, ce qui est avantageux pour les liens optiques à bas coût. Comme il le montre la FIGURE 5.16, lorsqu'un courant DC est employé pour moduler le VCSEL (caractéristique statique), le courant de seuil statique du VCSEL est égal à  $1.2mA$ . Pour des courants inférieurs à  $6mA$ , la caractéristique est quasi linéaire avec une pente de  $0.22W/A$ . Pour des courants supérieurs à  $6mA$ , la non-linéarité augmente considérablement avec le courant jusqu'à atteindre la saturation à  $12mA$ .

Contrairement à la caractéristique statique, la pente de la caractéristique quasi-statique, ainsi que le courant de seuil, varient en fonction du courant de polarisation. De plus, les caractéristiques quasi-statiques sont quasiment linéaires. En effet, un signal sinusoïdal étant employé pour moduler le VCSEL autour du point de fonctionnement, le VCSEL ne subit aucun échauffement supplémentaire dû au signal RF.

### 5.6.1.2 Résultats de simulation

La liaison optique considérée dans cette étude est composée du VCSEL Finisar photonics, une fibre optique multimode d'une longueur de  $1m$  et une photodiode PIN avec une sensibilité de  $0.55A/W$ . Dans cette liaison, deux types de bruit sont présents : le bruit lié à la non-linéarité du VCSEL et le bruit optique. L'impact des non-linéarités de la fibre et de la photodiode sont négligeables. Le SNR prenant en compte l'impact du VCSEL et du bruit optique peut être exprimé par,

$$SNR = \frac{P_{RFout}}{P_{noise} + P_{NLD}} \quad (5.29)$$

où  $P_{RFout}$  est la puissance RF en sortie de la liaison,  $P_{noise}$  la puissance du bruit optique et  $P_{NLD}$  la puissance de la distorsion liée à la non-linéarité du VCSEL. La puissance du bruit optique présent dans la liaison est donnée par,

$$P_{noise} = (RIN \cdot I_0^2 + 2qI_0) \Delta f \cdot R_L + 4kT\Delta f \quad (5.30)$$

où  $I_0$  représente le courant moyen en sortie de la photodiode,  $\Delta f$  la bande passante,  $RIN$  le bruit d'intensité relatif,  $q$  la charge de l'électron,  $T(K)$  la température ambiante,  $k$  la constante de Boltzmann et  $R_L$  la résistance de charge. Le bruit du TIA (transimpedance amplifier) intégré dans la photodiode est supposé négligeable.

Pour la plage des courants photodétectés considérés dans cette étude, le bruit dominant est le bruit RIN. Le SNR relatif au bruit optique peut donc être exprimé par,

$$SNR_{noise} = \frac{P_{RFout}}{RIN \cdot I_0^2 \cdot \Delta f \cdot R_L} \quad (5.31)$$

Une approche pour simuler et évaluer l'impact de la non-linéarité du VCSEL sur la modulation DMT est d'employer les caractéristiques statique et quasi-statique pour modéliser le VCSEL. Les non-linéarités de la fibre optique et la photodiode étant négligeables, le récepteur peut être modélisé par une fonction linéaire d'une pente égale à l'intensité de la photodiode. En effet, un signal DMT est tout d'abord généré sous matlab et un offset est ajouté au signal. Les modèles statique et quasi-statique sont ensuite appliqués au signal biaisé afin de modéliser la non-linéarité de la liaison optique. Les symboles QAM en sortie du récepteur sont finalement restitués et comparés aux

symboles émis afin de calculer l'EVM (Error Vector Magnitude) évaluant l'impact de la non-linéarité de la liaison sur la modulation DMT.

L'EVM total regroupant l'impact de la non-linéarité et le bruit optique sur le signal DMT peut être exprimé par,

$$EVM = \sqrt{EVM_{noise}^2 + EVM_{NLD}^2} \quad (5.32)$$

où  $EVM_{NLD}$  est le résultat de la simulation sous matlab, de l'impact de la non-linéarité du VCSEL sur la constellation transmise, et  $EVM_{noise}$  est l'EVM correspondant au bruit optique calculé à partir du SNR théorique (5.31) à l'aide de la formule reliant le SNR à l'EVM,

$$SNR \approx \frac{1}{EVM^2} \quad (5.33)$$

La FIGURE 5.17 représente les courbes d'EVM total correspondant aux caractéristiques statique et quasi-statique en fonction du courant de polarisation.

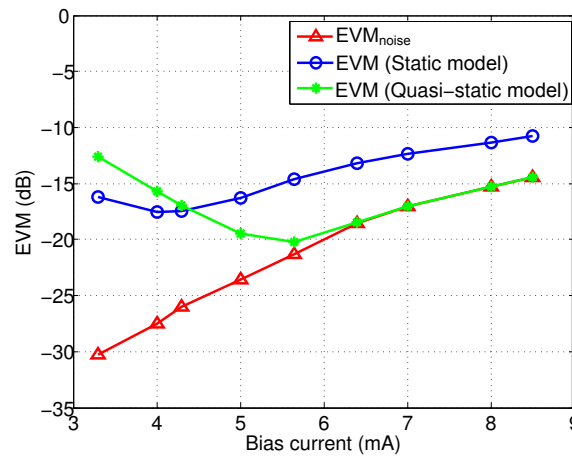


FIGURE 5.17: Comparaison des résultats de simulation des EVM statique et quasi-statique en fonction du courant de polarisation

Trois zones sont à distinguer sur la FIGURE 5.17. La première correspond à  $I_0 < 4.2mA$ , où les EVM statique et quasi-statique décroissent linéairement avec le courant de polarisation dû au bruit de clipping, qui est le bruit dominant. La différence entre les deux courbes est dû au fait que le courant de seuil quasi-statique est supérieur au seuil statique. La deuxième zone correspond à  $4.2mA \leq I_0 < 5.6mA$ . Dans cette zone, l'EVM statique commence à croître dû à l'effet de la non-linéarité, tandis que l'EVM quasi-statique continue à décroître parce que l'effet de la non-linéarité est négligeable et le

bruit de clipping est dominant. La troisième zone correspond à  $I_0 \geq 5.6mA$ , où le bruit optique est le bruit dominant. Ainsi, les deux courbes d'EVM statique est quasi-statique croissent en parallèle avec l'EVM issu du bruit optique (i.e. la courbe rouge sur la FIGURE 5.17). La différence entre les deux courbes est due à l'impact de la non-linéarité qui est négligeable dans le cas de la caractéristique quasi-statique.

### 5.6.1.3 Validation expérimentale

Afin de valider les résultats de simulation présentés dans la section précédente, et conclure par rapport à la pertinence de la caractérisation quasi-statique vis-à-vis des modulations DMT, un banc de test a été monté. Le protocole de mesure consiste à générer hors ligne un signal DMT sous Matlab et injecter le signal discret à un AWG qui permettra d'effectuer la conversion numérique analogique. Le signal résultant est ensuite injecté à l'entrée RF du VCSEL polarisé avec un courant de polarisation,  $I_{DC}$ . Le signal électrique en sortie de la liaison optique est ensuite mesuré et converti en un signal numérique à l'aide d'un oscilloscope. La constellation reçue est restituée hors ligne sous Matlab, et l'EVM comparant les constellations émise et reçue est finalement calculé pour les différents courants de polarisation considérés dans cette étude. La FIGURE 5.18 compare les résultats des mesures aux EVM issus de la simulation de l'impact des caractéristiques statique et quasi-statique sur le signal DMT.

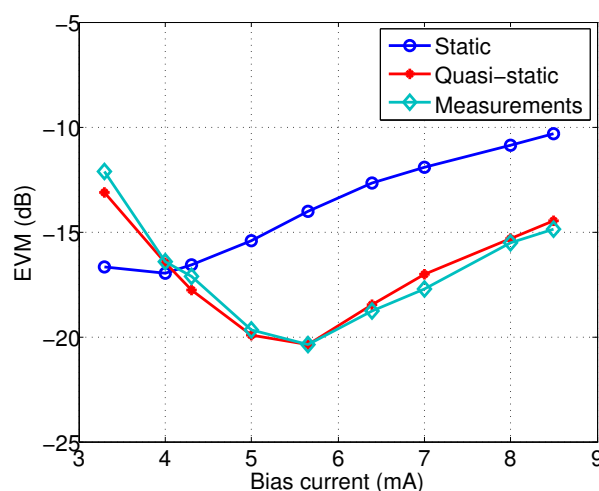


FIGURE 5.18: L'EVM mesuré vs les EVM statique et quasi-statique simulés en fonction du courant de polarisation

Comme le montre la FIGURE 5.18, l'EVM mesuré et l'EVM issu de la caractéristique quasi-statique sont superposés. En effet, comme prévu par l'analyse théorique et les

résultats de simulation, employer la caractéristique quasi-statique pour modéliser le comportement du VCSEL, permet de simuler correctement la non-linéarité du VCSEL et estimer son impact sur la modulation DMT.

### 5.6.2 DCO-OFDM compressée

Le banc de test présenté dans la section précédente a été également employé pour valider la technique DCO-OFDM compressée. Le VCSEL disponible au laboratoire étant un VCSEL à bas coût, a un bruit RIN très élevé et ne permettra donc pas d'avoir des résultats concluants quant à la réduction du bruit de clipping. De ce fait, l'émetteur optique utilisé pour la validation de la technique DCO-OFDM compressée est un laser DFB () avec un bruit RIN assez bas ( $-145dB/Hz$ ). Le bruit dominant dans ce cas, est le bruit de clipping. Les autres composants sont les mêmes que ceux présentés dans la section précédente.

Le protocole de mesure consiste à générer un signal DCO-OFDM sous matlab, avec et sans companding, et mesurer les EVM correspondants pour différents courants de polarisation. Les résultats de mesure, ainsi que les paramètres de la fonction de companding sont reportés sur la FIGURE 5.19. La modulation employée est une modulation 64 – QAM.

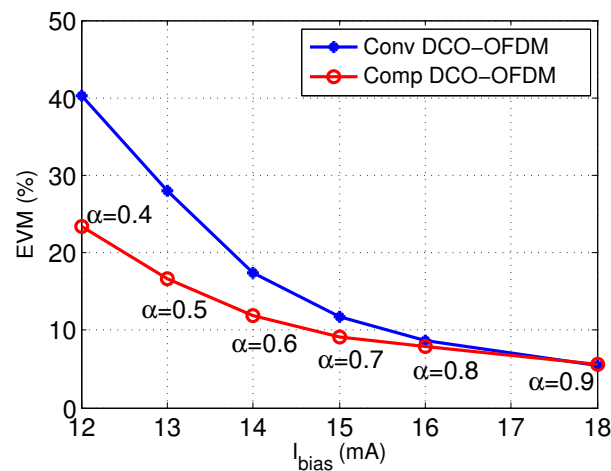


FIGURE 5.19: L'EVM mesuré de la technique DCO-OFDM sans (Conv) et avec (Comp) companding pour différents courants de polarisation

Pour des courants de polarisation assez élevés (i.e.  $I_{bias} > 18mA$ ), le bruit de clipping devient négligeable. Le paramètre  $\alpha$  est donc fixé proche de 1 pour ne pas amplifier le bruit optique. Le bruit de clipping est inversement proportionnel au



courant de polarisation. Ainsi, pour un courant de polarisation assez faible, le choix du paramètre  $\alpha$  doit satisfaire le meilleur compromis entre la réduction du bruit de clipping et l'amplification du bruit optique. La technique DCO-OFDM compressée avec un paramètre  $\alpha$  optimal, permet d'avoir un gain considérable en EVM. Pour un courant de polarisation de  $12mA$ , un gain de 17% en EVM ( $4.75dB$  en SNR) est atteint, permettant ainsi de réduire l'EVM de 40% à 23% (un système sans erreur).

## Conclusion

Le travail présenté dans cette thèse s'est focalisé sur deux thématiques principales : la réduction de la complexité liée à la propriété de la symétrie hermitienne dans les systèmes OFDM unipolaires et l'amélioration de l'efficacité en puissance optique des systèmes IM/DD.

Nous avons tout d'abord proposé une nouvelle technique permettant de générer des signaux OFDM réels sans avoir à imposer la symétrie hermitienne. Nous avons démontré que cette technique permet de réduire de 50% la complexité de calcul des systèmes IM/DD au niveau du récepteur et de l'émetteur, ce qui offre une réduction considérable de la consommation en puissance et en silicium (i.e. coût). Une variante de cette technique la combinant avec la Flip-OFDM a été également proposée. Cette dernière permet de réduire de 75% la complexité du récepteur.

Afin d'améliorer l'efficacité en puissance optique des systèmes IM/DD, nous avons proposé une nouvelle technique basée sur l'application d'une fonction de companding asymétrique au signal DCO-OFDM avant sa transmission via le canal optique. La fonction de companding inverse est appliquée au signal reçu afin de restituer les données transmises. Nous avons démontré que cette technique permet de réduire considérablement le bruit de clipping présent dans le signal DCO-OFDM, et par la suite l'offset requis. Les paramètres de la fonction de companding proposée permettent d'adapter la fonction aux caractéristiques statistiques du signal OFDM afin d'avoir un compromis optimal entre la réduction du bruit de clipping et l'amplification du bruit du canal. Ainsi, la technique DCO-OFDM compressée permet d'avoir un gain de  $4dB$  en puissance optique.

La dernière partie de ce travail a été consacrée à l'exploration expérimentale des modulations DMT. Nous nous sommes tout d'abord intéressées à l'impact du VCSEL sur les performances de la modulation DMT. Nous avons ainsi proposé une nouvelle modélisation de la non-linéarité du VCSEL basée sur la caractéristique quasi-statique. Nous avons ensuite démontré que cette modélisation est plus adaptée aux signaux dynamiques, tels que les signaux DMT. Les résultats de simulation basés sur cette modélisation sont en parfaite cohérence avec les mesures. Finalement, la DCO-OFDM

compressée a été expérimentalement validée. Les résultats de mesures ont montré que cette technique permet d'avoir à gain de  $4.75dB$  en SNR optique.

# Bibliography

- [1] R. W. Chang, "Synthesis of band-limited orthogonal signals for multichannel data transmission," *The Bell System Technology Journal*, vol. 45, no. 10, pp. 1775-1796, 1966.
- [2] P. Zhang, X. Tao, J. Zhang; Y. Wang, L. Li and Y. Wang, "A vision from the future: beyond 3G TDD," *IEEE Communications Magazine*, vol. 43, no. 1, pp. 38-44, 2005.
- [3] H. Schulze and C. Lueders, "Theory and Applications of OFDM and CDMA: Wideband Wireless Communications", Wiley, 2005.
- [4] W. Shieh and I. Djordjevic, "OFDM for optical communications," Academic Press, 2009.
- [5] S. Weinstein and P. Ebert, "Data Transmission by Frequency-Division Multiplexing Using the Discrete Fourier Transform," *IEEE Transactions on Communication Technology*, vol. 19, no. 5, pp. 628-634, 1971.
- [6] S. Hara and R. Prasad, "Multicarrier Techniques for 4G Mobile Communications," *Boston: Artech House*, 2003.
- [7] J. Liu and X. Lin, "Equalization in high-speed communication systems," *IEEE Circuits and Systems Magazine*, vol. 4, no. 2, pp. 4-17, 2004.
- [8] Cisco Visual Networking Index (VNI), February 2014.
- [9] David A. B. Miller, "Optical interconnects to electronic chips," *Applied Optics*, vol. 49, issue 25, pp. F59-F70, 2010.
- [10] I. B. Djordjevic and B. Vasic, "Orthogonal frequency division multiplexing for high-speed optical transmission," *Optics Express*, Vol. 14, Issue 9, pp. 3767-3775, 2006.

- 
- [11] W. Shieh and T. Yan, "Ultrahigh-Speed Signal Transmission Over Nonlinear and Dispersive Fiber Optic Channel: The Multicarrier Advantage," *IEEE Photonics Journal*, vol. 2, no. 3, pp. 276-283, 2010.
- [12] W. Shieh and C. Athaudage, "Coherent optical orthogonal frequency division multiplexing," *Electronics Letters*, vol. 42, no. 10, pp. 587-589, 2006.
- [13] J. M. senior, "Optical Fiber Communications Principles and Practice, 3rd Edition," *earson Education Limited*, 2009.
- [14] O. Gonzalez, R. Perez-Jimenez, S. Rodriguez, J. Rabadan and A. Ayala, "Adaptive OFDM system for communications over the indoor wireless optical channel," *IEEE Proceedings Optoelectronics*, vol. 153, pp. 139-144, 2006.
- [15] J. Armstrong and B. J. C. Schmidt, "Comparison of asymmetrically clipped optical OFDM and DC-biased optical OFDM in AWGN," *IEEE Communications Letters*, vol. 12, pp. 343-345, 2008.
- [16] J. Armstrong, "OFDM for Optical Communications," *Journal of Lightwave Technology*, vol. 27, pp. 189-204, 2009.
- [17] J. Armstrong and A. Lowery, "Power efficient optical OFDM," *Electronics Letters*, vol. 42, pp. 370-372, 2006.
- [18] J. Armstrong, B. J. C. Schmidt, D. Kalra, H. A. Suraweera and A. J. Lowery, "Performance of asymmetrically clipped optical OFDM in AWGN for an intensity modulated direct detection system," *Global Telecommunications Conference*, pp. 1-5, 2006.
- [19] S. C. J. Lee, S. Randel, F. Breyer and A. M. J. Koonen, "PAM-DMT for Intensity-Modulated and Direct-Detection Optical Communication Systems," *IEEE Photonics Technology Letters*, vol. 21, no. 23, pp. 1749-1751, 2009.
- [20] T. Anfray, "Etude et simulation des potentialités du Dual Electroabsorption Modulated Laser (D-EML) pour la montée en débit dans les futurs réseaux d'accès optique," *Laboratoire XLIM-C2S2*, 2013
- [21] "10-Gigabit-Capable Passive Optical Networks (XG-PON): Physical Media Dependent (PMD) Layer Specification," *ITU-T G.987.2*, 2009.

- [22] N. Ansari and J. Zhang, "Media Access Control and Resource Allocation: For Next Generation Passive Optical Networks, SpringerBriefs in Applied Sciences and Technology," *Springer Briefs in Applied Sciences and Technology*, 2013.
- [23] "IEEE Standard for Information technology– Local and metropolitan area networks– Specific requirements– Part 3: CSMA/CD Access Method and Physical Layer Specifications Amendment 1: Physical Layer Specifications and Management Parameters for 10 Gb/s Passive Optical Networks," *IEEE Std 802.3av-2009*, pp.1-227, 2009.
- [24] G. Kramer, M. D. Andrade, R. Roy, and P. Chowdhury, "Evolution of Optical Access Networks: Architectures and Capacity Upgrades," *Proceedings of the IEEE*, vol. 100, no. 5, pp. 1188-1196, 2012.
- [25] P. Vetter, "Next generation optical access technologies," *European Conference and Exhibition on Optical Communications*, pp. 1-42, 2012.
- [26] D. Qian, J. Hu, P. N. Ji, T. Wang, M. Cvijetic, "10-Gb/s OFDMA-PON for Delivery of Heterogeneous Services," *Conference on Optical Fiber communication/National Fiber Optic Engineers Conference*, pp.1-3, 2008.
- [27] A. W. Fang, B. Koch, E. Norberg, G. Fish, E. Hall, "Heterogeneous integration as a manufacturing platform for photonic integrated circuits," *IEEE Photonics Conferencs*, pp.87,88, 2013.
- [28] B. Charbonnier, S. Menezo, P. O'Brien, A. Lebreton, J. M. Fedeli, B. Ben Bakir, "Silicon photonics for next generation FDM/FDMA PON," *Journal of Optical Communications and Networking*, vol.4, no.9, pp.A29,A37, Sept. 2012
- [29] X. Q. Jin, E. Hugues-Salas, R. P. Giddings, J. L. Wei, J. Groenewald, J. M. Tang, "First real-time experimental demonstrations of 11.25Gb/s optical OFDMA PONs with adaptive dynamic bandwidth allocation," *Optics Express*, vol. 19, issue 21, pp. 20557-20570, 2011.
- [30] E. Hugues-Salas, R.P. Giddings, X.Q. Jin, J. L. Wei, X. Zheng, Y. Hong, C. Shu and J.M. Tang, "Real-time experimental demonstration of low-cost VCSEL intensity-modulated 11.25Gb/s optical OFDM signal transmission over 25km PON systems," *Optics Express*, vol. 19, issue 4, pp. 2979-2988, 2011.

- [31] Cisco, "The Zettabyte Era - Trends and Analysis," *Cisco White Paper*, 2013.
- [32] N. Cvijetic, "OFDM for Next-Generation Optical Access Networks," *Journal of lightwave technology*, vol. 30, no. 4pp. 384-398, 2012.
- [33] M. Jr. Finley, "Optical fibers in local area networks," *IEEE Communications Magazine*, vol.22, no. 8, pp. 22-35, 1984.
- [34] S. C. Webster, "Fiberoptic technology for local area networks," *Northcon/96*, pp. 147-150, 1996.
- [35] Y.-K. M. Lin, D. R. Spears, M. Yin, "Fiber-based local access network architectures," *IEEE Communications Magazine*, vol.27, pp. 64-73, 1989.
- [36] H. Azgomi, "Enabling enterprise 10 gigabit Ethernet deployment with long reach multimode optics," *Cisco White Paper*, pp. 1-10, 2007.
- [37] D. P. Clement, R. C. Lasky, D. Baldwin, (2002) "Alignment Metrology and Techniques in Handbook of Fiber Optic Data Communication," *Academic Press*, 2002.
- [38] S. Bois, "Next Generation Multimode Fibers and Standards," *Corning at the Spring BICSI Conference*, 2009.
- [39] P. Kolesar, "The Case for Extended Reach Multimode Objectives," *IEEE 802.3ba*, 2008.
- [40] Vixar Inc, <http://vixarinc.com/technology/vcSEL.html>.
- [41] J. A. Tatum, Y. Liu, "The VCSELs are coming", *Proceedings of the SPIE, Materials and Devices for Optical and Wireless Communications*, vol. 4905, pp 517-526, 2002.
- [42] J. Lee, F. Breyer, S. Randel, J. Zeng, F. Huijskens, H. P. van den Boom, A. M. Koonen, and N. Hanik, " 24-Gb/s Transmission over 730 m of Multimode Fiber by Direct Modulation of an 850-nm VCSEL Using Discrete Multi-Tone Modulation," *Optical Fiber Communication Conference and Exposition and The National Fiber Optic Engineers Conference*, paper PDP6, 2007.
- [43] J. Lee, F. Breyer, S. Randel, D. Cardenas, H. van den Boom and T. Koonen, "Discrete multitone modulation for high-speed data transmission over multimode

- fibers using 850-nm VCSEL,” *Optical Fiber Communication Conference*, paper OWM2, 2009.
- [44] E. Hugues-Salas, X.Q. Jin, R.P. Giddings, Y. Hong, S. Mansoor, A. Villafranca and J.M. Tang, “Directly Modulated VCSEL-Based Real-Time 11.25-Gb/s Optical OFDM Transmission Over 2000-m Legacy MMFs,” *IEEE Photonics Journal*, vol. 4, no. 1, pp. 143-154, 2012.
- [45] I. Neokosmidis, T. Kamalakis, J. W. Walewski, B. Inan and T. Spicopoulos, “Impact of Nonlinear LED Transfer Function on Discrete Multitone Modulation: Analytical Approach,” *IEEE Journal of Lightwave Technology*, vol. 27, pp. 4970-4978, 2009.
- [46] H. Elgala, R. Mesleh and H. Haas, “Predistortion in Optical Wireless Transmission Using OFDM,” *International Conference on Hybrid Intelligent Systems*, vol. 2, pp. 184-189, 2009.
- [47] T. Cseh and T. Berceci, “Optical transmission of OFDM NQAM signals by direct laser modulation,” *International Conference on Microwave Radar and Wireless Communications*, vol. 2, pp. 523-526, 2012.
- [48] International Engineering Consortium (IEC), “Operations Support Systems: Solutions and Strategies for the Emerging Network,” Janvier 2003.
- [49] S. C. J. Lee, F. Breyer, S. Randel, H.P.A. van den Boom and A.M.J. Koonen, “High-speed transmission over multimode fiber using discrete multitone modulation [Invited],” *Journal of Optical Networking*, vol. 7, issue 2, pp 183-196, 2008.
- [50] S. D. Dissanayake and J. Armstrong, “Comparison of ACO-OFDM, DCO-OFDM and ADO-OFDM in IM/DD Systems,” *Journal of Lightwave Technology*, vol. 31, no. 7, pp. 1063-1072, 2013.
- [51] B. Ranjha and M.Kavehrad, “Hybrid asymmetrically clipped OFDM-based IM/DD optical wireless system,” *Journal of Optical Communications and Networking*, vol. 6, no. 4, pp. 387-396, 2014.
- [52] F. Effenberger, D. Cleary, O. Haran, G. Kramer, Ruo Ding Li, M. Oron and T. Pfeiffer, “An Introduction to PON Technologies”, *IEEE Communications Magazine*, vol. 45, no. 3, pp. S17-S25, 2007.



- [53] M. Sharif, M. Gharavi-Alkhansari, and B. H. Khalaj, "New results on the peak power of OFDM signals based on oversampling," *IEEE International Conference on Communications*, vol. 2, pp. 866-871, 2002.
- [54] R. Bouziane, P. Milder, R. Koutsoyannis, Y. Benlachtar, J. Hoe, M. Glick and R. Killey, "Dependence of optical ofdm transceiver asic complexity on fft size," *National Fiber Optic Engineers Conference*, paper JW2A.58, 2012.
- [55] J. W. Cooley and J. W. Tukey, "An Algorithm for the Machine Calculation of Complex Fourier series," *Mathematics of Computation*, vol. 19, pp. 297-301, 1965.
- [56] A. Albert Raj and T. Latha, "VLSI Design," *PHI Learning*, 2008.
- [57] M. S. Moreolo, "Power efficient and cost-effective solutions for optical OFDM systems using direct detection," *International Conference on Transparent Optical Networks*, vol. 27, pp. 1-4, 2010.
- [58] N. Fernando, Yi Hong and E. Viterbo, "Flip-OFDM for Unipolar Communication Systems," *IEEE Transactions on Communications*, vol. 60, no.12, pp. 3726-3733, 2012.
- [59] E. Vanin, "Performance evaluation of intensity modulated optical ofdm system with digital baseband distortion," *Optics Express*, vol. 19, issue 5, pp. 4280-4293, 2011.
- [60] H. Elgala, R. Mesleh and H. Haas, "Practical considerations for indoor wireless optical system implementation using ofdm," *International Conference on Telecommunications*, pp. 25-29, 2009.
- [61] X. Huang, J. Lu, J. Zheng, K.B. Letaief and J. Gu, "Companding transform for reduction in peak-to-average power ratio of OFDM signals," *IEEE Transactions on Wireless Communications*, vol. 3, no. 6, pp. 2030-2039, 2004.
- [62] S. A. Aburakhia, E. F. Badran and D. A. E. Mohamed, "Linear Companding Transform for the Reduction of Peak-to-Average Power Ratio of OFDM Signals," *IEEE Transactions on broadcasting*, vol. 55, no. 1, 2009.
- [63] Pinlu Yang and Aiqun Hu, "Two-piecewise companding transform for PAPR reduction of OFDM signals," *International Wireless Communications and Mobile Computing Conference*, pp. 619-623, 2011.

- [64] W. O. Popoola, Z. Ghassemlooy and B. G. Stewart, "Pilot-Assisted PAPR Reduction Technique for Optical OFDM Communication Systems," *Journal of Lightwave Technology*, vol. 32, no. 7, pp. 1374-1382, 2014.
- [65] A. E. Jones, T. A. Wilkinson, and S. K. Barton, "Block coding scheme for reduction of peak-to-average envelope power ratio of multicarrier transmission systems," *IEEE Electronics Letters*, vol. 30, no. 8, pp. 2098-2099, 1994.
- [66] R. O'Neill and L.B. Lopes, "Envelope variations and spectral splatter in clipped multicarrier signals," *IEEE International Symposium on Personal, Indoor and Mobile Radio Communications (PIMRC'95)*, vol. 1, pp.71-75, 1995.
- [67] J. Tellado, "Peak to Average Power Reduction for Multicarrier Modulation," *PhD. dissertation, Stanford University*, 2000.
- [68] X. Wang, T. T. Tjhung and C. S. Ng, "Reduction of peak-to-average power ratio of OFDM system using a companding technique," *IEEE Transactions on Broadcasting*, vol. 45, no. 3, pp. 303-307, 1999.
- [69] Naiqian Zhang and Dong Li, "A New Nonlinear Companding Method for Reducing Peak-to-Average Power Ratio of OFDM Signals," *International Symposium on Antennas, Propagation and EM Theory*,
- [70] C. L. Wang and S. J. Ku, "A Low-Complexity Companding Transform for Peak-To-Average Power Ratio Reduction in OFDM Systems", *IEEE International Conference on Acoustics, Speech and Signal Processing*, vol. 4, pp.329-332, 2006.
- [71] X. Li, L. Tao, J. Zhang, Y. Wang, Y. Fang, J. Zhu, Y. Wang, Y. Shao and N. Chi, "Companding transform for PAPR reduction in coherent optical OFDM system," *Wireless and Optical Communications Conference*, pp. 46-47 , 2012.
- [72] J. Xiao, J. Yu, X. Li, Q. Tang, H. Chen, F. Li, Z. Cao and L. Chen, "Hadamard Transform Combined With Companding Transform Technique for PAPR Reduction in an Optical Direct-Detection OFDM System," *Journal of Optical Communications and Networking*, vol. 4, no. 10, pp. 1943-0620 , 2012.
- [73] M. Rostamzadeh, V. T. Vakily and M. Moshfegh, "PAPR reduction in WPDM and OFDM systems using an adaptive threshold companding scheme," *International Multi-Conference on Systems, Signals and Devices*, pp.1-6, 2008.

- [74] F. C. Lin, D. M. Holburn, V. A. Lalithambika, R. J. Mears, C. H. Hum and S. D. Walker, "A CMOS analogue predistortion circuit for wideband optical fibre links," *Canadian Conference on Electrical and Computer Engineering*, vol. 1, pp. 245-248, 2004.
- [75] T. Cseh and T. Berceci, "Optical transmission of OFDM NQAM signals by direct laser modulation," *International Conference on Microwave Radar and Wireless Communications (MIKON)*, vol. 2, pp. 523-526, 2012.
- [76] Z. Bouhamri, Y. Le Guennec, J. Duchamp, G. Maury, B. Cabon, "Quasi-static approach to optimize RF modulation of vertical-cavity surface-emitting lasers," *IEEE Topical Meeting on Microwave Photonics*, pp. 121-124, 2010.
- [77] P. V. Mena, J. J. Morikuni, S.-M. Kang, A. V. Harton and K. W. Wyatt, "A simple rate-equation-based thermal VCSEL model," *IEEE Journal of Lightwave Technology*, Vol. 17, pp. 865-872, 1999.
- [78] G. R. Hadley, K. L. Lear, M. E. Warren, K. D. Choquette, J. W. Scott and S. W. Corzine, "Comprehensive numerical modeling of vertical cavity surface-emitting lasers," *IEEE Journal of Quantum Electronics*, Vol. 32, pp. 607-616, 1996.
- [79] Chen Chen, P. O. Leisher, A. A. Allerman, K. M. Geib and K. D. Choquette, "Temperature Analysis of Threshold Current in Infrared Vertical-Cavity Surface-Emitting Lasers," *IEEE Journal of Quantum Electronics*, Vol. 42, no. 10, pp. 1078-1083, 2006.
- [80] A. Hangauer, J. Chen and M. C. Amann, "Square-root law thermal response in VCSELs: experiment and theoretical model," *Conference on Lasers and Electro-Optics (CLEO)*, pp. 1-2, 2008.
- [81] D. Root, J. Wood, and N. Tufflaro, "New techniques for non-linear behavioral modeling of microwave/RF ICs from simulation and nonlinear microwave measurements," *Design Automation Conference*, pp. 85-90, 2003.
- [82] B. Inan, S. C. J. Lee, S. Randel, I. Neokosmidis, A. M. J. Koonen, J.W. Walewski, "Impact of LED Nonlinearity on Discrete Multitone Modulation," *IEEE/OSA Journal Optical Communications and Networking*, vol. 1, no. 5, pp. 439-451, 2009.

- [83] G. Zhou, "Analysis of spectral regrowth of weakly nonlinear power amplifiers," *IEEE Communications Letters*, vol. 4, pp. 357-359, 2000.
- [84] A. A. M. Saleh, "Frequency-independent and frequency-dependent nonlinear models of TWT amplifiers," *IEEE Transactions Communications*, vol. 29, no. 11, pp. 1715-1720, 1981.
- [85] A. Ghorbani and M. Sheikhan, "The effect of Solid State Power Amplifiers (SSPAs) Nonlinearities on MPSK and M-QAM Signal Transmission," *International Conference on Digital Processing of Signals*, pp. 193-197, 1991.
- [86] C. Rapp, "Effects of HPA-Nonlinearity on a 4-DPSK/OFDM-Signal for a Digital Sound Broadcasting System," *Second European Conference on Satellite Communications*, pp. 179-184, 1991.
- [87] U. Onunkwo, Y. Li, and A. Swami, "Effect of timing jitter on OFDM based UWB systems," *IEEE Journal on Selected Areas in Communications*, vol. 24, no. 4, pp. 787-793, 2006.
- [88] L. Yang and J. Armstrong, "Oversampling to reduce the effect of timing jitter on high speed OFDM systems," *IEEE Communications Letters*, vol. 14, no. 3, pp. 196-198, 2010.
- [89] D. J. F. Barros, S. K. Wilson and J. M. Kahn, "Comparison of Orthogonal Frequency-Division Multiplexing and Pulse-Amplitude Modulation in Indoor Optical Wireless Links," *IEEE Transactions on Communications*, vol. 60, no. 1, pp. 153-163, 2012.
- [90] R. A. Shafik, S. Rahman and R. Islam, "On the Extended Relationships Among EVM, BER and SNR as Performance Metrics," *International Conference on Electrical and Computer Engineering*, pp 408-411, 2006.
- [91] [http://www.tek.com/sites/tek.com/files/media/media/resources/76W\\_22259\\_16.pdf](http://www.tek.com/sites/tek.com/files/media/media/resources/76W_22259_16.pdf)
- [92] <http://literature.cdn.keysight.com/litweb/pdf/5988-7976EN.pdf>
- [93] H. Samueli, "The design of multiplierless FIR filters for compensating D/A converter frequency response distortion," *IEEE Transactions on Circuits and Systems*, vol. 35, no. 8, pp. 1064-1066, 1988.

- 
- [94] J. Jung, S. Kim and K. Lee, "Droop Compensation Technique with Simple Structure for OFDM mobile transmitter," *IEEE International Symposium on Consumer Electronics*, pp. 1-4, 2006.
- [95] K. Van Acker, G. Leus, M. Moonen, O. van de Wiel and T. Pollet, "Per tone equalization for DMT-based systems," *IEEE Transactions on Communications*, vol. 49, no. 1, pp. 109-119, 2001.
- [96] T. Karp, M. J. Wolf, S. Trautmann and N. J. Fliege, "Zero-forcing frequency domain equalization for DMT systems with insufficient guard interval," *IEEE International Conference on Acoustics, Speech, and Signal Processing*, vol. 4, pp. 221-224, 2003.
- [97] M. H. Hsieh and C. H. Wei, "Channel estimation for OFDM systems based on comb-type pilot arrangement in frequency selective fading channels," *IEEE Transactions on Consumer Electronics*, vol. 44, no. 1, pp. 217-225, 1998.
- [98] S. Balasubramanian, G. Creech, J. Wilson, S. M. Yoder, J. J. McCue, M. Verhelst, W. Khalil, "Systematic Analysis of Interleaved Digital-to-Analog Converters," *IEEE Transactions on Circuits and Systems*, vol. 58, no. 12, pp. 882-886, 2011.